Evaluating the feasibility of studying propeller-wing interaction through ground-based high-speed experimental taxi-tests

A numerical study comparing a propeller powered aircraft in cruising free-flight with high-speed taxiing

Adithya Ramesh

Technische Universiteit Delft

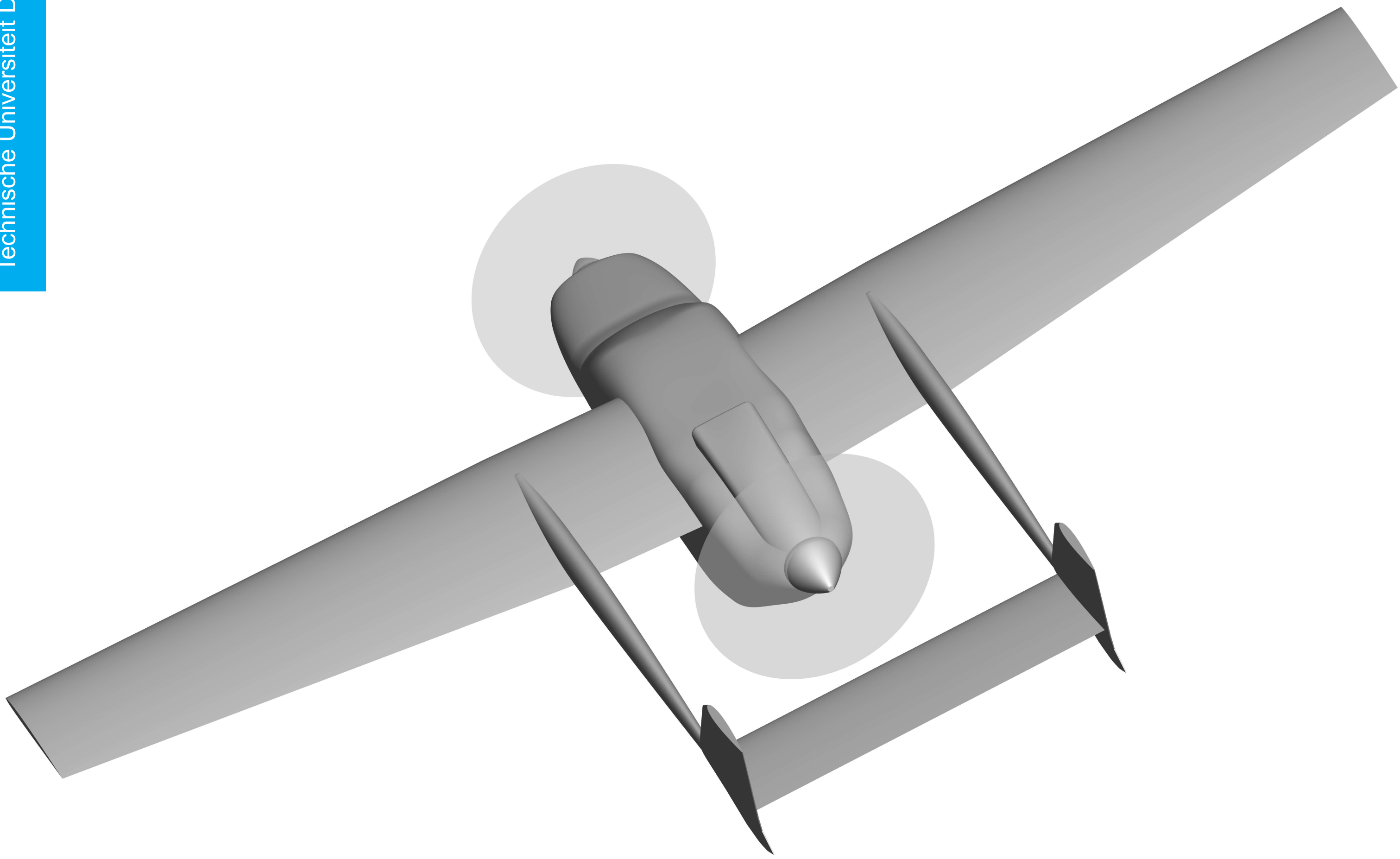

Delft
University of
Technology

Evaluating the feasibility of studying propeller-wing interaction through ground-based high-speed experimental taxi-tests

A numerical study comparing a propeller powered aircraft in cruising free-flight with high-speed taxiing

by

Adithya Ramesh

to obtain the degree of Master of Science
at the Delft University of Technology,
to be defended publicly on Friday June 17, 2022 at 13:30 hours.

Student number:	5059089	
Thesis committee:	Prof. dr. ir. L. L. M. Veldhuis,	TU Delft, Chair & supervisor
	Dr. ir. T. Sinnige,	TU Delft, Examiner
	Ir. J. Melkert,	TU Delft, Examiner

TU Delft

Preface

Rising sea levels, extreme summer heats and winter colds, and frequent adverse weather phenomena. Undeniable telling signs of the current climate crisis brought about by years of accumulation of greenhouse emissions in the atmosphere, deforestation, pollution and encroachment of nature, and unsustainable practices and development.

While there is no immediate solution to these problems, it is still possible to makes changes to mitigate these effects. As scientists, it is our responsibility to make fact and knowledge based technological progress and development to a more sustainable and less harmful future.

With the development and introduction of new propulsion systems comes the chance and need to test and evaluate them in novel ways. This thesis, that I have spent the last year working on, is to evaluate the feasibility of a novel ground-based approach to testing new integrated propeller powered propulsive systems being developed to make aviation cleaner.

Though small, I hope my contribution has a positive impact and helps in the development of cleaner airplanes that we should all be able to travel by and benefit from, guilt-free.

In recent years, I have frequently felt left behind and unable to cope with the way 'modern' technology has shaped our community. I have frequently found myself yearning for simpler times but, with the knowledge humanity possesses today. One of my related interests in this personal feeling is in history. I have felt that a revisit to the past would be a relief to my person. In this regard, I found my thesis to have a personal connection with me.

While I am definitely happy that my thesis encompassed a range of topics of my primary interest– low-speed aerodynamics and flight performance, personally and more importantly, I find it comforting that it involves propellers and the ground effect, two aspects that were responsible for success of the Wright Flyer, the first recorded powered flight. This comfort is further deepened by the fact that along with the Wright brothers, many early aviation pioneers were related to the bicycle business. While clean propeller airplanes are a solution for regional travel, it is my firm belief that bicycles are the future of everyday mobility.

Many are calling the current state of aviation and technological development as a revolution. The revolution began a while ago, but this thesis that is in regard to the testing of new systems, signals the beginning of my involvement.

I am grateful to my family and friends for supporting and encouraging me to pursue my passion and love for aviation. I have enjoyed my time at TU Delft and The Netherlands over the past three years and have been fortunate to meet the people I have.

I would like to thank my supervisor, Prof. Leo Veldhuis, for his constant support, feedback, enthusiasm, and active involvement in my thesis. It has been a privilege to work with someone I respect so much. This goes beyond just being a distinguished and accomplished professor. I look forward to seeing your success with the DEAC programme!

Adithya Ramesh
Delft, June 2022

Summary

The response of the aviation industry to the current climate crisis has been to accelerate, diversify, and further the development of sustainable propulsion systems and airframes. The propeller is an interesting choice for regional aviation due its high propulsive efficiency at low speeds and flexibility in combining with different propulsion systems being developed.

The DEAC has an experimental flying testbed on which new propulsion systems will be tested after replacing the current ones. However, there are concerns with reliability, certification, and the feasibility of performing thorough academic investigations in cruise flight. It is intended to initially investigate the testbed through high-speed taxi-tests, as testing on the ground offers a safe and accessible environment with the possibility of using a multitude of equipment, personnel, and instruments. This could allow for better understanding of the systems before they fly.

The interaction between the rear propeller and the horizontal tail of the testbed, that sits behind it and in its slipstream, has been likened to a propeller-wing combination found on larger regional airplanes. The associated acoustics, vibrations, and general interaction effects investigated with the testbed are of interest for the intended experimental tests dealing with propeller-airframe interaction, so that the findings could be used to benefit regional aircraft.

By numerically investigating the testbed in cruise flight and comparing it with investigations of it in taxi-tests, the expected differences and their consequences thereof, during the final experiments can be estimated. This would help determine whether such an approach to testing is feasible or if not, what possible changes could be made to utilise the testbed for a ground-based high-speed test.

A representative digital twin of the airplane was self-designed and developed. The operational settings and parameters were chosen for a typical steady and level cruise free-flight and a steady ground-run at a speed lower than the take-off decision speed, to satisfy regulatory requirements. High-fidelity fully viscous RANS based CFD numerical simulations were performed on a half-airplane model with half-propeller disks with a steady-state approach with the determined settings as boundary conditions. The fully turbulent Spalart-Allmaras turbulence model was used to estimate the viscous stresses.

The airplane being tested in ground-run had a Reynolds number 60% of its value in free-flight. The location of the quarter-chord point of the mean geometric chord of the wing had a ground clearance of 16.7% of a full-wing span. The angle of attack in free-flight was chosen to be the same as the incidence angle of the airplane on the ground at 2°. The required thrust to be produced by the propellers was the same as the drag of the unpowered airplane obtained from CFD, so as to keep a steady flight condition, and were numerically implemented as constant and uniform pressure rises across their faces.

The influence of the ground relatively increased the lift-to-drag ratio of the unpowered configuration by 16.9% and powered by 17.3%. The propeller power relatively decreased the lift-to-drag ratio in free-flight by 12.2% and by 11.9% in ground-run. The relative decrease in the dynamic pressure based thrust coefficient between free-flight and ground-run, required to maintain steady flight at the chosen speeds, for each propeller, was 7.07%. The ground restricted the formation of the downwash behind the wing and an upward postive offset in the vertical location of the flow features at the tail was seen.

The presence of wake vortices shed from the fuselage and interacting with the tail were discovered. The vortices on either side of the symmetry plane caused a positive lift force to be produced by the tail section located between them in their upward rotational direction side. The rest of the span on its outboard side, had a downward rotational influence. The propeller power increased the positive and negative lift force. In ground-run, an approximately consistent increment of 0.06 for the spanwise sectional lift coefficient distribution of the tail from free-flight, was seen, with the peaks influenced by the vertical position of the primary vortices.

The evolution of these vortices, both in the near-field around its development and in its trajectory downstream, and its interaction with the propeller and tail are inherently unsteady effects. By considering this along with the neglected propeller swirl, the expected differences between the current steady-state analysis and an unsteady realistic case, based on literature, were deemed large.

The limitations of this study, that were performed on a simplified representation of the decades old flying testbed, preclude a definitive answer to the research question. More thorough investigations are required to understand the unsteady interaction effects and implications to the airframe and acoustics, but, the findings offer future researchers an insight to the phenomena that could be encountered during the intended experimental flight tests.

Contents

List of Figures

List of Tables

Nomenclature

Abbreviations

AMSL	Above mean sea level
AVL	Athena Vortex Lattice
BVI	Blade vortex interaction
CAD	Computer aided design
CAS	Calibrated airspeed
CFD	Computational fluid dynamics
CG	Centre of gravity
CHT	Cylinder head temperature
DEAC	Dutch Electric Aviation Centre
DNS	Direct numerical simulations
ESDU	Engineering Sciences Data Unit
EW	Empty weight
GA	General aviation
GCI	Grid convergence index
HT	Horizontal tail
IAS	Indicated airspeed
IGE	In-ground effect
ISA	International standard atmosphere
LE	Leading edge
LES	Large eddy simulations
MGC	Mean geometric chord
MLDGW	Maximum landing weight
MTOW	Maximum take-Off weight
NS	Navier-Stokes
OAT	Outside air temperature
OEI	One-engine-inoperative
OGE	Out-of-ground effect
P0	Power-off
P1	Power-on

POH	Pilot operating handbook
RANS	Reynolds Averaged Navier-Stokes
RPM	Rotations per minute
SA	Spalart-Allmaras
SI	International system of units
TE	Trailing edge
VLM	Vortex lattice method
VSP	Vehicle Sketch Pad

Sub and superscipts

∞, 0	Freestream
i	Indexing variable
x	Streamwise/ axial/ longitudinal axis component (X-coordinate)
y	Lateral axis component (Y-coordinate)
z	Vertical axis component (Z-coordinate)
HT	Property related to horizontal tail
IGE	Property in in-ground effect
OGE	Property in out-of-ground effect
ref	Reference
W	Property related to mainwing

Variables

α	Angle of attack
$\alpha_{C_L=0}$	Zero-lift angle of attack
$\Delta\alpha_{0_g}$	Change in zero-lift angle of attack in ground effect
$\Delta C_{D\text{strut}}$	Additional drag due to struts
$\Delta C_{D_{\text{landing gear with tyre}}}$	Additional drag due to landing gear and tyre
ΔC_{D_S}	Component source drag coefficient based on component reference area
ΔC_D	Incremental drag coefficient
$\Delta C_{l_{HT}}$	Increment in HT sectional lift coefficient
ΔP	Rise in static pressure across actuator disk
ΔV	Velocity increment
$\dot{m}$	Mass flow-rate
μ	Coefficient of viscosity or molecular viscosity
μ_T	Turbulent viscosity or eddy viscosity
ν	$= \mu/\rho$, Kinematic viscosity

ν_T	$= \mu_T/\rho$, Turbulent kinematic viscosity
Φ	Solution used in estimating convergence ratio
ρ	Density
σ	Influence coefficient
τ_{w_x}	Streamwise component of wall shear stress, along X-coordinate
τ_w	Wall shear stress
$\tilde{\mu}$	Modified eddy viscosity
ξ_x	Streamwise vorticity component, along X-coordinate
AR	$=b^2/S$, Mainwing aspect ratio
AR_{eff}	Mainwing effective aspect ratio in ground effect
b	Span
b_{HT}	Horizontal tail span
b_W	Mainwing span
c	Chord
$C_{D\text{minPOH}}$	Minimum coefficient of drag as estimated from the POH
$C_{D\text{min}}$	Minimum coefficient of drag
C_{Di}	$= \frac{D_i}{q_\infty S_{ref}}$, Coefficient of induced drag
C_D	$= \frac{D}{q_\infty S_{ref}}$, Coefficient of drag
$C_{f_{\text{lam}}}$	Skin friction coefficient for laminar flow
$C_{f_{\text{trs}}}$	Skin friction coefficient for transitional flow
$C_{f_{\text{turb}}}$	Skin friction coefficient for turbulent flow
C_{f_x}	$= \frac{\tau_{w_x}}{\frac{1}{2}\rho_\infty V_\infty^2}$, streamwise component of coefficient of skin friction, along X-coordinate
C_f	$= \frac{\tau_w}{\frac{1}{2}\rho_\infty V_\infty^2}$, Coefficient of skin friction
$C_{L\text{max}}$	Maximum coefficient of lift
$C_{L\text{min}D}$	Coefficient of lift at minimum drag
$C_{L_{\alpha=0}}$	Lift coefficient at zero angle of attack
$C_{L_{\alpha_g}}$	Lift curve slope in ground effect
C_{L_α}	Lift curve slope in free-flight
C_{L_g}	Coefficient of lift in ground effect
$C_{l_{HT}}$	HT sectional lift coefficient
C_{l_W}	Wing sectional lift coefficient
C_L	$= \frac{L}{q_\infty S_{ref}}$, Coefficient of lift

C_l	Sectional lift coefficient
$C_{m\text{CG}}$	Coefficient of pitching moment about CG
C_{m_α}	Magnitude of pitch stability
C_m	$= \frac{M}{q_\infty S_{ref} c}$, Coefficient of pitching moment
C_{P_T}	$= \frac{P_T - P_\infty}{q_\infty}$, Coefficient of total pressure
C_P	$= \frac{P - P_\infty}{q_\infty}$, Coefficient of pressure
D	Drag force, propeller diameter
D_i	Induced drag force
e	Oswald efficiency factor
h_i	Representative grid element edge length
k	Lift-induced drag constant
L	Lift force, length
M	Pitching moment
P	Static pressure
P_∞	Freestream reference pressure
P_T	$= P + q$, Total pressure
q	$= \frac{1}{2}\rho V^2$, Dynamic pressure
q_∞	$= \frac{1}{2}\rho_\infty V_\infty^2$, Freestream dynamic pressure
R	Convergence ratio
r	Grid refinement ratio
Re	Reynolds number
Re_{MGC}	Reynolds number based on MGC
S_{ref}, S_W	Mainwing reference area
T	Propeller thrust
t	Thickness
T_C	$= \frac{T}{\rho_\infty V_\infty^2 D^2}$, Propeller coefficient of thrust based on freestream dynamic pressure
U, V	Velocity
U_0, V_∞	Freestream Velocity
U_x	Streamwise/ axial velocity component, along X-ccordinate
U_y	Tangential velocity component, along Y coordinate
U_z	Tangential velocity component, along Z coordinate
V_1	Decision speed
$V_{L/D_{\text{max}}}$	Glide speed at maximum lift-to-drag ratio

V_R	Rotate speed
V_S	Stall speed- clean configuration
x, X	Streamwise/ axial/ longitudinal location, along X-coordinate
y, Y	Spanwise/ lateral location, along Y-coordinate
y^+	Non-dimensional wall distance
z, Z	Vertical location, along Z-coordinate

1

Introduction

1.1. Aviation and the climate crisis

It is a well known scientific fact that the cumulative increase in global greenhouse emissions over the last decades has been having adverse effects on our climate. The alarming rise in global temperatures is causing melting polar ice caps to raise the sea-level and flood low-lying areas, cause unexpected and prolonged adverse weather phenomena such as heat waves and polar vortices, and strain the world's food security with droughts and floods.

The mobility industry has also contributed to this crisis, be it automotive, marine, or aerospace. The kerosene combustion based propulsion systems that drive the industry have been targeted as a reason for the emission of harmful greenhouse gases. The automotive industry has been successfully mass manufacturing battery electric vehicles for a few years now, as its response to decreasing the emissions produced by the vehicle itself. By using electricity stored in batteries to drive motors, there is no combustion and release of gases by the vehicle itself.

A similar response by the aviation industry to introduce electric aircraft has been difficult in the recent past owing to the limitations of current day battery technology that limits the flight time and range [1]. However, there has been technological development of hybrid/ electric propulsion systems to power airplanes and these systems are likely to be a part of our near future. The current state of aviation technology seems to be at a transitional one and moving away from kerosene based combustion and towards alternative combustion, hybrid, or electric designs. In addition to their advantages of being more quiet, environmentally clean, and supposedly economical than current aircraft [2], there is an urgency to become less dependent on the limited oil resources [1].

Unlike the automotive industry that virtually only uses the piston engine, the aviation industry makes use of different types of engines depending on the mission requirements of the aircraft. With the growing interest in regional aviation, the choice of the propulsion system as a whole can have consequences on the feasibility and acceptance of new-age aircraft, which are expected to be produced in large numbers [3]. It is therefore important that the most promising systems be well understood and responsibly developed.

The purpose of a propulsion system is to provide kinetic energy to a certain mass flow of air. The thrust produced is the product of this added velocity increment ΔV to the mass flow rate $\dot{m}$, as given in Equation 1.1 [4].

$$T = \dot{m}\Delta V \tag{1.1}$$

The propulsive efficiency of a system is defined as its ratio of useful power output to rate of energy input [5]. This is represented in Equation 1.2 in terms of velocity increment, and is one of commonly efficiencies used to indicate the effectiveness of a propulsive system.

$$\eta_\mathrm{p} = \frac{2}{2 + \Delta V/V_\infty} \tag{1.2}$$

For a given required thrust, a high propulsive efficiency would be achieved by increasing the mass flow rate and decreasing the velocity increment to the flow by the system.

Turbojet and turbofan engines are designed to add a large velocity increment to the flow. This leads to having low propulsive efficiencies at low speeds. Turbofans have a large compressor fan situated ahead of the main engine core. While some of the air passing through the fan will be used in combustion, the rest would accelerate and pass around the core. This increase in bypass ratio increases the propulsive efficiency as a larger mass flow is accelerated, thereby, reducing the need to add velocity through combustion for the same required thrust [4].

Such engines have been growing bigger in diameter to increase their bypass ratios. However, physical constraints on the size, and the associated drag and structural penalties of the nacelle and pylons, place a limitation on doing so.

Though these systems allow for faster travel, the consequences of the low efficiencies of these systems for regional transport, has historically been seen during the aviation industry's response to the oil crisis of the 1970s– a rethink of the propeller [6].

Propellers have a high effective bypass ratio and provide a large mass of air with a small amount of velocity increment to generate the required thrust. They have an inherently higher propulsive efficiency than turbojets and turbofans, at low speeds [5].

With the growth in regional aviation and the interest in utilising airplanes and airports of different sizes, the propeller is the prime choice of propulsion due to these advantages, amongst others such as size and weight, over turbojet and turbofan engines, for these mission requirements. This choice of having a high propulsive efficiency device allows for focusing on making its driving system more efficient, thereby, making the entire system more efficient and attractive.

However, propellers have their drawbacks such as noise and unsteady loads on the airframe. These can limit their usage at airports, reduce cabin comfort, and prevent maximisation of the airframe design. Studies have been performed on propeller integration in different configurations to better understand and limit these undesirable effects during design and development [7][8].

1.2. Dutch Electric Aviation Centre

International agreements, such as the Paris Agreement signed in 2016, have motivated countries to focus their technological growth on sustainability. The requirement of reducing *all* greenhouse emissions in regional aviation, falls to the member countries that signed the agreement.

The Dutch Electric Aviation Centre (DEAC) [9] at Teuge, The Netherlands, is a consortium of research and educational institutions of various academic levels, companies, and government bodies, formed to contribute to national schemes and meet the desired climate goals within aviation. The body intends to provide knowledge to the industry in its transition to a more sustainable future by conducting research into hybrid and electric aviation, such as infrastructure, fuels and propulsion, safety and regulations, and of course, aircraft. TU Delft is responsible for the scientific study and has outlined a set of work packages to be done over the coming years. Within this umbrella, the university has performed research into noise measurements [10] and hydrogen centric engine modification [11][12].

For performing their investigations related to propulsion system integration, the DEAC procured a Reims built Cessna Skymaster 337F, shown in Figure 1.1, to be used as an evolutionary flying testbed.

Figure 1.1: The Cessna Skymaster 337F being used as an experimental flying testbed by the Dutch Electric Aviation Centre [9]. Image credits and source: DEAC website.

1.3. Cessna Skymaster

The Cessna Skymaster family of airplanes, was developed by Cessna during the 1950s and produced from 1960 through to 1980 [13] [1].

The Cessna Skymaster features a rather unique engine installation for a twin engine airplane; the two engines are mounted in an inline configuration. This design, with the pusher and tractor propellers having their thrustlines along the fuselage centreline, has a certain advantage over conventional wing mounted installations. In the conventional designs, in an one-engine-inoperative (OEI) condition, there is a significant increase in the drag generated on the side with the dead engine. This can cause an unfavourable yawing moment [14]. With an inline configuration, this problem is negated, as any excess drag caused by a wind-milling propeller is approximately along the fuselage centreline. Hence, no significant correction to the rudder will be required [15].

The DEAC intends to modify the components of the propulsion systems for its studies related to electric aviation. The modifications will include replacing the propeller and engine, as part of progressing to a hybrid and eventually, electric airplane. Tests could involve running only one engine which has a modified propulsor or propeller. This configuration allows for this to be done safely. Even companies such as Ampaire [16] and VoltAero [17] are using variants of the Cessna Skymaster as experimental flying testbeds to prove their concepts and have successfully retrofitted their airplanes with electric motors. Different versions of the Skymaster have also been investigated by NASA, with a focus on the acoustics of its power-plant [18] [19].

The DEAC has a research oriented intention to this airplane and has identified another design feature that would be helpful in studying the propulsion systems. The ‘enclosure’ provided by the booms can allow for fitting instruments around the rear propeller to conduct measurements during tests.

1.4. Motivation

As part of the workpackages outlined in the DEAC programme, this thesis focuses on the one related to the interaction between the rear propeller and the horizontal tail. The rear propeller is scheduled to be replaced and investigated with the above mentioned advantages of the ‘enclosed’ inline configuration. The current two-bladed McCauley [20] propeller is planned to be replaced by a three-bladed MT [21] MTV-18 series propeller.

To study the characteristics and interaction effects of the integrated propeller, instruments will be placed on the outside of the airplane. These instruments will be used in acoustic, structural, and aerodynamic tests, to name a few. The DEAC intends to initially perform dynamic high-speed taxi-tests on the ground before flying it with the new systems [2]. This offers a safer testing environment with the possibility of utilizing more equipment and personnel. Moreover, such an equipment laden aircraft would need additional clearance and certification to fly. Changes to operational limits after re-certification [22] could further hinder flight tests due to new constraints.

The changes in the testing environment and operating conditions between ‘free-flight’ and ‘ground-run’, are expected to affect the aerodynamics and performance characteristics of the aircraft. Hence, it is required to know what these changes are, and compare the two scenarios, to identify the consequences of performing these tests. By doing so, the possibility and/ or extent to which these ground-run tests can be done before actual flight, can be determined. Moreover, different research groups can individually define the envelope of their test programmes, once they are aware of the modifications in the flow-field. This could also possibly increase the number and types of tests, as the ground-runs offer a safer testing environment, a shorter turn around time, and the possibility of using more instruments.

The interaction of the testbed’s rear propeller slipstream with the tail can be likened to a wing-mounted propeller-wing interaction as seen on regional aircraft. Hence, the results derived from this interaction would be valuable to larger aircraft.

The rear propeller is situated directly in the wake of the front propeller, fuselage, and exhaust from the rear engine. The local flow-field that will interact with the installed propeller is an interesting topic to be investigated as these will further influence the horizontal tail-slipstream interaction that is to be investigated.

---

[1] For the remainder of this report, ‘Skymaster’ will be used to refer to the DEAC airplane under investigation, whereas ‘Cessna Skymaster’ will be used in generic terms.

[2] Such tests will be referred to as ‘ground-run’ for the remainder of this report

Prior to conducting experiments, it is valuable to have an insight into the aerodynamic flow-fields that would be encountered and the possible effects due to them. Such an insight would aid in reducing and understanding experimental data and in planning and executing the experiments. High-fidelity numerical studies on a digital twin are a viable option for such a preliminary investigation intended to be used for experimental planning, as they have become economical, fast, developed, and allow for closer inspection of interesting characteristics calculated over the entire desired flow-field.

1.5. Thesis objective

The primary research question that has been formulated based on the motivation of investigating the interaction between the rear integrated propeller and horizontal tailplane is

> *What are the propeller-airframe interaction effects, and what are the consequences of the changes to these effects when the airplane is investigated in high-speed taxi-tests instead of in free-flight?*

The differences in effects of propeller interaction is dependent on the differences between the two testing environments and settings. By having an experimentally validated digital twin with good correlation for the ground-run studies, the expected changes in free-flight can be better approximated and derived. Additionally, the basic aerodynamic characteristics of the testbed need to be established. Hence, these requirements form the following sub-research questions that support the main question and need to also be answered.

1. What are the general aerodynamic characteristics of the Cessna Skymaster digital twin?
2. What are the aerodynamic interaction effects due to the installed propellers?
3. What are the different environmental testing conditions and their associated influences thereof?
4. What are the different aircraft operational settings and their associated influences thereof?
5. How do results based on a simplified digital twin of the aircraft and its propellers compare with experimental flight testing?

The objective of this reported research study aimed at answering this research question is

> *To evaluate the feasibility and consequences of testing new integrated propellers in ground-run by comparing it with free-flight, through a combined CFD–flight test study*

This ground-based approach to testing provides a novel method to experimentally investigate and evaluate propeller-airframe interaction with the use of a full-scale flying testbed.

1.6. Thesis approach

Being a ‘preliminary’ investigation in the wider view of this research programme, the chosen approach of developing a numerical digital twin that could be used for planning experiments in the future was essential and done on the basis of feasibility, reliability, speed, cost, and efficiency.

The geometry of the digital twin was self-designed and developed based on information obtained from literature. Hence, there were differences between it and the flying experimental testbed.

Low-fidelity potential flow-based numerical tools were used to gain an initial and basic understanding of the characteristics of the lifting surfaces of the intended digital twin. This provided a baseline for comparing the more representative and detailed high-fidelity fully-viscous simulations with.

For the finite lifting surfaces, vortex-lattice-method (VLM) simulations were utilised with inviscid analyses. The ability of one of the used VLM tools to include a ground clearance and study its influence thereof, was valuable in understanding the change in airplane characteristics in ground effect. Another of the used tools, had the ability to include viscous effects into its inviscid VLM results. This was possible as it interpolated viscous results from a 2D panel-method based numerical solver that could also solve the boundary layer equations in an iterative manner with considerations to the essentially inviscid flow outside of the layer. This feature allowed for studying the influence of the Reynolds number on aerodynamic properties to make limited comparisons with the fully-viscous numerical results.

A majority of this research was performed with high-fidelity Reynolds Averaged Navier-Stokes (RANS) equations based Computational Fluid Dynamics (CFD) numerical method on the complete airframe model of the simplified digital twin of the Skymaster. The numerical studies were steady-state analyses of a half-airplane and half-propeller disk model. The fluid medium was defined as incompressible with constant density and viscosity representative of the altitudes of flight operations. The propellers were numerically modelled as actuator disks with constant and uniform pressure rises across their faces.

Limited experiments were to be performed to validate the developed digital twin. However, the CFD analyses brought to light underlying unsteady phenomena that could not be treated within the framework of this research. Hence, the flight tests were not performed due to the large deviation expected between the simplified model developed here and an experiment.

However, these findings could be treated as *'lessons towards experiments'*, which is also the theme of this report.

1.7. Thesis limitations

The simplified geometry of the digital twin will have differences with the Skymaster. The consequences of the chosen simplifications to the airframe are unknown without experimental data or comparisons with more detailed models, but can be qualitatively guessed, as has been done wherever possible and deemed required. Similarly, the simplified propeller model does not account for the shape and influence of the blades. That has been left untreated at this stage. But, the choice of propeller parameters is an important operational setting that should be considered for more accurate models, and has been recommended after comparing the numerical findings of this reported research with more detailed studies reported in literature.

The swirl velocity in the slipstream was not modelled for either propeller to keep the computational cost of this preliminary investigation with two centreline propellers, low. While the influence of the swirl on a wing interacting with a slipstream is qualitatively known, the effect of this simplification is not quantified here. However, it was concluded that by including the opposite swirls of the propellers' slipstreams, the symmetric representation of results reported here, due to a half model being analysed with a numerical symmetry boundary condition along its plane of symmetry, would no longer be symmetrical, in addition to having other effects, as discussed later on.

Unsteady blade loading and propeller-airframe interaction effects relevant to acoustic and vibrational studies were not modelled. The steady-state approach also meant that the newly discovered fuselage wake vortices that passed through the rear propeller plane and interacted with the tail, which is expected to be inherently unsteady, could not be addressed appropriately. However, wherever necessary, the report mentions literature sources to highlight what changes could be expected by evolving this study from a steady-state approach to an unsteady time dependent solution. This has been deemed crucial due to the results found in this study.

1.8. About this report

This master thesis report contains the relevant works and important findings of the student researcher's study. The thesis is split into different chapters to offer a logical and clear understanding of the research.

- **Chapter 1:** Introduction

  The current chapter is the first and introductory chapter of this report. It describes the need, motivation, and research framework of the performed study.

- **Chapter 2:** Overview of Related Topics

  This chapter provides an overview of related topics that were of interest here.

- **Chapter 3:** Background Information

  This chapter talks about the design and development of the geometry and the associated airplane parameters. It lists the operating conditions and parameters and is the basis for the performed numerical studies and intended experiments.

- **Chapter 4:** Numerical Methods

  This chapter provides details on the numerical methods that were used in this research.

- **Chapter 5:** Results

  This chapter contains results from the numerical studies. A breakdown of the performance characteristics of the Skymaster along with the flow-field phenomena at the settings of interest, have been discussed.

- **Chapter 6:** Conclusions and Recommendations

  The conclusions that have been drawn based on the discussed results are covered here. These conclusions are of the research statement and indicate the degree to which they were answered. Recommendations to further develop this study have been made here.

- **Appendix A:** Geometry: Supplementary material

  This section contains drawings of the developed digital twin along with certain images used for this process and presents some extremely relevant information that could have an impact on the numerical results discussed in this report.

- **Appendix B:** Rear engine air intake of the Cessna Skymaster: Supporting information

  This section presents and discusses certain important design specifications of the air intake for the rear engine that were considered during the development of the numerical model, and their consequences.

  This air intake was found to be crucial and much effort was put into its understanding and inclusion.

- **Appendix C:** Numerical results: Supplementary material

  This section contains additional results or information relevant to it, and supplements the main content.

Note on units

A large amount of information gathered for this study was obtained in imperial units due to their popularity in general-aviation (GA) usage. Such information has been mentioned in their native units along with their international-system-of-units (SI) converted values that were used in this study.

2

Overview of Related Topics

This chapter presents findings from literature that were used for understanding the expected, discovered, and investigated phenomena.

2.1. Introduction

Using the Cessna Skymaster 337F flying testbed, the DEAC intends to experimentally study certain aspects of propeller-airframe interactions. Topics, such as the unsteady loading on the airframe due to the propeller slipstream and the contribution of the propeller to the acoustic field, are of interest to be experimentally investigated. Experimental tests to understand these topics for the cruise phase of a flight plan, the longest phase that is usually considered while characterising airplane efficiency and cabin comfort, would normally be performed in cruising free-flight. By doing so, the testing environment and aircraft operational settings could be the same as a typical flight operation, thereby, providing investigators with highly relevant and directly usable information.

The DEAC is considering performing investigations on an airport runway in the form of high-speed taxi-tests, before flight tests. Such a testing approach in a safer and more accessible environment allows for the use of more equipment and personnel and avoids the need for certification to fly with externally mounted instruments in possibly precarious positions.

The focus of this reported research was at understanding the differences that would occur to the propeller-airframe interaction when investigated in such a fashion rather than in cruising free-flight, and their consequences thereof.

A key difference in the testing environment between free-flight and ground-run is the proximity of the aircraft to the ground. The ground is known to alter the flow-field by acting as a barrier and preventing its development around the aircraft, as would normally occur far away from it [23]. This influence is commonly referred to as the ‘ground effect’ and is considered important when an aircraft is flying in proximity to the ground with a ground-clearance less than two full-wing spans [15].

Information from literature relevant to the ground effect and applicable to the research reported here, are discussed in section 2.2.

During a ground-run operation, the testbed would be accelerated to achieve a desired airspeed, held constant at that airspeed while acquiring data (like a steady and level cruise flight), and decelerated to finally stop at the end of the runway. As per the regulations defined in 14-CFR-Part-23 / EASA-CS-23, a multi-engine airplane, like the testbed under investigation, exceeding a certain decision speed referred to as V_1, has to take-off as it will not be able to stop without performing a runway excursion. This airspeed is defined to be between the stall speed V_S and 110% of V_S. During the intended experiments, the testbed has to remain on the ground. Hence, it cannot exceed this definition of the decision speed. Thus, for this study, an airspeed of 80% of the decision speed V_1 was considered as the testing speed during a ground-run operation.

A typical economical cruise airspeed is 150% of the stall speed [15], which is higher than what can be achieved during a ground-run operation when the testbed is operated on an airport runway length subject to the above mentioned regulations.

Atmospheric properties, such as air density and viscosity, vary with altitude [24]. By considering such a difference in the atmospheric properties between the different testing altitudes along with the difference in airspeeds, there is a difference in the operating Reynolds number between free-flight and ground-run. This Reynolds number is a crucial parameter in understanding and characterising aerodynamic investigations, as it has an influence on the nature of the viscous boundary layer that forms on any object moving in a viscous fluid medium [25]. The Reynolds numbers for every component in a ground-run operation were considered as being 60% of their values in free-flight, for this study.

The difference to the boundary layer characteristics that would occur due to a reduction in Reynolds number, will affect the performance, that is the generation of lift and drag forces, of an airfoil section [26]. Lifting surfaces and propeller blades utilise airfoils for generating the required forces and their performance would also be influenced by the Reynolds number [27].

Information from literature relevant to the influence of the Reynolds number and applicable to the research reported here, are discussed in section 2.4.

Propeller performance characteristics are influenced by their installation and exposure to non-uniform inflow [27]. Here, the front propeller of the testbed is integrated into the nose of the fuselage having a typical general aviation design. This propeller is located in the upwash of the fuselage and the fuselage is located in its slipstream. The fuselage of the testbed has air inlets on its nose which are located just behind the front propeller nearer to its hub. The rear propeller is installed in a pusher configuration into the fuselage. In this study, it was seen that this propeller plane encountered the wake and downwash of the main wing, wake from the fuselage located ahead of it, and vortical structures being shed from the fuselage.

Information from literature relevant to the propeller model considered here, and the propeller related effects witnessed in the research reported here, are discussed in section 2.3.

The discovered vortical structures being shed from the fuselage passed through this rear propeller plane and were convected downstream where they interacted with the horizontal tail. A difference in relative vertical locations between such an oncoming streamwise oriented vortex and the leading edge of the wing it interacts with, results in different interaction effects, both on the influence of the vortex on the wing and the influence of the wing on the vortex [28]. It was found in this research, that the modification to the flow-field caused by the presence of the ground, resulted in a shift in vertical locations of the cores of the fuselage wake vortices at the leading edge of the horizontal tail.

The influence of such an interacting vortex on a wing is similar to the influence of a propeller slipstream interacting with a wing. The rotational or tangential velocity component of a vortex alters the spanwise distribution of the angles of attack along the wing it interacts with [29]. The swirl of a propeller slipstream also has a similar influence on a wing located in its slipstream [30].

Like how a vortex influences a wing, the wing also influences the vortex. This would usually be to the structure of the vortex. The leading edge of the wing causes a decrease in the axial velocities of the flow-field in its upwash. The resulting stagnation and possible flow reversal could alter the structure of the vortex in an unsteady and time varying manner [31]. A vortex influenced by this would also lead to it influencing the wing in an unsteady and time varying manner [32].

The passing of a vortex through a propeller plane, as was found in this reported study, is also a form of vortex-wing interaction like mentioned above. The rotation of the propeller blades, which are essentially twisted wings, adds additional factors to the interaction. Any vortex-propeller interaction is dependent on the relative rotational directions of both the propeller and the oncoming vortex, as this will determine the changes to the vortex behaviour that would occur due to it being influenced by the propeller blade [33]. The spanwise influence on the propeller blade due to the vortex will affect its thrust and torque production depending on the relative rotational directions [34].

Information from literature relevant to vortices and vortex-wing or vortex-propeller interaction, and applicable to the research reported here, are discussed in section 2.5.

Being a preliminary investigation with no prior information available to motivate the need of complex models, simplifications were incorporated into the methodology devised and followed in this research. Along with the topics relevant to the research, topics discussing the consequences of the simplifications and why the simplifications were eventually considered as limitations, are also discussed in the following sections of this chapter. These topics support the arguments put forth and discussed in section 5.9.

These limitations are mostly centred around the behaviour of the fuselage wake vortex and its interaction with the rear propeller plane and the horizontal tail. As was stated in section 1.6, a part of the methodology involved in answering the research question, included performing high-fidelity fully viscous RANS CFD numerical simulations on a simplified airplane model having half-propeller disks which were treated as having infinite blades producing a constant and uniform pressure rise and only changing the axial flow velocities with no introduction of swirl into the slipstream. This was done with the use of a steady-state approach. However, vortex dynamics are inherently unsteady phenomena, as will be explained in section 2.5

2.2. Influence of ground proximity

The common consensus in literature is that the influence of the ground was studied as early as 1912 by Albert Betz [35][3], who reported a decrease in the drag and an increase in the lift of a wing as it approached the ground.

This results in an increase in lift-to-drag ratio for aircraft operating in its proximity [36]. With increasing height, this ground influenced contribution to an increased lift-to-drag ratio decreases [37]. Once the ground-clearance of the aircraft is more than two times its full-wing span, it is considered to be free of the ground effect [15].

For the research of this report, the testbed in cruising free-flight has a ground-clearance far greater than this value. However, while performing a ground-run operation, its wing has a ground-clearance less than one wing span, as will be discussed in the next chapter. This warrants the consideration of the ground effect and treating it in a 'static' fashion as the ground-clearance of the airplane will remain constant as long as it does not leave the runway and perform a take-off maneuver [38], which it will not.

2.2.1. Ground effect: Fundamental model

Wieselsberger [23] extended Betz's work and developed the powerful 'method of images' where a mirror image wing was placed on the other side of the ground plane. This is diagrammatically represented in Figure 2.1. The vertical component of the disturbing velocities calculated by the Biot-Savart law for a representative vortex system act opposite the induced velocities of an undisturbed wing. This decreases the induced velocity and increases the effective angle of attack at the wing section, seen in the figure as a rotation of the resulting flow velocity vector (result of freestream and downwash) from V in free-flight to V' in ground effect, and consequently, decreases the induced drag produced by the wing.

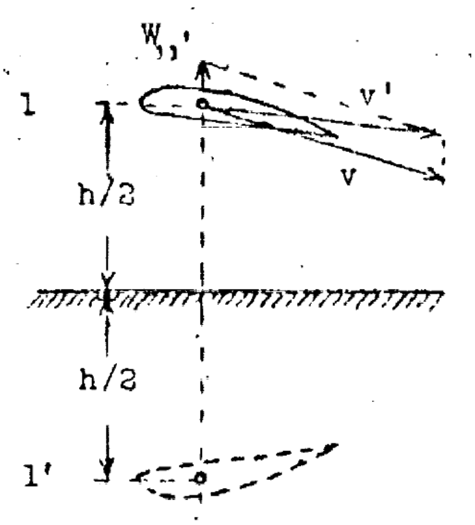

Figure 2.1: The 'method of images' developed by Wieselsberger [23], that shows the change in the induced flow velocity due to the opposing induction of the mirror vortex system. Image taken from Wieselsberger [23].

---

[3] An English translation of the document could not be found

Wieselsberger [23] developed a formulation for an influence coefficient, σ, that could be used as a multiplicative factor to convert an induced-drag polar calculated from a wing in free-flight to one in ground proximity. This relation is shown in Equation 2.1.

$$\sigma = \frac{1 - 0.66\ h/b}{1.05 + 3.7\ h/b} \tag{2.1}$$

This relation was based on experimental results of a wing at a height of half its wing span and with an assumed elliptical loading. This formulation agreed well with experimental flight tests performed using a biplane, over the linear part of the lift polar and away from both extremities of the polar [39].

Over the years, different formulations have been developed to be applicable to different height-to-span, h/b, ratios, other than just the originally investigated $h/2$.

Equation 2.2 is an extension of Equation 2.1 and is applicable for wings having their height-to-span ratios between 0.033 and 0.25 [40]. By calculating the influence coefficient σ in this manner, the induced drag polar in ground effect can be obtained from a known free-flight polar through Equation 2.3.

$$\sigma = \frac{1 - 1.32\ h/b}{1.05 + 7.4\ h/b} \tag{2.2}$$

$$C_{D_i}\text{IGE} = (1 - \sigma) \times C_{D_i}\text{OGE} \tag{2.3}$$

As will be shown in the next chapter, the digital twin of the Skymaster under investigation had a height-to-span ratio of 0.16 . As this falls within the allowed value for using Equation 2.2, which has been developed from the flight test validated formulation in Equation 2.1, it has been used in subsection 5.2.2 to convert the estimated induced drag in free-flight over a polar obtained from the CFD studies to include the ground effect at the clearance under investigation.

The method of images has also been utilised in studying the ground effect in a potential flow-based vortex lattice method solver, for the numerical methods described in chapter 4. subsection 4.2.2 mentions the activation of the mirror vortex system in the numerical tool while investigating the influence of the ground on a numerical model of the lifting surfaces of the intended digital twin.

2.2.2. Influence of mirror vortex system

When implementing the method of images, the vortex system used to describe an undisturbed wing is mirrored about the ground plane. The bound and trailing vortices of the image have their individual contributions to the modification at the wing. These individual contributions are discussed below and supported by Figure 2.2 [41].

- The figure *(a)* shows the influence of the trailing vortices. The vertical induced velocity component of the downwash field is decreased and the effective angle of attack is increased. The induced upwash field is stronger near the centre. This increases the lift curve slope, reduces the induced drag, and concentrates more lift towards the centre. These effects increase with decreasing height and are not very dependent on the angle of attack.
- The figures *(b)* and *(c)* show the induced velocity field by the bound vortex on two uncambered airfoils at different angles of attack. The induced velocity fields are against the free-stream and tend to decrease lift. For the low to moderate angle, there is an induced vertical velocity near the rear which is similar to an increase in camber, and hence, lift. This effect decreases with increasing angle or camber. The increase in camber is proportional to $\Delta V/V_\infty$ and the effects are less for a wing than an airfoil, due to the finite length of the bound vortex [42]. Rather, the reduction in velocity causes an increase in pressure and hence, an increase in lift [15].
- Figures *(c)* and *(d)* show the effect of thickness by representing the airfoil as a doublet with the source at the leading edge and the sink at the trailing edge. The induced field is relatively independent of angle of attack. It tends to increase the effective velocity over the wing. The induced field also induces a negative camber effect that decreases lift. However, the resulting changes to the forces are very small compared to the induction caused by the bound vortex.

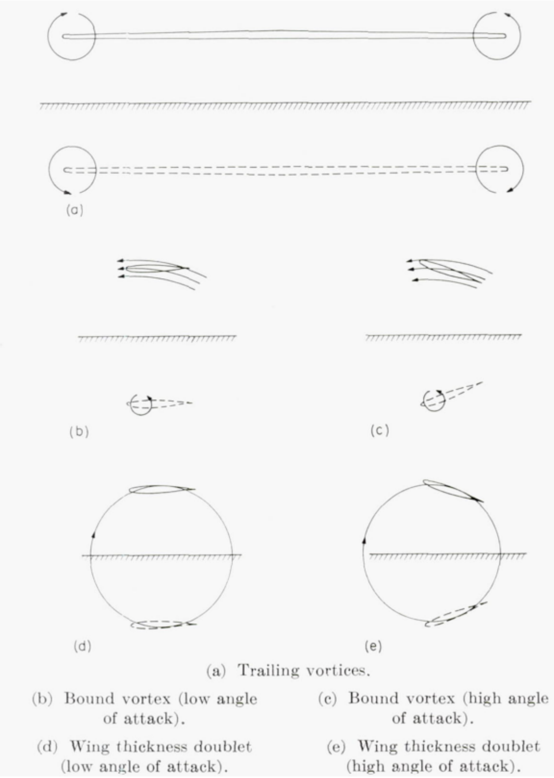

(a) Trailing vortices.

(b) Bound vortex (low angle of attack).

(c) Bound vortex (high angle of attack).

(d) Wing thickness doublet (low angle of attack).

(e) Wing thickness doublet (high angle of attack).

Figure 2.2: Interference effects due to the bound and trailing image vortices mirrored about a ground plane, by Furlong and Bollech [41].

2.2.3. Ground influence on aerodynamic performance

For a two-dimensional airfoil, the change in lift and drag forces with height from the ground, is dependent on the geometry of the airfoil, particularly its camber and thickness. Figure 2.3 presents compiled results showing the influence of camber and thickness on the variation of lift coefficient with decreasing height for moderate angles of attack [43][44][45]. Interpretation of this figure is discussed following it.

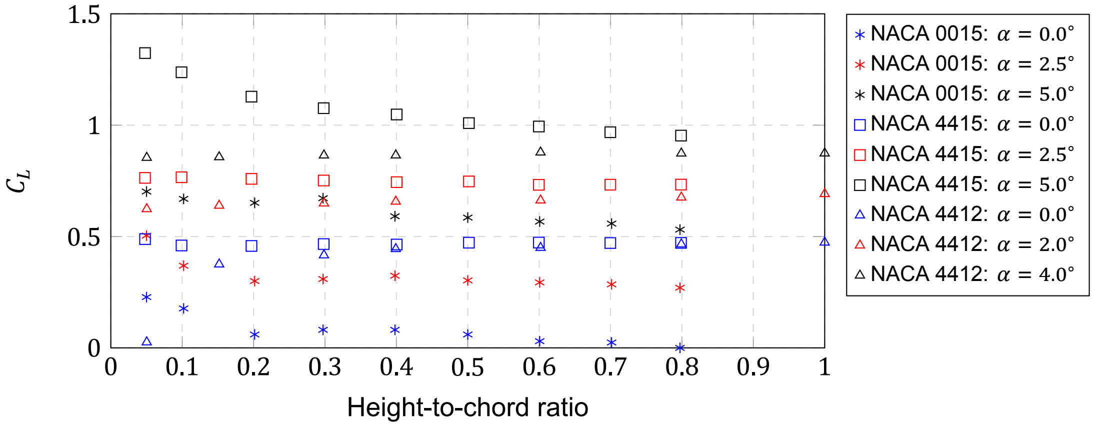

Figure 2.3: Compiled results from [43][44][45] showing influence of camber and thickness on lift coefficient of airfoils at different heights, at angles of attack relevant to the Skymaster in this study.

For moderate height-to-chord ratios, which are greater than 0.6[46], the influence of camber and thickness to the airfoil lift in ground effect are not very significant. At lower clearances, the symmetric airfoil shows a decrease in lift with decreasing height, due to a suction force generated by accelerating air in the convergent passage formed between the lower side of the airfoil and the ground [43].

With the addition of camber, the lower side of the airfoil becomes more ‘flat’ and decreases the suction force, thereby marginally increasing the lift [44].

As an interpretation of the modifications in ground effect is the increase in camber, there is an increase to the suction peak at the leading edge. With decreasing thickness, a loss in upper surface suction due to separation could occur, thereby resulting in lower coefficients than a thicker airfoil with the same geometric camber [45].

The height-to-chord ratios of the mainwing and the horizontal tail of the Skymaster are well above 1, as later mentioned in subsection 4.2.2. The height-to-span ratio, is the more important parameter to be considered for ground effect related discussions of these finite wings, at least for the main wing. Due to the presence of the large vertical tails at the ends of the horizontal tail, finite wing tip-effects would not be present. Figure 4.9 which is discussed later, shows the interaction between the symmetrical airfoil of the Skymaster’s tail and the ground plane.

The convergent-divergent passage that an airfoil forms with the ground, would lead to ‘blockage’ between the airfoil’s lower side and the ground, at positive angles of attack. This would force air to flow to the upper side of the airfoil and increase the suction at the leading edge [47]. This increase in suction is better understood as occurring due to an increase in the effective angle of attack as the local flow velocity vector has an increased tendency to pass above the airfoil due to the restricting blockage between the lower side and the ground [46].

For a finite wing, this would occur more prominently near the root, as the only direction for air encountering the blockage would be to go above the wing. At the wing tips, the excess air would flow outward rather than over it. This results in a difference in the spanwise increment to the lift coefficient in ground effect, with more lift being concentrated towards the centre [47].

With the addition of end plates, like the twin vertical tails on either side of the horizontal tail of the Skymaster, a larger ram pressure is built up on the underside of the wing. This increases the lift increment of the finite wing section by a larger amount than a wing with free tips [40]. The increase in pressure provides a ‘cushioning’ effect to the tail of the aircraft [39].

The increase in induced camber with decreasing height in ground proximity is airfoil dependent but can be seen from measured drag polars. An increase in the minimum drag coefficient for a 2D airfoil and its shift to a higher lift coefficient is interpreted as an increase in camber [48]. The addition of vortex drag in a wing, which is not present in an airfoil, limits this shift to a lower coefficient of lift. This was reasoned in subsection 2.2.2. The increase in lift-to-drag ratio for a wing is higher than for an airfoil [49]. This is due to the ground effect being more dominant on the three-dimensional induced velocities generated with finite wings, as described by the trailing vortex system.

Boom mounted angle of attack vanes and pressure sensors require to first be calibrated in free-flight outside of ground effect with upwash data. The influence of the ground on these sensors seems to be test dependent. For constant height fly-bys, it was found that nose-boom located flight measured angle of attack was seen to be affected by the ground and required a correction based on pitch attitude data from a tracking camera and upwash data from the wind tunnel test. A linear correction was derived with a value of $-2°$ at an indicated angle of $14°$ [50]. In a descent type [51] test with constant power and angle of attack setting, the nose-boom vane showed no sensitivity in angle of attack measurement in ground proximity when compared with non-aerodynamic sensors [52]. Though these are two experimental references that were looked at to understand the influence of the ground on a boom mounted vane, the different types of tests performed result in different treatments of the ground effect. The constant power sink would be a dynamic ground effect scenario whereas a constant height fly-by would be static ground effect [53]. The presence of dynamic ground effect factors in one of the tests does not really make them comparable and it remains for the DEAC to experimentally calibrate its own sensor in free-flight and derive its own correction, if required for ground-run.

The ground blocks the development of the downwash behind a wing. The change in the downwash field can be calculated by superimposing the downwash field of the mirror image on the original and algebraically summing the two with the assumption that the bound and trailing vortices are independent of ground height. The change in the field affects the tail of the aircraft. To maintain constant lift coefficient with decreasing height, the angle of attack needs to be reduced. The consequent increase in angle of attack at the tail is less than the decrease in the downwash angle [54].

The ground can influence control surfaces [50][55]. The increase or decrease in control surface effectiveness is dependent on the configuration, as there is an increase of pressure on the underside of the surface. For a GA aircraft, there is usually a decrease in effectiveness [15]. In the absence of a tail, the pitching moment coefficient increases [47] [56].

The general trend of ground influence with decreasing height is to increase the lift curve slope, decrease the drag coefficient, and increase the nose down pitching moment for conventional tail airplanes. However, the pitching moment change is significant and causes a loss in lift while trying to keep the nose up. Hence, the effective increase in lift coefficient in trimmed flight is lower than in untrimmed cases [51]. There is a rearward shift in the centre of pressure of the aircraft.

These expectations based on literature were also seen in the numerical results obtained during this research. These are presented and discussed in chapter 5.

While the lift increases and induced drag decreases with decreasing height, the profile drag is barely affected [40]. The peak lift-to-drag ratio which also increases, is achieved at higher lift coefficients [57]. At higher angles of attack and low clearances, the increased suction at the leading edge needs to overcome an increased adverse pressure gradient, and a thicker wake forms [43].

The increase in lift and lift curve slope is compared to an increase in the effective aspect ratio of the wing at that height [58]. By interpreting Wieselsberger's [23] formulation as, the percentage increment in aerodynamic efficiency (here, lift-to-drag ratio) or effective aspect ratio for a wing in ground effect at a given height would be the same irrespective of the aspect ratio of the wing, Figure 2.4 can be used to estimate the increase in effective aspect ratio [57].

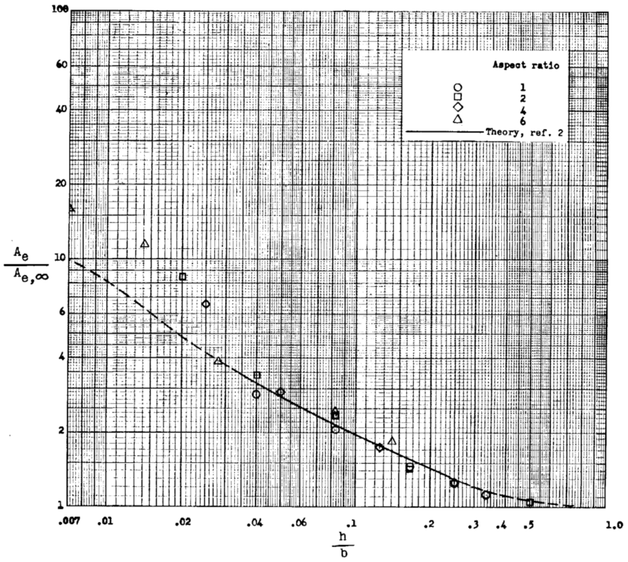

Figure 2.4: Change in effective aspect ratio, represented as a ratio of the effective aspect ratio in ground effect to the original geometrical aspect ratio, with height of the wing from the ground represented in terms of the height-to-span ratio, by Fink and Lastinger [57].

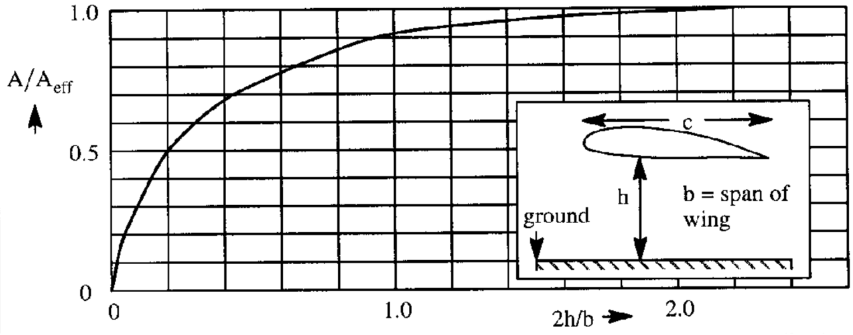

Figure 2.5: Clearer interpretation of the increase in effective aspect ratio for a wing in ground effect at different height-to-span ratios, based on Figure 2.4 by Fink and Lastinger [57]. Image obtained from Roskam [59].

Figure 2.5 obtained from Roskam [59] is a clearer representation of the increase in aspect ratio with decreasing wing height from the ground and is based on the original interpretation made by Fink and Lastinger [57] to Wieselsberger's [23] formulation, which was shown in Figure 2.4.

This particular plot has been used later on in section 5.2 while estimating the effective aspect ratio for the Skymaster in ground-run having a height-to-span ratio of 0.167 and original aspect ratio of 7.1, as will be presented along with other aircraft specifications in chapter 3.

The increase in the lift curve slope is usually accompanied with a decrease in the zero-lift angle of attack, which is proportional to the thickness-to-chord ratio of the mean geometric chord of the wing [59]. This has been numerically stated and used in Equation 5.1.

It is common to describe the increase in lift as a 2D effect and the decrease in drag as a 3D effect, due to the nature of changes to these forces with decreasing height. But, the spanwise and chordwise effects interact in a non-linear fashion and predictions based on individual approaches could differ from measured data [60].

2.2.4. Wake vortices in ground proximity

In free-flight, the wingtip vortices descend downward due to mutual induction [61]. In ground proximity, the tip vortices move outward, a consequence of mutual induction with their mirror images. The vortices follow a downward trajectory till they 'bounce' off the ground and into an upward trajectory [62].

As the vortex descends, it induces a crossflow with a peak suction beneath it. Under sufficiently strong gradients, a secondary vortex is formed on the ground and causes the primary vortex to rise [63]. This occurs at the 'rebound' point. The rebound point shifts closer to the wing with decreasing height and increasing angle of attack [64].

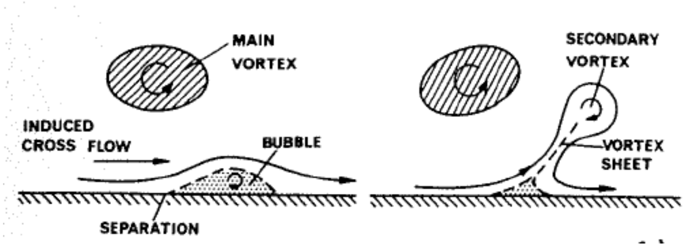

Figure 2.6: Suggested explanation of the formation and movement of vortices interacting with a ground plane, by Harvey and Perry [63].

This phenomenon is more applicable to wings with lower ground clearances than the Skymaster investigated here. It has been mentioned previously that from the RANS CFD results, it was discovered that the fuselage of the Skymaster's digital twin generated vortices. The strong primary vortices were involved in the formation of secondary satellite [65] vortices in a manner as represented here in Figure 2.6. This is later mentioned in section 5.4.

The similarity between this ground vortex phenomenon and the fuselage wake vortex discovered, was the presence of strong primary vortices, a wall, a secondary vortex formed between the two, and the bouncing of the primary vortex. These CFD results were obtained with a steady-state approach. It is likely thie process is a time-dependent phenomenon.

In the presence of crosswind, the upstream vortex is strengthened and the downstream vortex is weakened [66]. The occurrence of this very same phenomenon in the numerical results reported here was not discovered or even expected. However, it has been used in section 5.9. The investigated propeller model did not introduce any swirl velocity into the slipstream. In this report, due to the use of a symmetry boundary condition, the wake vortices evolving on either side of the fuselage were seen to be of the same strength. However, by including the shearing due to the propeller swirl velocity that would influence the formation of these vortices evolving in its slipstream, a difference in strength between the vortices on either side of the fuselage would be expected when a full airplane model is investigated with the inclusion of propeller swirl. By temporarily not considering the vorticity shed by the propeller into its slipstream, the impact of the tangential swirl velocity component to the fuselage vortex stength during its evolution near the fuselage wall can be compared to this crosswind effect on vortices in ground proximity.

2.2.5. Boundary condition for CFD analysis

The numerical boundary condition specified to model the ground plane can adversely affect the results if done incorrectly. Four possible options exist– symmetry (to satisfy the image vortex method), stationary wall, slip wall with no shear stress, and moving ground plane. Only the moving ground plane is representative of a real life scenario [67]. The moving ground has been compared with the efforts made in wind tunnel studies to prevent the boundary layer from developing on the ground plane [68].

For the low-fidelity potential flow-based vortex lattice method tool used for numerical estimations to understand the behaviour of the lifting surfaces of the intended digital twin in ground proximity, the symmetry boundary condition was used. This is mentioned in subsection 4.2.2.

For the high-fidelity fully viscous RANS CFD numerical simulations, the ground was specified as a moving plane with a finite velocity equal to the freestream. This is mentioned in subsubsection 4.3.2.3.

The flow-field between the ground and the wing is differently affected by these boundary conditions. For moderate clearances, the differences are not very prevalent. The lifting surfaces of the investigated digital twin fall within this category as their height-to-span ratios are greater than 0.05 and their height-to-chord ratios are greater than 0.6 .

The differences become more evident at low clearances. The fuselage of the digital twin is far closer to the ground than its lifting surfaces. Hence, even though the choice of any of these boundary condition would not be expected to negatively impact the lifting surfaces, it could affect the fuselage, as later shown in Figure 4.9. Thus, the recommended and most relevant boundary condition was required to be chosen– the moving ground plane. This has been covered again in subsubsection 4.3.2.3.

Figure 2.7 shows the differences to the flowfield between a wing and the ground that could occur with the different boundary conditions possible for the ground plane. The ground stationary model shows a re-circulation region under the leading edge and can lead to erroneous results [69]. The image (symmetry) condition also shows a similar effect. The slip condition shows no re-circulation, but does show a trend towards it where the velocity vectors slow near the wall. The moving ground is the most accurate and shows an increase in the velocity vectors as it tries to meet the wall speed.

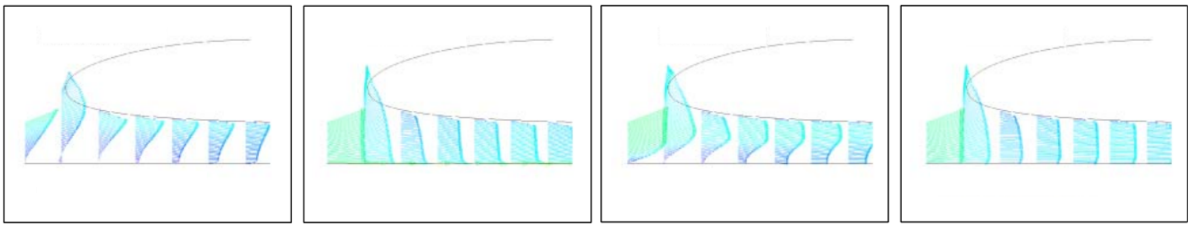

Ground Stationary **Ground Moving** **Image** **Slip**

Figure 2.7: Effect of different CFD boundary conditions for the ground plane, by Barber and Hall [70].

2.2.6. ESDU Items for including the ground effect

ESDU provides two Items that can be used to convert free-flight polars to include the ground effect at specified ground clearances. ESDU 71007 [71] is applicable for slender wings with sharp leading edges, low aspect ratios, and straight trailing edges. ESDU 72023 [72] is made up of empirical relations based on the method of images that can be used on isolated wing and wing-body combinations to calculate the changes to the lift, drag, pitching moment, and downwash.

The ESDU 72023 [72] Item was found to be the relevant item and has been used in this study in subsection 5.2.1 while converting the lift polar of the digital twin calculated from the CFD studies to indicate the influence of the ground on the lift for the relevant ground clearance expected during a ground-run operation.

ESDU 72023

This Item is developed from semi-empirical methods based on the method of images where the lifting surfaces of both the wing and its image are replaced by a vortex system.

By considering that the changes in forces on the tail are relatively small as compared to the whole, and that their contribution is more important for the pitching moment than lift, this Item can be used on complete configurations within the linear range of a typical lift polar and for height-to-chord ratios above 0.3, as has been with the Skymaster under investigation and reported in subsection 5.2.1.

The inclusion of the ground effect is done by combining the required change in angle of attack for a given lift coefficient and the change in lift coefficient at the new angle. The contribution of the induced vertical velocity of the image trailing vortices are to change the required angle of attack. It is given by,

$$\delta\alpha = -\frac{\sigma C_L}{\pi A}$$

The image bound vortex contributes to the lift increment at the new angle of attack as

$$\delta C_L = rC_L\left[\frac{N}{(1+\tau N C_L)^2} - 1\right]$$

Empirical relations are used to calculate σ, r, N, τ, which can be found in the Item.

The change in lift polar is expected to be as in Figure 2.8. This expected change to both the angle of attack and the lift coefficient is visible in the results discussed in Figure 5.1.

The tool is available online on the ESDU website. The online tool was used in this research as mentioned in subsection 5.2.1 and no manual calculations using the same graphs and information available in the written document were performed.

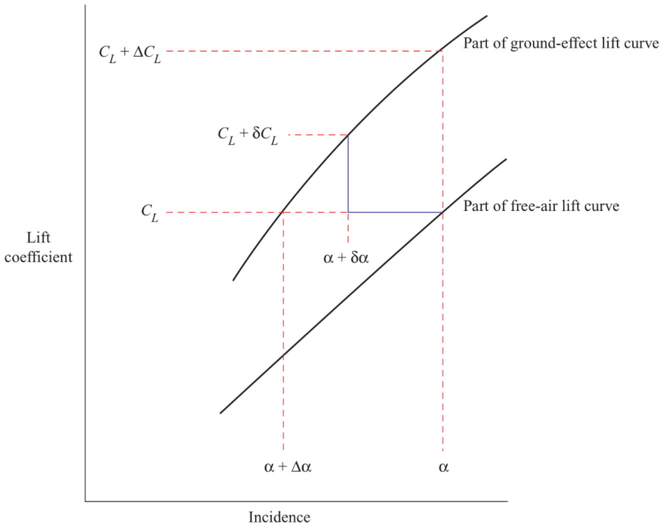

Figure 2.8: Method of reconstruction of free-flight polar to include the ground effect at an input determined height-to-span ratio that shows the contribution of the image trailing vortex system to decrease the required angle of attack for a constant lift coefficient and the increase in lift coefficient at the new angle of attack due to the image bound vortex. Image from ESDU 72023 [72].

subsection 5.2.1 shows that the ESDU Item under-predicts the lift coefficient when compared with the fully-viscous RANS CFD results. This could be due to the Item neglecting the airframe [73], or not considering an increased lift at the tail for the case, here, with the large vertical end-plates expected to aid in a ram pressure build up and contribute to the increase in lift [40].

2.3. Integrated propeller aerodynamics

Propellers are sensitive to the flow-field they operate in. The forces and moments that they generate are influenced by the inflow to their blade sections [27]. Isolated propellers could experience a uniform inflow in certain cases. However, propellers are almost always used in an installed condition where they are operated in proximity to other objects, such as the airframe or other propellers. The surrounding flow-field and the inflow to the propellers would be influenced by these objects that make the inflow non-uniform [27].

Propellers experience non-uniform inflow during almost every flight operation and hence, it is vital to understand them in their installed conditions at which they will be used and operated. Some examples of non-uniform inflow cases are shown in Figure 2.9.

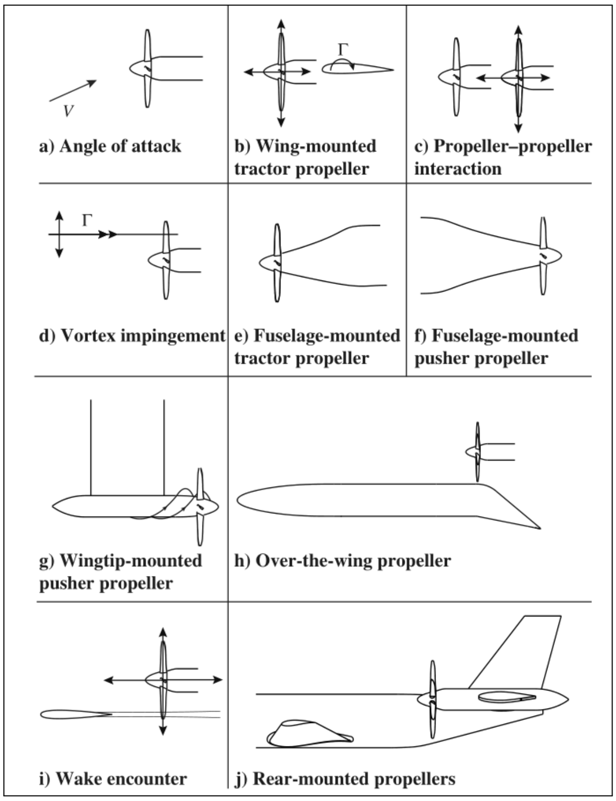

Figure 2.9: Typical non-uniform inflow conditions experienced by propellers, by van Arnhem et al[27].

For the cases investigated here, there was a tractor propeller installed into the nose of a GA aircraft fuselage and a pusher propeller installed into the tapering rear end of the same fuselage. From the CFD numerical analyses, it was found that the rear propeller encountered the wake and downwash of the upstream mainwing. It also encountered a wake from the fuselage it was installed into, in addition to vortical structures being shed from the same fuselage. The tractor propeller's slipstream also passed through the plane of the rear propeller. Given that the centrelines of these two propellers are staggered, so was the tractor propeller's slipstream at the rear propeller plane. As notionally will be shown in Figure 2.16, the tractor propeller's streamtube was modified due to the fuselage that is present between the installed tractor and pusher propellers. The nature of this front propeller's slipstream at the rear propeller plane was also influenced by the angle with respect to the flow, the restriction by the ground, and the specification of required thrust. The angle of attack at which the aircraft was investigated at, would also have an influence on the inflow angle to the propellers.

The resulting twin propeller slipstreams that interact with the downstream tail, a body of interest, is presented and discussed in subsubsection 5.6.1.1 with the use of the total pressure coefficient whose definition is given later in Equation 5.11.

As will be explained in the next section, in this reported research, the propeller was numerically modelled as an infinitesimally thin disk having infinite blades. For a more realistic understanding of the influence of the non-uniform inflow features, discovered here, on the propeller characteristics, a more detailed numerical model considering the blades of the propeller with its suction and pressure side geometries are required and has been recommended in section 6.2 to be used in future studies. The changes to the forces and moments generated by the propeller, based on the flow-field characteristics discovered here, are beyond the scope of this investigation but, believed to be important.

Like most typical GA aircraft seen today, the testbed under investigation has air inlets situated on the frontal section of the fuselage on either side of the propeller spinner and directly behind the propeller. For the numerical studies performed in this reported research and as will be discussed later in subsection 3.2.1, these air inlets were not included. The frontal area of the fuselage would be treated as a completely solid wall. The interaction between such an installed tractor propeller and this part of the fuselage with the excluded air inlets, is considered similar to a wing in ground proximity. The fuselage would have a ground effect like behaviour and cause a stagnation of the flow in the region just ahead of it, resulting in a build up of pressure on the pressure side of the propeller plane. This rise in pressure would increase the drag on the fuselage, but would also increase the thrust produced by the propeller [74][75].

This particular study by Janus [74][75] used a 2-bladed McCauley propeller like the ones on the testbed under investigation, installed into a generic GA fuselage in a tractor configuration, similar to the testbed's tractor propeller installation and environment. It was found that the blades were not designed to optimise their thrust production near their root sections. A resulting negative angle of attack at blade sections near the root was calculated by these numerical investigations performed on the authentic full-blade design provided by McCauley to Janus [74][75]. These old and stiff propeller blades were compared with a then new propeller blade design that was seen to be optimised to have positive flow angles of attack for the blade sections near the root.

This information could not be used for this reported research as propeller blades were not considered. However, relying on the improvement of propeller blade technology from the time of these investigations in 2001 to today, the student researcher would like to make future researchers aware of possible differences in the spanwise thrust production capability of the currently (at the time of commencement of writing this report) installed 2-bladed McCauley propellers and the new 3-bladed MT MTV-18 series propellers scheduled as replacements.

2.3.1. Numerical modelling

The Rankine-Froude momentum theory, or actuator disk theory, is based on an infinitesimally thin disk that is uniformly loaded and imparts a constant rise to the static pressure of the air passing through it, while not offering any resistance itself. The control tube contracts behind the disk as the flow accelerates while converting the static pressure to dynamic pressure for the maintained rise in total head [15]. This is shown in Figure 2.10 for a free and isolated propeller disk in uniform inflow conditions.

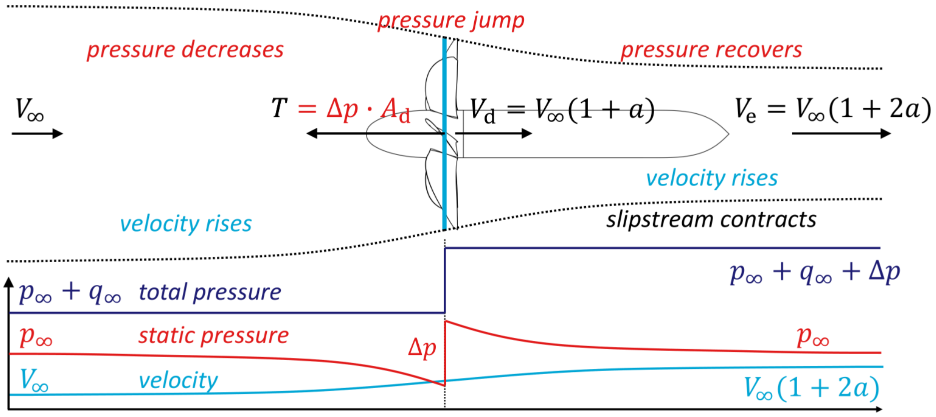

Figure 2.10: Rise in pressure across an actuator disk and change in velocity within the streamtube [76].

Due to the lack of detailed information of the propeller geometries, and this being a preliminary investigation, the two propellers of the digital twin of the Skymaster were modelled on this theory as infinitesimally thin disks with infinite blades.

The boundary condition to implement this numerical model in the RANS CFD simulations performed in this research, are discussed in subsubsection 4.3.2.3. Figure 4.8 shows how this theory was implemented across the disc diameter in the performed RANS CFD numerical investigations with the specific chosen numerical solver. The pressure rise was both constant and uniform. However, the front propeller was seen to influenced by the upstream stagnation of the fuselage that is located behind it and in its slipstream.

The thrust produced by these propeller disk planes, is a product of the rise in static pressure across the disk face and the disk area, as given in Equation 2.4. This is used later in Equation 4.9 to calculate the pressure rises mentioned in Table 4.1 for the required thrust value that the propellers with different diameters were required to produce.

$$\text{Thrust} = \text{Rise in pressure} \times \text{Propeller disk area} \tag{2.4}$$

The reported CFD analyses were first performed on an unpowered configuration of the digital twin. There was no specified rise in static pressure across the propeller plane. The drag calculated in this unpowered configuration was then equated to the thrust required to be produced, so as to maintain steady flight. The additional drag caused by the propeller slipstream influencing the airframe within it [59] was not considered while deciding the thrust requirement. The required rise in static pressure for each disk was then calculated by splitting the required thrust equally between the propellers, and across their respective disk areas. The reasoning behind splitting the required thrust in such a ratio is later discussed in section 3.3.

2.3.2. Propeller performance parameters

The performance of propellers are characterised by parameters relating the different forces and moments produced by it to its operational setting. By treating the propeller in the CFD investigations of this study as a thin disk with a constant and uniform specified pressure rise across its face, as described previously in subsection 2.3.1 and again shown in Figure 4.8 in its numerically implemented form, the only force found to be relevant in characterising the propeller performance, for this study, was the thrust produced by it, or in this case, numerically specified to produce.

The freestream velocity of the flowfield a propeller is situated in, or its own rotational speed, is typically used in the formulation of propeller performance parameters[8][34]. As this reported study treated the propellers as devices that would only increase the axial velocity and not introduce swirl, the freestream dynamic pressure was used in characterising the thrust based propeller performance.

The propeller performance parameter used throughout this study and later quantitatively addressed in subsection 5.2.4, is formulated in Equation 2.5

$$T_C = \frac{T}{\rho_\infty V_\infty^2 D^2} \tag{2.5}$$

where D is the disk diameter and $\rho_\infty V_\infty^2$ twice the freestream dynamic pressure. As the thrust required to be produced by the propellers has been considered to be equally split between them, the difference in any reported dynamic pressure based thrust coefficients between the two propellers from a CFD investigation for a certain powered configuration, that is either during free-flight or ground-run, is due to the rear propeller of the testbed having a smaller disk diameter than the front propeller. This smaller diameter is covered in the airplane specifications discussed in the next chapter.

2.3.3. Propeller slipstream

As a focus of this research involves understanding the interaction between the propeller slipstream and the horizontal tail, this section discusses topics relevant to understanding the propeller slipstream and its interaction with objects located within it.

In any propeller-airframe interaction, the propeller slipstream would have an influence on the airframe located within it, and the airframe would have an impact on the slipstream. These mutual influences are discussed below after identifying the parameters important in characterising the slipstream produced by the implemented numerical propeller model in this reported research.

2.3.3.1. Characterisation of slipstream

In the high-fidelity fully viscous RANS CFD numerical investigations reported here, the twin half-propeller disks were numerically treated as actuator disks with constant uniform pressure rises as per the theoretical description provided in subsection 2.3.1.

Propeller slipstreams are characterised by different parameters [7]. The flow-field quantities important to characterise the slipstream produced by the studied half-disks that neglected the rotational speed are:

- Axial velocity
- Total pressure distribution
- Static pressure distribution

The distribution of these flow-field quantities, both in cruising free-flight and ground-run, as calculated with the CFD numerical investigations performed on the digital twin in its powered configuration, are later discussed in subsubsection 4.3.2.3 alongside Figure 4.9 to Figure 4.12. These parameters, that were manually obtained from the CFD results are seen to have a mean distribution similar to the intention of the implemented boundary condition shown in Figure 4.8.

Another factor that would be relevant to characterise the propeller slipstream, would be the contraction of the streamtube. However, this has not been exclusively addressed in this report and hence, not included in the above list.

2.3.3.2. Influence on wings

The occurrence of propeller-wing interaction is quite common on current-day turboprop regional airplanes and is what the DEAC intends to experimentally study using the flying testbed. A reason for using an airplane version from the Cessna Skymaster family of airplanes, to study this, is the fact that the horizontal tail of the airplane is situated behind the rear propeller and is expected to be influenced by the propeller slipstream.

The DEAC has likened this particular arrangement of the testbed, to the wing mounted propeller configurations seen on many larger regional airplanes of today and new concepts being developed around the propeller. Hence, their findings could be used to benefit larger aviation.

The propeller-wing interaction is characterised by mutual influences, as will be discussed and shown. The propeller slipstream will influence the wing characteristics, such as its spanwise loading and local angle of attack distributions while generating unsteady loads on the aiframe. The wing will also influence the structure of the propeller slipstream it interacts with.

In the numerical investigations of this reported study, the propeller was treated as a device that only increases the axial velocity component of its slipstream and not introduce any swirl. While comparing the numerically obtained results with literature, it was found that if the swirl had been included, it would have had quite an impact on the results. This is discussed in detail in section 5.9. Moreover, propellers are rotary devices and understanding the influence and characteristics of their swirl component is considered important. A crucial operating factor to be looked at for future experiments is the choice of the rotational speed that the pilot would set for the tests. This would be in the pilot's control. However, if the required RPM for a steady flight is desired to be set, as was the considered flight condition in both free-flight and ground-run simulations performed here, it would be chosen on the basis of the desired airspeed. By referring to the engine manifold pressure and propeller RPM data provided in the pilot's operating handbook (POH) [77] of the Cessna Skymaster, the recommended RPM setting for the airspeeds investigated have been estimated. For the investigated free-flight speed the RPM could be 2400. For the investigated ground-run speed, the RPM could be 1600 based on charts designed for cruise. A possible difference between propeller operating characteristics in free-flight and ground-run is already evident. To repeat and clarify, these are settings that can be controlled by the pilot.

The important point being made by referring to the POH and looking into the operational settings of future experiments, is that the choice of RPM is a critical parameter. Further explanations into this could be provided but are not relevant to the contents of this report.

Hence, in the following discussions, topics relating to both swirl and axial velocity increment are covered and discussed. The importance of the influence of the propeller to the topics mentioned here are referred to again in section 5.9.

The increase in axial velocity causes an increase in the dynamic pressure within the slipstream. The swirl causes a change in the local flow angle of its slipstream– an increase in the upward blade rotation side and a decrease in the downward blade rotation side. The individual contributions of these components of the slipstream on a wing for a tractor propeller-wing installation is shown in Figure 2.11.

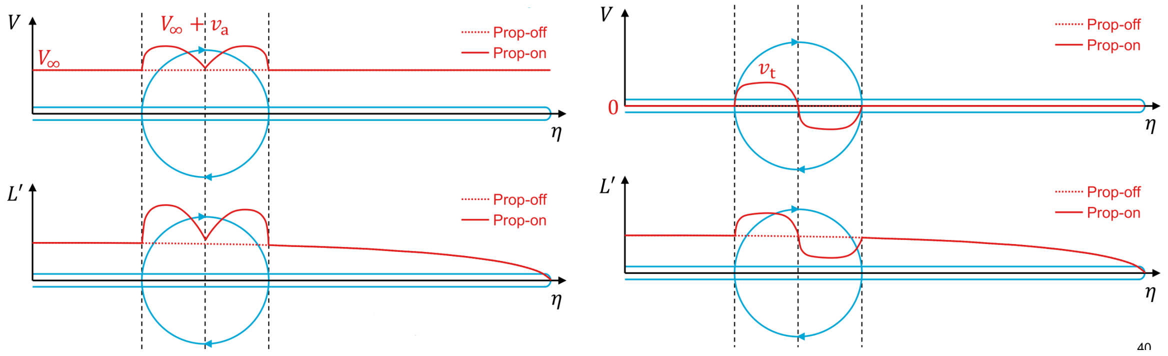

(a) Influence of axial velocity component **(b)** Influence of swirl velocity component

Figure 2.11: Independent influences of axial and swirl velocity components of a propeller slipstream on the spanwise lift distribution at a wing section, of a larger wing, that is located in the slipstream, for a tractor propeller-wing configuration [76].

The relative vertical location between the propeller axis and the wing also influences the change in spanwise lift distribution. Figure 2.12 shows the differences in the influence of the axial and swirl components of the slipstream for different relative heights between propeller and wing. As will be shown later with Figure 5.10, the rear propeller of the Skymaster is staggered with respect to the tail. The propeller centreline has a slight negative offset in its relative vertical location. However, as will be discussed with numerical results and design information, the geometric lower side of the horizontal tail of the Skymaster is its suction side. Hence, the staggered rear propeller has its centreline on the suction surface as shown in both figures in Figure 2.12 as $Z_P > 0$.

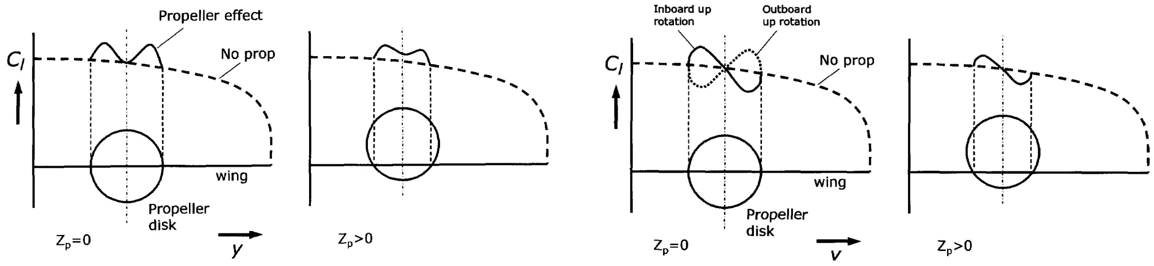

(a) Influence of axial velocity component **(b)** Influence of swirl velocity component

Figure 2.12: Independent influences of axial and swirl components of a propeller slipstream on a wing for different relative vertical locations, by Veldhuis [7].

The resulting change in the spanwise distribution of a wing interacting with a propeller slipstream is a combination of these discussed axial and swirl component influences. Figure 2.13 shows these changes for different propeller rotation directions. With the inclusion of swirl to the numerical results here, the spanwise loading distribution shown later in Figure 5.32 will be altered in a similar manner to Figure 2.13, with the difference being the presence of large vertical endplates in the form of the twin vertical stabilisers, and the location and influences of the fuselage wake vortices that are expected to be displaced from their positions reported in this study when accounting for the swirl in the propeller slipstream.

Propeller-wing interactions are mutual and the wing also influences the propeller slipstream. The slipstream structure could undergo strong deformation as shown in Figure 2.14.

Figure 2.15 shows a similar distribution as obtained from the CFD results of this research, on a survey plane defined downstream of the horizontal tail's trailing edge, at a location of 1 chord lengths of the tail. The influence of the tail is not seen to be very strong on the slipstream, but does make the low pressure regions on either side of it larger. As this is not a focus of this study, it is not reported or discussed elsewhere.

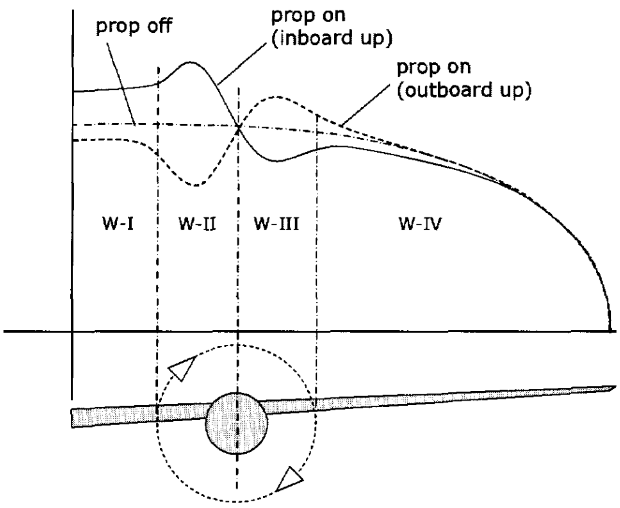

Figure 2.13: Change in spanwise lift distribution with different propeller rotation directions for a tractor propeller-wing installation showing the combined influences of axial and swirl velocity components, by Veldhuis [7].

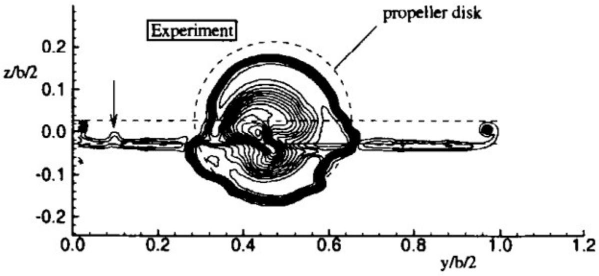

Figure 2.14: Experimentally measured total pressure contours at a downstream location showing the deformation of a tractor propeller slipstream interacting with a wing, by Veldhuis and Nebiolo [30].

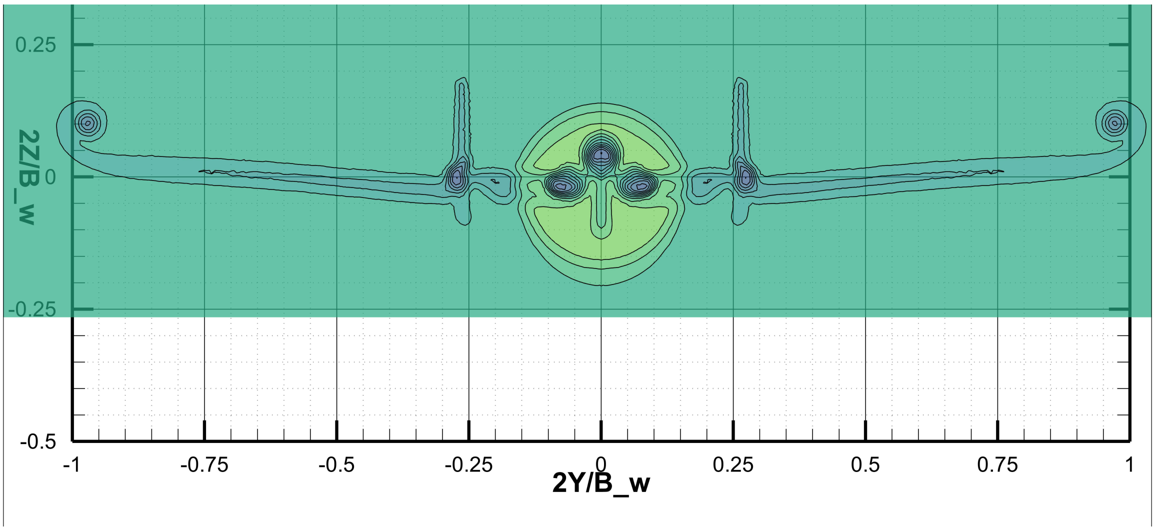

Figure 2.15: Total pressure coefficient distribution downstream of the horizontal tail showing limited influence of the tail on the rear propeller slipstream. CFD results of the digital twin in ground-run.

2.3.3.3. Blockage effects

The presence of the fuselage in the slipstream of the tractor propeller, like the Skymaster being investigated, could prevent the slipstream from contracting properly. This restricted contraction, as seen in Figure 2.16 could cause a decrease in flow velocity within the tube and a decrease in the thrust [15].

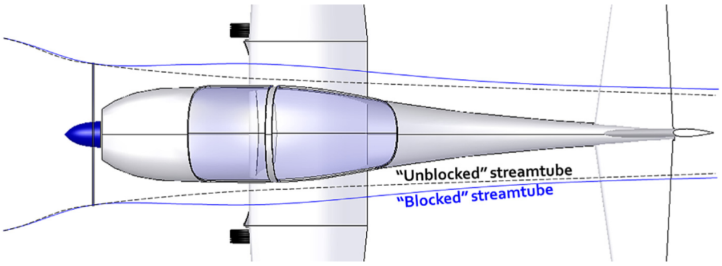

Figure 2.16: Blockage effect of fuselage on a tractor propeller slipstream, by Gudmundsson [15].

2.4. Influence of the Reynolds number

The Reynolds number is the ratio of inertial to viscous forces and is defined in Equation 2.6 [25]

$$Re_x = \frac{\rho \cdot V \cdot x}{\mu} \tag{2.6}$$

It is a very important parameter for viscous aerodynamic studies and many works can be found in literature that stress on its importance and influence on aerodynamic phenomena. Attempting to cover this parameter in detail and any associated changes to aerodynamic phenomena that could occur by decreasing the Reynolds number from a value expected in free-flight to the one in ground-run, would only result in an incomplete theoretical section. Hence, the topics of the following sections are kept brief and relevant to the most important phenomena believed to contribute to the discussed results of this reported research.

2.4.1. Boundary layer and transition

The dependence on the nature of the viscous boundary layer with respect to the freestream air and chord based Reynolds number is usually depicted in a similar manner to Figure 2.17. This figure also shows the typical range of Reynolds numbers that the wings of GA aircraft would experience in cruising free-flight.

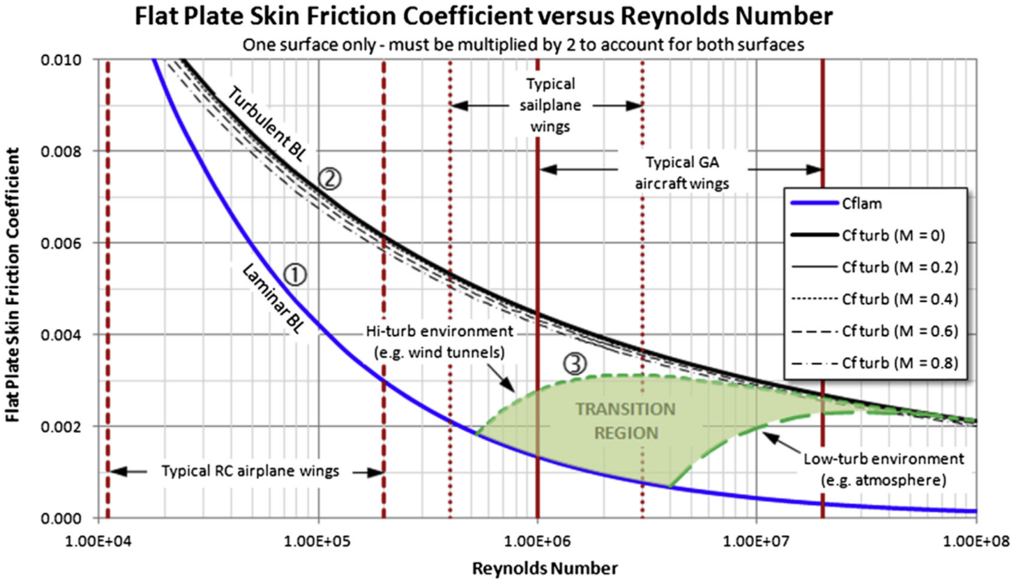

Figure 2.17: Variation of skin friction coefficient with Reynolds number, by Gudmundsson [15].

The skin-friction coefficient is a non-dimensionalised representation of the wall shear stress that is exerted by the boundary layer on the surface of the objects. The definition of the wall shear stress is given in Equation 2.7

$$\tau_w = \mu \left(\frac{du}{dy} \right) \bigg|_{y=0} \tag{2.7}$$

Within a laminar boundary layer, the streamlines are smooth and regular. When turbulent, they exhibit random fluctuations with more mixing [78]. By considering time-averaged boundary layer profiles for a turbulent flow, it is seen that the velocity gradient is far steeper, which increases the shear stress and explains the associated higher skin-friction coefficient depiction in Figure 2.17.

The Blasius solution given in Equation 2.8 is used for the estimation of skin-friction coefficient in laminar flows, while experimentally validated Equation 2.9 by Schlichting is common for turbulent flows.

$$C_{f_{\text{lam}}} = \frac{1.328}{\sqrt{Re}} \tag{2.8}$$

$$C_{f_{\text{turb}}} = \frac{0.455}{\left(\log_{10} Re\right)^{2.58}} \tag{2.9}$$

Figure 3.4 which is given later, shows the Reynolds numbers calculated for every major component of the Skymaster for both free-flight and ground-run conditions. Equation 2.8 and Equation 2.9 are used to represent the laminar and turbulent states respectively. The transitional state, which is shown in two types in Figure 2.17 (high and low turbulent environments) is represented by a low turbulent setting in the form of Equation 3.3.

The occurrence of transition is Reynolds number dependent. Instabilities are generated in the laminar flow when a certain critical Reynolds number is achieved. The flow finally transitions to turbulent when the amplifications to these instabilities cause sustained erratic behaviour [79]. Furthermore, the nature of the transition and the presence of accompanying associated phenomena like laminar separation bubbles are also Reynolds number dependent [80], but not exclusively.

The occurrence of transition is dependent on the presence of instabilities. The sources of these instabilities could include external disturbances such as roughness, acoustic energy, freestream turbulence [81], ambient conditions, and the local pressure gradients [82].

As will be shown in Figure 3.4, the range of Reynolds numbers for the components of the Skymaster fall within the transitional region. This could result in the existence of a mixed laminar-turbulent flow on the different surfaces. However, to numerically model transition in CFD analyses, is a complicated process which requires tuning of an appropriate model to the specific application [83], as will be discussed in subsubsection 4.3.2.2 while explaining the reasons behind the final choice of the turbulence model used in the RANS CFD studies reported here.

From the CFD results, it was seen that the horizontal tail would encounter the turbulent wake of the upstream airframe. This could lead to it undergoing bypass transition [84]. This is shown and discussed at two instances in paragraphs supporting Figure 4.6 and Figure 5.12. Moreover, the interaction of the oncoming streamwise oriented fuselage wake vortex with the tail, could affect natural transition, as mentioned in the following subsection 2.5.1.

For the moment, the reader is informed that the nature of transition was not modelled in the CFD studies due to the associated complexities expected as explained here. There was no prior information available that could indicate the need for modelling it. Hence, the CFD studies were performed using a fully turbulent RANS turbulence model that was seen here to instantaneously generate turbulent boundary layers on all surfaces. However, in reality, mixed laminar-turbulent flow, at least on the mainwing which would experience clean and free air, could exist.

2.4.2. Influence on airfoil performance

The growth of a viscous boundary layer on an airfoil generally results in a decambering effect that leads to a decrease in lift for a given angle of attack and an increase in pressure and friction drag, when compared with an inviscid flow [26]. The lift polar would slightly rotate about its zero-lift angle of attack to have a decreased lift curve slope. This ‘growth’ is associated to the thickness of the boundary layer.

Laminar boundary layers are less thicker than turbulent boundary layers. Hence, the decambering effect of a sustained laminar flow would be less than that seen on a sustained turbulent flow at the same Reynolds number [27]. For sustained turbulent flows, the increase in boundary layer thickness with decreasing Reynolds number, leads to a decrease in lift and increase in drag due to a decambering effect.

For the CFD studies performed in this research, and as will be discussed in subsubsection 4.3.2.2, the boundary layers across all surfaces were essentially forced to be turbulent owing to the choice of a fully turbulent RANS turbulence model that activates the treatment of turbulence at a Reynolds number lower than what is shown later in Figure 3.4 for all surfaces calculated for both free-flight and ground-run conditions. This has been done despite an indication to the presence of mixed laminar-turbulent flow as shown in Figure 3.4, due to reasons again mentioned in subsubsection 4.3.2.2.

A critical numerical parameter of the chosen turbulence model for the CFD investigations was the freestream turbulence value. High values would impact the nature of the boundary layer being developed and result in more decambering. To limit this incorrect treatment of the numerically calculated boundary layer, the lowest possible value for the definition of the freestream turbulence was chosen as strongly discussed in subsubsection 4.3.2.3 in relevant paragraphs.

section 5.8 talks about the impact of this decambering effect on the lift and drag polars on the airoil section of the horizontal tail of the Skymaster at the Reynolds numbers relevant to this study. For the sake of completeness of this section in this chapter, a few important parameters influenced by boundary layer induced decambering are shown and briefly discussed below.

Results from potential flow-based 2D panel-method analyses coupled with the iteratively solved boundary layer equations were used in explaining the significance of this decambering effect on airfoil performance, in section 5.8. The theoretical background to this is briefly discussed in section 5.8 but also earlier in subsubsection 4.2.3.2.

The Reynolds number in ground-run was 60% of its value in free-flight. However, as mentioned and will be made clear in Figure 3.4, this falls within the transitional range. By performing the panel-method analyses at these Reynolds numbers, transition was seen to occur over a finite length at a significant distance from the leading edge. To keep the results comparable to the fully turbulent CFD results as has been described, the boundary layer was forcefully tripped at a certain location near the leading edge. Figure 2.18 shows the influence of the decambering with decreasing Reynolds number on an airfoil of interest at Reynolds numbers of interest. Figure 2.18a shows the decrease in lift curve slope and Figure 2.18b shows an increase in drag. These results are for the horizontal tail section of the Skymaster investigated, the relevant body to this study, at Reynolds numbers in free-flight (3.75×10^6) and ground-run (2.28×10^6) calculated based on its chord.

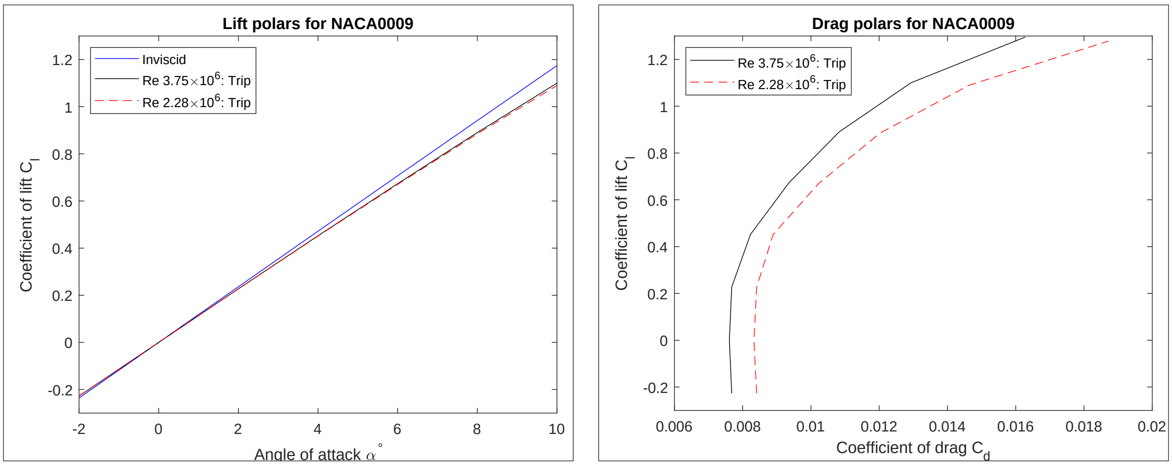

(a) Lift polar **(b)** Drag polar

Figure 2.18: Influence of Reynolds number on lift and drag polar of the Skymaster's horizontal tail's NACA 0009 airfoil, from XFoil simulations with user-specified trips at 10% of the chord, to represent the influence of airfoil decambering with increasing boundary layer thickness.

As propeller blades are also made up of airfoils, it is reasonable to expect that their performance characteristics will also be influenced by the Reynolds number [85]. However, as the blades were not treated in this study, no comments on this topic, though could be important for future investigations, have been made.

Another consequence of the Reynolds number on an airfoil's performance, is its influence on the maximum lift coefficient. Increasing the Reynolds number increases the maximum lift coefficient as the flow can negotiate more severe adverse pressure gradients at higher angles of attack [86]. This however, is not very relevant for this study that deals only with a low angle of attack. The lift curve slope that determines the lift coefficient at the angle of interest is the important parameter to consider.

2.5. Vortex-airframe interactions

The results obtained from the high-fidelity fully-viscous RANS CFD numerical investigations performed in this reported research, strongly indicated to the presence of vortical structures that merged into a vortex. This vortex was seen to pass through the rear propeller plane, be convected downstream, and interact with the horizontal tail.

Once the structures were identified as vortices, the topics in this section were retroactively covered to gain an understanding of the expected nature and effects of the interaction between the vortex and the airframe components it interacted with– the rear propeller and the horizontal tail (a lifting surface).

An identified difference to the nature of the vortices between free-flight and ground-run, for the reader to be made aware of at this moment, was the vertical location of the vortex cores relative to both the rear propeller and the leading edge of the tail. This is later discussed in subsubsection 5.6.1.1

The topics in the following sections are related to vortex-airfame interaction and later mainly referred to in section 5.9 that compares the results of the numerical studies performed here with literature sources focused on certain similar phenomena, but also referred to intermittently. Based on such comparisons of the steady-state CFD studies reported here with the time varying unsteady nature of vortex dynamics and vortex-airframe interaction, a major limitation of this work was identified as not doing justice to the underlying inherently unsteady phenomena, due to the chosen approach.

2.5.1. Vortex-wing interaction

The interaction between a streamwise oriented vortex and a wing is very much dependent on their relative vertical locations. The vortex has a tendency to be convected with the accelerating flow over a wing. When the vortex passes entirely over the wing, it does not have any influence on the pressure side of the wing. When it directly interacts with the wing or has a negative offset, the stagnation from the leading edge leads to instabilities at the vortex core. The instabilities are seen as opposite vorticity within the core. While this may not affect the time-averaged forces, significant unsteady loads would be generated. Also, larger the vortex radius, further upstream the instabilities, and more wing area is influenced by it [28]. A representation of the effects of different vertical locations for a streamwise oriented vortex interacting with a wing is shown in Figure 2.19.

In the CFD results reported here, the vortices were directly interacting with the leading edge of the tail. Due to the differing vertical locations between free-flight and ground-run, the ratio in which the oncoming vorticity was split by the leading edge was different. In contrast to this discussion, there were no leading edge stagnation induced instabilities seen at the core of the vortex as estimated with the steady-state numerical analyses.

The interaction between a streamwise oriented vortex and a wing has an effect similar to the slipstream of a tractor propeller-wing configuration. A vortex induces upwash on the interacting wing's side that is located in its upward rotation direction, and a downwash on the other side. This is analogous to the influence of an upward-passing blade and downward-passing blade in tractor propepller-wing combination. The extent of this upwash can be large and seen as an enhanced suction over a large chord and span length as reproduced in Figure 2.20 [32]. Such a distribution on the surface pressure on either side of the vortex is focused on and discussed later in subsection 5.6.2 that shows the influence of the vortices, as treated in this study, on the surface pressure and the accompanying skin-friction coefficient for the unpowered and powered configurations of the Skymaster in free-flight and ground-run.

The upwash shifts the stagnation point downstream and downwash shifts it upstream. The induced upwash could shorten a transition bubble and shift its position upstream whereas the downwash could maintain laminar flow. By using a fully turbulent single equation model for estimating the effects of turbulence for the reported CFD investigations, transition was essentially not allowed to occur, as the freestream Reynolds numbers were high enough to cause this chosen turbulence model to generate a fully turbulent boundary layer from the leading edge of any surfaces it started developing on.

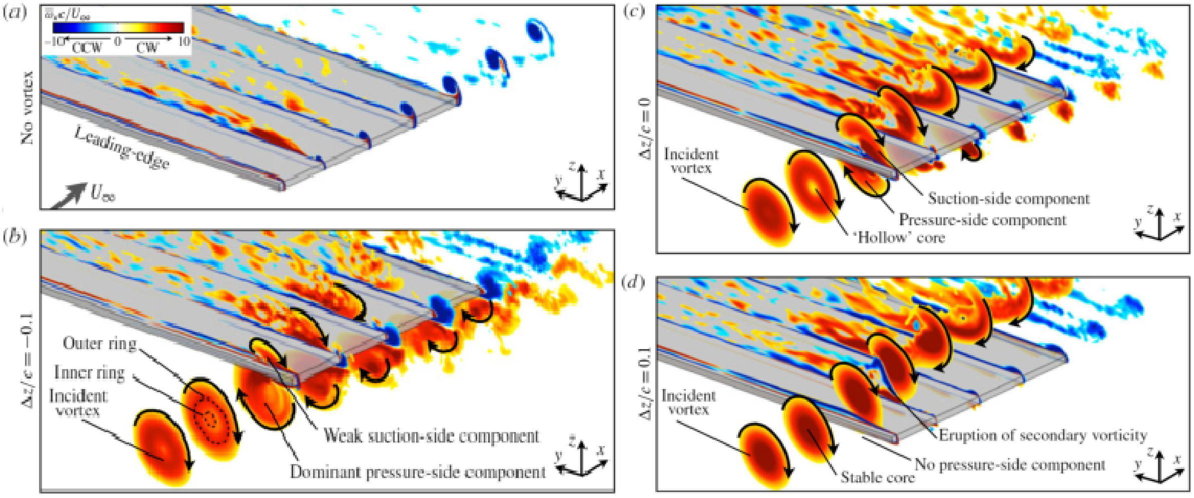

Figure 2.19: Different interaction effects between a streamwise oriented vortex and a flat plate due to different relative vertical locations, by Barnes, Visbal, and Huang [28].

The induced upwash rotates the lift force vector forward by such an amount that a thrust like drag force is resolved across the span. Due to an inability in accurately capturing this thrust-like force, as discussed in section 5.7, a notional representation is only included in section C.2 and not the main content of the report.

The difference in the chordwise location of the stagnation region near the leading edge is seen in the surface pressure distributions reported and discussed in subsection 5.6.2. The reported spanwise lift distribution where a positive upward lift force was seen to be produced by the tail near its centreline but transition to a downward generated force is also a consequence of this shift in stagnation brought about by vortex-wing interaction.

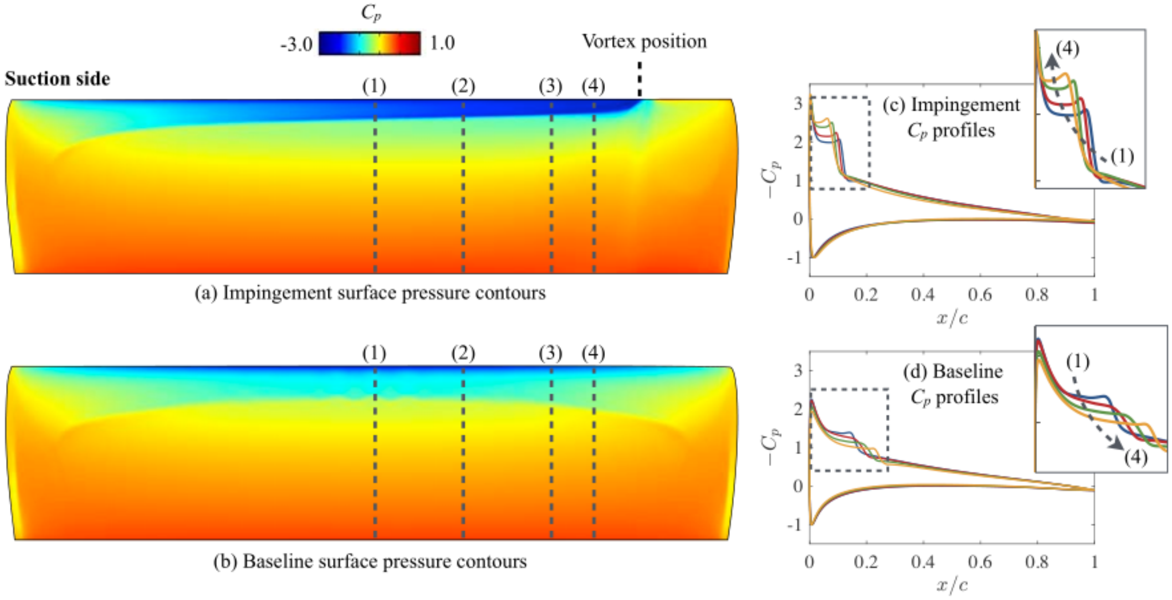

Figure 2.20: Change in wing surface pressure distribution due to streamwise oriented vortex interacting with it, by Garmann and Visbal [32].

Figure 2.21 shows a time-averaged and instantaneous state of a vortex interacting with a wing. The influence of the leading edge induced stagnation and flow reversal on the structure (causing an abrupt change) of the streamwise oriented oncoming vortex is also clearly shown. The nature and presence of this behaviour is dependent on the Reynolds number. The phenomenon shown in Figure 2.21 was simulated at a Reynolds number of the order of 10^5 where transition is accompanied with a laminar separation bubble [32]. Such a behaviour was not seen on studies at lower Reynolds numbers [28]. With the Skymaster operating at Reynolds numbers in the order of 10^6, as will be shown in Figure 3.4, the occurrence of such instantaneous changes to the oncoming vortex structure is more likely but should be treated with a time varying approach, not like the steady-state analysis performed here.

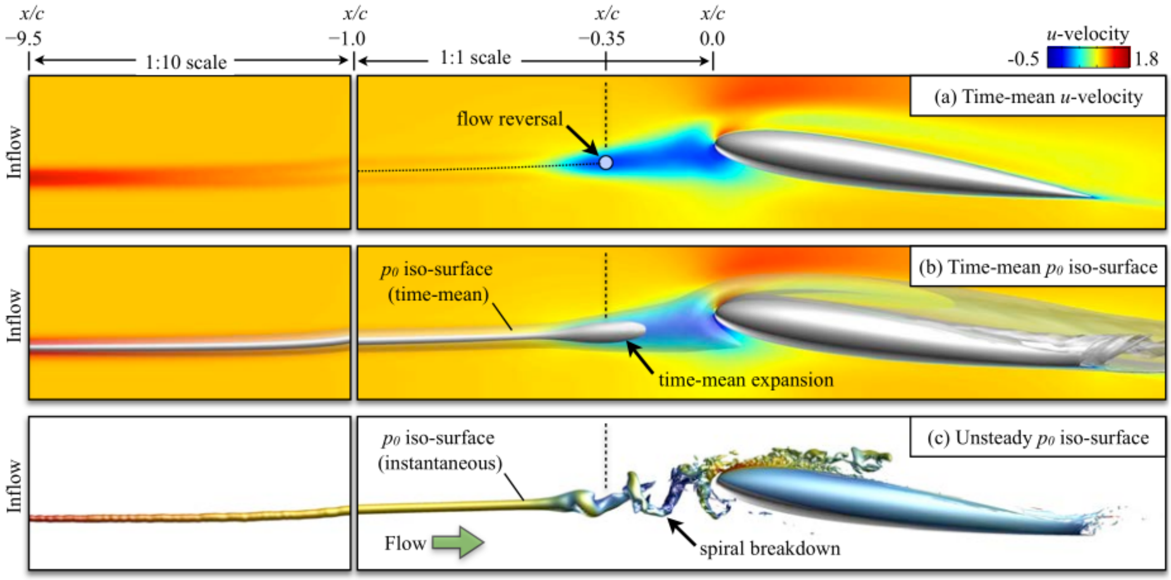

Figure 2.21: Time averaged and instantaneous flow-field showing an abrupt change to the structure of the oncoming streamwise oriented vortex interacting with a wing, due to wing-leading edge stagnation induced instabilities, by Garmann and Visbal [32]

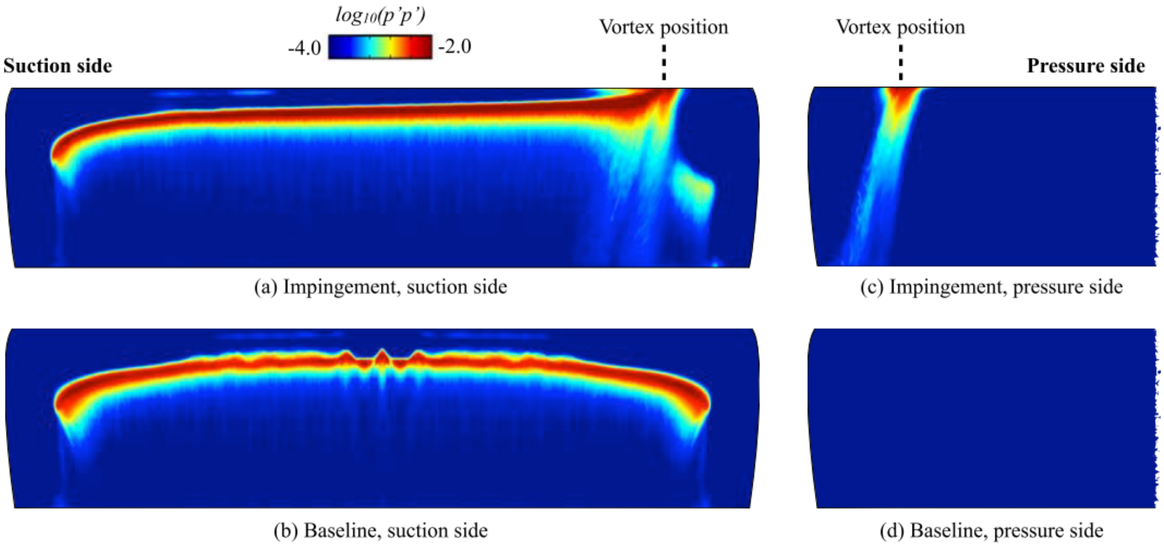

(a) Impingement, suction side

(c) Impingement, pressure side

(b) Baseline, suction side

(d) Baseline, pressure side

Figure 2.22: Mean square pressure fluctuations due to vortex interacting with a wing, by Garmann and Visbal [32].

.

Such a change to the structure of a vortex leading to its time-mean bifurcation where it alternatively attaches to either side of the wing, will generate significant unsteady loads. This is shown in Figure 2.22 and seen to be along the line of transition. For this study from literature, transition occurred over a finite length and was accompanied with a bubble, as shown in the previous Figure 2.20.

By investigating the pressure distributions on the tail of the Skymaster, a similar kink in the steady-state pressure distribution on the suction side was seen for the cases of free-flight, both unpowered and powered, at a chordwise location similar to the one in Figure 2.22. This kink was not present in the ground-run simulations which also featured the vortices being at a different vertical location at the leading edge of the tail.

Though this has to be investigated in an unsteady manner given the nature of this interaction, it could indicate the region of unsteady pressure fluctuations. This is shown in Figure 5.11 and later compared with this section in section 5.9.

2.5.2. Vortex-propeller interaction

A propeller blade is essentially a twisted wing. The phenomena occurring during a vortex-wing interaction, like the one described in the preceding section, can be extended to a propeller with the additional consideration of its rotational velocity. Understanding propeller-vortex interaction for this numerical study is stated to be essential as it was seen that the vortical structures being shed from the fuselage of the testbed's digital twin passed through the rear propeller plane. As will be discussed later in section 5.4, swirling flows with concentrated vorticity from the top and bottom sides of the fuselage separately passed through the rear propeller plane and merged downstream of it into a single vortex core.

Though the propeller was numerically treated in the CFD investigations performed here as an infinitesimally thin disk with infinite blades, the purpose of this particular comparison is to highlight the importance of understanding the influence of the oncoming vortex on the pressure and suction sides of the propeller blades and the influence of the propeller blades on the vortex. This supports the recommendation made in section 6.2 to utilise full-bladed propeller geometries for future numerical investigations.

Concentrated vorticity passing through a propeller plane will affect the propeller performance depending on the relative rotation direction between propeller and vortex, and the spanwise location it interacts with. As a vortex interacts with the propeller blade and splits, the parts of the vortex passing above and below the blade will induce a velocity in the spanwise direction, either outboard or inboard.

This direction of induction would be dependent on the local blade section's angle with respect to the vortex. This is determined by studying the propeller-vortex interaction at the relevant spanwise location where the interaction occurs.

As has been stated previously and will be discussed in section 5.9, the vertical locations of the vortices in both free-flight and ground-run are different. Consequently the spanwise section it would interact with are also different.

Moreover, changes to the tangential velocity component of the vortex would occur due to the swirl of the propeller, depending on its relative rotational direction [33]. Though important to know to understand a possible difference that would arise between this analysis and one where swirl is also modeled, it is not discussed in detail due to not being relevant to the results presented.

The general influence of a propeller to a vortex passing through its plane, is to stretched and displace the vortex tube, move the core radially inward and in the direction of rotation, while seeing a decrease in radius but, does not lose its concentrated feature [33]. The changes to the vorticity within the vortex are again dependent on the relative rotational directions. From the CFD results obtained here, a decrease in the vorticity was seen to occur with the chosen propeller model and is discussed in subsubsection 5.6.1.2.

The impact on time-averaged propeller coefficients due to the differing interaction effects between co and contra-rotating propeller-vortex combinations for a case investigated where the interaction occured at the 75% spanwise location of an 8-bladed propeller, is shown in Figure 2.23 from a study reported in literature [33].

The changes to these forces was due to the differing spanwise induced velocity gradients by the oncoming vortex on the propeller blades. A co-rotating vortex was seen to induce an outward spanwise velocity gradient on the pressure side and an inward spanwise velocity on the suction side. As shown in Figure 2.23 for a negative Γ parameter, this resulted in increasing the thrust coefficient of the blade which followed the same definition as Equation 2.5. The changes to the direction of induced velocity gradients by the contra-rotating vortex, decreased the thrust coefficient.

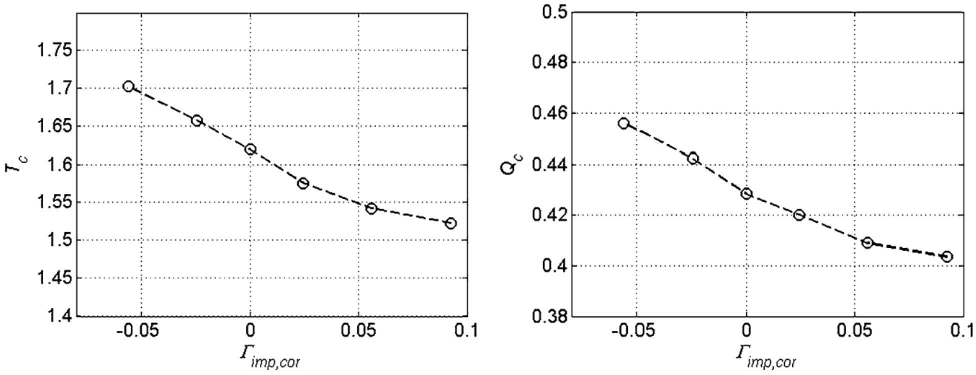

Figure 2.23: Change in measured propeller thrust and torque due to BVI at 75% radial location and at an advance ratio of 0.58, by Yang et al [33].

Based on the CFD results on the numerical model, it is expected that the vortices being generated on either side of the fuselage will have different relative rotational directions with the rear pusher propeller when its swirl component is considered. Moreover, the evolution of the vortices at the walls of the fuselage will be impacted by the front tractor propeller's slipstream. The different relative rotational directions with the front propeller implies that the vortices will not evolve in similar manners. Hence, and as discussed in section 5.9 with the use of Figure 5.41, the rear propeller characteristics would be differently affected on its upward blade rotation and downward blade rotation sides during its interaction with different oncoming vortical structures. The change in the relative vertical location of the vortices also means that different spanwise sections of the blade would be affected in free-flight and ground-run.

2.5.2.1. Propeller-vortex–wing interactions

The interaction between the tip vortices shed by a propeller with a wing also have similar effects. The vortices themselves are 'cut' by the wing and bend at the boundary layer. The wing also distorts the helical structure of the propeller-tip vortex, but rejoins once it leaves the interference of the wing. The rejoined vortices are skewed and misaligned. Such an interaction, and its influence on the pressure distribution on a wing is shown in Figure 2.24.

Due to the chosen simplification of neglecting the propeller swirl in the numerical models studied here, this was not seen. However, their consideration is important for obtaining more accurate data to be experimentally validated with future experiments that might measure the surface pressure distributions at certain spanwise locations on the tail of the testbed.

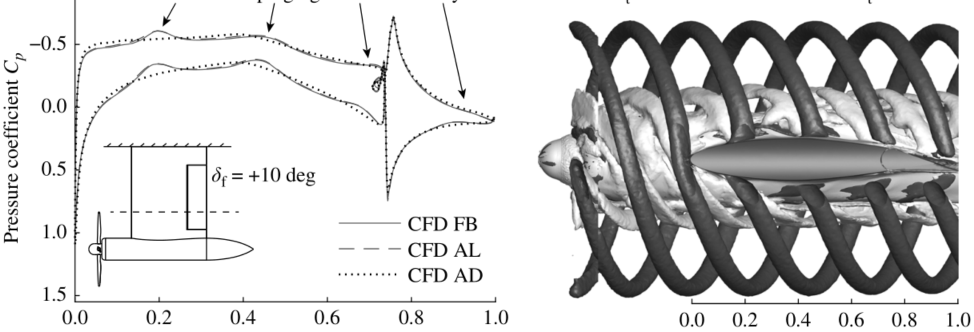

Figure 2.24: Influence on wing surface pressure distribution due to propeller tip vortex interacting with a wing in its slipstream, by Stokkermans et al. [87].

3

Background Information

This chapter presents important information used in the design and development of the digital twin and the operating conditions the investigations were performed at.

3.1. List of software packages

As described in section 1.6, the methodology followed in answering the formulated research question involved the use of low-fidelity potential flow based tools and a high-fidelity fully viscous CFD solver.

The potential flow based analyses were mostly performed with a VLM tool to get an initial and basic understanding of the characteristics of the lifting surfaces of the Skymaster so as to have a reference for the fully viscous high-fidelity numerical studies. A 2D panel-method based tool with the capability of iteratively solving the boundary layer equations which has been utilised in making remarks based on the influence of the Reynolds number in this reported study was also used. Freely available and popular software packages were chosen on the basis of their familiarity and ability to investigate the lifting surfaces of the model in free-flight and ground-run.

The general process of the high-fidelity CFD numerical study utilised here involved the creation of a computer-aided-design (CAD) model, generating a grid on this model, numerically solving the RANS equations on the grid, and finally, post-processing and viewing the solved data. The choice of software packages as listed below, for these steps, was motivated by familiarity and proven-use in simulations involving aircraft and propeller models being specified with the chosen pressure rise boundary condition [87].

- Geometry design & CAD : OpenVSP [88], CATIA V5 [89]
- Potential flow based tools : XFoil [90], AVL [91], XFLR5 [92]
- Grid generation : ANSYS DesignModeler and ANSYS Mesher [93]
- CFD solver : ANSYS Fluent 2019R1 [94]
- Post-processing : Tecplot 360EX [95]

3.2. Geometry

Due to the lack of a previous geometry definition, the CAD model for this study was made from scratch. Different sources were used in obtaining information about the Cessna Skymaster. Wherever satisfactory information was not available, design guidelines for GA aircraft recorded in literature were followed. The goal was to obtain the most representative and accurate geometry possible with the chosen simplifications. The geometry evolved through the research and improvements to iterations were made based on the results and visible effects of choices. Only the final geometry specifications have been reported here, except for cases where strong supporting statements were found to be needed.

Though there was an attempt at scanning the Skymaster to create an accurate digital twin as done with the Faculty’s Cessna Citation [96], it was not finalized in time. However, the scan was completed towards the end of this study with the processed data being made available. Wherever required and possible, comparisons between the self-designed geometry and the 3D scanned one have been provided.

3.2.1. Simplifications to the digital twin

After examining the aircraft, certain design features that were not deemed as ‘features of interest’ for this preliminary study, were excluded. This list of ‘Practical differences’ is supported with reasons, justifications, and consequences.

1. **Struts**

   The struts were removed in the geometry as they were deemed to not be of significant interest. This would also reduce the number of mesh elements. It would also aid in steady-state CFD numerical stability by ignoring any unsteady wake that could be generated by the struts. In practice, these struts will generate additional drag that is dependent on their thickness-to-chord ratio and skin-friction coefficient. An empirical relation can be used to include the additional drag [15] into the results reported here

   $$\Delta C_{D\text{strut}} = \left[2C_f\left(1+\frac{t}{c}\right)+\left(\frac{t}{c}\right)^2\right]\left(\frac{L\times c}{S_{ref}}\right) \tag{3.1}$$

   where, C_f is based on the chord dependent Reynolds number and can be approximated from the Blasius formulation for a standard roughness profile.

2. **Fairings**

   The Skymaster has fairings at the junctions of different components, such as between the struts and fuselage, struts and wings, and horizontal and vertical stabilizers. By calculating its form factor, empirical relations can be used to estimate the additional drag that would be generated.

3. **Downward booster wingtips**

   Due to the lack of proper geometrical information, these booster wingtip shapes were replaced with standard flat edges. Booster wingtips provide almost no benefit over straight wings [15]. The expected gain in effective aspect ratio with booster wingtips is 0.0 . For this study, the original aspect ratio of the wing is important to find the increase in effective aspect ratio in ground effect from empirical relations. Hence, the exclusion of these booster wingtips is justified.

4. **Tips of vertical tail**

   The tips on the Skymaster’s two vertical stabilizers are rounded. However, the geometrical reproduction of these rounded edges resulted in a large number of faces that were difficult to create good quality meshes with. Hence, they were replaced with flat edges.

5. **Landing gear and tyres**

   In a typical cruise flight, the landing gears would be retracted. But, they have to be deployed on the ground. This preliminary investigation has omitted the landing gear to utilise the same geometry between free-flight and ground-run. The additional aerodynamic drag due to the landing gear-tyre combination can be calculated from empirical relations such as [15]

   $$\Delta C_{D_{\text{landing gear with tyre}}} = \frac{(\text{Tyre diameter}\times\text{Tyre width})}{S_{ref}}\Delta C_{D_S} \tag{3.2}$$

   Based on the Skymaster’s configuration, ΔC_{D_S} is approximately 0.5 for each main landing gear component and 0.45 for the nose landing gear [15]. Frictional forces also act on the aircraft when the tyres are in contact with the runway. The forces and moments diagram for such a situation is shown in Figure 3.1. In addition to the friction coefficient of the runway, the friction forces due to the nose and main landing gear tyres are dependent on the loading of those tyres. The estimation of the additional drag due to friction is not simple and in reality, is a dynamic value that depends on the lift and moment of the aircraft.

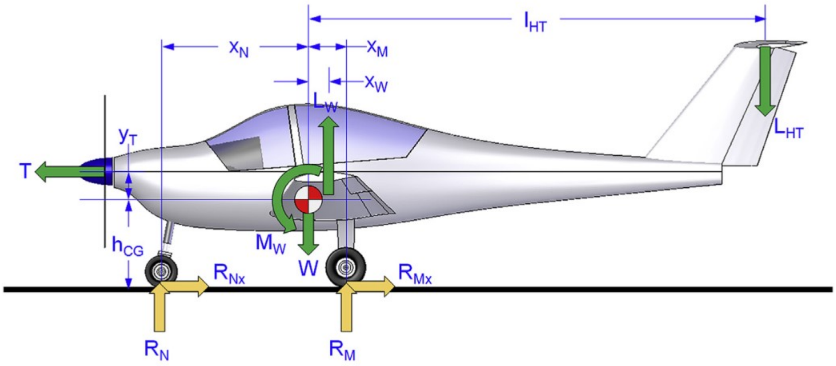

Figure 3.1: Forces and moments acting on an aircraft with a tricycle landing gear in ground-roll, from Gudmundsson [15].

6. **High-lift devices and control surfaces**

   No high-lift devices or control surfaces were incorporated into the geometry. All wings were designed as simple single element wings with no trace of these additional elements.

7. **Front engine cooling/air inlets, exit/exhaust, and cowl flaps**

   Suitable boundary conditions were not available. The requirement of their inclusion has not been determined.

   The absence of the frontal fuselage inlets in this model would result in a higher pressure build-up on the front side and hence, increase the thrust produced by the front propeller, similar to the positive influence felt by a wing in ground effect [74][75]. It would also increase the drag at the front of the fuselage. This expected behaviour was earlier discussed in section 2.3.

   The cowl flaps are situated under the nose on either side of the nose landing gear and are expected to remain open during a ground-operation. Their influence on the surrounding fuselage wall bounded flows, and the introduction of the exhaust is not considered.

8. **Rear engine exit/exhausts and cowl flaps**

   Suitable boundary conditions were not available. The requirement of their inclusion has not been determined.

   The exhaust could be sliced, deflected, and entrained by the slipstream as it passes through the rear pusher propeller. It could also affect the performance of the blades as they pass through it [97]. The propellers blades were also not modelled here, neglecting this entire possible interaction.

   The Cessna Skymaster is notorious for experiencing overheating of the rear engine. At least as long as the current combustion system is retained, the cowl flaps are expected to stay open in ground operations. Their influences should ideally not be simplified.

9. **Rear engine air intake**

   The rear engine air intake has been included as it was found to be essential in keeping the flow at the tail representative of the real case. The estimate described in the section supporting Table 3.2 was made for the mass flow rate of air passing through it. Important information on design and necessity of the rear intake and scoop inlet body for this study is presented in Appendix B.

   The model developed was not designed to separate the boundary layer of the fuselage from interacting with the intake plane, due to complications that arose while creating the mesh for the geometry. The lips of the intake were found to be bigger with respect to the 3D scanned model, which leads to more stagnation area. It is recommended that improvements be made to this geometry as it is important to the operation of the aicraft and the flow over the tail.

10. **Stall strips on main wings**

    Typically, these are retroactively installed features that promote controlled stall [14]. They are not expected to cause flow separation over the upper surface of the wings at the low angles of attack that are of interest here.

11. **Excrescences, protuberances, deformity in surfaces**

    Objects such as antennae, lights, bolt heads, or anything else that protrudes from the surface were not modeled. Empirical relations can be used to estimate their drag, depending on their orientation and shape. Moreover, as the aircraft has been in service for a very long time, there are many deformities on the surface which could not be accurately captured and modeled in this approach.

3.2.2. Important specifications

The final design specifications of the simplified digital twin that were used in the development of the CAD are given below. They have been compiled from Jane's [13], Gudmundsson [15], Roskam [59], and the Pilot Operating Handbook (POH) [77].

1. **Main wing**
    - Root airfoil : NACA 2412
    - Root airfoil chord length : 1.882 m
    - Root airfoil incidence : 4.5°
    - Tip airfoil : NACA 2409
    - Tip airfoil chord length : 1.223 m
    - Tip airfoil incidence : 2.5°
    - Wing span b_W : 11.6 m
    - Wing area S_W : 19.1 m^2
    - Wing aspect ratio AR : 7.1
    - Dihedral angle : 3°
    - Taper ratio : 0.650
    - Quarter-chord sweep angle : 0°
    - Mean geometric chord MGC: 1.684 m
    - Spanwise location of MGC : 2.687 m
    - Non-dimensionalized spanwise location of MGC $2y/b_W$: 0.4632
2. **Vertical stabilizer**
    - Airfoil : NACA 0009
    - Made up of constant airfoil across its span
3. **Horizontal stabilizer**
    - Airfoil : NACA 0009
    - Incidence angle : -2°
    - Span : 3.06 m
    - Chord : 1 m
    - Constant-chord straight wing
4. **Propeller**
    - Front propeller diameter : 78 in
    - Front propeller incidence angle : -3°
    - Rear propeller diameter : 76 in
    - The two propellers are contra-rotating and rotate clockwise from the pilot's perspective.

5. **Engine**
   - Maximum power : 210 hp ⇒ 156.5 kW
   - Due to wear over the years, the engines probably cannot produce the specified power.
   - A common engine manifold pressure that determines the power output is set for both piston engines.

6. **V-speeds**
   - Stall speed- flaps up IAS (V_s) : 83 mph ⇒ 37 m/s
   - Decision speed (V_1) : 95 mph ⇒ 42.5 m/s

7. **Weights**
   - Empty weight EW : 2800 lbs ⇒ 1270 kg
   - Maximum take-off weight MTOW : 4630 lbs ⇒ 2100 kg
   - Maximum landing weight MLDGW : 4400 lbs ⇒ 1996 kg

3.2.3. Design methodology

A design of the Cessna Skymaster by B. Litherland was available in the OpenVSP Hangar [98]. This geometry was designed from 3-view drawings, as has been done with other models [99] due to its possibility with OpenVSP. From the open source model, only the fuselage and boom geometries were taken as baseline designs, while the rest was self-designed on CATIA V5. Modifications to the fuselage were made based on the cross-sections seen in section A.3. The boom was left as is.

For the aircraft's incidence with respect to the ground plane, an image from the POH [77] reproduced in section A.3 was used.

The MGC was calculated as per the relations in Appendix A of Torenbeek [42] specifically meant for straight-taper wings as seen in the Skymaster.

All images that were used in the creation of this model are provided in section A.3. Figure 3.2 shows an isometric view of the finalised geometry along with the definition of the axis system that has been consistently followed in this report. The finalized geometry views can be found in section A.2.

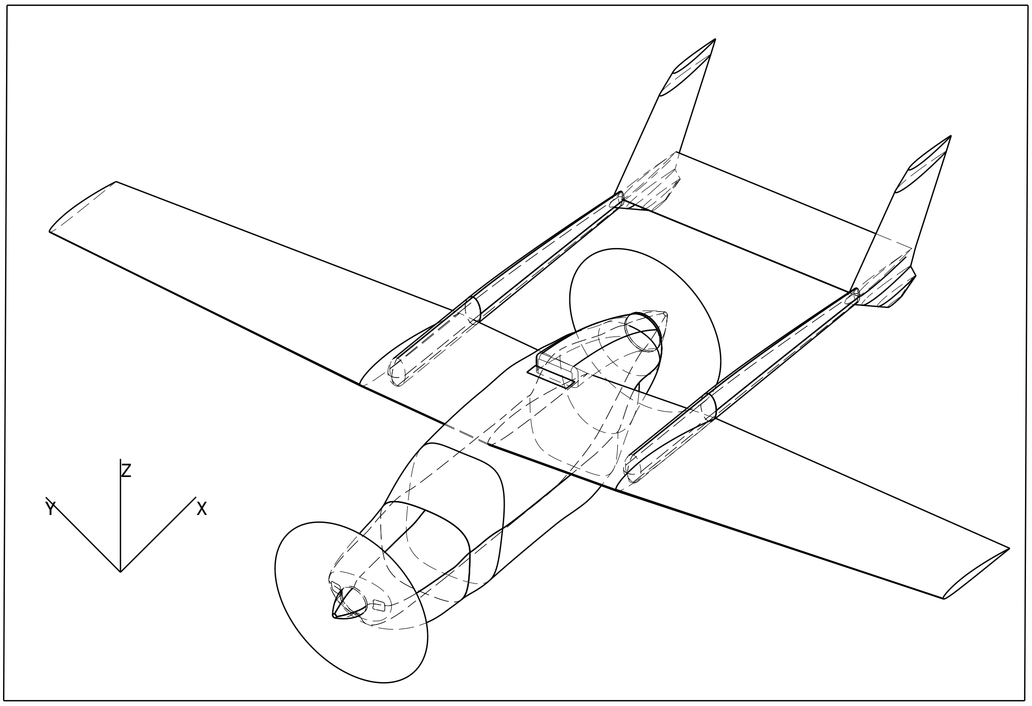

Figure 3.2: Isometric view of the finalised digital twin CAD model with axis system.

3.3. Operating parameters

The aircraft operation settings for the cases studied are given in the following lists.

1. **Free-flight conditions**
    - Cruising altitude : 5500 ft ⇒ 1676 m
    - Cruising speed : 230 km/h ⇒ 64 m/s
    - Cruising pitch angle : $3°$
    - Chosen angle of attack : $2°$
    - Chosen centre of gravity location : 19.77% of MGC
    - Rear-engine cooling air requirement : 1.2 kg/s
2. **Ground-run**
    - Test speed : 80% of V_1 ⇒ 34 m/s
    - Incidence angle : $2°$
    - Height of quarter-chord location of the MGC from the ground : 1.9 m
    - Rear-engine cooling air requirement : 1.0 kg/s

The motivation for choosing these parameters for the numerical studies are explained in detail in the following sections. The intention was to keep them as representative as the actual operating parameters of the Skymaster in such conditions.

Angle of attack/ incidence

The angle of attack can be calculated as the difference between the pitch angle and flight-path angle of an aircraft. For a level flight, the flight-path angle is parallel to the ground and is $0°$. Hence, the angle of attack would be the pitch angle.

It was internally communicated that the pitch angle of the Skymaster in cruise, as viewed in the flightdeck is $3°$. But, this study used an angle of $2°$ for two reasons.

The chosen angle was the same as the angle of incidence of the Skymaster when resting on the ground. Hence, this choice would also indicate the ground influence on the angle of attack measured from a wing-boom mounted vane.

A lift polar discussed in subsection 5.2.1 was constructed with the CFD analyses to gain an understanding of the performance characteristics of the Skymaster. It was found that the digital twin could be in steady flight at the chosen speed for an allowed weight condition, when operating at a lift coefficient obtained at an angle of $2°$.

Centre of gravity

The POH provides a loading diagram which dictates the envelope of the centre of gravity (CG). The choice of the CG made here was an estimate made on the loading at the cruise coefficient of lift. This choice was not made based on the final results, but on preliminary results obtained in the development of this research, which has not been reported here. As will be shown in subsection 5.2.3, the chosen CG location was such that the aircraft was almost at trim at the angle of attack of interest in the final reported studies of powered free-flight, a necessity for level flight. Hence, the ground-run test would indicate the shift in pitching moment with reference to the trimmed condition.

Should any researcher wish to translate the pitching moment to another location, it can be done with the reported lift polar, pitching moment coefficient, and the provided location of the centre of gravity.

Distribution of thrust

One of the key operating choices for this study is the distribution of thrust between the two propellers in a steady flight scenario. Experimentally measured thrust data was not available. Hence, estimating the distribution of thrust production between the propellers was motivated from literature. Roskam [59] reports authentic information on the 2-bladed McCauley propellers of the Cessna Skymaster which was obtained directly from the McCauley Accessory Division of Cessna Aircraft Company. This information is given in Table 3.1.

Propeller	Blade Activity Factor	Integrated lift coefficient
Front	112	0.510
Rear	105	0.570

Table 3.1: Information on the Cessna Skymaster 337 2-bladed propellers from McCauley Accessory Division of Cessna Aircraft Company, from Roskam [59].

The installed efficiencies for *similar*[4] tractor and pusher propellers depend on the ratio of the body diameter ahead/behind them to the diameter of the propeller. Roskam [59] provides Figure 3.3 to show the variation in installed efficiences of tractor and pusher propellers with fuselage diameter. Roskam [59] makes a comment that if the fuselage rear is tapered as done in the Skymaster (based on a pictorial representation of the aircraft without actually naming it), the installed efficiencies can be assumed to be the same.

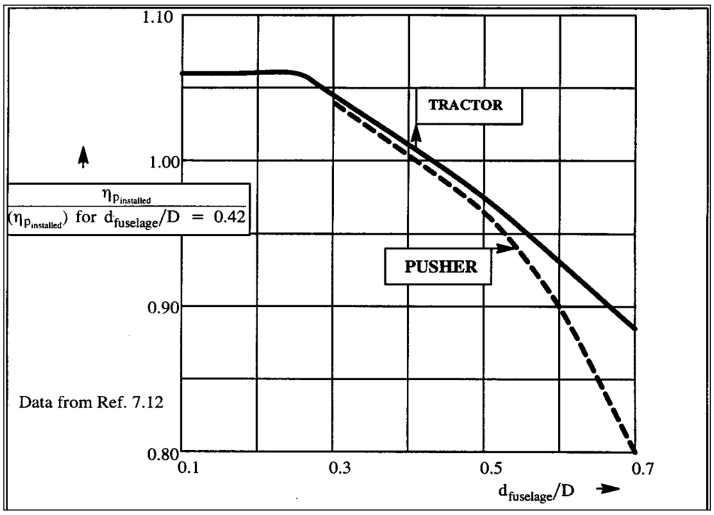

Figure 3.3: Effect of fuselage diameter on installed efficiencies for tractor and pusher propellers, from Roskam [59].

Note on Figure 3.3

The installed propeller efficiency is obtained by considering factors for blockage effects and scrubbing drag at an effective advance ratio accounting for loss in velocity near the hub.

The image by Roskam [59] is derived from Wood [100]. The data in Wood [100] is for the *maximum* efficiency with respect to efficiency for a body ratio of 0.42, and not installed efficiency as shown here. The rest of the axes definitions are the same, but the graph trends are not.

For a ratio of 0.42, this maximum efficiency is the same for tractor and pusher. At lower values, pushers have slightly higher maximum efficiencies. For larger ratios, tractors have comparatively higher maximum efficiencies.

The projected area of the Skymaster digital twin's fuselage is $1.687m^2$. The projected area is quite rectangular, like a low aspect ratio wing, which can also be used to describe much of the fuselage shape. This area was converted to an equivalent circular area with a diameter of 1.466 m. The ratio of this equivalent circle with the rear propeller diameter is 0.76 .

This indicates that a propeller in pusher configuration will have a lower installed efficiency than a similar propeller in tractor installation.

The higher integrated lift coefficient of the rear propeller was understood to be a design choice to compensate for the loss in installed efficiency. The POH indicates that the pilot sets a common RPM (engaging the propeller synchroscope is optional and dependent on the flight phase) and manifold pressure (engine power) for both propellers. Moreover, this aircraft is certified to fly in an OEI condition,

---

[4] Similarity of activity factor and integrated lift coefficient

which *could* be difficult if the distribution of thrust produced between the propellers is large. This reasoning concludes with this report assuming that the two propellers generate an equal amount of thrust to maintain steady flight, for this preliminary investigation.

Future studies could show the validity of this assumption in both free-flight and ground-run for the current 2-bladed McCauley and new 3-bladed MT propellers.

This reasoning explains the distribution of the thrust produced between the two propellers for a common RPM and manifold pressure setting. The amount of thrust required to be produced is dependent on the drag force it has to overcome to maintain steady flight. In this study, the required thrust force was estimated to be the same as the drag force calculated in the unpowered numerical analyses.

Rear engine air intake

The front and rear engines of the Cessna Skymaster have their cooling and air systems designed in a downward draft method [15]. While the front engine intake and exhausts, and the rear engine exhaust has been omitted in the model developed here, the rear engine air inlet has been included[5].

The inclusion of this rear engine inlet was found to be crucial for obtaining a more representative flow above it, around it, and more importantly, at the tail. Appendix B is dedicated to the rear engine intake and has important information on its design, necessity, and geometry, along with other comments. Appendix B also explains the choice of the location of the intake plane on which the numerical boundary condition has been applied.

The numerical boundary condition to be applied on this intake plane depends on the mass flow rate of air passing through it. No experimental data was available. Hence, an estimate for the intake area and the mass flow rate through it was made based on a study by Katz, Corsiglia, and Barlow [101] that focused on the intake and exit sizing and cooling requirements for GA aircraft. The size of the intake area and the mass flow of cooling air required is dependent on the cylinder head temperature (CHT).

The maximum expected CHT for the Continental-IO-360 engine was obtained from its maintenance manual [102]. With the data in Katz et al [101], the estimated mass flow in cruise condition was made. For the ground-run case, this mass flow requirement was slightly decreased as it was reasoned that the CHT would be lower. For a practical test, the CHT *could* depend on the duration for which the engine has been kept running, amongst other factors, such as the outside air temperature (OAT).

No information on the engine air requirement which is also obtained through the same intake was found. However, it was deemed that small differences between the chosen air mass flow and the actual would not significantly affect the flow at the tail, and that the inclusion of the rear intake had served its purpose for this preliminary study.

The final intake mass flow rates estimated for the operation are given in Table 3.2.

Case	Mass flow rate (kg/s)
Free-flight	1.2
Ground-run	1.0

Table 3.2: Estimated mass flow rate of cooling air requirement for rear engine of the Skymaster.

The area of the rear intake for the self-designed model based on the study by Katz et al [101] was 0.040 m^2. The area obtained from the 3D scanned geometry was 0.043 m^2.

The study by Katz et al [101] was for the inlets on wing mounted nacelles housing opposed piston engines. According to the ESDU 85015 [103] Item, rear cooling inlets avoid the problem of interacting with the propeller slipstream at the expense of a larger inlet area due to lower kinetic energy of the air. This explanation *possibly* justifies the reason why the self-designed air inlet had a smaller area than the one on the aircraft. As a side note, from the 3D scanned geometry, the front air inlet designed for the same engine and operational settings was measured to have an area of $0.04m^2$.

It has already been mentioned in this report that the lips of this intake in the self-designed geometry was found to be larger. While the outer boundary of the scoop inlet body was the same, as it was designed from the 3-view drawings, the larger lips account for the additionally required $0.003m^2$.

---

[5] Covered in Simplifications to the digital twin

Atmospheric conditions

The Skymaster is currently located at Teuge, The Netherlands, which has an elevation above mean sea-level (AMSL) of 5m. Atmospheric conditions for ground-run and cruise as calculated based on the ISA are given in Table 3.3.

Case	Altitude AMSL [ft (m)]	Density [kg/m^3]	Viscosity [Pa.s]	Pressure [Pa]
Free-flight	5,500 (1676)	1.040	1.76×10^{-5}	82,745
Ground-run	0 (0)	1.225	1.81×10^{-5}	101,325

Table 3.3: Atmospheric conditions of the two cases under study.

An important feature of the ambient atmosphere is the local turbulence profile of the Earth's boundary layer. This profile has not been considered for the numerical studies reported here due to lack of information. This simplification is another 'practical' difference between the numerical study and a flight experiment. However, the freestream turbulence could be higher in ground-run than in free-flight [104].

The acceleration due to gravity has the same value of $g = 9.8\ m/s^2$ at both altitudes.

Summary

Table 3.4 summarises the important operating settings for this research as based on the information provided in the preceding sections. To convert the free-flight lift and induced drag polars to ground-run, the height-to-span ratio h/b is defined.

Case	Re_{MGC}	Angle of attack/incidence	h/b
Free-flight	6.38×10^6	2°	∞
Ground-run	3.87×10^6	2°	0.167

Table 3.4: Summary of essential operating parameters in this study.

The freestream velocity based Reynolds numbers calculated for every surface using its characteristic length is plotted in Figure 3.4. The skin-friction coefficient values for laminar flow is estimated from the Blasius equation in Equation 2.8 and the turbulent flow from Schlichting's equation in Equation 2.9. The transition flow values are from a Prandtl-Schlichting relation for a flat plate

$$C_{f_{\text{trs}}} = \frac{0.455}{\left(\log_{10} Re\right)^{2.58}} - \frac{A}{Re} \tag{3.3}$$

The constant A is dependent on the transition Reynolds number based on freestream turbulence. Here, it has a value of 3300 for a transition Reynolds number of 1.0×10^6, typical of low-turbulence conditions like in the atmosphere [15]. This is only a representative value chosen to indicate whether the Reynolds number for the component falls within fully laminar, fully turbulent, or mixed flow region.

For any viscous CFD analyses, the requirement of treating the boundary layer as fully laminar, fully turbulent, or mixed flow, is made based on knowing the region within which the characteristic length based Reynolds number of the object lies in, among other factors. In Figure 3.4 it is seen that by decreasing the Reynolds number from the ones expected in free-flight to those expected in ground-run, the resulting estimated boundary layer state shifts from almost fully turbulent to a more transitional value on all bodies.

These values are referred to again while making remarks on the influence of the Reynolds number and in supporting the choice of the turbulence model for the CFD studies.

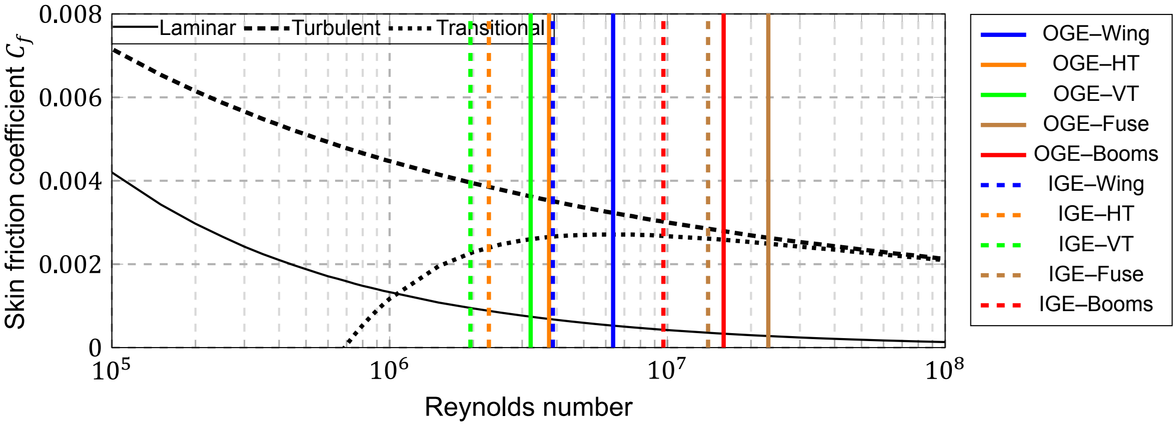

Figure 3.4: Reynolds numbers in free-flight (OGE) and ground-run (IGE) for each component based on their characteristic lengths at the associated conditions.

4

Numerical Methods

This chapter provides details on all numerical studies that were performed in this research.

4.1. Introduction

Two types of numerical methods were chosen as part of the methodology devised to address the research question to evaluate the feasibility of a high-speed taxi-test to experimentally study propeller-airframe interactions with a flying testbed.

The low-fidelity potential flow based numerical approach involved the use of vortex lattice method (VLM) and panel-method based tools. The VLM analyses were used to gain an initial and basic understanding of the performance characteristics of the finite lifting surfaces of the Skymaster's intended digital twin. As no other relevant information was found that could be used for comparing the high-fidelity studies with, these low-fidelity analyses were essential to the aerodynamic database being developed. The panel-method based tools were used either as a standalone component, or as being coupled with the VLM tools. The panel-method based tool provided numerical results on the influence of the Reynolds number as opposed to the purely inviscid analyses of the VLM tools.

The following high-fidelity fully viscous computational fluid dynamics (CFD) simulations were performed on the complete simplified digital twin described in the previous chapter. These results were the crucial component of the chosen numerical approach that forms this preliminary investigation aimed at providing an insight into the aerodynamic phenomena expected during the intended experimental tests with the flying testbed.

4.2. Vortex lattice method

The well known potential flow based VLM places vortex elements on the mean camber line of finite lifting surfaces and along their wakes [86]. The strength of these vortices is determined based on the implemented boundary condition of zero induced vertical velocity at the collocation point of the discretized element [105].

Among the potential flow based tools mentioned in section 3.1 that were used in this study, the VLM solvers were AVL [91] and XFLR5 [92]. These two tools were chosen due to their familiarity and ability to include the ground effect. However, the developer of XFLR5 has warned that the ground effect module has remained untested for a long time and has always been experimental [106]. Once this information was discovered, XFLR5 was not used for the ground-run studies and hence, is not reported in the ground effect associated content of this report.

The intention of using two different VLM numerical tools, in addition to the tools having their own advantages over the other, was to compare their results and cross-check for human error during model design and development, and compare the independence of the data solution from discretisation of the lifting surfaces. A comparison of the inviscid analyses of the lifting surfaces in free-flight conditions obtained from AVL and XFLR5 to address this concern is discussed in the upcoming subsubsection 4.2.3.1.

An advantage of XFLR5 over AVL, is its ability to include viscous effects for the airfoil sections that make up the lifting surfaces. XFLR5 incorporates the 2D XFOIL [90] tool that has the ability to solve the boundary layer equations in an iterative manner based on the essentially inviscid flow outside of the layer and numerically estimate transition and stall (numerical divergence) of a 2D section based on the numerically calculated local chord based Reynolds number. The inclusion of the panel-method based results for the airfoil section to the VLM results only affects the numerically calculated drag. It does not affect the lift coefficients which remain the same as a fully inviscid analysis comparable to AVL.

This inclusion of the panel-method based results for the 2D airfoil sections that make up the lifting surfaces could provide the location of the numerically estimated natural transition on the lifting surfaces and help in the choice of the turbulence model for the transitional Reynolds numbers expected here and as was shown in Figure 3.4.

Moreover, and as summarised in Table 3.4, while the angle of attack in free-flight and ground-run has been maintained constant, the ground clearance and its effect thereof and the Reynolds numbers are two parameters that differ. Though the ground might affect an experimentally measured angle of attack, for the purposes of reporting, it is the constant value here. The ability of XFLR5 to include a viscous correction to the drag coefficient, has been used later on in this report to make a remark on the effects of different boundary layer states expected between free-flight and ground-run. Unfortunately, the influence of viscous effects on the lift polar cannot be derived. However, from 2D analyses from XFOIL performed on the airfoil section that constitutes the horizontal tail, an understanding of the influence of Reynolds number and numerically estimated transition location on the lift polar has been discussed.

From the high-fidelity fully viscous CFD studies, the presence of vortices being shed from the fuselage were discovered. The vortices interacted with the horizontal tail of the digital twin. Such an interaction was seen to generate significant three-dimensional flow which cannot be captured by these low-fidelity numerical tools.

The fuselage on the VLM bodies were omitted as the tools are not specifically designed to treat them in an accurate manner. These VLM tools treat the fuselage as non-lifting bodies, but the numerical codes themselves, have been developed for lifting surfaces [107] [108].

A comprehensive comparison between AVL and XFLR5 can be found in Agten [107].

4.2.1. Numerical model

The number of vortex elements required for the lifting surfaces was found by performing ‘sensitivity’ studies, where the total lift and drag coefficients were checked with respect to the elements.

A total of 2250 vortices on the 6 lifting surface bodies were found to be sufficient for the model developed on AVL.

XFLR5 required more elements totaling at 5250. It was seen that the wakes extending from the mainwing interacted with the horizontal tail. This resulted in the trailing wake not being force free and caused difficulties in achieving numerical convergence. Based on guidelines to address this shortcoming, a slight stagger to the location of the horizontal tail in the XFLR5 model was made [108]. This change along with the increased panel density ensured convergence of the solutions. The final numerical models of the lifting surfaces for both VLM models is shown in Figure 4.1. .

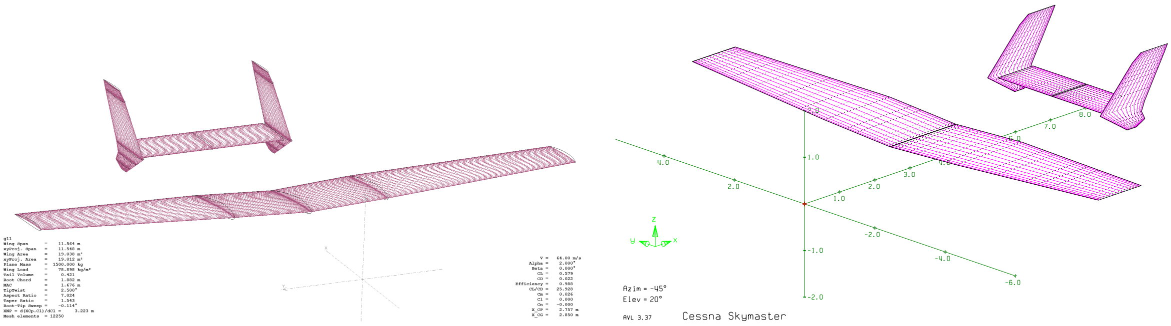

```
gl1
Wing Span      =    11.564 m
xyProj. Span   =    11.548 m
Wing Area      =    19.038 m²
xyProj. Area   =    19.012 m²
Plane Mass     =  1500.000 kg
Wing Load      =    78.898 kg/m²
Tail Volume    =     0.421
Root Chord     =     1.882 m
MAC            =     1.676 m
TipTwist       =     2.500°
Aspect Ratio   =     7.024
Taper Ratio    =     1.543
Root-Tip Sweep =    -0.114°
XNP = d(XCp.Cl)/dCl =     3.223 m
Mesh elements  = 12250
```

```
         V =   64.00 m/s
     Alpha =    2.000°
      Beta =    0.000°
        CL =    0.579
        CD =    0.022
Efficiency =    0.988
     CL/CD =   25.928
        Cm =    0.026
        Cl =    0.000
        Cn =   -0.000
      X_CP =    2.757 m
      X_CG =    2.850 m
```

(a) XFLR5 **(b)** AVL

Figure 4.1: Numerical models developed on XFLR5 and AVL for vortex-lattice simulations.

4.2.2. VLM for ground proximity studies

As mentioned earlier, only AVL was used for simulating the ground effect on the lifting surfaces of the VLM model, as this capability in XFLR5 was not considered to be reliable [106].

The simulation in AVL was executed by activating a mirror vortex system about the ground plane and treating the system of vortices like the method of images discussed earlier in subsection 2.2.1.

AVL has been noticed to overpredict the lift coefficient at low height-to-chord ratios for finite wings, as shown in the experimental–numerical study by Traub [49], and reproduced in Figure 4.2. This questions its validity at low clearances. For comparison with this study of the lifting surfaces, the main wing has a height-to-chord ratio of 1.14 while the tail has a ratio of 1.537 . It is expected that AVL would not provide a vastly different value at these higher clearances. However, a validation study would address this concern.

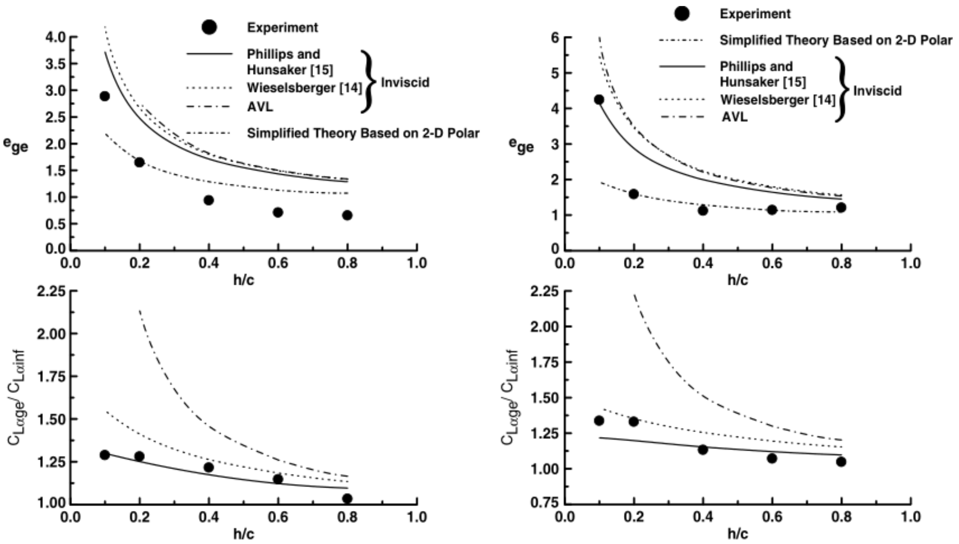

a) AR = 3.46 b) AR = 5.18

Figure 4.2: Comparison of vortex-lattice results from AVL with wind tunnel experiments of finite wings in ground effect that highlight the overprediction of the lift curve slope by AVL, by Traub [49].

4.2.3. Numerical simulations

This section discusses results from the potential flow based numerical simulations that are important at this stage to clarify choices made in following sections.

4.2.3.1. Comparison of AVL and XFLR5: Inviscid analysis

Due to the lack of previous aerodynamic information to validate self-designed models with, two tools, namely, AVL and XFLR5, were used to cross-check for human error in model design and development.

XFLR5 has a user-friendly interface that makes developing a model easy. The model for AVL has to be specified with a text-based self-written file. A model developed in XFLR5 can be exported to AVL in the required format. However, as the purpose of using two different tools was to check for error, these two models were manually and separately developed. Sensitivity analyses were also separately performed to achieve the mentioned element density in the respective tools.

While XFLR5 can incorporate viscous effects by interpolating airfoil data from the 2D panel-method based XFoil tool, an inviscid analysis was performed for the sake of comparing the AVL and XFLR5 models, as AVL is purely inviscid.

The lift polar and inviscid/ induced drag polar obtained from both AVL and XFLR5 are given in Figure 4.3 and indicate that the two separately designed and independently investigated models showed limited and acceptable differences.

This provided the necessary confidence for using both VLM tools separately due to their advantages. The advantage of AVL was the ability to numerically treat the ground effect through the activation of a mirror vortex system. The advantage of XFLR5 was its ability to incorporate interpolated viscous effects from XFoil, the results of which have been used to make comments on the influence of the Reynolds number for the different values considered here for free-flight and ground-run.

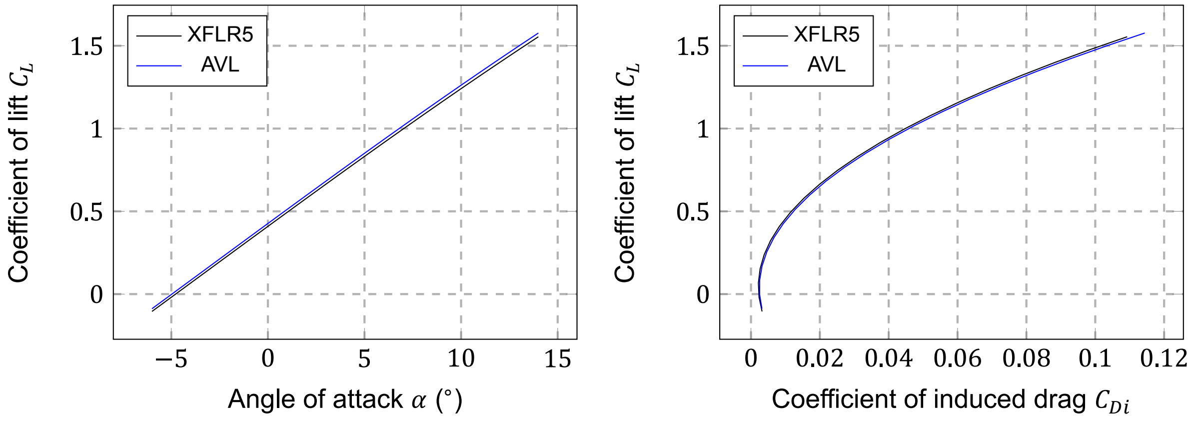

(a) Lift polar **(b)** Induced drag coefficient polar

Figure 4.3: Comparison of results between AVL and XFLR5 from the low-fidelity inviscid vortex-lattice analyses of the lifting surfaces of the intended digital twin, to cross-check for error in their independent development and allow for further independent investigations.

4.2.3.2. Location of boundary layer transition

The state of the boundary layer as expected from the Reynolds number ranges shown earlier in Figure 3.4 could have mixed laminar-turbulent flow. It is therefore important to consider this while choosing the turbulence model for the fully viscous CFD studies.

For getting a basic understanding on the state of the boundary layer for the different Reynolds numbers expected in free-flight and ground-run, the potential flow based XFoil tool has proved valuable.

XFoil, the 2D panel-method based tool that is incorporated into the XFLR5 VLM tool and has also been used in this reported study in a standalone manner, utilises the e^N method to predict the occurrence of transition [109]. The validity of this method in predicting transition is well known and many works can be found in literature [110].

The important parameter about this method relevant here is the choice of N. N is a function of the freestream turbulence level [111]. It is the logarithm of the amplification factor of the most-amplified frequency that triggers transition. Transition would occur at that chord-wise location where the amplification factor achieves the set value of N. Ideally, the user-specified value of N is made based on the known freestream turbulence level at the situation under investigation [109]. Historically, a value of 9 has shown to be sufficient for most cases and is the default 'N_{crit}' value in XFoil. In this report, for cases where it was required to obtain the numerically estimated location of transition, whether it be in the standalone use of XFoil or in its VLM-coupled form in XFLR5, this critical parameter has been left at the default value of 9.

One of the primary bodies of interest of the digital twin is its horizontal tail. As will be shown and discussed later, the horizontal tail will encounter the turbulent wake of the upstream airframe and interact with streamwise oriented wake vortices shed from the fuselage. In such a scenario, it is expected that there will be three-dimensional cross-flow and that the boundary layer would undergo bypass transition. The validity of the e^N method in XFoil is limited to mechanisms where the growth of 2D Tollmien-Schlichting waves is dominant [109].

Based on the flow characteristics seen in the CFD studies reported here, it is recommended that 'trip' locations be set in XFoil to mimic the transition nature [109]. Moreover, the CFD analyses reported here used a fully turbulent RANS turbulence model which is not designed to predict the nature of transition [112], as will be discussed in subsubsection 4.3.2.2. Hence, this is another reason for the use of user-specified trip locations to forcefully achieve turbulent boundary layers. For all instances in this report that mention the use of trips in supporting XFoil results, the trip locations were at 10% of the airfoil chord on both its upper and lower surfaces. This location was chosen prior to the CFD analyses based on van Arnhem et al. [113] that compared a wind tunnel model with CFD results obtained using the same fully turbulent turbulence model used here, due to a personal lack of known expectation of the behaviour of the turbulence model and was not modified afterwards.

The input to XFLR5 is the freestream velocity, density, and viscosity. It then calculates the local chord dependent Reynolds number on its own to interpolate sectional data from XFoil. The values that were used for this study have been covered in the previous chapter for the ground-run and free-flight scenarios. Figure 4.4a shows the estimated location of transition for the free-flight settings. Figure 4.4b shows the estimated location of transition for the ground-run settings. Figure 4.4c shows the trip speicified location of transition which is independent of freestream parameters.

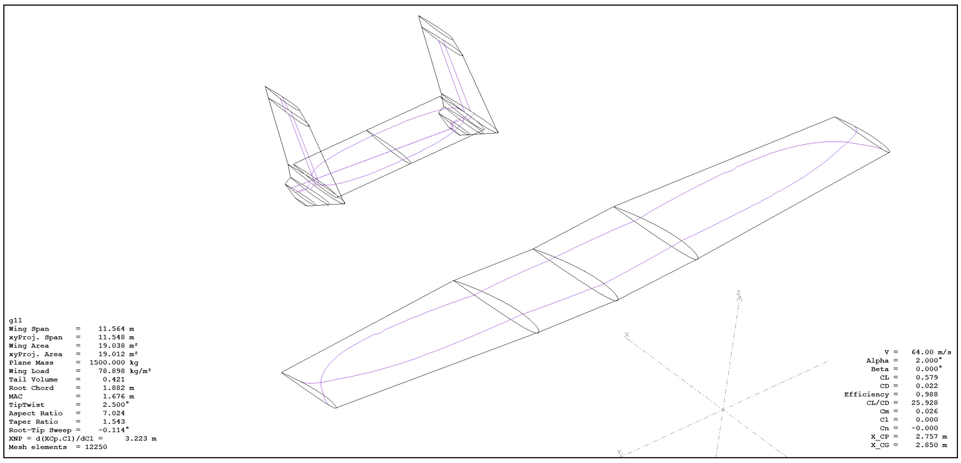

```
g11
Wing Span       =    11.564 m
xyProj. Span    =    11.548 m
Wing Area       =    19.038 m²
xyProj. Area    =    19.012 m²
Plane Mass      =  1500.000 kg
Wing Load       =    78.898 kg/m²
Tail Volume     =     0.421
Root Chord      =     1.882 m
MAC             =     1.676 m
TipTwist        =     2.500°
Aspect Ratio    =     7.024
Taper Ratio     =     1.543
Root-Tip Sweep =    -0.114°
XNP = d(XCp.Cl)/dCl =     3.223 m
Mesh elements  = 12250
```

```
          V =   64.00 m/s
      Alpha =    2.000°
       Beta =    0.000°
         CL =    0.579
         CD =    0.022
 Efficiency =    0.988
      CL/CD =   25.928
         Cm =    0.026
         Cl =    0.000
         Cn =   -0.000
       X_CP =    2.757 m
       X_CG =    2.850 m
```

(a) Free-flight

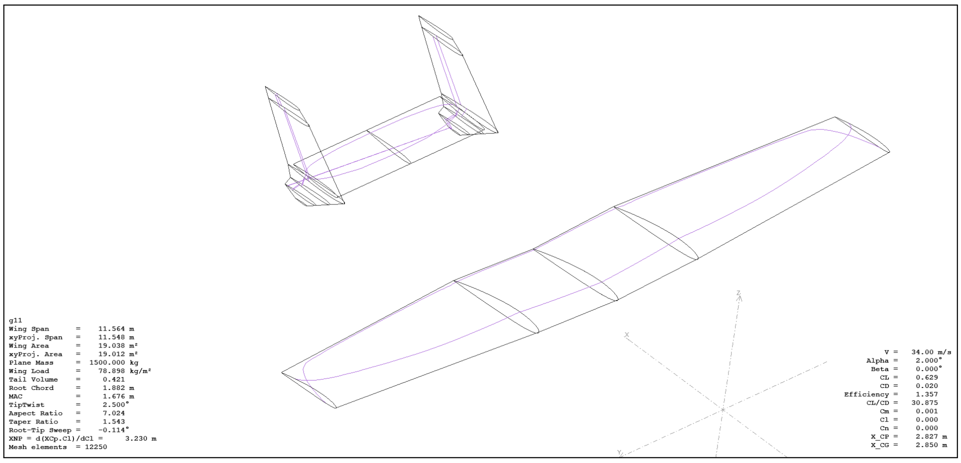

```
g11
Wing Span       =    11.564 m
xyProj. Span    =    11.548 m
Wing Area       =    19.038 m²
xyProj. Area    =    19.012 m²
Plane Mass      =  1500.000 kg
Wing Load       =    78.898 kg/m²
Tail Volume     =     0.421
Root Chord      =     1.882 m
MAC             =     1.676 m
TipTwist        =     2.500°
Aspect Ratio    =     7.024
Taper Ratio     =     1.543
Root-Tip Sweep =    -0.114°
XNP = d(XCp.Cl)/dCl =     3.230 m
Mesh elements  = 12250
```

```
          V =   34.00 m/s
      Alpha =    2.000°
       Beta =    0.000°
         CL =    0.629
         CD =    0.020
 Efficiency =    1.357
      CL/CD =   30.875
         Cm =    0.001
         Cl =    0.000
         Cn =    0.000
       X_CP =    2.827 m
       X_CG =    2.850 m
```

(b) Ground-run

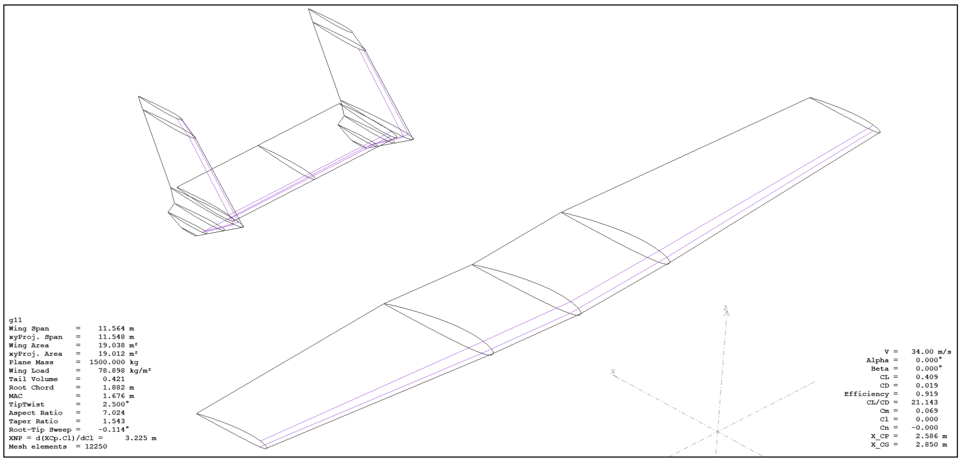

```
g11
Wing Span       =    11.564 m
xyProj. Span    =    11.548 m
Wing Area       =    19.038 m²
xyProj. Area    =    19.012 m²
Plane Mass      =  1500.000 kg
Wing Load       =    78.898 kg/m²
Tail Volume     =     0.421
Root Chord      =     1.882 m
MAC             =     1.676 m
TipTwist        =     2.500°
Aspect Ratio    =     7.024
Taper Ratio     =     1.543
Root-Tip Sweep =    -0.114°
XNP = d(XCp.Cl)/dCl =     3.225 m
Mesh elements  = 12250
```

```
          V =   34.00 m/s
      Alpha =    0.000°
       Beta =    0.000°
         CL =    0.409
         CD =    0.019
 Efficiency =    0.919
      CL/CD =   21.143
         Cm =    0.069
         Cl =    0.000
         Cn =   -0.000
       X_CP =    2.586 m
       X_CG =    2.850 m
```

(c) Specified trip location at 10% of the chord on all upper and lower surfaces

Figure 4.4: Location of numerically estimated transition on the lifting surfaces analysed on XFLR5 with the VLM and 2D panel-method (XFOIL) coupled numerical simulations.

4.3. Computational fluid dynamics

The need for CFD

As was initially stated in section 4.1, two different types of numerical methods were used in this research as part of the methodology followed to answer the research question. One of these was the potential flow type based on an inviscid treatment of the fluid medium, and was discussed at length in the preceding section 4.2. The influence of viscosity was included in a limited two-dimensional capability by iteratively solving the boundary layer equations using the essentially inviscid flow outside the layer as its input.

Neglecting the viscosity of a medium and the effects it would have on an object moving through it, is quite a simplification and significant deviation between numerical computations and the real world applications they are being used to model. The purpose of determining and using the Reynolds number is to provide an indication to the importance of viscosity, as it is defined as the ratio of inertial forces to viscous forces [25].

While the movement of air at a moderate distance from an object, such as the airframe of a flying aircraft, can be modelled by treating it as an inviscid fluid, the thin boundary layer that forms on the surface of the airframe is the region within which the effects of viscosity are most significant [86]. The characteristics and implications of the viscous boundary layer is dependent on the Reynolds number. At low Reynolds numbers where the viscous forces dominate and damp out instabilities, the flow within the laminar boundary layer is described as being steady. With increasing Reynolds numbers and with the decrease in the effect of viscosity to dampen instabilities, the turbulent flow starts showing an erratic motion [79]. Significant strides in the understanding of this viscous boundary layer have been made since the experiment performed by Osborne Reynolds in 1883 that showed the development and transition of a boundary layer between these two states [78]. It is only at very high Reynolds numbers reaching the limit of infinity, where the boundary layer becomes very thin, that the viscous effects could be ignored.

By considering Figure 3.4 that indicates that the range of Reynolds numbers expected for every major airframe component of the Skymaster during a cruising free-flight or ground-run test falls within the region of transition or low turbulent, it is understood, based on the above discussions and the supporting material provided earlier in section 2.4, that viscous effects would be present and their inclusion in any numerical study would prove valuable and make the dataset more relevant for the experiments intended to be executed with the testbed.

Hence, the results of an inviscid analysis using the numerical methods described in the preceding section 4.2, will show differences when compared with future experimental data. A better numerical method based on viscous flows, was required to include and model its effects so as to get a better and more relevant understanding of aerodynamic phenomena that might occur during the experiments.

The Navier-Stokes (NS) equations, made up of the incompressible continuity Equation 4.1 and the incompressible momentum Equation 4.2, are the complete and detailed equations that are used to describe viscous flows [114].

$$\frac{\partial u_i}{\partial x_i} = 0 \tag{4.1}$$

$$\rho \frac{\partial u_i}{\partial t} + \rho \frac{\partial}{\partial x_j}\left(u_j u_i\right) = -\frac{\partial p}{\partial x_i} + \frac{\partial}{\partial x_j}\left(2\mu s_{ij}\right) \tag{4.2}$$

where the strain-rate tensor $s_{ij} = \frac{1}{2}\left(\frac{\partial u_i}{\partial x_j} + \frac{\partial u_j}{\partial x_i}\right)$

CFD is one possible method with the capability of modelling viscous flows, as governed by the Navier-Stokes (NS) equations shown above. It replaces the partial derivative terms of the famous equation with discretized algebraic forms and uses numerical algorithms to solve for parameters describing the flow-field at various created grid points. Its ability to treat non-linear quantities, as seen in fluid mechanics, without simplifying the geometry, makes it an attractive numerical tool to study contoured surfaces such as the fuselage of the Skymaster, here.

The advancements over the years since it was conceptualised, in the numerical algorithms that form a part of CFD, computing systems on which the numerical iterations are performed, and lower cost than experiments, makes it an ideal numerical tool to understand the characteristics of the Skymaster and evaluate the feasibility of the proposed experimental campaigns before performing the experiments themselves. As CFD solves all relevant numerical parameters for the entire flow-field considered as the computational space, it also allows for many investigations to be easily performed, that would otherwise be unknown or difficult to study had experiments been performed directly.

With these advantages, CFD has been chosen as the major and important numerical method in studying the characteristics of the Skymaster, the influence of the propellers as per the theory in subsection 2.3.1, and in evaluating the feasibility of studying propeller-airframe interaction with the proposed experimental plan in section 1.4.

However, the importance of the results of the potential flow-based methods cannot go unacknowledged in providing an initial insight to the expected performance characteristics and in supplementing the fully viscous CFD results with simple calculations that would otherwise have taken far longer to perform and with greater uncertainty due to the associated complexities in numerical modelling in CFD.

CFD can be used to prepare for experiments by providing an initial indication of the expected phenomena, as is the purpose here. However, it is still a numerical method that is very much dependent on the algorithms used in its computations, and will require to be experimentally validated.

RANS equations

As laminar flows are steady in nature, the terms of the Navier-Stokes equations do not raise difficulties while being numerically simulated. The fluctuations occurring with turbulent flows, as the type of flow expected here based on Figure 3.4, requires an appropriate approach to be numerically treated [114].

Direct-Numerical-Simulations (DNS) are algorithms that directly solve the unsteady turbulent fluctuations on sufficiently fine grids capable of resolving the fastest fluctuations in the length scale. Though there is no averaging or approximation in solving the governing equations, except for the discretization performed on them, this is a very computationally expensive method and not suitable for the case here, both, in terms of time and resources. Large-Eddy-Simulations (LES) solve for the larger turbulent structures of a length scale, as they are the structures that transport the conserved properties, and model the smaller structures [115]. Though this is cheaper than DNS due to the simplifications made, it is still expensive for a study as being investigated here, due to the size of the study, the complicated object, and the number of investigations required to be performed. Moreover, such detailed information from either of these two methods is not required for a preliminary investigation such as this reported research.

Reynolds averaging is a method that is based on decomposing a variable as the sum of a mean and fluctuating component, as shown below, and then averaging it

$$u_i = U_i + u_i^{'}$$

where u_i is the total component shown in the Navier-Stokes above, U_i the mean, and $u_i^{'}$ the turbulent fluctuation.

By averaging the terms in this Reynolds decomposition, either over time or as an ensemble, the turbulent fluctuations are considered as zero. Hence, the average flow quantity is the mean quantity.

By performing this Reynolds averaging on every term in Equation 4.1 and Equation 4.2, the Reynolds Averaged Navier-Stokes (RANS) in Equation 4.3 and Equation 4.4 are obtained [114].

$$\frac{\partial U_i}{\partial x_i} = 0 \tag{4.3}$$

$$\rho \frac{\partial U_i}{\partial t} + \rho \frac{\partial}{\partial x_j}\left(U_i U_j\right) = -\frac{\partial P}{\partial x_i} + \frac{\partial}{\partial x_j}\left(2\mu S_{ij} - \overline{\rho u_i' u_j'}\right) \tag{4.4}$$

where S_{ij} is the mean strain-rate tensor.

CFD based solutions using the RANS equations are far more computationally efficient and cheaper than LES and DNS. This makes it a very popular choice for a wide variety of applications where the mean turbulent flow features are far more important than the fluctuations that would occur in the boundary layer. Many advancements made in CFD over the years, have been focused on RANS applications due to its popularity [115].

Hence, it was also the chosen method in estimating the turbulence in the CFD based numerical simulations of the Skymaster in this reported research.

By performing the Reynolds averaging, the RANS equations now contain the new symmetric Reynolds stress tensor

$$\tau_{ij} = -\overline{u_i' u_j'}$$

the components of which are not known and cannot be directly solved for. Additional equations are required to be considered to 'model' this stress tensor and close the RANS equations.

One of the ways of modelling these stresses, is based on the Boussinesq hypothesis that assumes that the turbulent shear stresses linearly depend on the mean rate of strain. For an incompressible flow, this hypothesis is given as in Equation 4.5 [114]

$$-\overline{u_i' u_j'} = 2\nu_T S_{ij} - \frac{2}{3} k \delta_{ij} \tag{4.5}$$

where $\nu_T = \mu_T/\rho$ is the kinematic eddy viscosity that is the proportionality factor of the hypothesis, and k is the turbulent kinetic energy.

Various turbulence models based on this hypothesis have been developed over the years to solve for the terms and close the RANS equations. The discussion of the model chosen in this reported research is provided in subsubsection 4.3.2.2.

subsection 4.3.1 discusses the grid that was generated in the computational space to discretize the different transport equations involved into algebraic forms to be numerically solved. subsection 4.3.2 discusses the various numerical settings, such as the specified boundary conditions and algorithms used in the CFD method.

4.3.1. Grid characteristics

The chosen numerical solver used a finite volume scheme for the spatial discretisation of the NS equations. This discretisation of the integral form of the conservation equations, is performed in the physical domain, also referred to as the computational domain. To do so, the domain is first broken up into tiny control volumes. This is done here through the process of generating a grid within the physical space discussed in subsubsection 4.3.1.1 using elements of different shapes and sizes as discussed in subsubsection 4.3.1.2.

The accuracy of spatial discretisation also depends on the schemes chosen for estimating the fluxes passing through the faces of the control volumes, and are discussed later in subsubsection 4.3.2.4.

The generation of the grid only defines the nodal points that can be used to define control volumes. The choice of the central node of the control volume at which the flow quantities are evaluated and stored, depends on the scheme used to define it. Here, the cell-centred scheme was used with the chosen numerical solver. With this scheme, the control volumes used for the numerical computations were the same as the grid generated. The centroid of each element was the location at which the flow quantities were evaluated.

The following sections discuss the manner in which the grids were generated in the computational domains used for the numerical CFD investigations.

4.3.1.1. Computational domain and bodies of influence

The distances between the boundary faces of a computational domain and the object within are known to affect the numerical solution [116]. A suitable rectangular computational domain with a size based on the recommendations of Goetten et al. [117] was chosen and iteratively studied to check that the solution was not affected. This was done through the monitoring of normal and axial forces calculated on the surfaces of the digital twin and the recovery of the pressure downstream of the twin.

For both the free-flight and ground-run cases, the length of the domain was 40 full-wing spans with the front face 12 spans ahead of the base of the front spinner. The width of the half-model rectangular domain was the same, at 10 spans. The height of the domain was 12 spans in free-flight and 9 spans in ground-run.

The choice of the size of the element can define the resolution of the flow that it can solve for [117]. As discussed in subsubsection 4.3.1.2, smaller elements were required closer to the surfaces of the digital twin. As creating a grid across the whole computational domain with the same small element size required around the object would lead to an extremely large number of grid points and increase the computational cost, smaller computational domains called 'bodies of influence' were defined within the total computational domain. Defining these bodies allowed for better control over the selective refinement of elements in the required regions only. This allowed to have increased grid resolution at a limited increase in computational expense.

Figure 4.5a shows the computational domain and bodies of influence ‘away’ from the Skymaster defined for the simulations of free-flight. Figure 4.5b shows the same for the ground-run case. The location of origin in these images is at the base of the front spinner of the Skymaster and depicted by the visible axis placed at that location. Figure 4.5c shows the different bodies of influence defined around the full model (only half model was used but this representation is clearer) of the Skymaster to obtain optimum and efficient refinement in the near-wake region. This arrangement was the same for the two cases. The body of influence around the rear propeller intended to aid in element refinement in the slipstream, had a diverging shape. This was to capture the slipstream in spite of any displacements that would occur to its location over the range of angles of attack studied, as will be mentioned in section 5.2. This choice was inspired from a study focusing on the propeller slipstream [118].

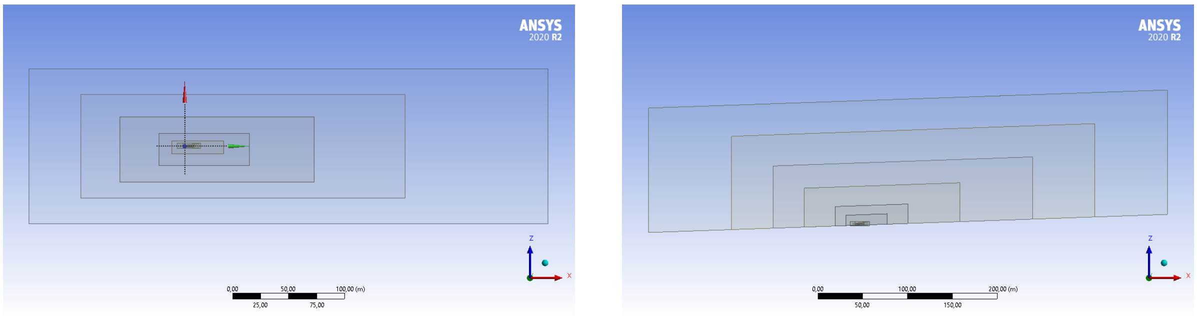

(a) Computational domain and bodies of influence defined for the grid generation process of the numerical model for free-flight conditions

(b) Computational domain and bodies of influence defined for the grid generation process of the numerical model for ground-run conditions

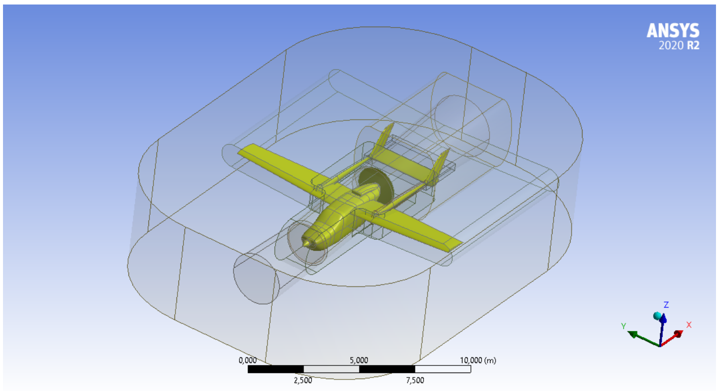

(c) Common and unchanged bodies of influence defined around the parts of the digital twin for better control of grid refinement in the near-wake regions during grid generation (only a half model was used for the CFD analyses but, this image provides a better understanding)

Figure 4.5: Computational domain and bodies of influence defined for the grid generation process of the numerical model.

4.3.1.2. Element types and refinement

An advantage of the finite volume scheme is that it is compatible with arbitrary elements arranged in an unstructured manner. Here, both the volume mesh and surface mesh were made up of unstructured tetrahedral elements. These elements easily conform to complex geometries [114].

The element sizes defined on the wings was such that approximately 180 elements would be obtained along the chord for the baseline finest mesh. Similar to the choice of the size of the computational domain, this too was made on the recommendations of Goetten et al. [117]

The volume in the wake region had the same element size definition as the surface elements on the wings. Coarser sizes were seen to increase the numerical diffusion and not capture the wake effectively. This ‘effectiveness’ was judged based on the existence of the wing’s wake till a downstream location of 2 horizontal tail chord lengths behind the trailing edge of the horizontal tail. This method of inspection was inspired from wind tunnel-CFD comparison where data was monitored on a downstream wake survey plane [113]. In essence, this location chosen to monitor the presence of the wake was a wake-survey plane where it is required to capture the wake.

From the innermost elements in the bodies of influence seen in Figure 4.5c, a baseline constant volume growth of approximately 15% was successively applied to the elements in the next outer body, which are shown in Figure 4.5a and Figure 4.5b.

The treatment of the boundary layer near the walls in this domain along which it will form, as will be discussed in subsubsection 4.3.2.3, was done by fully resolving it and not treating it with any wall functions. This was considered essential due to the interest in investigating the influence of the Reynolds number which is known to affect the boundary layer height.

To fully resolve the boundary layer for these low Reynolds number studies, non-dimensional height of the first grid element was kept well below 1 and within the sub-viscous layer [116], that is

$$y^+ < 1$$

This was done by specifying the height of the first grid element as $5.0 \times 10^{-6} m$. This choice would also make the generated grid compatible with the chosen turbulence model discussed in subsubsection 4.3.2.2. 25 layers of prismatic elements were inserted near the wall with a growth rate of 1.20 .

Hence, the combined usage of the unstructured tetrahedral elements and the prism elements resulted in the formation of a hybrid mesh.

4.3.2. Numerical settings

As computational fluid dynamics (CFD) is a numerical method designed to solve the RANS equations, the choice of algorithms utilised in doing so are important along with any specified numerical value.

These include the method of treating the fluid and the associated formulations as given in subsubsection 4.3.2.1, the choice of the turbulence model that has been used to estimate the effects of turbulence as based on the Boussinesq hypothesis in Equation 4.5 and is discussed in subsubsection 4.3.2.2, the boundary conditions specified at the faces of certain grid elements as described in subsubsection 4.3.2.3, and the numerical algorithms used in the computational analyses which are given in subsubsection 4.3.2.4.

4.3.2.1. Incompressible fluid

The Mach numbers, calculated as the ratio of the aircraft speed to the speed of sound at that altitude, was 0.19 for free-flight and 0.10 for ground-run. Compressibility effects are usually considered for Mach numbers above 0.3 [86]. For the incompressible fluid, the density and viscosity were defined as constant as per the values mentioned in Table 3.3. The energy equation was not solved for. The influence of the propeller would only be to add momentum to the flow, but not change the enthalpy.

4.3.2.2. Turbulence model

The single equation Spalart-Allmaras(SA) [119] turbulence model was chosen for modelling the Reynolds stresses in the CFD simulations of this reported research. The SA model is an efficient, robust, less grid sensitive turbulence model widely used and preferred in aerospace related investigations for cases with adverse pressure gradients [114][115]. It is also a proven choice in propeller and wingtip vortices related simulations [87].

The SA model does not calculate the kinetic energy in Equation 4.5. It solves for the eddy viscosity by introducing another viscosity term, the modified turbulent viscosity $\tilde{\nu}$. $\tilde{\nu}$ is the same as ν_T in the freestream, but not in viscous regions.

The new variable is related to the kinematic eddy viscosity as

$$\nu_T = \tilde{\nu} f_{v1} \tag{4.6}$$

where f_{v1} is a wall damping function defined as

$$f_{v1} = \frac{\chi^3}{\chi^3 + C_{v1}^3} \tag{4.7}$$

where

$$\chi = \frac{\tilde{\nu}}{\nu} \tag{4.8}$$

and C_{v1} is one of the model coefficients that have been calibrated based on empirical research.

The ‘Strain/Vorticity’ correction based on the modification proposed by Dacles-Mariani et al. [120] was used. This modification includes both the rotation and strain rate tensors to reduce the production of eddy viscosity in regions where the vorticity exceeds the strain rate, such as vortex cores. This prevents over-prediction of the viscosity.

The SA model is not designed to predict the nature of transition [112]. As shown in Figure 3.4, all components fall within the range of transitional Reynolds numbers, hinting that a ‘transition’ turbulence model could be used. However, these require to be calibrated for specific applications for best results [83]. The SA model activates when the ratio of eddy viscosity to molecular viscosity $\mu_T/\mu \geq 1$. It has quite a low activation Reynolds number [112] which is far below any of the calculated values shown in Figure 3.4.

As was discussed in subsection 2.4.1, transition of the boundary layer from laminar to turbulent would occur when the instabilities in the flow are amplified sufficiently and sustained without being damped out by viscosity or other active control measures.

Figure 3.4 shows that for free-flight, the Reynolds numbers calculated for every component of the Skymaster is quite high and almost fully turbulent. Hence, it is reasonable to expect that most of the airframe would feature a turbulent boundary layer just due to the natural instabilities introduced at this Reynolds number, justifying the use of the fully turbulent SA model, as done here.

A similar expectation for the lower Reynolds numbers seen in ground-run need not be valid. In fact, the mainwing will operate in relatively clean air that is undisturbed by the rest of the airframe, unlike the tail surfaces, and could feature laminar flow at least to some extent. In fact, In the earlier shown results in Figure 4.4 from the low-fidelity potential flow-based tools that estimated the location of transition with the e^N method, it is seen that the location of transition on the lower side of the mainwing is pushed to the trailing edge at the lower Reynolds number corresponding to the ground-run case.

Further motivation was required to continue with the same fully turbulent model for the CFD simulations performed in ground-run at the lower Reynolds numbers. These are discussed now.

The surfaces of the Skymaster have many features that could introduce instabilities into the boundary layer, such as protruding nuts, bolts, rivet heads, deformations of the surfaces of the old aircraft that would alter pressure gradients, stall strips, amongst others.

The atmospheric turbulence levels is expected to be higher near the ground than at cruising altitudes, as based on comments found in literature [104]. Though this remains to be experimentally proven, it is a valid assumption given that this is well within the earth’s boundary layer and influenced by the surrounding terrain. This could also possibly lead to the generation of instabilities.

In addition to the freestream turbulence level, the local acoustic field could also be responsible in introducing instabilities into the flow [81]. A noise source close to the mainwing, would be both propellers of the Skymaster [18] and the noisy piston engines [19].

The total effect of these discussed sources are expected to trigger transition on both surfaces of the mainwing in ground-run, just like in free-flight, though it is unknown at what chord and spanwise locations along its surfaces. This would result in a turbulent wake being generated by the mainwing and the fuselage which will be convected downstream in the direction of the tail.

Figure 4.6a shows the presence of turbulence in the freestream at the leading edge of the horizontal tail as depicted by $\mu_T/\mu \geq 1$ and is from the CFD results that used this fully turbulent SA model. The spanwise sections that encounter this turbulent flow will show an instantaneous transition to turbulent boundary layer, like in figures (b)$2y/b_{HT} = 0.00$ and (c)$2y/b_{HT} = 0.35$, just like most of the span. This form of transition would bypass the formation of small amplitude disturbances [84]. For the small area of sections outside this wake, natural transition would occur, like in figure (c)$2y/b_{HT} = 0.36$.

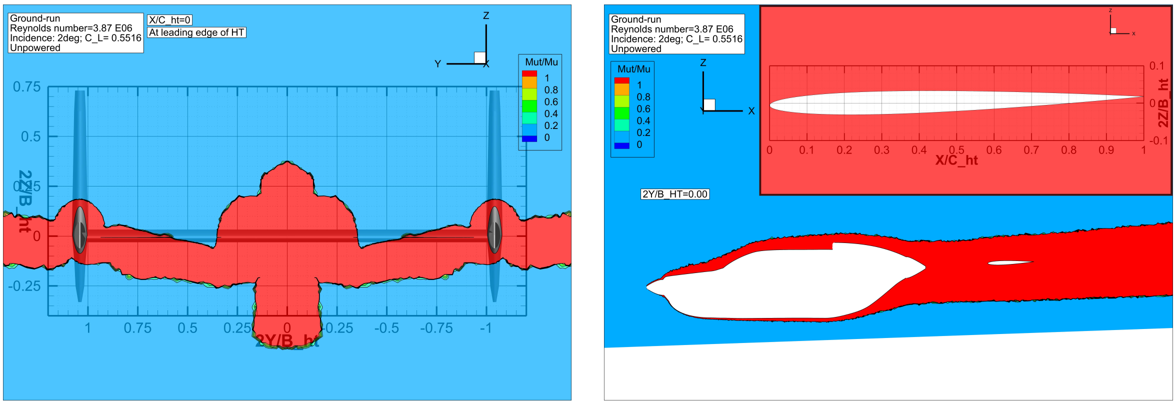

(a) Turbulent wake region across the span of the HT

(b) Sectional view at symmetry plane

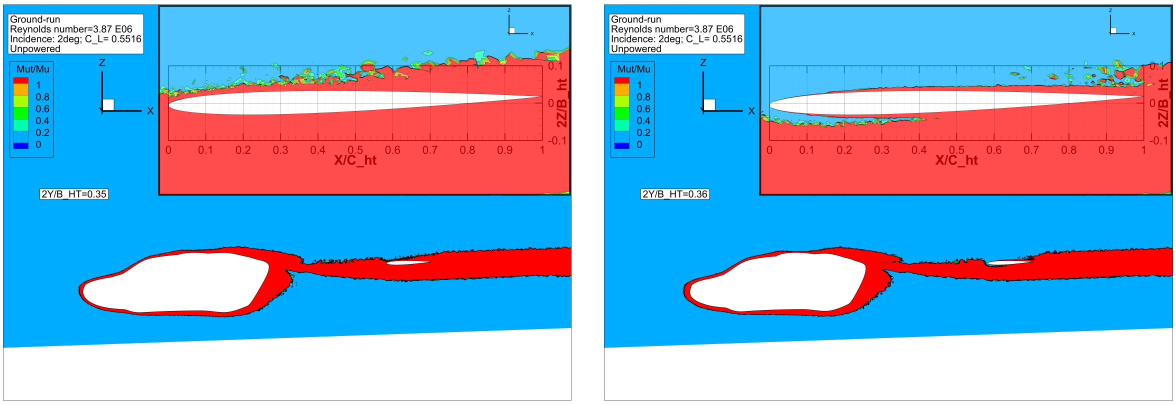

(c) Sectional view at $2y/b_{HT} = 0.35$, on the edge of the turbulent fuselage wake influence region

(d) Sectional view at $2y/b_{HT} = 0.36$ with no turbulent fuselage wake influence

Figure 4.6: Distribution and influence of turbulent wake interacting with the tail, shown by $\mu_T/\mu \geq 1$, for unpowered ground-run.

As will be shown and discussed in many sections of the next chapter, wake vortices were seen to be shed by the fuselage and convected downstream and interacted with the horizontal tail of the Skymaster. Based on subsection 2.5.1, this interaction would also affect transition. Here, it was seen that the vortices induced high angles of attack along the tail, as will be shown in Figure 5.33. Considering that the tail uses a thin NACA 0009 airfoil, the high angles of attack would lead to strong suction peaks and strong adverse pressure gradients in the recovery region.

The combined influences of the high turbulence due to the upstream airframe, the three-dimensional flow due to vortex-wing interaction, and the tail's airfoil's response to large angles of attack, was expected to promote transition rather than maintain laminar flow.

Hence, even though the possibility of the presence of laminar flow on the mainwing and horizontal tail exists, at some currently unknown chord and spanwise location, there are sufficient reasons, as just discussed at length, to expect the occurrence of transition to a turbulent boundary layer, and justify the use of a fully turbulent model for simulations at both free-flight and ground-run Reynolds numbers. As will be discussed in subsubsection 4.3.2.3, care was taken to keep the inlet turbulence setting low, so as not to contaminate the results with artificial numerical decambering effects of the airfoils.

Additionally, there is no available experimental data indicating that a different turbulence model would be required. By fixing tufts on the lifting surfaces of the testbed and studying their motion during a taxi-test, a better, albeit, crude understanding of the nature of the boundary layer can be derived. This could then dictate the choice of the turbulence model and the location of transition.

4.3.2.3. Boundary conditions

Boundary conditions are specified at the faces of certain specific and known grid elements, so that the information originates from those elements and propagates through the rest of the domain. The discretised equations being solved on the generated grid would be modified to incorporate these conditions [115]. Here, the boundary conditions were specified as per the following paragraphs and its influence on the computational space was investigated, as shown by the contour based results in the following chapter.

The operating conditions which were translated to boundary conditions for the CFD studies have been covered in detail in section 3.3 Operating parameters.

Walls of the control volumes

For the free-flight simulation, 4 velocity inlet faces were defined with a velocity magnitude of $64m/s$ and directional components for an angle of attack $2°$ with no sideslip.

For the ground-run simulation, 3 velocity inlet faces were defined with a velocity magnitude of $34m/s$ and parallel to the ground plane. The ground plane was defined as having a finite velocity equal to the freestream $34m/s$ as per the recommendation of Barber et al. [67] covered in subsection 2.2.5.

The outlets in both types of simulations were the faces directly behind the Skymaster and were defined as pressure outlets with default pressure and turbulence settings.

A symmetry boundary condition was defined at the symmetry plane for this half-model simulation. This implies that there is a zero normal velocity and zero normal gradients of all variables at this plane.

All walls on the Skymaster were defined as no-slip walls.

These definitions are shown in Figure 4.7.

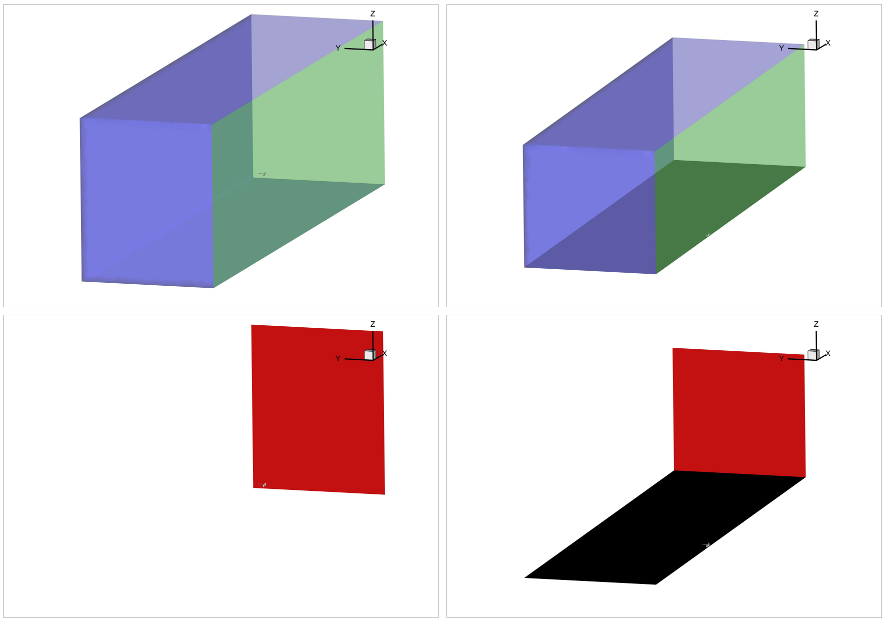

Figure 4.7: Boundary conditions at faces of the control volume.
Blue: Inlets, Red: Outlet, Green:Symmetry, Black: Ground.

Propellers

The propellers were treated as infinitesimally thin disks that were uniformly loaded and imparted a constant static pressure rise to the flow passing through it, as per the theory discussed earlier in subsection 2.3.1. This was done using the *Fan* boundary condition on ‘internal faces’ created for the fans. The boundary condition definition was set as a constant and uniform pressure rise. This pressure rise was user-specified as per the calculation discussed in the following paragraph. Figure 2.10 showed the increase in pressure occurring across the face of the disk, as a whole. Figure 4.8 shows the implementation of the actuator disk theory along the disk, in the form of a uniform and constant pressure rise at every location, irrespective of its radial or azimuthal location.

This is seen later in Figure 4.11 and Figure 4.12 where results from the performed CFD studies show this same intended pressure rise across the faces of the disks, along with the influence that the airframe located within the disks' slipstream has on the slipstream parameters.

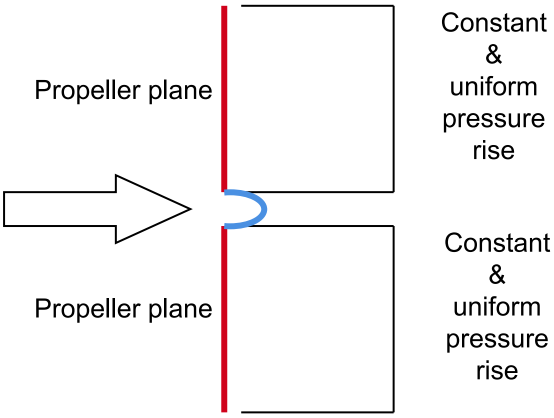

Figure 4.8: The constant and uniform pressure rise (profile in black) implemented as a boundary condition in the numerical CFD studies that treated the disk as an actuator disk. Shown on an isolated propeller (in red) - spinner (in blue) arrangement.

For the numerical simulations of the unpowered configuration of the digital twin, the pressure rise was set as $0Pa$. For the simulations performed to investigate the influence of power, the thrust required to be generated by the propellers was equated to the drag of the digital twin calculated from the numerical simulations of the unpowered configuration. This was chosen so as to obtain a steady flight scenario in both free-flight and ground-run.

To repeat the reason for this choice as initially mentioned in section 2.1; it is assumed that data acquisition during future experiments would be done at a steady flight condition, at least initially. This required thrust was then split equally between the propellers as deeply discussed in section 3.3, in the relevant paragraphs alongside Table 3.1 and Figure 3.3. This basically means that each propeller was intended to produce half of the total required thrust.

Using Equation 2.4 that relates the disk diameter and pressure rise to the thrust generated, the pressure rise specified as the boundary condition in this Fan model was calculated for each disk with their respective disk diameter, as in Equation 4.9. The diameters of the disks have been reported ealier in subsection 3.2.2 in chapter 3.

The resulting and final specified pressure rises are given in Table 4.1.The required thrust force reported in newtons can be compared to the drag force it has to equal to, by converting the drag coefficients of the unpowered configuration in subsection 5.2.2 to their respective force values.

$$\Delta P = \frac{Thrust}{Area} \tag{4.9}$$

		Front propeller	Rear propeller
Case	Total Thrust (N)	ΔP (Pa)	ΔP (Pa)
Free-flight	615.46	199	210
Ground-run	190.18	63	66

Table 4.1: The specified boundary condition in the CFD numerical solver for the pressure rises across the propeller disk faces, as calculated using the Rankine-Froude momentum theory with the respective disk area for an estimated thrust to maintain steady flight and overcome the drag calculated from the unpowered configuration studies that was equally split between the two propellers.

As was mentioned in subsection 2.3.3, the flow-field quantities relevant for this study to characterise the propeller slipstream are the axial velocity, total pressure distribution, and static pressure distribution across the propeller disk. These are discussed in the following paragraphs with the results obtained from the CFD analyses that used the boundary conditions compiled in Table 4.1.

Figure 4.9 shows the axial velocity ratio distribution on the plane of symmetry. The gradual increase in the velocity as it approaches the propeller plane is seen to occur in a similar manner to the theoretical description provided earlier in Figure 2.10, albeit with the added influence of the airframe. The influence of the airframe makes the flow non-uniform, with accelerations or decelerations influenced by the wall curvature and leading edge stagnation that influences locations upstream of it.

A key factor seen is the direction of flow depicted by isolines separating the contour bands, as they pass through the rear propeller plane. The isolines are seen to be forced to remain on a slightly ‘straight’ path rather than than follow the trajectory it was on before reaching the propeller plane. This is referred to again in subsection 5.7.2 to justify the argument that a reduction in angle of attack at the tail is due to increased axial velocities introduced by the propeller into the flow. The resulting flow velocity vector is modified due to the change in this velocity component.

At the underside of the fuselage, at the location where the near-straight underside changes direction and starts tapering towards the rear spinner, a high velocity locally exists. This is higher in ground-run than free-flight, due to the formation of a convergent-like passage between the ground and the fuselage. The resulting wake following this higher velocity is larger in ground-run. This velocity distribution also supports subsubsection 5.6.1.1, which discusses the surface pressure distributions along the same fuselage centreline as seen here, and the presence of a vertically larger wake shed by the fuselage due to more separation occurring in ground-run. No flow reversal is seen along this plane and supports the discussion and results shown later in section 5.5.

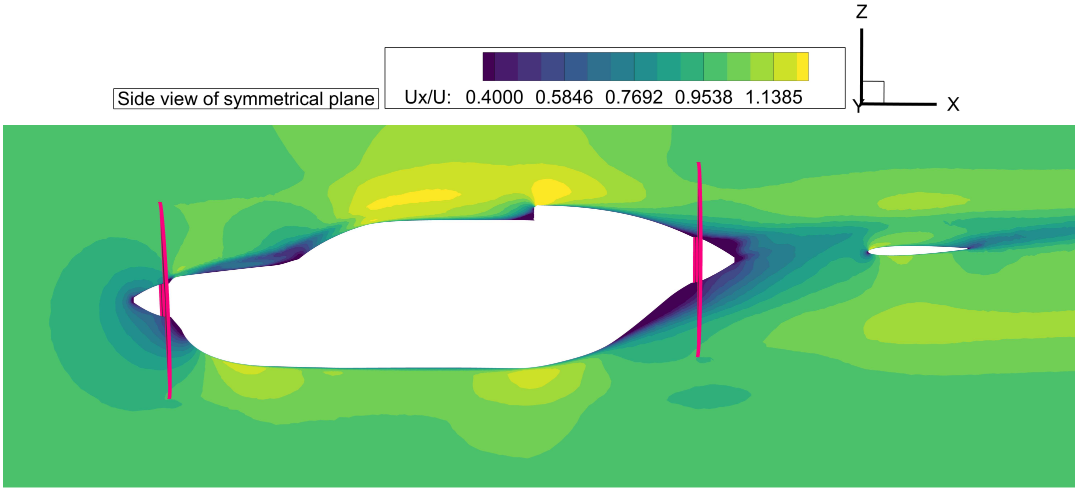

(a) Powered free-flight

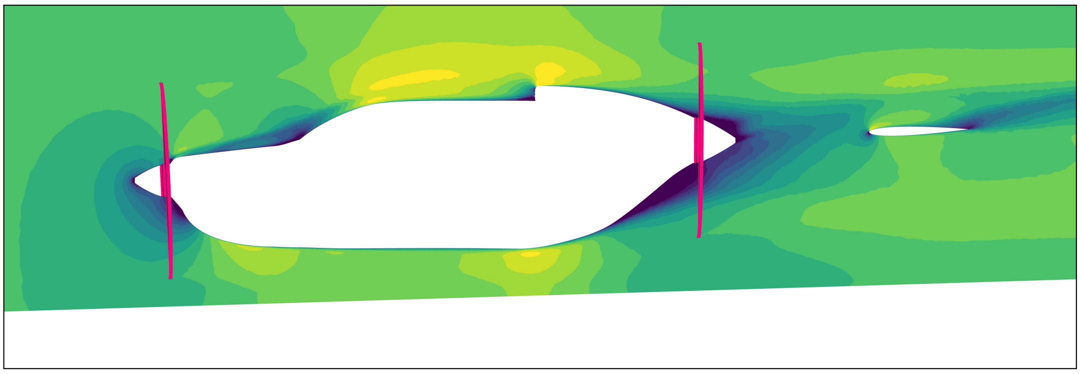

(b) Powered ground-run

Figure 4.9: Axial velocity ratio (U_x/U_0) distribution shown on the plane of symmetry with propellers in pink, from the CFD numerical investigations performed on the powered configuration as a parameter to characterise the slipstream.

In addition to the axial velocity ratio, the rise in total and static pressures across the propeller disks are also parameters that characterise the slipstream produced by this propeller model here.

Figure 4.10 shows the locations of the installed front tractor and rear pusher propellers. The rise in total and static pressure coefficients were investigated along the diamteric centreline of the disks, indicated by the blue dashed line passing vertically along its centre and through the spinner.

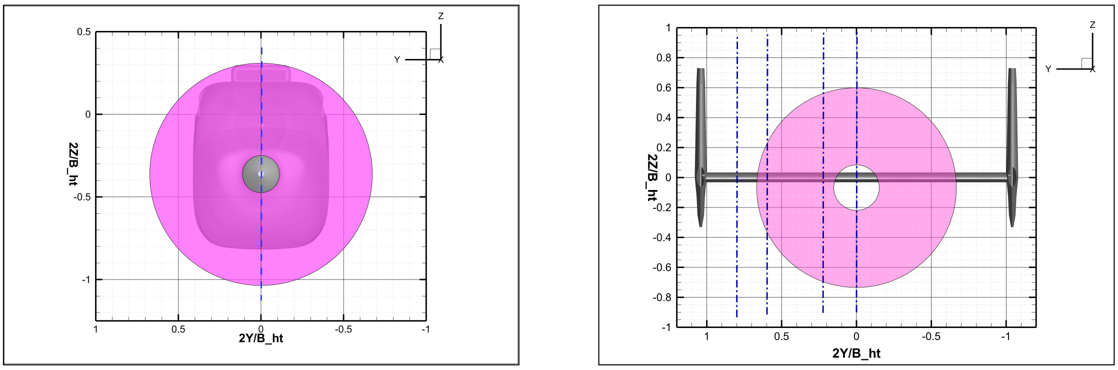

(a) Front tractor propeller disk shown with respect to the fuselage it is installed in

(b) Rear pusher propeller disk shown with respect to the empennage its slipstream influences

Figure 4.10: Locations of the front tractor and rear pusher propeller disks that show the diametric centreline across which the rise in static and total pressure coefficients was investigated as parameters relevant in characterising the slipstream produced by the model under investigation.

For the rear propeller, the two relevant flow-field quantities were taken on manually defined planes on either side of the propeller. It was attempted to keep the distance of the plane within 1 grid element. However, as the grid in the volume was unstructured, as was discussed in subsection 4.3.1 this could not be done at every location along the axisline of interest.

The front propeller is installed at an angle of -3° with respect to the fuselage, as was mentioned in chapter 3. An attempt at rotating the shifted plane to be parallel to the propeller plane was not successful. Hence, the two planes created on either side of the front propeller, to obtain the quantities and calculate their differences to indicate the rise in that quantity, had different lengths between it and a face of the propeller disk.

Figure 4.11 shows the rise in the total pressure coefficient. This flow-field quantity is defined later in Equation 5.11 and can be understood as the ratio of total pressure to freestream dynamic pressure. The rise is calculated as the difference in the flow-field quantity between a plane behind the propeller and one ahead. By considering the mean of the profiles, the rise in pressure is the same as the intention of the boundary condition that was presented earlier in Figure 4.8.

Figure 4.12 shows the rise in the static pressure coefficient. This flow-field quantity is defined later in Equation 5.9 and can be understood as the ratio of static pressure to freestream dynamic pressure. The rise is calculated as the difference in the flow-field quantity between a plane behind the propeller and one ahead. By considering the mean of the profiles, the rise in pressure for the rear propeller shown in Figure 4.12b is the same as the intention of the boundary condition that was presented earlier in Figure 4.8. For the rise in pressure coefficient across the front propeller as shown in Figure 4.12a, the upstream influence of the fuselage seems to be considerable.

By also considering the installed negative angle and the angle of attack of the freestream, it is seen that the lower side of the fuselage creates a slight stagnation region ahead of it. This ground-effect like behaviour for propellers operating in this installed condition ahead of fuselages with no cooling inlets was discussed earlier in section 2.3 [74][75]. The positive pressure across this lower frontal part of the fuselage is seen to be an upstream stagnation effect due to the fuselage shape and is supported with the results in Figure 5.22 that show a similar pressure profile along the frontal part of this centreline section of the fuselage. Again as a consequence of the installed angle and freestream angle of attack, such a stagnation on the upper parts of the frontal fuselage nose influenced by the propwash is not seen. In fact, the propwash very slightly decreases the pressure coefficient and leads to a suctional force over the upper parts of the fuselage nose. This is shown later in the images in section 5.3 and the pressure distribution in Figure 5.22.

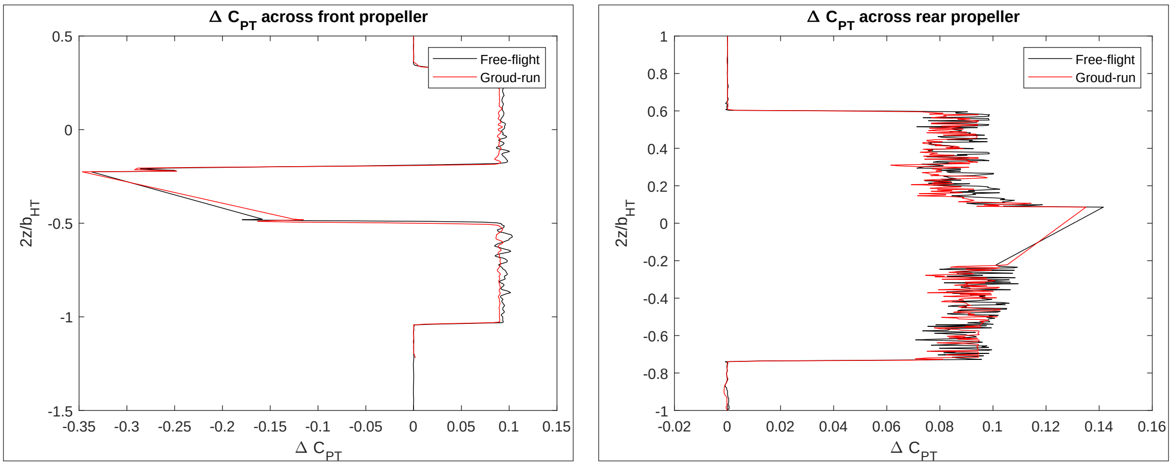

(a) Rise across front propeller **(b)** Rise across rear propeller

Figure 4.11: Rise in the total pressure coefficient across the front and rear propellers in both free-flight and ground-run.

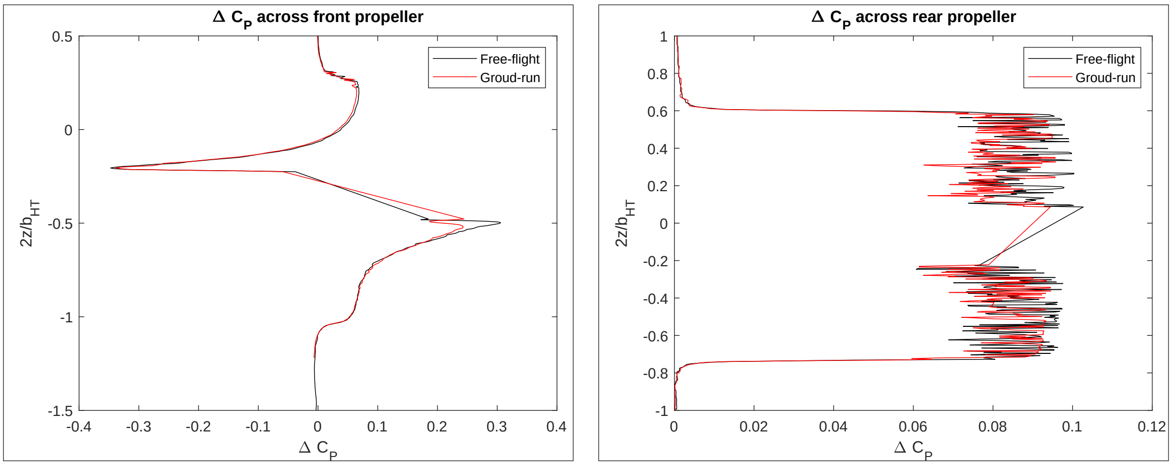

(a) Rise across front propeller **(b)** Rise across rear propeller

Figure 4.12: Rise in the static pressure coefficient across the front and rear propellers in both free-flight and ground-run.

This concludes the investigation into the flow-field quantities that have been used to characterise the propeller slipstream and prove the intended numerical operation of the chosen boundary condition for rear propeller that is not influenced by any component of the airframe downstream of it. The front propeller is influenced by the upstream stagnation caused due to the downstream located fuselage. The location of these propellers on the finally investigated half-airplane model are shown in Figure 4.13.

Rear enigne air inlet

The available *Mass flow outlet* boundary condition was used for the rear engine air intake face visible in Figure 4.13. The reason for choosing this location as the face for the required boundary condition has been discussed in Appendix B. The numerical CFD solver internally converts the input mass flow rate into a flux. By defining the mass flow rate, it was seen that there were some unphysical regions with high velocities across the inlet near to the symmetrical plane (these results are not reported her). Hence, the flow rate was specified as its equivalent mass flux. An average mass flux was also specified so that the solver would adjust the distribution by its self and in an unspecified manner (due to a lack of a user-specified target profile that it is otherwise designed to aim for) and prevent such unphysical values being estimated. Hence, the final mass flow rates were slightly different, as shown in Table 4.2. Not being a focus of this study and due to the lack of better information, this was a means to an end.

Case	Target mass flow rate (kg/s)	Mass flux $(kg/(m^2s))$	Average mass flux $(kg/(m^2s))$	Resulting mass flow rate (kg/s)
Free-flight	0.6	25	30	0.627
Ground-run	0.5	20	25	0.523

Table 4.2: Specified boundary condition and difference in targeted and resulting mass flow rates for the rear engine air intake of the half model studied with the CFD numerical tool.

Figure 4.13 shows the two propellers and the rear engine air intake face on which the boundary conditions were applied.

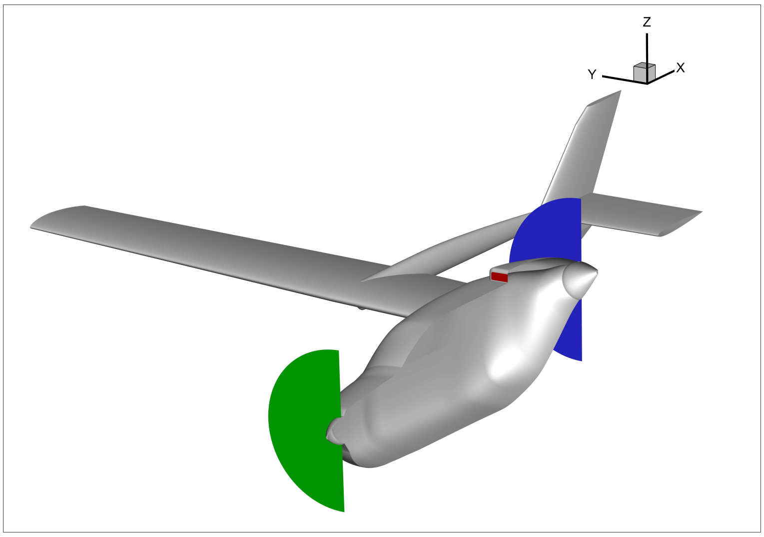

Figure 4.13: Location of propellers and rear air intake of the numerical model on which relevant boundary conditions were imposed
Green: Front propeller, Blue: Rear propeller, Red: Rear engine air intake

Inlet turbulence setting

The turbulence setting defined at the inlet is very crucial to any numerical analysis [121].

In the absence of experimental data, numerical estimates have to be made for the inlet turbulence settings to obtain the necessary ambient turbulence settings at the object with considerations for spatial decay. For the SA model, Spalart and Rumsey [121] recommend an inlet value of $\tilde{\nu}/\nu = 3$ for low Reynolds numbers as the corresponding ν_T/ν will be less than 1.0.

Spalart and Rumsey [121] state that there is no reason to specify $\tilde{\nu}/\nu$ as greater than 3, as a fully turbulent boundary layer would already be achievable with this setting. Increasing this ratio would cause the ambient values to affect the interior of the boundary layer and contaminate its results by increasing turbulence.

As already discussed earlier in subsubsection 4.3.2.2 and supported by Figure 3.4, there is a likely possibility that the wing could have some amount of a laminar boundary layer over its surfaces during the ground-run operation as it operates at a Reynolds number that falls within the transitional range. If a higher inlet turbulence viscosity ratio was specified for the freestream than the one chosen above, it could contaminate the boundary layer by increasing turbulence. The contamination would lead to the decambering effects discussed earlier in subsection 2.4.2, and could lead to large deviations between the results of this fully turbulent analysis and a real-life scenario where some laminar flow does exist on the mainwings. This is notionally shown in Figure 4.14 which is from studies performed by Spalart to make this recommendation. The importance of this setting is again mentioned in section 5.8 that compares some results of the fully turbulent CFD studies with those fom 2D panel-method based numerical tools.

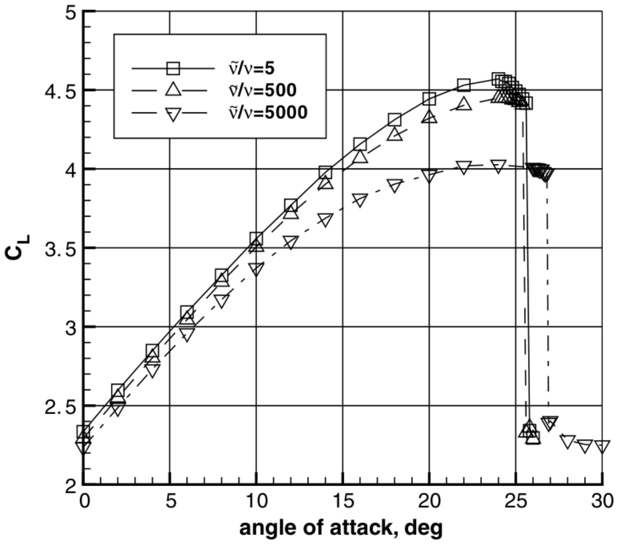

Figure 4.14: Impact of decambering on a 3-element airfoil lift polar at $Re = 9.0 \times 10^6$ due to the increasing turbulent contamination of boundary layer nature with high inlet turbulence settings specified in RANS CFD numerical studies using the Spalart-Allmaras turbulence model. Image from Spalart and Rumsey [121].

Using Equation 4.7 with model constant $C_{v1} = 7.1$ and χ defined in Equation 4.8, and converting the modified turbulent viscosity ratio to eddy viscosity ratio, the obtained value is

$$\frac{\mu_T}{\mu} = 0.2104$$

This is also consistent with the works within the Faculty [87][113][118][122] at similar or lower Reynolds numbers.

As this low value is also the ‘floor’ value in the chosen finite volume cell centred solver, no source terms were required to be defined through the control volume to control the decay rate. This ambient value is clearly seen in all images in Figure 4.6 and again in Figure 5.12.

4.3.2.4. Numerical algorithms

The choice of numerical algorithms and schemes used in CFD will affect the accuracy of the results, and also the stability of the numerical solution process [114]. The final choices of the below mentioned algorithms was motivated by the recommendations of the numerical solver that provided comparisons of the different schemes available for different calculations [94]. The primary goal was to use the most accurate schemes and control the stability by tweaking its relaxation parameters if required. There was no need to tweak any such parameter for all schemes chosen. Only the manner in which the pressure-velocity coupling was achieved had to be changed from a more robust coupled scheme to a more stable but less accurate segregated scheme due to the inability to achieve convergence with the preferred fully implicit coupled scheme.

Only the continuity and momentum equations were considered in the numerical model as there were no known requirements or specified boundary conditions that would require the use of the energy equation.

For the low Mach numbers less than 0.2 expected at the operational settings of interest, no compressibility effects were expected and be required to model. Hence, a pressure-based solver was used to discretise the governing equations.

As being a preliminary investigation, and with no known prior information on the nature of the flowfield to be expected, it was desired to get a numerical estimate of the mean quantities of the flow. Hence, a steady-state approach was utilised that disregarded the temporal terms in the governing equations.

Pressure is not a conserved value and does not have its own governing transport equation. To achieve pressure-velocity coupling for this pressure based solver, a coupled algorithm based on a Rhie and Chow type scheme was initially used. This coupling provides accurate results in a robust and efficient manner with increased rate of convergence, albeit with an increased computational expense than segregated solvers. This method solves the governing equations together through implicit discretisations of the pressure gradients and face flux terms. However, converged solutions could not be achieved for fine grids created with the intention of resolving the wake between the rear propeller and the horizontal tail. Hence, this coupled scheme was dropped and a segregated manner to solving the pressure and velocity fields was pursued.

The Semi-Implicit Method for Pressure Linked Equations, SIMPLE, is applicable for steady state flows and uses a predictor-corrector method to calculate pressure on the staggered grid. The iterations in the solution process are much faster than the coupled scheme, but the results are very slow to converge with the residuals are usually unable to reach the same levels as with the coupled scheme. The accuracy of the results is also decreased. Using a guessed pressure field, a velocity field is obtained from the discretised momentum equations. If the resulting flux does not satisfy the continuity equation, a correction is made to the initial guess and the process repeated. Under-relaxation factors are involved in the correction term to stabilise the solution.

For higher accuracy and stability, second-order upwind schemes were used for the spatial discretisation of momentum and modified turbulent viscosity, as these were the governing transport equations to be solved for, along with the SA turbulence model.

Gradients are needed to be estimated at cell centroids to calculate scalars and velocity derivatives on the cell faces, as the values across a face have to be interpolated in a finite volume method. Three schemes were available– Green-Gauss cell-based, Green-Gauss node-based, and Least Squares cell-based. The Green-Gauss node-based scheme was chosen, as it is the most accurate, albeit having a higher computational expense than the others. This algorithm calculates the scalars at the cell faces as the mean of the values of the nearby nodes with a weighted average dependent on the properties within the cells that are formed by the nodes. This results in increased accuracy for meshes with high skewness or aspect ratios.

For the unpowered simulations where the rise in pressure across the propeller disk was defined as 0Pa, the second-order discretisation algorithm was used to interpolate pressure to calculate its value at the face from the cell, as both pressure and velocity are stored at the cell centres. This is a higher order accurate scheme and limits numerical dissipation that would otherwise negatively impact the propeller slipstream being studied here.

As per the recommendations of Fluent, that say the second order algorithm cannot be used for cases with jump or fan boundary condition, the PRESTO! scheme was used when pressure rises across the propeller disks were specified [123]. It uses a balance for a staggered control volume about the face to calculate the staggered pressure at the face. It is comparable to the second order method in terms of accuracy and stability.

The unpowered simulations were first initialised using the ‘Full Multigrid Initialization’. This solves the inviscid Euler equations on a field already initialized by a Laplace equation. The final solution of the unpowered case was then used to initialise the powered simulations.

The convergence criteria was set at the scaled residuals reaching a value of 1×10^{-6}. However, as typical of using SIMPLE, the *continuity* residual only dropped till 1×10^{-5} while the *momentum* and *nut* reached 1×10^{-10} and 1×10^{-6} respectively.

The normal and axial forces were measured on every individual body, in a total of 9 combinations, and were steady to $\pm 2N$. These forces were averaged over 4000 iterations in a total 10,000 iteration computation, and were resolved into lift and drag as per their directions.

4.3.3. Grid sensitivity analysis

A grid sensitivity study was performed for free-flight and ground-run using the grids developed as discussed in subsection 4.3.1 with the numerical settings discussed in subsection 4.3.2. Consistent with Stokkermans et al. [87], all elements except the prism elements in the inflation layers were successively coarsened.

The initial fine mesh and element refinement and distribution is very important to choose to examine the spatial convergence [124]. An attempt at reporting the error estimate using Richardson’s extrapolation and following the standard Grid Convergence Index was made.

For the GCI, the lift and drag coefficients were used. Three meshes were part of the study. A further fine mesh would have been computationally very expensive and a coarser mesh would have penalised the solution. An initial fine mesh was designed as the baseline, and then successively coarsened with a constant refinement ratio. The effective refinement ratio was calculated with the total number of elements in the same volume. The findings are given in Table 4.3 and Table 4.4. The medium mesh was used for the final studies reported here.

Where, h_i is a representative edge length and r the refinement ratio. The capability to estimate the error with Richardson extrapolation depends on the apparent convergence condition. The convergence ratio R for a triplet is [125]

$$R = \frac{\Phi_2 - \Phi_1}{\Phi_3 - \Phi_2}$$

where 1,2,3 are for the solution Φ from fine, medium, and coarse grids respectively.

Refinement	Total elements ≈	h_i	r	C_L	C_D
Coarse	44 Mil	0.5161	1.2	0.5124	0.0285
Medium	89 Mil	0.4300	1.2	0.5091	0.0303
Fine	161 Mil	0.3584		0.5107	0.0303

Table 4.3: Grid sensitivity study for free-flight.

The lift coefficient has $-1 < R < 0$, indicating an oscillatory convergence. The drag coefficient is on the verge of monotonic and oscillatory convergence $R \approx 0$, but just oscillatory.

Refinement	Total elements ≈	h_i	r	C_L	C_D
Coarse	42 Mil	0.8144	1.2	0.5521	0.0284
Medium	80 Mil	0.6615	1.2	0.5516	0.0281
Fine	145 Mil	0.5426		0.5478	0.0284

Table 4.4: Grid sensitivity study for ground-run.

The lift coefficient has $R > 1$ and is monotonic divergent. The drag coefficient has $R \approx -1$, making it just oscillatory divergent.

Only the monotonic convergent condition allows for error estimation based on Richardson extrapolation, which could not be done here.

Throughout this study, it was quite difficult to achieve converged solutions for the steady-state analyses, especially with finer meshes required to capture the characteristics and impact of the wakes, as will be discussed in section 5.9. The divergence in order of convergence for these coefficients could also indicate that the flow in this scenario is inherently unsteady as the resolution and influence of its features are differently approximated with the different grid refinements and distributions.

5

Results

This chapter discusses the results obtained using the numerical methods described in the previous chapter.

5.1. Introduction

The results obtained from the numerical studies have generally been split into two types– performance polars and flow-field analysis.

As was summarised earlier in Table 3.4, only the particular angle of attack/ incidence of 2° was finally found to be important to this study. It was at this angle that the influence of propeller power was numerically investigated both in free-flight and ground-run. This was done so, as this was the angle of attack during cruise and the angle of incidence while on the ground at which the intended experiments are expected to be performed, at least initially. The results of the flow-field analyses comparing free-flight and ground-run and investigating the influence of power, which begins from section 5.3, are reported only for this angle of interest.

As will be discussed in the next section, the performance polars were investigated over a range of angles of attack. One of the reasons for constructing the polar over a range was to find the cruise coefficient of lift at which experiments in free-flight would be performed. This could be compared with the internally communicated cruise pitch angle that the pilot operates the Skymaster at. Another reason for the extended analyses was to compare the performance polars with data found in literature. This was done to build confidence into the self-designed and developed digital twin and indicate the resulting model was not egregiously incorrect. Furthermore, the accuracy of the results obtained from an used ESDU tool for estimating the changes to a free-flight lift polar due to the influence of the ground would be higher with more initial data points, as will be discussed.

For ease of reporting results, the four different cases that are of interest, the unpowered and powered configurations in free-flight and ground-run, have been referred to with a standard key in the form of *xxx-xx*.
The first three characters represent the ground proximity as standardised in literature.

- Free-flight : OGE
- Ground-run : IGE

The last two characters follow a simple binary representation of the state of power.

- Power-off : P0
- Power-on : P1

Hence, the key would be interpreted as

- OGE-P0 : Unpowered free-flight
- OGE-P1 : Powered free-flight
- IGE-P0 : Unpowered ground-run
- IGE-P1 : Powered ground-run

Many variables are used in the reporting of the results. A complete list of the variables and their definitions including formulations can be found in the Nomenclature. Only a few important definitions are reported here in text.

The fixed angle that the Skymaster sits at when on the ground has so far been referred to as the *incidence angle* with the reasoning behind this choice explained in the following paragraphs. For ease of reporting, it is called as angle of attack in this chapter.

Angle of attack vs angle of incidence, in ground-run

The final goal of the DEAC programme is to experimentally evaluate the propeller-airframe interactions on the flying testbed. The numerical results reported here and from any future studies are intended to be translated to the final experiments.

At the time of writing this report, it is the student researcher's understanding that the angle of attack will be measured using a wing-boom mounted vane. Based on the literature covered in subsection 2.2.3, it is expected that these vanes will have to first be calibrated in free-flight with upwash data obtained either from CFD or wind-tunnel studies. When used in ground-proximity, it is currently unknown if the vane will show a difference in value due to the ground influenced modification to the upwash field. The influence of this modification on the measured value would depend on the position of the vane with respect to the leading edge of the wing. As neither the location of measurement of angle of attack nor the modifications to the upwash field due to the boom itself (the boom has not been modeled) are unknown, the student researcher has refrained from referring to the angle of incidence at which the Skymaster is positioned with respect to the ground while stationary, as the angle of attack.

Additionally, the student researcher believes that an experimentally measured value will be dynamic in nature. This would not only be due to a fluctuating pressure field in the surrounding atmosphere, but due to the operational nature of the aircraft. The choice of location of the centre of gravity and its influence on the movement of the suspension of the nose-wheel during a ground-run when the wheels are in contact with the runway and subject to reaction forces are factors to be considered during experiments and could not be treated here.

The angle of attack is an aerodynamic property to be measured with an aerodynamic pressure based sensor, while the angle of incidence can be measured using non-aerodynamic sensors mounted within the aircraft.

5.2. Performance characteristics

Understanding the change in performance characteristics between free-flight and ground-run are an essential component to this research and any experiments.

Performance polars for the unpowered configuration of the digital twin in free-flight cruise conditions were constructed from results obtained with the CFD tool over the range of angles of attack of -4° to 14° .

The cruise coefficient of lift and the corresponding angle of attack, for the digital twin, had to be self-estimated due to a lack of information. This polar was beneficial in choosing the final angle at which the influence of power on the digital twin was investigated. This was found to be a degree smaller than the internally communicated cruise angle of attack of the testbed.

As the digital twin was also self-designed and developed, the purpose of this polar was to prove that the model was not egregiously incorrect. This has been done so by comparing different performance parameters obtained from the CFD results with information found in literature. Such a comparison could not be done with the potential flow-based numerical results as those models featured only the lifting surfaces of the digital twin. The nature of the fuselage to shed structures having tangential velocity gradients and concentrated vorticity that passed through the rear propeller plane and interacted with the horizontal tail, could not be treated by the low-fidelity approach as it did not include the fuselage in its numerical models.

Due to the lack of data for validation of the results, this effort was deemed necessary and could also provide future researchers with a baseline reference.

To remind the reader, the thrust force required to be generated by the propellers was assumed to be the same as the numerically estimated drag force obtained from the CFD results at the settings of interest of the unpowered simulations. This was done so as to study the aircraft in steady flight where the propellers are producing a constant amount of thrust. During an experiment, the pilot would choose the engine manifold pressure and the propeller rotational speed so as to obtain the desired velocity. However, these parameters are not relevant here as they have/could not be modeled.

Plots and tables; reading the document

The plots shown in the following sections provide results on the entire polar range investigated. Though these plots are currently not validated through experiments, they provide future researchers with a basis and source of comparison.

The powered simulations were performed only at one particular angle of interest. The reader is directed to the plots to understand the performance polar over the range of angles studied with unpowered configuration, and to the accompanying tables that present the most relevant data values at the angle of interest for the unpowered and powered configurations.

Effective aspect ratio in ground effect

The changes in lift and drag forces for an aircraft operating in proximity to the ground can be explained by the increase in 'effective' aspect ratio AR_{eff}, as was covered in chapter 2. For the current height-to-span h/b ratio of 0.167 and aspect ratio of 7.1, the effective aspect ratio in ground-run, as estimated from Figure 2.5 which is based on the interpretation of Fink and Lastinger [57] in Figure 2.4, was 11.72 .

The modifications to the lift polar and the induced drag polar in ground effect has been discussed using the change in aspect ratio from 7.1 in free-flight to an effective value of 11.72 in ground effect at the specified clearance.

5.2.1. Lift polar

Lift polars were constructed for the free-flight operational settings over a range of angles of attack between $-4°$ and $14°$ using the potential flow-based vortex-lattice solver AVL and the fully viscous RANS CFD numerical solver.

The expected changes to a lift polar in ground effect, as discussed in subsection 2.2.2, are a decrease in the zero-lift angle of attack and an increase in the lift curve slope.

By activating the mirror vortex system in AVL, the ground effect for the wing based clearance on the inviscid lift polar was numerically estimated. Two methods were followed to convert the fully viscous CFD results to include ground effect at the specified wing clearance.

The ESDU 72023 [72] Item which was discussed in subsection 2.2.6 was used. The free-flight polar CFD results were fed into the online tool and the modified ground influenced lift polar was obtained. The accuracy of this polar increases with increasing initial data points. This method calculates both the change in angle of attack required to maintain a constant lift coefficient due to the contributions of the mirror trailing vortices, and the change to the lift coefficient at the new angle of attack due to the contributions of the mirror bound vortices.

The second method was an empirical method suggested by Roskam [59] to convert free-flight polars to include ground effect at the required clearance.
The change in the zero-lift angle for the lift curve in ground effect was calculated by

$$\Delta\alpha_{0_g} = \left(\frac{t}{c}\right)\left\{-0.1177\frac{1}{(h/c)^2} + 3.5655\frac{1}{h/c}\right\} \text{ in deg} \tag{5.1}$$

The lift curve slope for the wing with new aspect ratio of 11.72 was calculated by

$$C_{L\alpha_g} = \frac{C_{L\alpha}}{1 + \frac{C_{L\alpha}}{\pi}\left\{\frac{1}{(AR\,e)_{IGE}} - \frac{1}{(AR\,e)_{OGE}}\right\}} \tag{5.2}$$

where the Oswald efficiency factor e was left the same at 1. This was done as per the direction of Roskam [59] as the original theory assumed this value of 1.
The resulting lift polar in ground effect was then calculated by

$$C_{L_g} = C_{L_{\alpha_g}}(\alpha - \alpha_0 - \Delta\alpha_{0_g}) \tag{5.3}$$

$$= C_L\frac{C_{L_{\alpha_g}}}{C_{L_\alpha}} - C_{L_{\alpha_g}}\Delta\alpha_{0_g} \tag{5.4}$$

Lift polars can be characterised by their lift curve slope $C_{L\alpha}$, zero-lift angle of attack $\alpha_{C_L=0}$, lift at zero angle of attack $C_{L_{\alpha=0}}$ and maximum coefficient of lift $C_{L\text{max}}$ at a certain Reynolds number. Table 5.1 summarises these parameters based on the results obtained from the inviscid VLM analyses in free-flight and ground-run, the viscous CFD studies of the digital twin in free-flight, and the two approaches to converting the CFD free-flight polar to include ground effect.

	$C_{L\alpha}$ (per deg)	$\alpha_{C_L=0}$ (degree)	$C_{L_{\alpha=0}}$
AVL–OGE	0.0828	-5.1495	0.4265
CFD–OGE	0.0857	-3.8788	0.3326
AVL–IGE	0.0887	-5.3294	0.4729
Empirical method–IGE	0.0932	-3.5766	0.3362
ESDU–IGE	0.0894	-3.6784	0.3586

Table 5.1: Characteristics of lift polar in free-flight and converted polars in ground effect.

The cruise angle of attack for the Skymaster was internally communicated to be 3° at the chosen airspeed. From the lift polar generated here, it was found that the lift coefficient at 2° allowed for a steady level flight at this airspeed. Hence, this was the chosen angle for which the powered studies in cruise free-flight were performed.

With the Skymaster having a fixed incidence of 2° while on the runway, this would also give a direct indication to the influence of changes to the angle of attack measured on a wing-boom mounted angle of attack vane.[6] As only a single pre-determined angle of attack for the ground-run studies was chosen, it was the angle of attack at which the influence of propeller power was studied.

Table 5.2 reports the lift coefficients for the unpowered and powered cases of interest for the angle of attack of 2° as estimated from the CFD studies. The ESDU estimate is also included for a comparison. The empirical method suggested by Roskam [59] was not deemed to be as accurate as the ESDU method, as it changes the lift polar just based on the increase in effective aspect ratio. This is more of a three-dimensional effect. However, as was mentioned in subsection 2.2.3, the changes to the performance characteristics is a combination of two-dimensional and three-dimensional effects [60], which is captured by the ESDU tool that considers the influences of the bound and trailing mirror vortices.

	C_L
OGE–P0	0.5091
OGE–P1	0.5030
IGE–P0	0.5516
IGE–P1	0.5512
ESDU	0.5374

Table 5.2: Lift coefficients at the conditions of interest for the angle of attack of 2° as calculated by the CFD numerical studies.

The under-prediction of the ESDU estimate when compared with the ground-run CFD simulations, could be due to it ignoring the airframe. The fuselage of the Skymaster is much closer to the ground than the wings. However, as discussed later on with Figure 5.22 that shows the coefficient of pressure along the fuselage centreline, the relative increase in pressure in ground-run on the underside of the fuselage is concentrated near the nose. There is also a slight increase in the pressure recovery region in rear fuselage sections beyond the location of the omitted main landing gear. However, much of the fuselage underside actually experiences a reduction in pressure as the flow is accelerated in a convergent channel-like passage formed between it and the ground.

---

[6] Results to support the choice of operating parameter mentioned in section 3.3 Operating parameters

The ESDU tool considers the lift coefficient as a total for the entire aircraft irrespective of its configuration. The tail of the Skymaster is designed to produce a downward lift force to keep the nose up. This results in the suction side of the tail being in closer proximity to the ground than its pressure side. The mirror vortex system decreases the velocity of the flow between the tail and the ground plane, as will be shown by comparing the dynamic pressure ratio in Figure 5.30. The rise in pressure on the suction side (geometric lower side) is of a higher magnitude than the increase in suction on the pressure side (geometric upper side), as will be discussed with Figure 5.11 in section 5.3. Hence, the change in the total lift coefficient of the Skymaster due to the ground-effect may not be fully treated with this tool.

Moreover, the Reynolds number in ground-run is 60% of its value in free-flight. This could also alter the lift coefficient due to differing boundary thickness and decambering. The only possible way of treating this with the chosen methodology was with the coupled VLM and 2D panel-method based numerical solutions from XFLR5. Unfortunately, XFLR5 does not correct the lift polar for viscous effects. Hence, no conclusion can be drawn from this.

The decrease in the lift coefficient due to the propeller power, in both flight scenarios, is due to an increase in tail effectiveness. As will be shown with the change in pitching moment coefficient and the spanwise lift distribution on the tail, the tail produces more downward force in the powered configuration.

These lift polars are diagrammatically represented in Figure 5.1 along with a comparison found in literature for the maximum lift coefficient. Gudmundsson [15] reports the maximum lift coefficient of the Cessna Skymaster as 1.390 from a self-determined analysis.

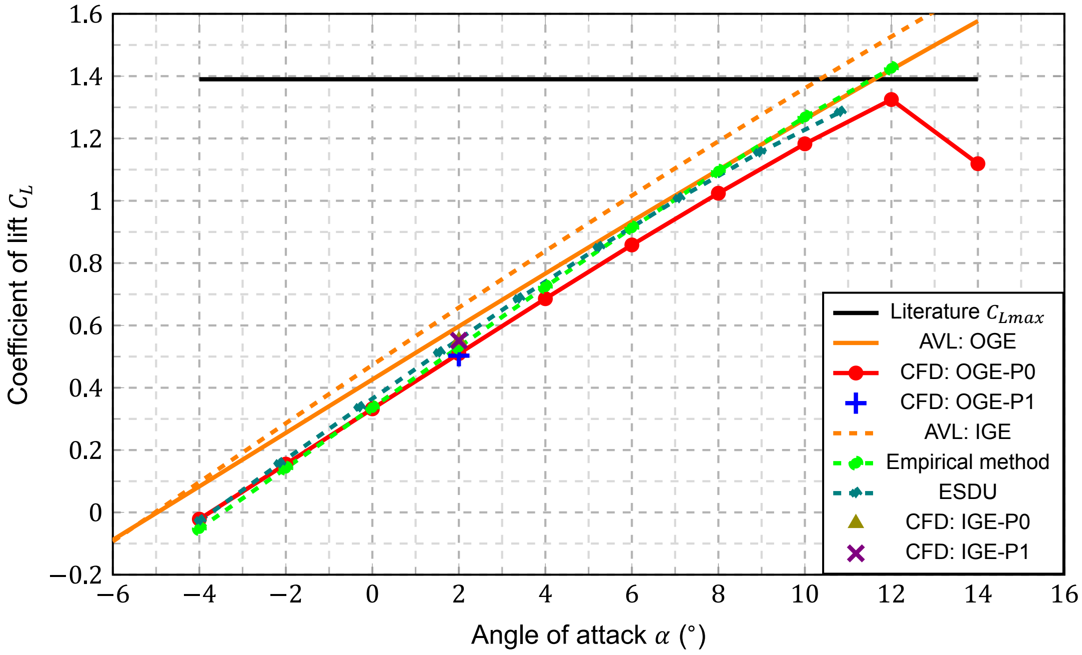

Figure 5.1: Lift polars of the Skymaster in free-flight and ground run obtained from VLM, CFD analyses, and with modifications to the CFD results to include ground effect.

5.2.2. Drag polar

Drag analysis is a very important and challenging part of evaluating the performance of an aircraft. Though the differences between the investigated digital twin and the testbed would result in a difference in drag force distribution, an effort was made to compare the drag polar obtained from the numerical analyses with estimations from/ based on literature.

The drag polar obtained from the viscous CFD simulations of the digital twin in cruising free-flight conditions, which is shown in the following drag polar plots as ‘CFD: OGE-P0’, had the equation of

$$C_D = C_{D\text{min}} + k\left(C_L - C_{L\text{min}D}\right)^2 \tag{5.5}$$

With this, the Oswald efficiency factor e was calculated from the derived lift-induced drag constant k and known aspect ratio AR

$$e = \frac{k}{\pi\, AR} \tag{5.6}$$

A correction of a 20% increase to the zero-lift drag obtained from the CFD analyses, was applied to account for the drag due to leakage, protuberance, cooling, and miscellaneous sources [99]. This is shown in the following drag polar plots as 'CFD:OGE:Corrected'.

Gudmundsson [15], from a self-determined study, reports the minimum drag coefficient for the Cessna Skymaster 337 as 0.302 which is also shown in the following drag polar plots with the key 'Literature'.

Gudmundsson [15] provides a method to calculate the minimum drag based on the simplified drag polar equation using the glide speed data available in the POH. The POH provides the IAS in mph (117 mph) for a loading condition very similar to the CFD study at 4630 lbs. This was then corrected to the CAS (113 mph) with the data in the POH. The lift coefficient for this glide speed was calculated with the CAS and POH specified loading at the chosen altitude. Gudmundsson [15] self-determines the maximum lift-to-drag ratio L/D as 12.5 and this was used with the CFD data reduced e to finally obtain the minimum drag coefficient.

$$C_{D\text{minPOH}} = \frac{C_L}{L/D_{\text{max}}} - \frac{C_L^2}{\pi\, AR\, e} \tag{5.7}$$

where

$$C_L = \frac{2W_0}{\rho V_{L/D_{\text{max}}}^2 S} \tag{5.8}$$

is the lift coefficient at best glide speed and has a value of 0.5213 when derived by this procedure.

The CFD data reduced induced drag constant and Oswald efficiency factors were compared with available data of Cessna aircraft. This comparison is provided in section C.1 and justifies the use of it to calculate the minimum drag from POH data, as it is very similar to other Cessna aircraft.

The important drag parameters for the Skymaster digital twin as calculated with the viscous CFD tool in this study and compared/ modified with (based on) information in literature as discussed just above, are given in Table 5.3.

Source	$C_{L\text{min}D}$	$C_{D\text{min}}$	k	e
CFD	0.1066	0.02020	0.05905	0.7666
CFD with correction		0.02424		
Literature [15]		0.0302		
Derived from POH		0.02599		

Table 5.3: Drag parameters reduced from CFD results and compared with literature.

Figure 5.2 shows the drag polar obtained with the viscous CFD simulations, the drag polar expected with the above discussed literature based correction to the minimum drag, and the literature sourced minimum drag coefficient as a reference.

NASA had performed flight experiments with the O2 piston-propeller variant of the Skymaster (a turbine variant also exists) [18]. The fly-over flight tests were performed at a height of 1000 ft at a cruising true-airspeed of around 100 miles-per-hour in its clean configuration. This translates to a Reynolds number of around 6.6×10^6 when calculated with the MGC of the digital twin and at sea-level conditions. Which is very comparable to the 6.38×10^6 investigated here. The drag polar obtained from that investigation has been extracted and reproduced in Figure 5.2 as 'NASA: O2'. The results from the CFD studies are comparable to this at low lift coefficients, which is the range of interest here.

Figure 5.3 shows polars obtained from the CFD results for the lift-to-drag C_L/C_D ratio of the Skymaster and the drag power $C_L^{3/2}/C_D$. The literature reference shown for the lift-to-drag ratio is the previously mentioned value estimated by Gudmundsson [15]. These two quantities were not explicitly used in the relevant studies reported here. However, they could act as a baseline reference for other researchers requiring this information. The polar information obtained from the NASA study [18] provides a direct comparison with CFD results for the powered free-flight configuration.

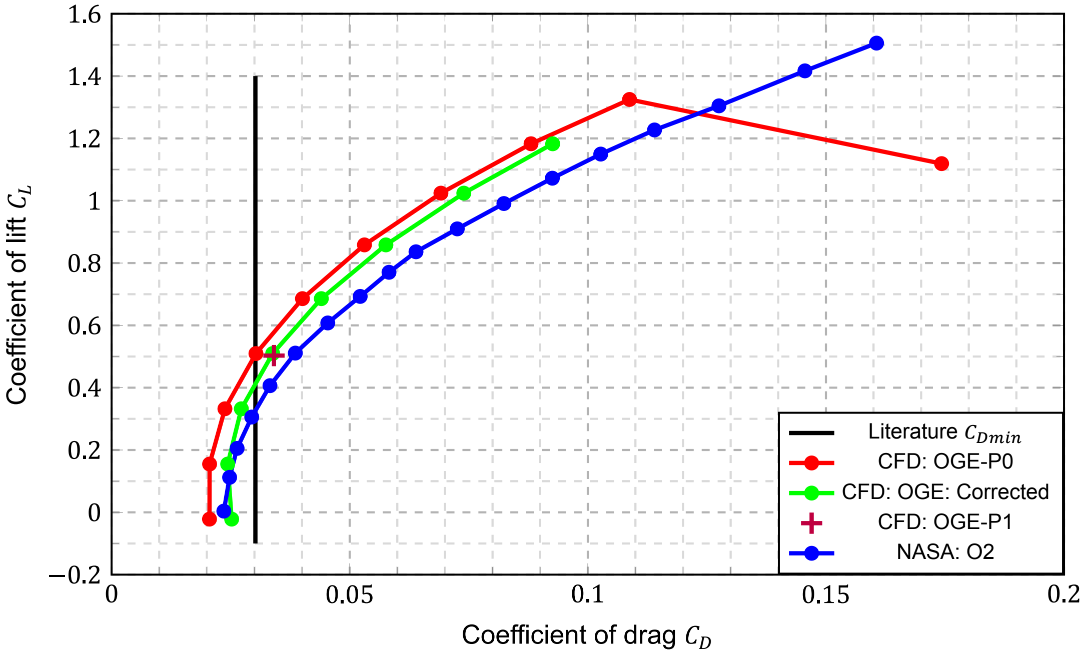

Figure 5.2: Drag polars of Skymaster in free-flight based on CFD results.

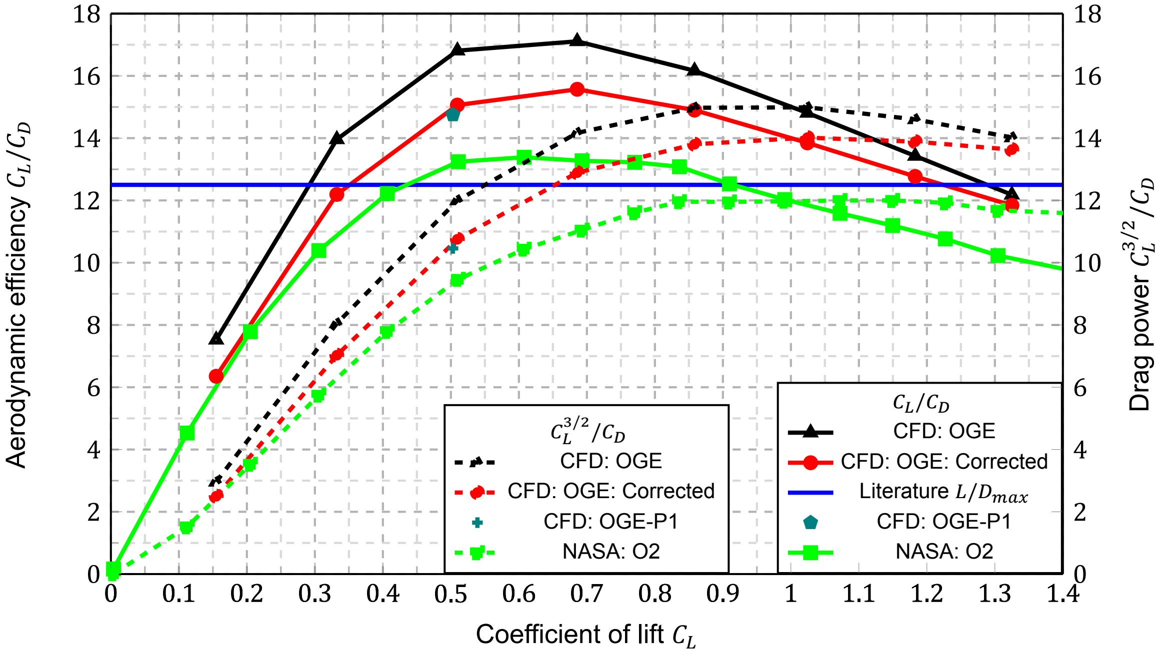

Figure 5.3: Lift-to-drag ratio and drag power polar of Skymaster in free-flight based on CFD results.

The induced drag in free-flight was approximated by deducting the minimum drag, i.e the lift coefficient part of the drag polar equation is zero. This assumption that the increase in drag with change in lift coefficient is due to the lift induced drag only is not strictly true. This estimated induced drag polar was converted to include ground effect by the earlier discussed Equation 2.2 and Equation 2.3 for $h/b = 0.167$.

Other formulations for the conversion factor for induced drag in ground effect exist and could have been used. With the popularity of Wieselsberger's [23] method, and the comparison with AVL that used Wieselsberger's [23] method of images, it was the chosen method of conversion. Moreover, errors in reproduction of print are common in some of the other theorised formulations for the conversion factor [126]. Figure 5.4 shows the induced drag coefficient polars for free-flight, Wieselsberger [23] based ground effect convert, and VLM.

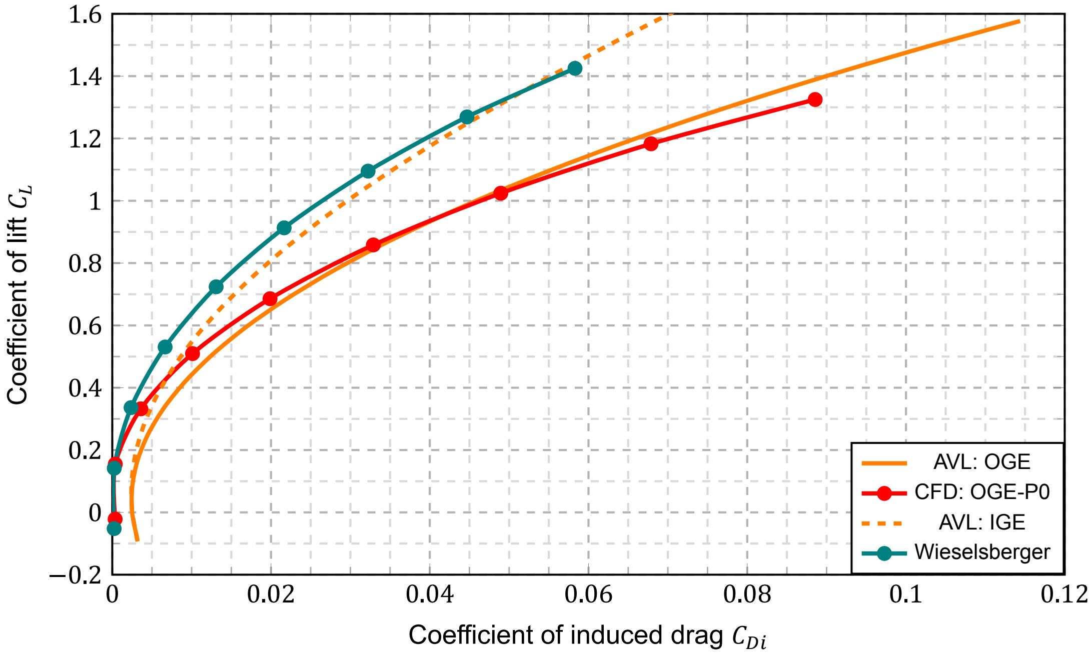

Figure 5.4: Estimated induced-drag polars of Skymaster in unpowered free-flight and ground-run obtained from VLM, CFD, and Wieselsberger's [23] formulation based conversion of CFD results.

The drag coefficients at the cases of interest, that is, the unpowered and powered configuration of the Skymaster in free-flight and ground-run at the common angle of 2° is reported in Table 5.4.

	C_D
OGE–P0	0.0303
OGE–P1	0.0341
IGE–P0	0.0281
IGE–P1	0.0318

Table 5.4: Summary of drag coefficients at the conditions of interest for angle 2° as calculated by the CFD numerical studies.

The differing contributions of the reduction in induced drag and increase in drag due to lower Reynolds numbers are discussed later in section 5.8.

In free-flight, the drag coefficient in powered configuration increases by 38 drag counts. In ground-run, it increases by 37 drag counts[7]. The propellers only contribute to scrubbing drag of the objects in its slipstream and does not impact the tip vortices of the main wing.

The simplifications made to the digital twin will result in a difference in drag force distribution with more detailed models. While the additional drag due to the struts and landing gears can be approximated from Equation 3.1 and Equation 3.2, the cooling drag is a little more complicated, especially

---

[7] 1 drag count is $\Delta C_D = 1 \times 10^{-4}$

given the Skymaster's cooling requirements during ground operations and slow speed flying. To estimate this based on empirical relations using the information (estimations) available in this report (mass flow rate and inlet area), the exit area and velocities need to be additionally known.

5.2.3. Pitching moment polar

The pitching moment was calculated from the CFD studies about the same chosen CG at longitudinal location of 19.77% MGC and vertical location the same as the tip of the front propeller spinner, for the different cases at angle of interest and are reported in Table 5.5. To remind the reader, this location was chosen from the aircraft CG and loading diagram in the POH, based on a loading estimate at the chosen cruise coefficient of lift from initial studies which are not reported here. Figure 5.5 shows the pitching moment polar and the coefficients at the cases of interest.

	$C_{m\text{CG}}$
OGE–P0	-0.0128
OGE–P1	-0.0050
IGE–P0	-0.0370
IGE–P1	-0.0329

Table 5.5: Summary of pitching moment coefficients at the conditions of interest for angle 2° as calculated by the CFD numerical studies.

The increase in negative moment in ground proximity is due to an increase in the positive lift force at the tail due to ground proximity. This has been shown later on in Figure 5.32 that discusses the lift distribution along the span of the horizontal tail.

The magnitude of pitch stability, $C_{m\alpha}$, was -1.1374 per radian. GA aircraft usually have a $C_{m\alpha}$ in the range of -0.6 to -1.0[15].

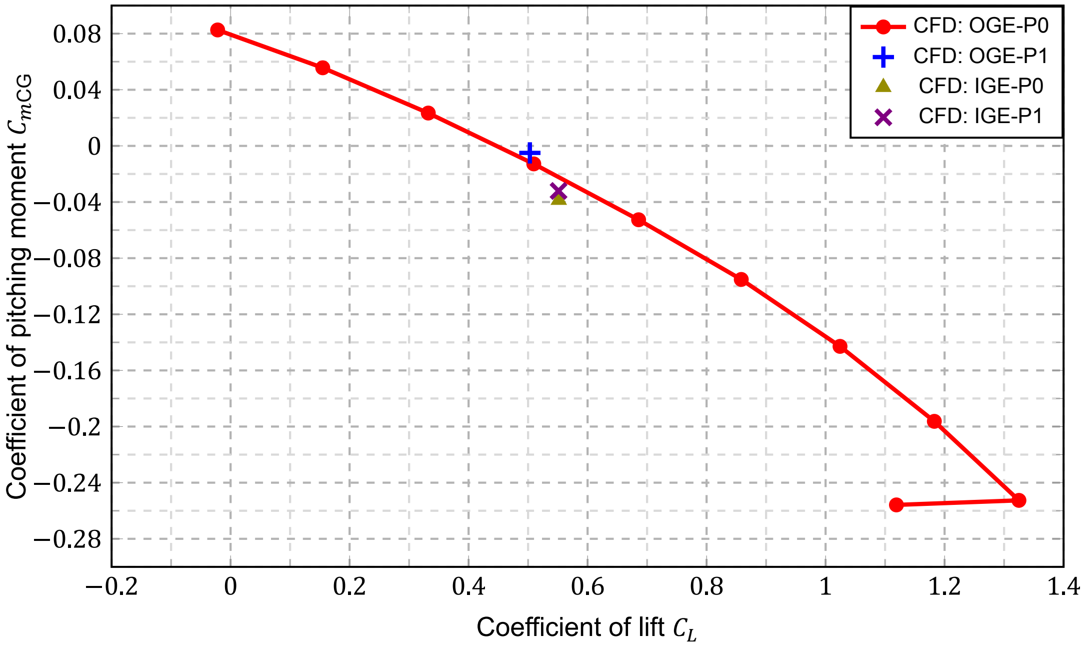

Figure 5.5: Pitching moment polars of Skymaster in free-flight and ground-run.

While neither these values of the moment nor the choice of CG, are very relevant to this reported research, the change in this reported moment parameter calculated for the same location of CG and angle of attack could help in the planning of experiments. Any moment created by the tail would mostly be balanced by the nose landing gear. The moment arm of the nose landing gear is more than the main landing gear, making its involvement in balancing the tail more important. Additional reaction forces at the nose due to an aerodynamically increased loading would lead to additional frictional forces at that wheel-runway interface, and increase the drag measured by an onboard instrument like an accelerometer. This could also result in some dynamic changes to the attitude (as constantly referred to as an incidence angle) due to the movement of the suspension of the nose landing gear strut.

It is the student researcher's belief that the choice of CG for ground-run studies performed at this current default angle or at other angles obtained by manipulating the length of the suspension arm, is of importance for these reasons, amongst others that could also possibly exist. It remains to be seen if the location of the CG is required to remain the same between tests conducted in free-flight and those in ground-run.

5.2.4. Summary

The important coefficients from the CFD results in the above sections have been summarised in Table 5.6 for convenience. Table 5.7 lists the propeller coefficient based on the dynamic pressure as described earlier insubsection 2.3.2 and defined in Equation 2.5, relevant to these results. To remind the reader, the specified thrust was the same as the drag force obtained from the unpowered CFD simulations. This was chosen so that the numerical simulations would be performed for a steady flight operation.

Case	C_L	C_D	$C_{m\text{CG}}$
OGE-P0	0.5091	0.0303	-0.0128
OGE-P1	0.5030	0.0341	-0.0050
IGE-P0	0.5516	0.0281	-0.0370
IGE-P1	0.5512	0.0318	-0.0329

Table 5.6: Summary of performance coefficients from all cases of interest at angle of attack/ incidence of $2°$, as obtained from the CFD analyses.

	Front propeller	Rear propeller
Case	T_C	T_C
Free-flight	0.0368	0.0388
Ground-run	0.0342	0.0360

Table 5.7: Summary of propeller coefficients for applied boundary conditions for the CFD studies.

The relative change in coefficient has been calculated as

$$\text{Relative change in \%} = \frac{x - x_{\text{reference}}}{x_{\text{reference}}} \times 100$$

The relative increase in C_L/C_D from unpowered free-flight to unpowered ground-run was 16.9% .

The relative decrease in C_L/C_D in free-flight due to power was 12.2% while it was 11.9% in ground-run.

The relative increase in C_L/C_D from powered free-flight to powered ground-run was 17.3% .

A relative decrease of 7.07% in T_C for each propeller was required to satisfy a steady condition.

The discussion of results specifically dedicated to the performance characteristics have been done in the sections preceding this statement. The following sections are dedicated to discussing the flow-field analysis for the unpowered and powered CFD simulations of the Skymaster in free-flight and ground-run conditions.

5.3. Pressure distribution over the Skymaster

Figure 5.6 to Figure 5.9 show the pressure distribution, represented by the pressure coefficient as defined below, on all surfaces of the Skymaster from different views.

$$C_P = \frac{P - P_\infty}{\frac{1}{2}\rho_\infty V_\infty^2} \tag{5.9}$$

Mainwing

As compared to free-flight, the leading edge suction on the mainwing is more pronounced in ground-run, a consequence of ground effect.

Fuselage

For the powered case, there is a slight increase of the pressure coefficient on the front part of the fuselage that is influenced by the front propeller.

There are visible high pressure circles just ahead of the rear engine air intake. This is a stagnation area that is a result of not modelling a boundary layer splitter.

The start of the pressure recovery region on the fuselage underside towards the rear beyond the main cabin, is further upstream in ground-run with a steeper adverse pressure gradient. This is seen by the elongated positive pressure contour and is discussed later alongside Figure 5.22.

Horizontal tail

The tail is designed to produce lift in the downward direction and keep the nose up. It is expected to have higher pressure on the geometric upper side. This is seen across most of its span, except near the middle which is situated behind the fuselage.

There is an inversion of the forces in this small region along with a shape resembling an elongated *pompeblêden*. A strong suction force, depicted by the low pressure coefficient is present in this region. This suction force is increased in ground proximity

This shape is a result of vortices interacting with the tail and has been more thoroughly discussed in the following sections.

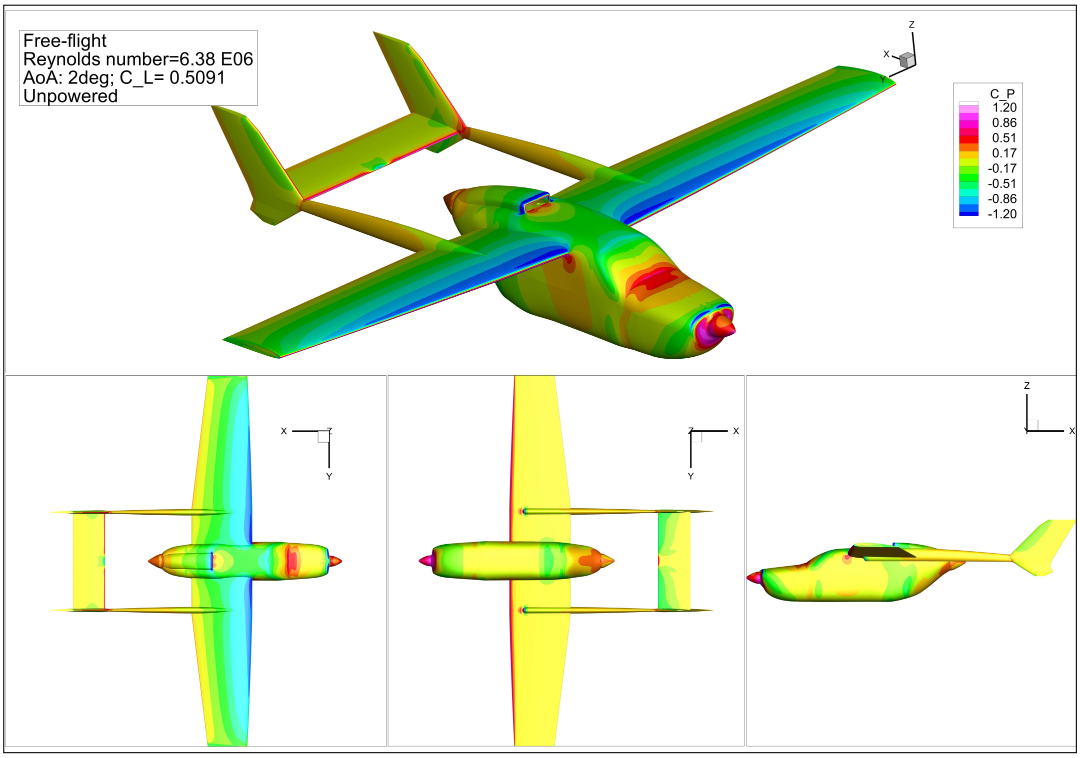

Figure 5.6: C_P distribution on the Skymaster
Free-flight, $Re_{\text{MGC}} = 6.38 \times 10^6$, $\alpha = 2°$, $C_L = 0.5091$, Unpowered.

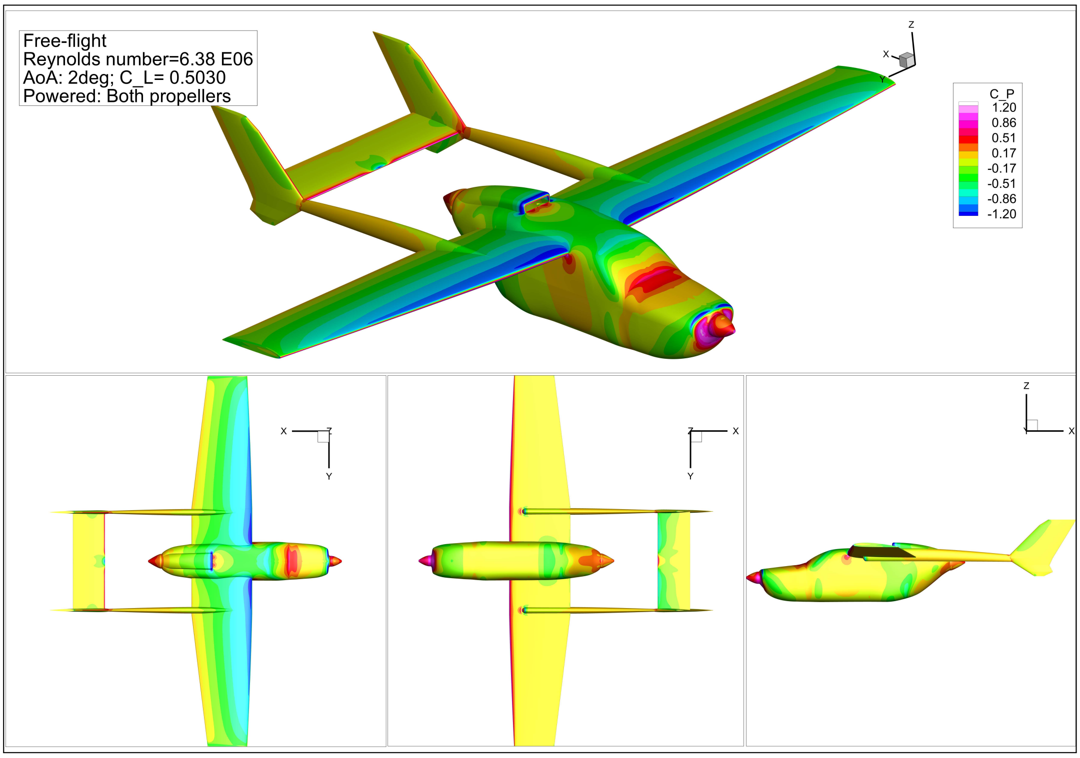

Figure 5.7: C_P distribution on the Skymaster
Free-flight, $Re_{\text{MGC}} = 6.38 \times 10^6$, $\alpha = 2°$, $C_L = 0.5030$, Powered.

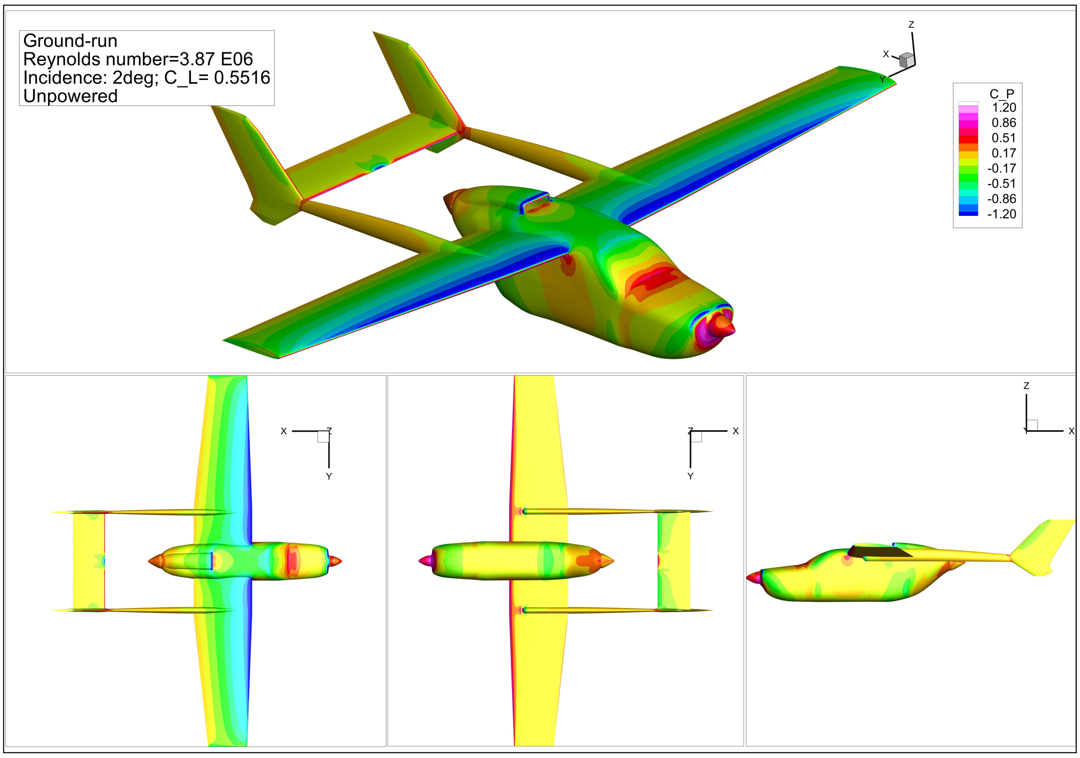

Figure 5.8: C_P distribution on the Skymaster
Ground-run, $Re_{\text{MGC}} = 3.87 \times 10^6$, $\alpha = 2°$, $C_L = 0.5516$, Unpowered.

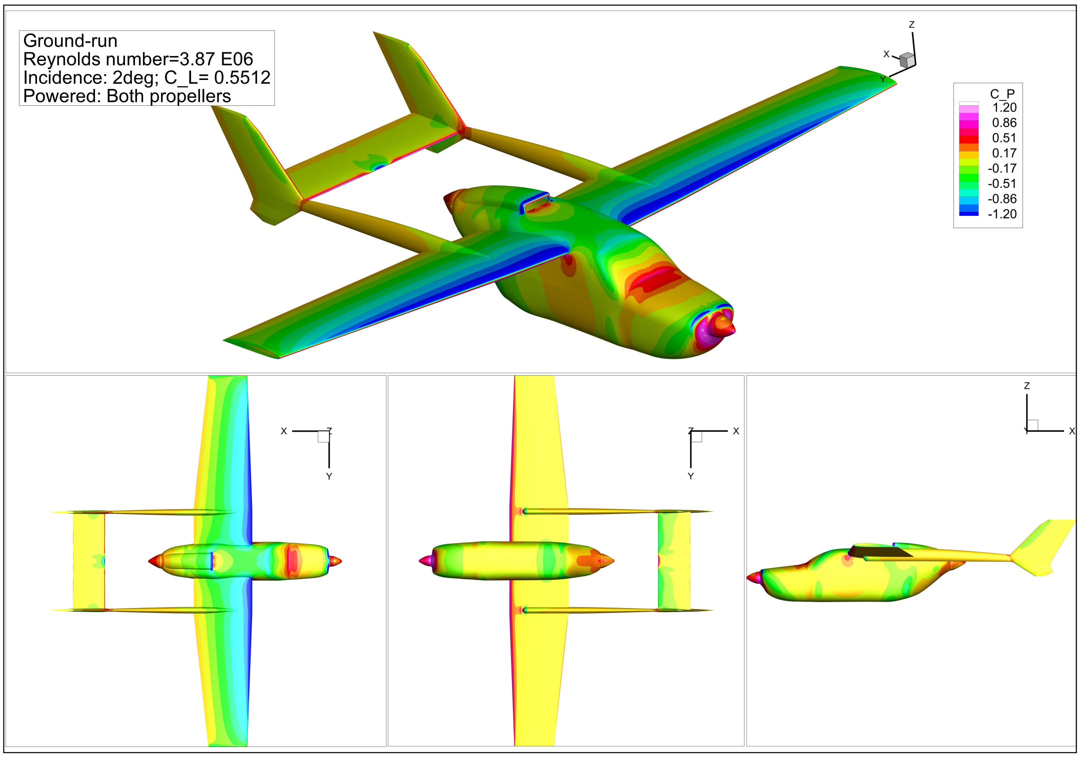

Figure 5.9: C_P distribution on the Skymaster
Ground-run, $Re_{\text{MGC}} = 3.87 \times 10^6$, $\alpha = 2°$, $C_L = 0.5512$, Powered.

The presence of the ground tends to increase the pressure on the lower side and decrease (increase suction) the pressure on the upper side, as per the findings from literature covered in subsection 2.2.3. For the spanwise locations shown in Figure 5.10 ,the C_P distributions were investigated. The distributions between free-flight and ground-run will show some difference due to the difference in shape of trailing edge geometry, as discussed in section A.1. These locations have been retained as constant for the chordwise pressure distributions reported in Figure 5.11, Figure 5.34, Figure 5.35, and Figure 5.38

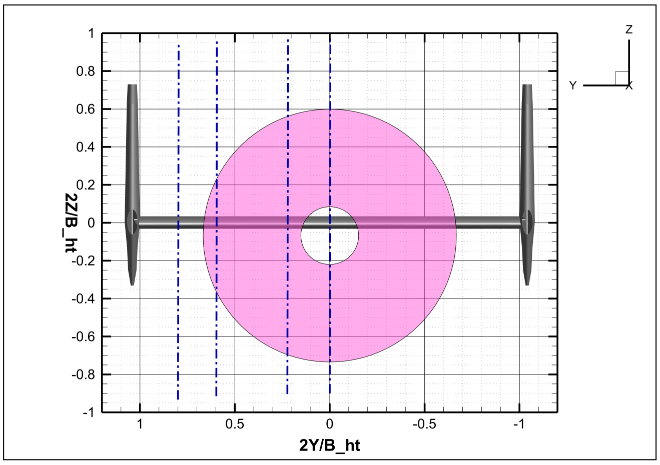

Figure 5.10: Spanwise locations along the HT at which C_P was compared.

$2y/b_{HT} = 0.0$ lied within the region of inverted forces and at the symmetrical plane. $2y/b_{HT} = 0.225$ was approximately at the location where the oncoming streamwise oriented fuselage wake vortices landed on the leading edge of the tail. $2y/b_{HT} = 0.6$ was a location just within the propeller slipstream. The idea was that this location would be within the slipstream on one side, and outside the slipstream on the other spanwise side, if it is maintained the same in future studies that include propeller swirl and witness the slipstream deforming as shown earlier in Figure 2.14. $2y/b_{HT} = 0.8$ lied outside the propeller slipstream and was not too close to the vertical tail to be influenced by any interactions between the horizontal and vertical tails.

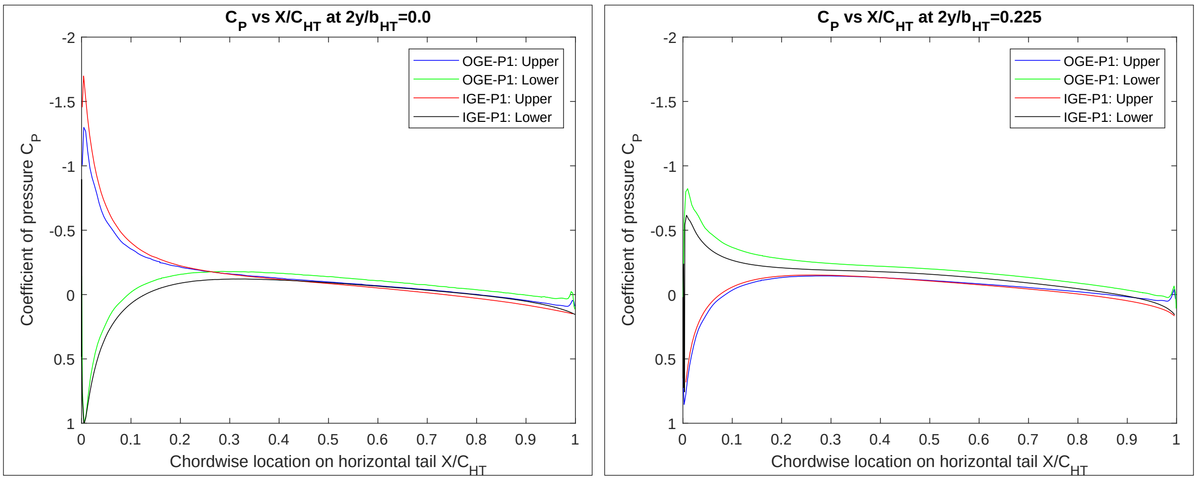

(a) $2y/b_{HT} = 0.0$ **(b)** $2y/b_{HT} = 0.225$

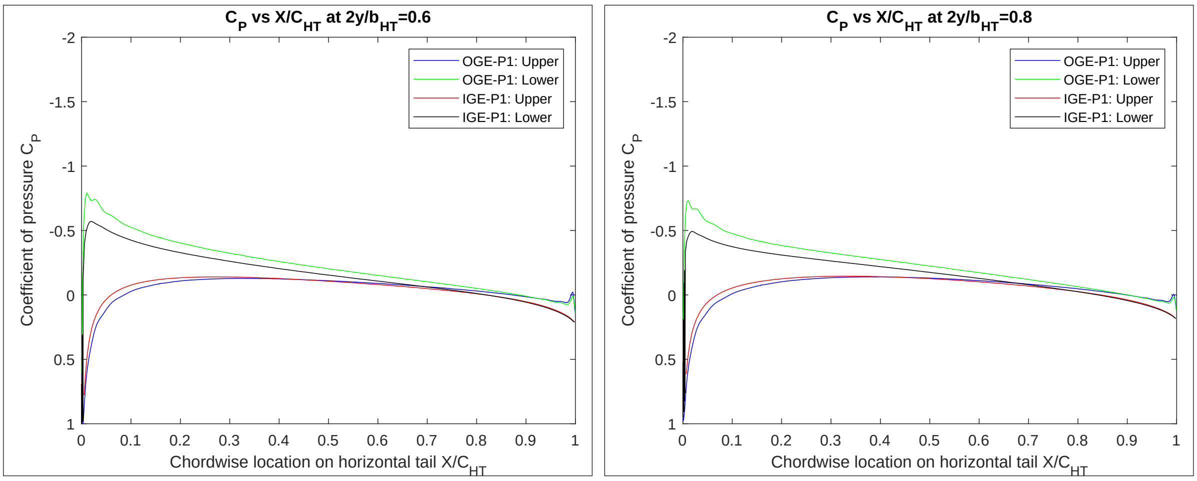

(c) $2y/b_{HT} = 0.6$ **(d)** $2y/b_{HT} = 0.8$

Figure 5.11: Pressure along the chord of the HT at different spanwise locations comparing powered free-flight with powered ground-run
Blue- OGE:P1:Upper, Green- OGE:P1:Lower, Red- IGE:P1:Upper, Black- IGE:P1:Lower.

Only $2y/b_{HT} = 0.0$ falls in the region where inversion of the forces is seen. Most of the lift in this section is generated near the leading edge due to the strong suction peak. The pressure distribution is quite constant for the remainder of the chord. The boundary layer is not separated as the Kutta condition is met at the trailing edge. The influence of the ground increases the lower side pressure. It also increases upper side suction as seen, but the magnitude is quite small, probably due to it already being very high. The influence of the vortex interacting with the tail is to cause a very high angle of attack at this location, as will be discussed later.

The other three locations have their suction and pressure sides as intended, to generate a downward directional lift force. The lower side is the suction side. There is a significant reduction in suction pressure due to pressure build up. The upper side is the pressure side. There is only a marginal reduction (more suction) in pressure side pressure due to the increase in suction in ground effect, and only near the leading edge, a difference with the lower side behaviour.

$2y/b_{HT} = 0.6$ and $2y/b_{HT} = 0.8$ show two kinks near the leading edge only for the lower surface pressure distribution in powered free-flight. The exact reason for these kinks is unclear.

Similar to the earlier explanation linking natural/ bypass transition with the turbulence in the freestream done with Figure 4.6, Figure 5.12 is the distribution of turbulent wake for powered free-flight.

For $2y/b_{HT} = 0.8$, the airfoil section is submerged in this wake, shown in Figure 5.13b. For $2y/b_{HT} = 0.6$, the wake convects along the local flow direction, that is in the downward direction, and does not interact with the leading edge of the section. It joins with the wake of the section at around its mid-chord location, and is shown in Figure 5.13a. These are two different cases that still show the same kink. This kink is also visible at $2y/b_{HT}$ locations of 0.4 and 0.5 .

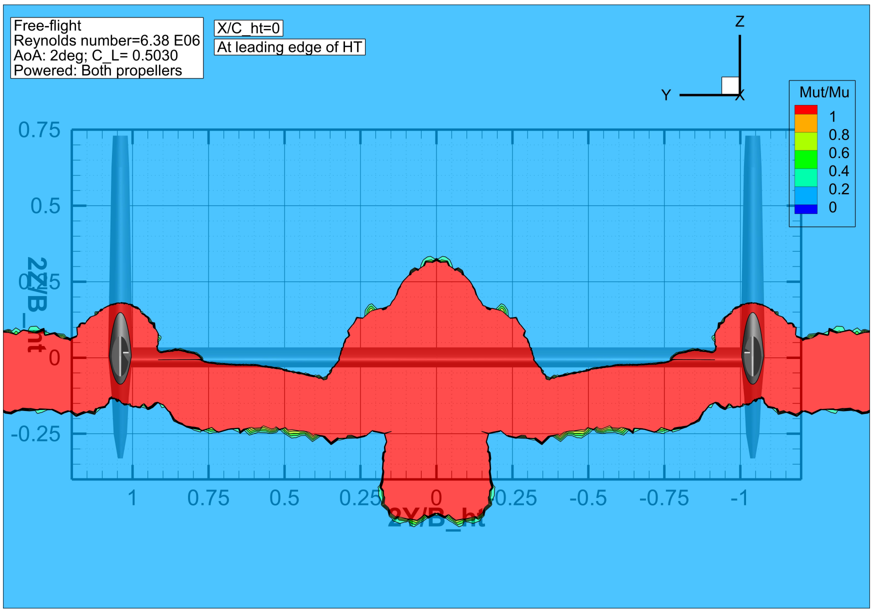

Figure 5.12: Distribution of turbulent wake, $\mu_T/\mu \geq 1$, interacting with the tail for powered free-flight For comparison with Figure 4.6.

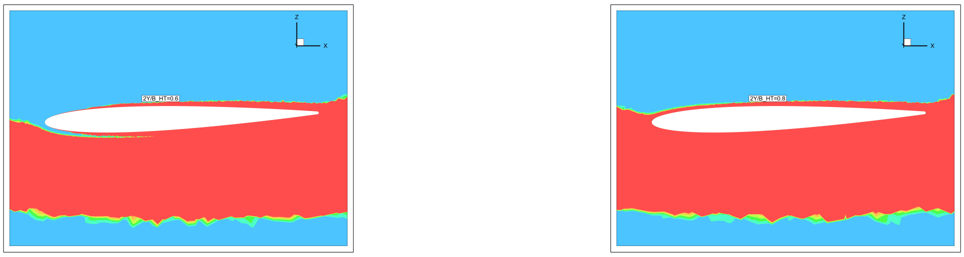

(a) $2y/b_{HT} = 0.6$

(b) $2y/b_{HT} = 0.8$

Figure 5.13: Turbulence at the HT section plane at $2y/b_{HT}$ of 0.6 and 0.8 .

There is no clear evidence of transition over a finite length on the suction side (lower). It seems to be fully turbulent as seen in Figure 5.14, but not smooth. With the chosen turbulence model, a fully turbulent development from the leading edge is expected for this Reynolds number [112]. Hence, the kink may not be related to transition.

A possible explanation for this kink is the change in local flow-field due to the induction caused by the fuselage vortices interacting with the tail. The *possible* significance of this kink is discussed later on in section 5.9. The difference in vertical location the between free-flight and ground-run could diminish its effect in ground-run. A more in-depth study is required for this for better comparison with experimental data and for choosing the locations of pressure ports on belts.

The skin friction coefficient shown in Figure 5.14 is defined as below, where τ_w is the wall shear stress.

$$C_f = \frac{\tau_w}{\frac{1}{2}\rho_\infty V_\infty^2}$$

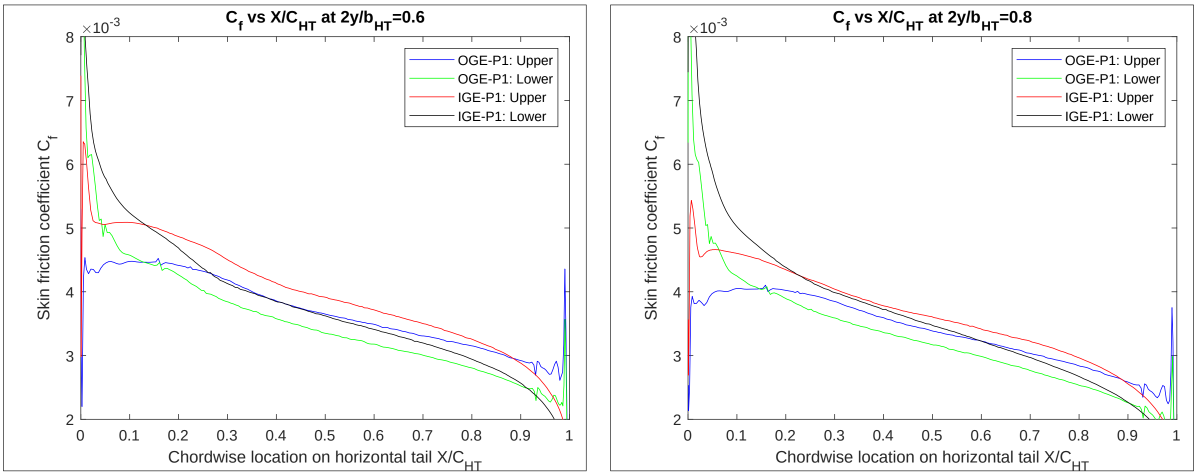

(a) $2y/b_{HT} = 0.6$ **(b)** $2y/b_{HT} = 0.8$

Figure 5.14: Skin friction coefficient at the HT section plane at $2y/b_{HT}$ of 0.6 and 0.8
Blue- OGE:P1:Upper, Green- OGE:P1:Lower, Red- IGE:P1:Upper, Black- IGE:P1:Lower.

5.4. Evolution of fuselage wake vortices

The distortion in pressure distribution on the tail has been linked to vortical structures shedding off the fuselage and interacting with the tail.

These vortical structures are confirmed as vortices as they satisfy three conditions [127]

1. Presence of vorticity
2. A pressure minimum
3. Swirling streamlines

The axial vorticity has been non-dimensionalised with the freestream velocity and the chord length of the horizontal tail and is used for comparison of all cases here.

$$\frac{\xi_x C_{HT}}{U_\infty} \tag{5.10}$$

All figures reported here that are related to vorticity have the same view– from the pilot's perspective. Hence, the positive y axis in the side of the starboard wing is to the reader's left. Positive vorticity points into the plane (x axis), for using the right-hand rule.

The coefficient of total pressure that shows the pressure minimum is defined as below such that it would have a value of 1 in the undisturbed freestream

$$C_{P_T} = \frac{P_T - P_\infty}{\frac{1}{2}\rho_\infty V_\infty^2} \tag{5.11}$$

Figure 5.15 and Figure 5.17 show the streamwise vorticity and total pressure distributions in the evolution of the fuselage wake vortices through cut section views. This is for the powered ground-run case. For the free-flight case, the vertical location of the vorticity cores is slighty negatively offset when compared to ground-run, as will be discussed in subsubsection 5.6.1.1.

There is significant vorticity formed at the lower side of the fuselage. At a location of $X/C_{HT} \approx -2.5$, the vorticity starts leaving the fuselage from the bottom of the vortical structure. The low pressure core of the structure starts forming with iso-surfaces of constant vorticity around it. While leaving the fuselage, it also creates a secondary structure of opposite sign between its core and the plane of symmetry. This is diffused by the presence of secondary vorticity of opposite sign on the other side of the fuselage (plane of symmetry).

The formation of secondary vorticity due to primary vorticity passing over a surface, both for this description and otherwise, is expected to be similar to the fashion shown and discussed with Figure 2.6.

At $X/C_{HT} = -2.0$, most of the vorticity has left the surface. This is also when the vorticity at the top side of the fuselage starts definitively forming on the side of the rear air intake, starts wrapping around a core, and is caught in a locally downward flow.

At $X/C_{HT} = -1.5$ the entire lower vortical structure has left the fuselage and its core has an upward trajectory as it is caught in the upsweep of the fuselage. The vortical structure from the top side has also left the surface. While doing so, a secondary structure of opposite direction was created. Unlike the secondary vortical structures being diffused on the lower side, the upper side structures prevail as they are protected from their opposite pairs by the spinner. The secondary vorticity satellite [65] around the primary.

The Skymaster is usually operated with the rear spinner removed. This would change the behaviour of these structures. Additionally, the spinner in the digital twin is larger than the one the DEAC has (but, the larger design exists in other Cessna Skymasters). It was designed so as to provide the boundary layer with a continuous surface rather than a stepped surface, as a converged solution could not be attained with the stepped design.

After both structures leave the fuselage, the lower core is caught in the upwash of the fuselage and travels upwards. The upper core is caught in the downwash of the wing and the downward local direction due to the fuselage shape, and descends down. The two cores of same sign start merging into a larger core between $X/C_{HT} = -1.5$ and $X/C_{HT} = -1.0$.

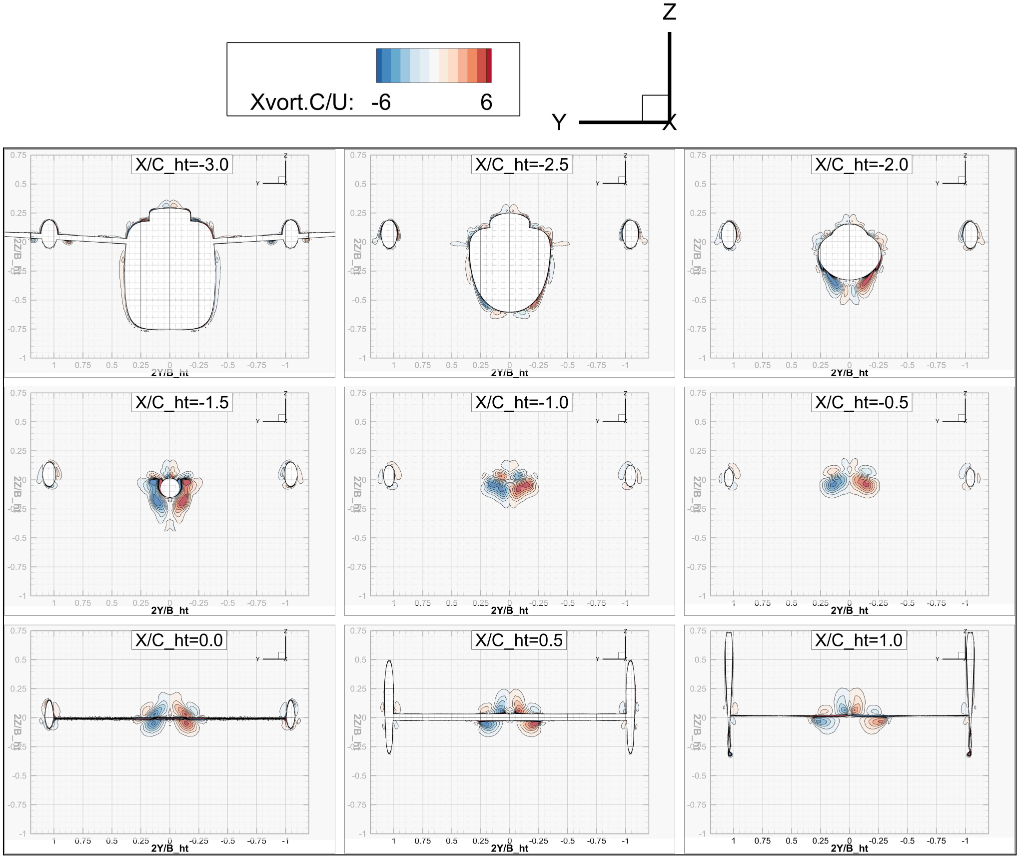

Figure 5.15: Evolution of fuselage vortices: $\xi_x C_{HT}/U$
Ground-run, $Re_{\text{MGC}} = 3.87 \times 10^6$, $\alpha = 2°$, $C_L = 0.5512$, Powered.

Prior to merging, the tangential velocity gradients are very strong in one direction as seen in Figure 5.16a. Their merging causes rotational streamlines to be ‘wound tighter’ around the core and have a more definitive vortex-like tangential velocity distribution shown in Figure 5.16b. The tangential velocity ratio is defined as

$$U_y/U_0$$

Throughout its path from formation to interaction with the tail, the vortex is not isolated and not free of shear. The vortex is caught between the upwash of the fuselage and downwash of the wing. This causes the vortex tube to stretch and tilt.

For reference, the rear propeller is located at $X/C_{HT} = -1.7$. Hence, these two detached flows pass through the propeller plane and then form the definitive vortex.

The streamlines around the fuselage and tail that make up the vortex are shown in Figure 5.18.

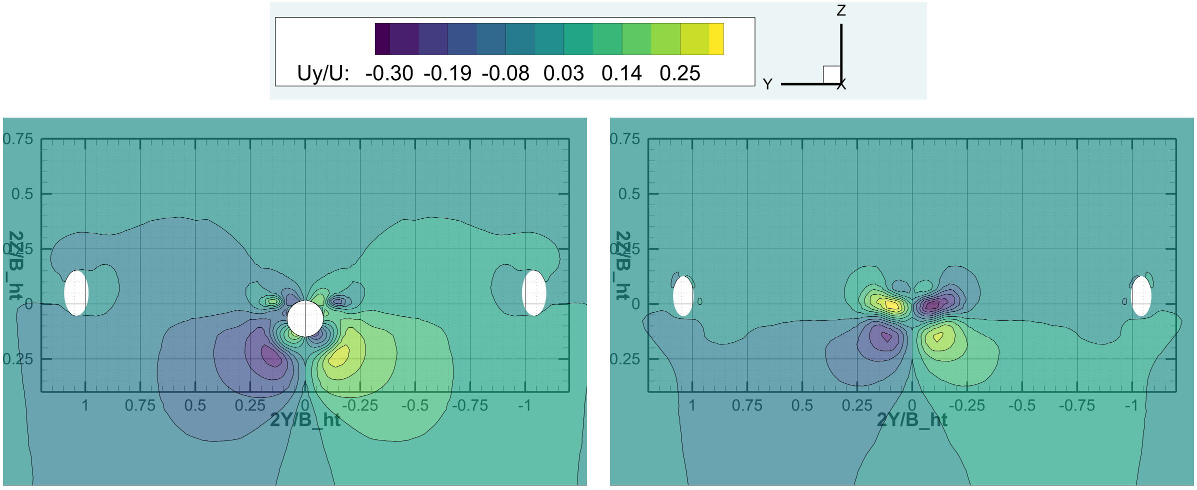

(a) Location at $X/C_{HT} = -1.5$

(b) Location at $X/C_{HT} = -1.0$

Figure 5.16: Tangential velocity ratio U_y/U_0 before and after formation of vortex in the wake Ground-run, $Re_{\text{MGC}} = 3.87 \times 10^6$, $\alpha = 2°$, $C_L = 0.5512$, Powered.

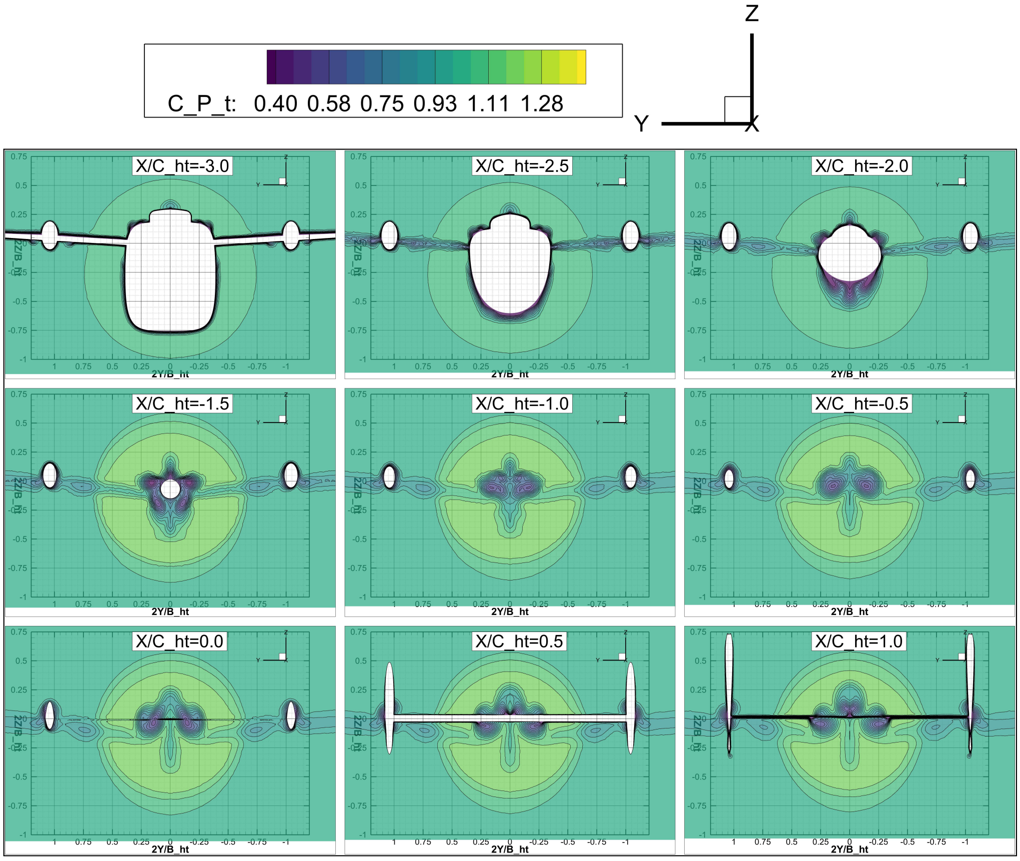

Figure 5.17: Evolution of fuselage vortices: C_{P_T}
Ground-run, $Re_{\text{MGC}} = 3.87 \times 10^6$, $\alpha = 2°$, $C_L = 0.5512$, Powered.

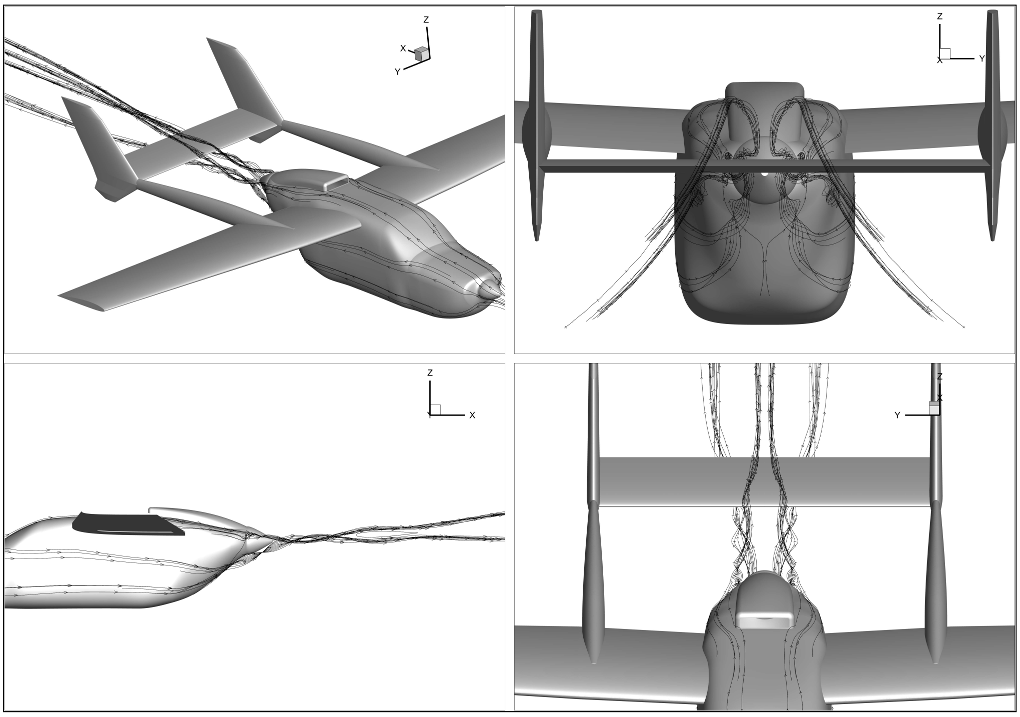

Figure 5.18: Streamlines around the fuselage forming a vortex
Ground-run, $Re_{\text{MGC}} = 3.87 \times 10^6$, $\alpha = 2°$, $C_L = 0.5512$, Powered.

5.5. Boundary layer separation from the fuselage

Due to the shape of the rear part of the fuselage, there was concern that boundary layer separation would be prevalent. To check for regions with recirculation or separation, the x-component (streamwise) of the wall shear stress was non-dimensionalised into its component skin friction coefficient.

$$C_{f_x} = \frac{\tau_{w_x}}{\frac{1}{2}\rho_\infty V_\infty^2}$$

Figure 5.19 shows the distribution at the rear of the fuselage. The contour has been cut-off at 0.0 to highlight only regions of recirculation/ separation. Hence, even though the entire fuselage has a colour representative of 0.0, its true value would be higher.

As was shown earlier in Figure 4.9, no flow reversal was seen in the velocity field downstream, indicating that the general boundary layer of the fuselage does not separate from its surface in an undesirable manner.

Two distinct separation regions are seen on a half of the fuselage. These are the locations where the vortical structures from the lower and upper side finally leave the fuselage. The vertical locations of the upper separation region is shifted slightly higher in ground-run, whereas the lower separation region is slightly lower. This is due to a stronger adverse pressure gradient being formed on the lower side in ground-run, as will be discussed in the next section. In free-flight, these regions are smaller indicating the boundary layer is less diffused and less separated.

The importance of this difference is that the difference in the nature and characterisation of the vortical structures that interact with the tail, begins at their source. This is further explained in section 5.9.

The small separation seen on the top side of the rear spinner behind the rear intake is expected to be a consequence of the simplification to the boundary layer splitter at the intake face of the rear engine scoop inlet, for this digital twin, and need not exist in a real case.

While both unpowered and powered configurations in free-flight maintain attached flow except for the vortical structures shedding off, there is a recirculation region at the bottom side of the fuselage for the unpowered ground-run. This is at a location beyond the shortest distance between the ground and fuselage, where the convex shape changes to concave, and the adverse pressure gradient in the recovery region is quite steep.

The influence of power is to reduce this region and slightly enhance attached flow. In ground-run, the flow is attached at the area of change of geometrical curvature.

The differences in C_P and C_f in this region between free-flight and ground-run and the changes due to propeller power are discussed in the following section.

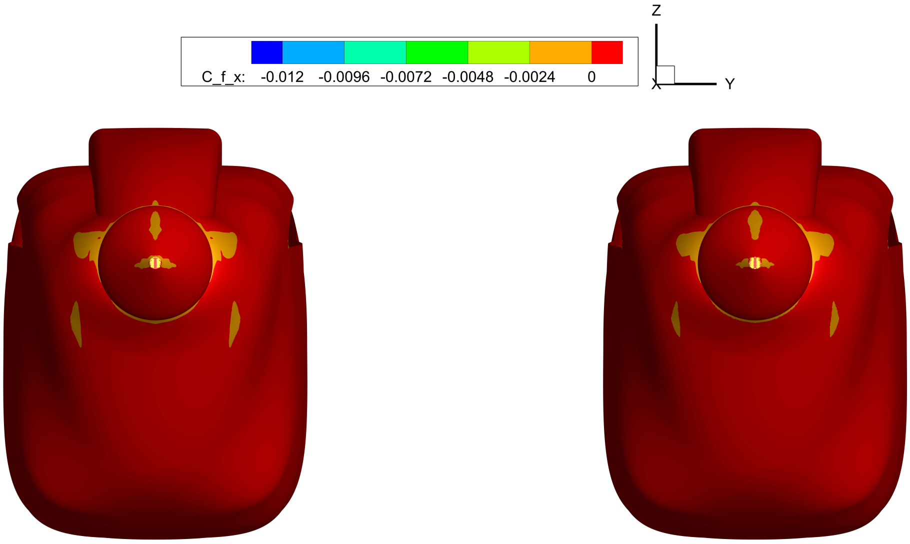

(a1) Unpowered, $C_L = 0.5091$ **(a2)** Powered, $C_L = 0.5030$

(a) Free flight, $Re_{\text{MGC}} = 6.38 \times 10^6$, $\alpha = 2°$

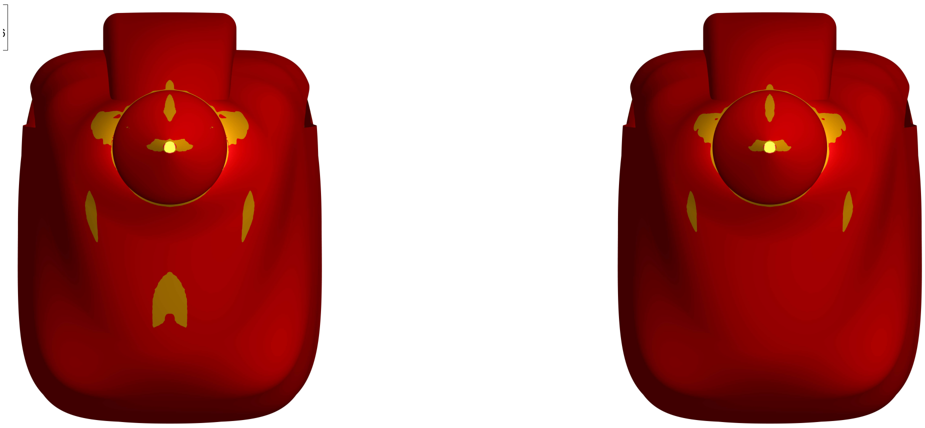

(b1) Unpowered, $C_L = 0.5516$ **(b2)** Powered, $C_L = 0.5512$

(b) Ground-run, $Re_{\text{MGC}} = 3.87 \times 10^6$, $\alpha = 2°$

Figure 5.19: C_{fx} distribution across the rear of the fuselage.

5.6. Flow at the tail

The previous sections explained the overall changes to the Skymaster and focused on the formation and development of the wake vortices. The presence of the vortices were confirmed due to the vortical structures displaying three criteria- swirling streamlines, a pressure minimum core, and

This section will focus on the impact of the vortices and the flow-field at the tail, as the interaction of the propeller slipstream with the tail is the content of interest and can be understood by looking into its structure before and after interaction.

The changes to the total pressure coefficient and streamwise vorticity parameter at the leading edge of the horizontal tail between free-flight and ground-run are discussed along with the associated propeller influences on these parameters.

The interaction of the vortices on the upper and lower sides of the tail, as numerically estimated with the followed methodology, are shown by discussing the surface pressure distributions and skin-friction coefficients.

5.6.1. Vortices at the leading edge of HT

5.6.1.1. Total pressure

The total pressure coefficient encompasses the viscous drag and downwash and has been used to study the airframe-propeller interaction. Its distribution at a plane at the leading edge of the horizontal tail is shown in Figure 5.20. The choice of location of probes to measure total pressure during future experiments can be made from these results.

The vortex cores are visible as the low pressure centre in the circular structure. The vertical location of this core is positively offset in the ground-run than free-flight. The influence of power is to regain some of the lost C_{P_T} and radially shift the cores on either side of the symmetry plane closer together due to the contraction of the propeller streamtube.

The wake from the wing is also visible as the region with reduced total pressure. The wake too is vertically offset in ground-run. In the powered configuration, a larger extent of the wake passing through the propeller plane is recovered in free-flight than in ground-run.

A faint hint of the front propeller's slipstream is present along with the rear propeller's. The nature of the sliptreams, indicated by $C_{P_T} > 1$, is seemingly the same between free-flight and ground-run for vertical locations above the visible leading edge of the HT. However, the ground restricts the formation of the slipstream on the propeller plane side below the visible leading edge of the HT. This is probably due to the ground influence rather than the lower thrust coefficient, at least for the rear propeller. For the front propeller which has a negative incidence with respect to the fuselage, the combined influences of its installed angle, the freestream relative angle of attack, the presence and shape of the fuselage, and the blockage due to the ground, could lead to this difference in its slipstream structure.

A distinctive low-pressure 'nose' to the low-pressure 'face-like' figure is visible. This nose is longer in ground-run, indicating a larger span section of the propeller blade will encounter it. The source of this nose can be linked to the flow at the fuselage. Figure 5.22 and Figure 5.23 show the variations in C_P and C_f across the fuselage at the symmetry plane. Figure 5.21 can be used to relate the distribution to its physical location.

At the front of the fuselage, there is a significant increase in the C_P on the lower side of the fuselage, in ground run. The near straight underside of the fuselage forms a convergent passage with the ground plane from $X/L_{fuse} = 0.2$ to $X/L_{fuse} = 0.65$. The flow is accelerating in this region as shown by the sharp increase in suction. The suction peaks at the 'throat' of this passage at $X/L_{fuse} = 0.66$.

The powered ground-run shows significantly larger suction at $X/L_{fuse} = 0.66$. For the remainder of the fuselage till the spinner, the C_P becomes positive very sharply and has two distinct kinks over which the gradient drastically reduces as the pressure recovers. The C_f displays an even more steep decrease. The nose-like wake originates from here. In ground-run, the adverse pressure gradient is steeper in the region of recovery and causes separation at a lower vertical height. The sharp sweep in the fuselage shape decreases laterally outward, allowing for better pressure recovery. This does not have much impact on the width of the nose, as it is almost the same in free-flight and ground-run. In both cases, the propellers make the nose thinner and shorter as it marginally increases suction in the recovery zone and decreases the steepness of the adverse gradient.

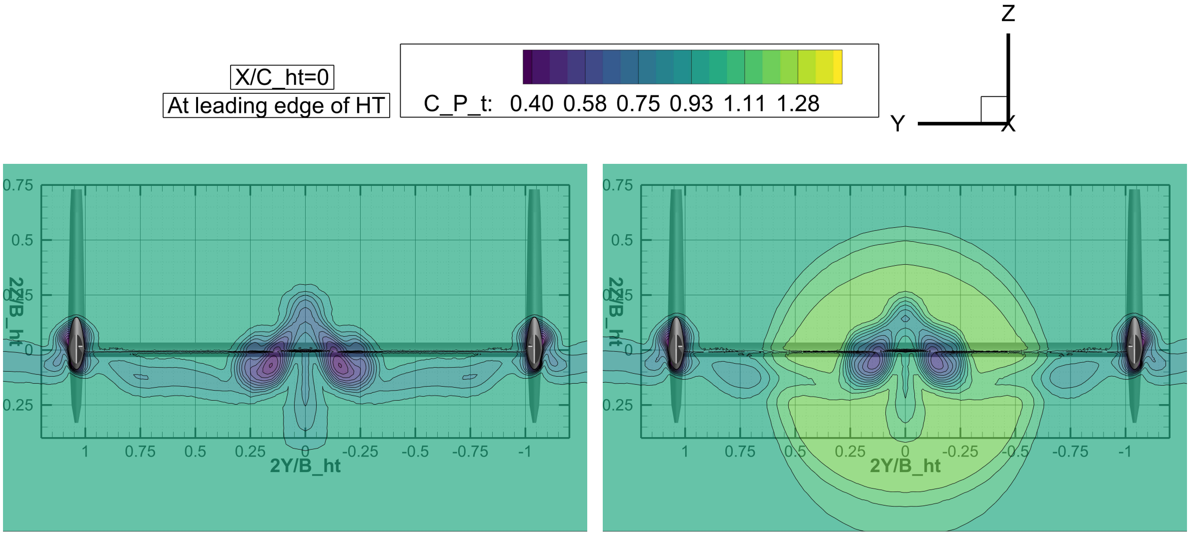

(a1) Unpowered, $C_L = 0.5091$

(a2) Powered, $C_L = 0.5030$

(a) Free flight, $Re_{\text{MGC}} = 6.38 \times 10^6$, $\alpha = 2^\circ$

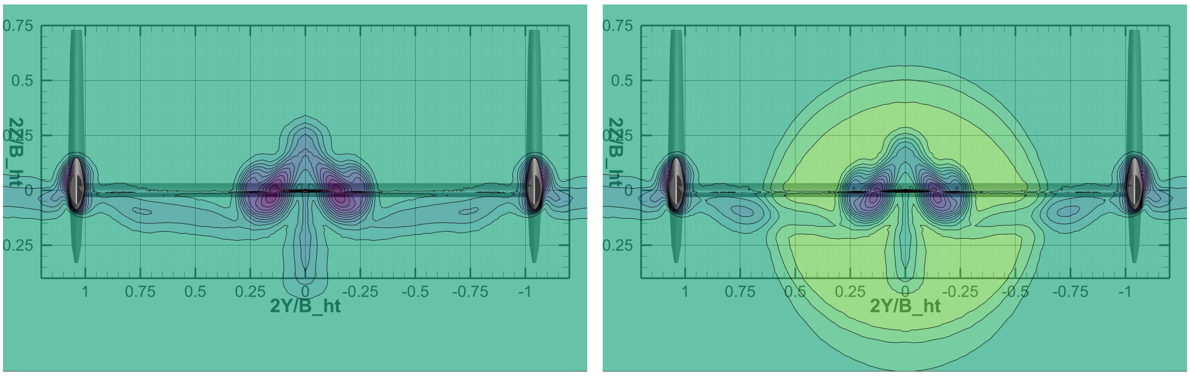

(b1) Unpowered, $C_L = 0.5516$

(b2) Powered, $C_L = 0.5512$

(b) Ground-run, $Re_{\text{MGC}} = 3.87 \times 10^6$, $\alpha = 2^\circ$

Figure 5.20: C_{P_T} distribution at the leading edge of the horizontal tail.

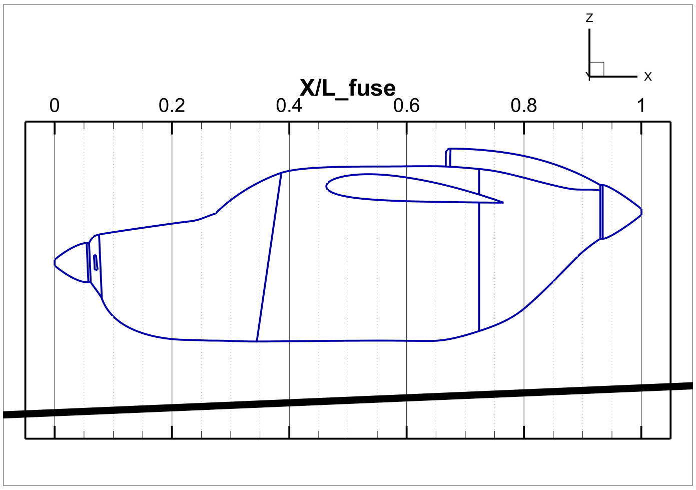

Figure 5.21: Non-dimensional length definition for fuselage.

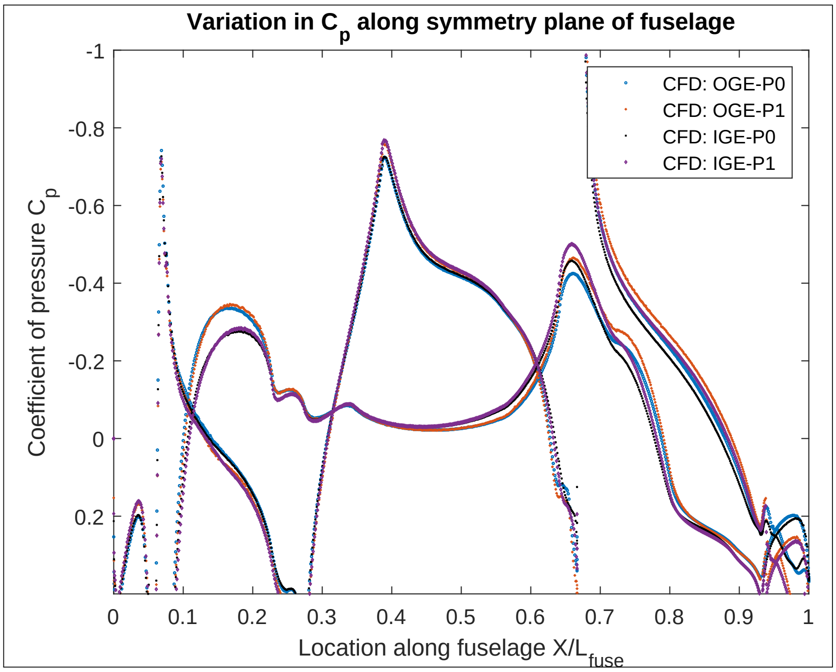

Figure 5.22: Variation in C_P along the length of the fuselage at the symmetry plane.

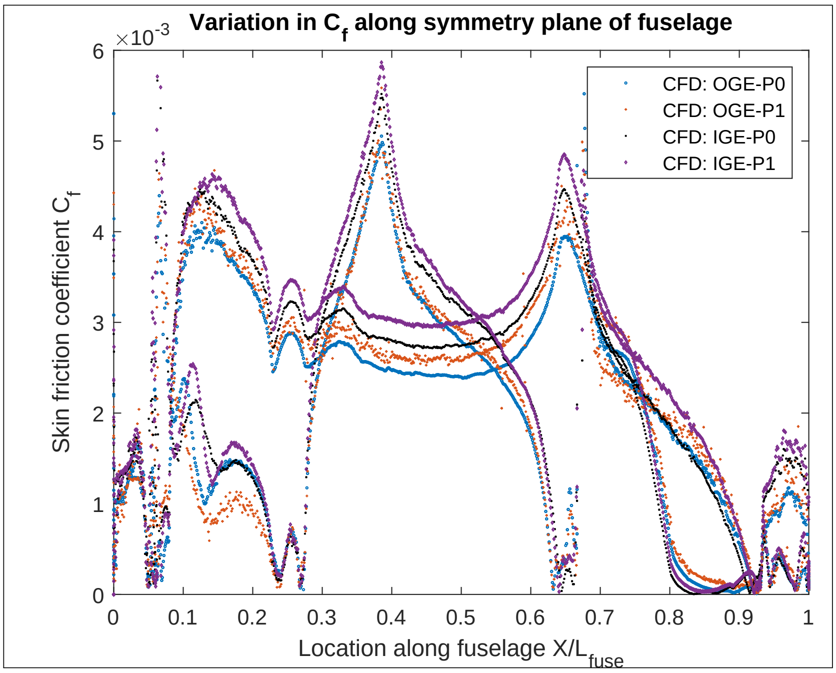

Figure 5.23: Variation in C_f along the length of the fuselage at the symmetry plane.

The earlier presented and discussed Figure 4.9, contains the axial velocity distribution that supports the stronger suction at the throat of the formed passage and the larger vertical wake shed by the fuselage.

A more thorough comparison, such as looking at the shape factor can be done, but was deemed not to be very relevant to experiments owing to the simplified surface of the digital twin. Moreover, the Skymaster has a comparatively large antenna like structure along this plane situated between 0.76 and 0.81 of X/L_{fuse} which was not included here.

The 3D scanned geometry was found to have a slightly 'tighter' packaging with a sharper sweep across all directions at the rear, not just along the centreline. Hence, the adverse pressure gradients could be steeper.

5.6.1.2. Streamwise vorticity

The interaction of the wing with the vortex leads to the ‘splitting’ of the vortex and is shown in Figure 5.24. As the vertical location of the vortex cores are positively offset in ground-run, the splitting results in relatively more vorticity passing over the tail than under.

The propeller is seen to decrease the peak vorticity within the inwards radially shifted cores of the primary and secondary vortical structures. There is a ‘horn-like’ feature visible in the unpowered configurations but not in the powered configurations. This is due to the absence of a boundary layer splitter ahead of the rear engine air intake. The stagnation seen in the earlier discussed C_P contours causes a separated blob of vorticity to pass over the fuselage and join with the other structures. However, its absence in the powered cases is essential as these cases are the most relevant.

Though the legend range is the same for the non-dimensionalised variable being presented, the actual vorticity magnitudes are different. The vorticity in s^{-1} is almost twice in free-flight as in ground-run. It is believed to be scaled by the Reynolds number, as that too has a very similar ratio between the two cases.

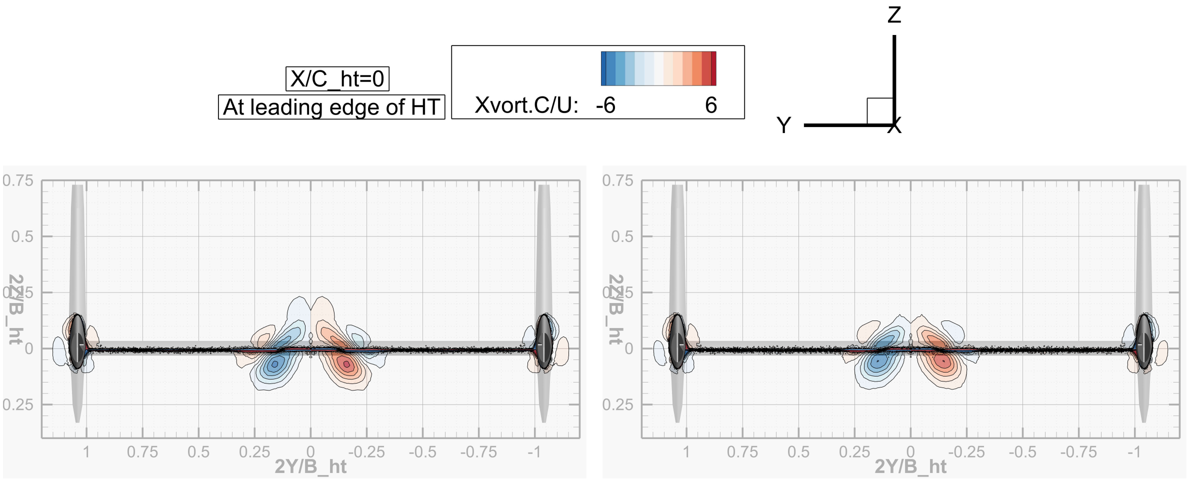

(a1) Unpowered, $C_L = 0.5091$ **(a2)** Powered, $C_L = 0.5030$

(a) Free flight, $Re_{\text{MGC}} = 6.38 \times 10^6$, $\alpha = 2^\circ$

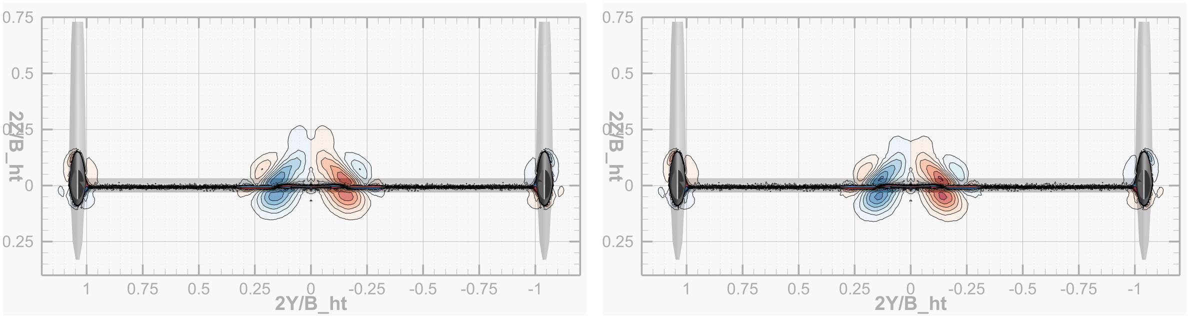

(b1) Unpowered, $C_L = 0.5516$ **(b2)** Powered, $C_L = 0.5512$

(b) Ground-run, $Re_{\text{MGC}} = 3.87 \times 10^6$, $\alpha = 2^\circ$

Figure 5.24: $\xi_x C_{HT}/U$ distribution at the leading edge of the horizontal tail.

5.6.2. Vortices interacting with HT

The influence of the vortices on the upper and lower surfaces of the tail, due to their interaction, are individually shown for the different cases from Figure 5.25 to Figure 5.28.

The tail splits the oncoming vortex and causes a part of it to go above and the rest below it. The amount of vorticity that passes over and below is determined by the vertical location of the vortex with respect to the tail's leading edge. As the cores are positively offset in ground-run, there is relatively more vorticity passing over the tail when compared with free-flight. Consequently, there is a decrease in vorticity passing below it.

The cores of the vortices are caught in the fuselage upwash on one side and the wing downwash on the other side, and shear and twist. But, the core is further stretched at the leading edge, and the splitting of the vortices is seen to occur at the core, that is, a part of the core is passing both above and below the tail and is rubbing along the tail as it convects downstream.

The two oncoming vortices from either side of the fuselage have opposite rotations. After splitting, the path taken by the vortex on the surfaces of the tail depends on its rotation. The movement after splitting is similar to being induced by an image pair about a ground plane with opposite direction of rotation. The path taken by the vortex as it rubs along the wing surface is seen in the C_P plots as an extended region of low pressure. The low total pressure low axial velocity core leaves a trail of very low C_f, while its outer edges with higher tangential velocity produces more shear stress.

The part of the split vortices that pass above the tail have their rotation direction towards each other. The vortices move towards each other and start diffusing each other. They convect along the chord in a parallel fashion till they both are almost dissipated towards the trailing edge.

By comparing Figure 5.26 and Figure 5.28, the split vortices on the upper side in free-flight are more diffused and have less vorticity left in them at the trailing edge. While this could be attributed to the structures leaving the fuselage at a more 'inner' location, as show earlier in section 5.5, and the streamtube contraction radially shifting them closer together, the spread of the vorticity within the vortex is also of importance. A combination of these effects result in higher diffusion in free-flight.

The split part passing underneath the tail have opposite relative rotating directions. Hence, they tend to move outboard on their respective half spans. As these vortical structures do not directly interact with each other, they have sufficient strength to leave the trailing edge of the tail and proceed along their trajectories in downstream fluid medium.

The vorticity shed by the trailing edge of the HT also interacts with the fuselage wake vorticity that passes over and under it. The HT vorticity for each symmetrical half has an opposite sense to the respective oncoming primary vortices. Hence, the vorticity layer forms a barrier and prevents the two parts of the split streamwise vortices from rejoining.

The magnitude of C_f in ground-run is higher than in free-flight due to the lower Reynolds number. The influence of propeller power in both cases is seen as an increase in the C_f within the streamtube influenced area due to higher axial velocities.

The region on the tail that produces the *inverted* lift force, seen by the suction pressure on the top side instead of the stagnation pressure like the rest of the span, is contained within these vortices. These vortices separate the upwash from the fuselage and the downwash from the mainwing. The rotating streamlines of a vortex have the same influence as a propeller slipstream at a wing. The rotation changes the relative angle of attack and hence, the direction and magnitude of lift, as will shortly be discussed.

Both vortices on either side of the symmetrical plane induce an upward flow and higher angle of attack in the region between them, the region with force inversion. The rest of the span is induced a downward flow and increased angle of attack for the negative tail incidence, thereby increasing their downward lift generation. The stagnation point along the span varies accordingly. Another consequence of the interaction between the vortex and the leading edge is the forward tilting of the lift force vector. The drag force in this region would also be negative and behave like thrust.

In the ground-run, as the vortex cores are vertically positively offset, the induction on the downward rotation side is slightly decreased. This is seen as a slight increase in the spanwise area that produces an upward lift force. There is slightly more area producing an upward lift force.

The suction pressure within the inverted area is further increased in ground-run as compared with free-flight. It is unclear if this can be individually attributed to the influence of the ground, or the offset in vortex core. At the moment, it is understood to be a combined effect.

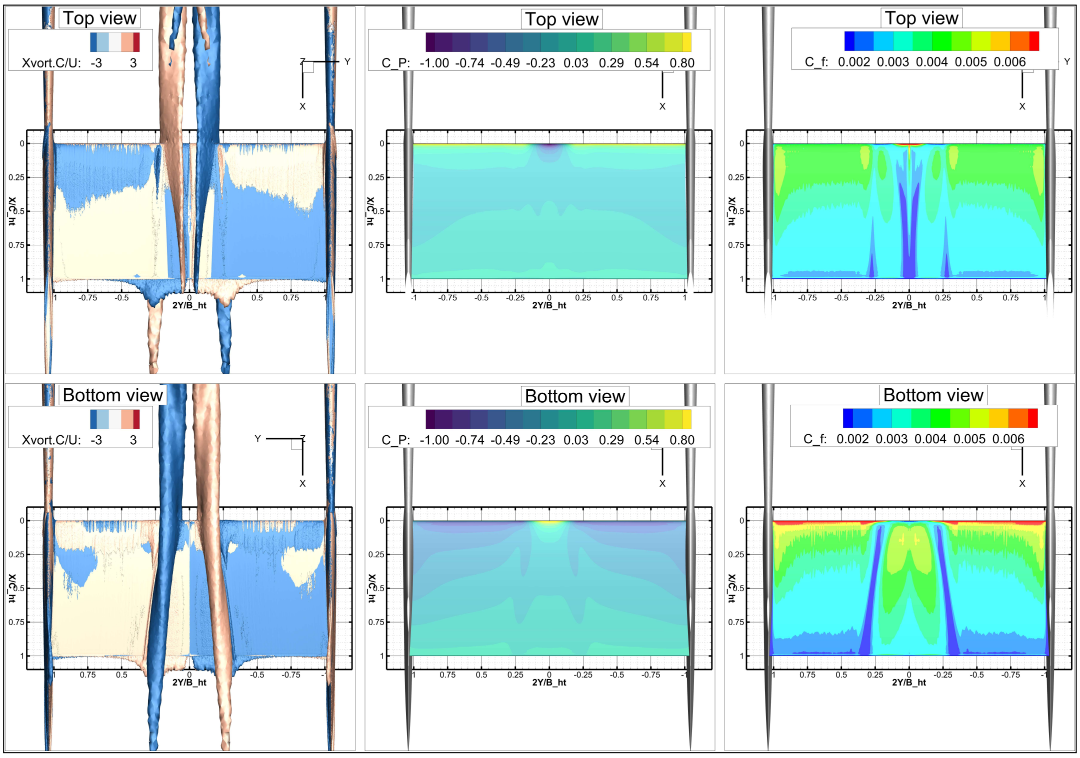

Figure 5.25: Influence of fuselage wake vortex on C_P and C_f distribution on HT Free-flight, $Re_{\text{MGC}} = 6.38 \times 10^6$, $\alpha = 2°$, $C_L = 0.5091$, Unpowered.

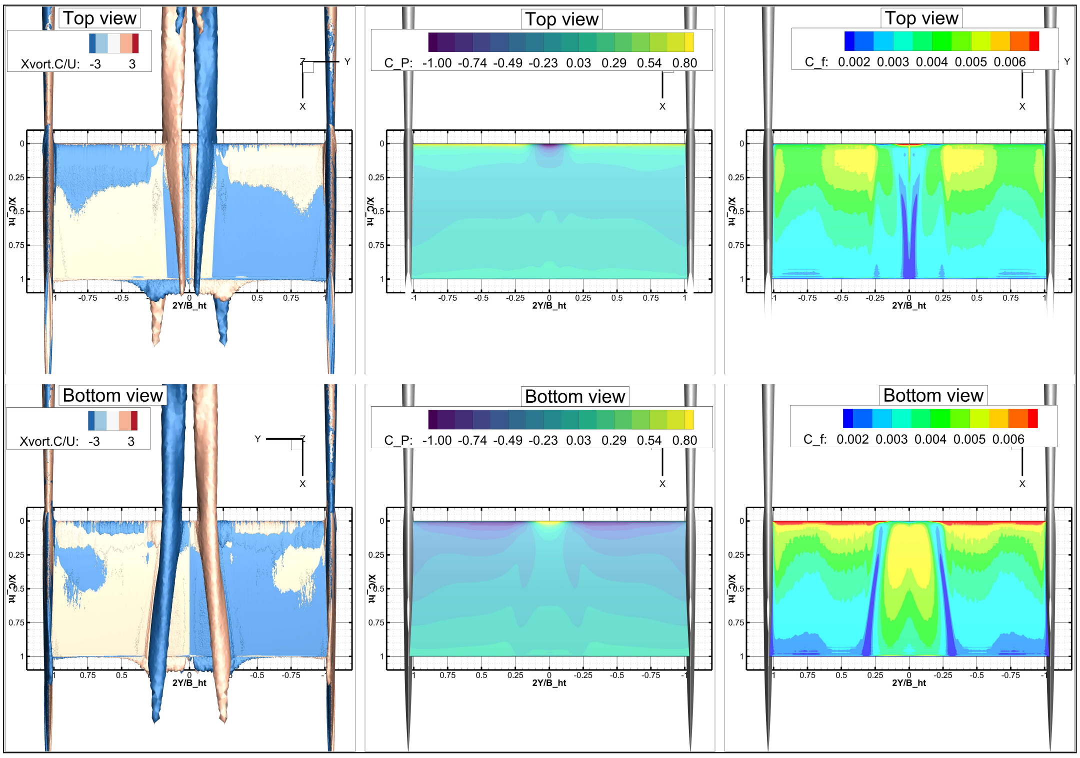

Figure 5.26: Influence of fuselage wake vortex on C_P and C_f distribution on HT Free-flight, $Re_{\text{MGC}} = 6.38 \times 10^6$, $\alpha = 2°$, $C_L = 0.5030$, Powered.

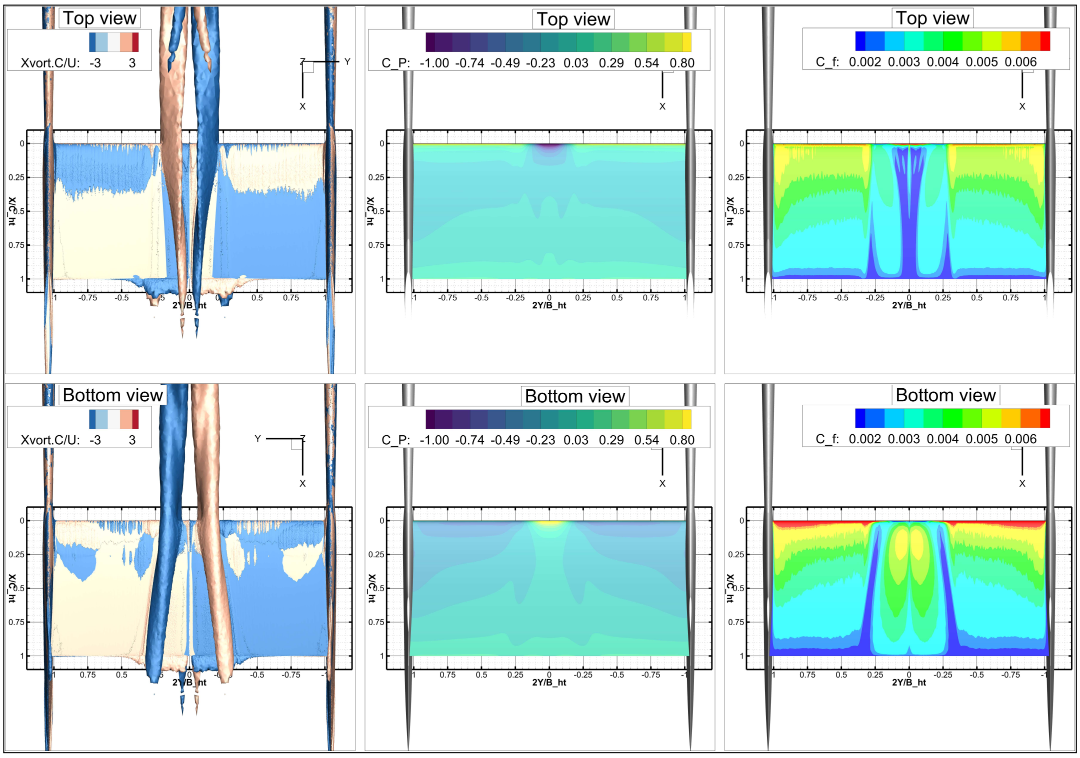

Figure 5.27: Influence of fuselage wake vortex on C_P and C_f distribution on HT Ground-run, $Re_{\mathrm{MGC}} = 3.87 \times 10^6$, $\alpha = 2°$, $C_L = 0.5516$, Unpowered.

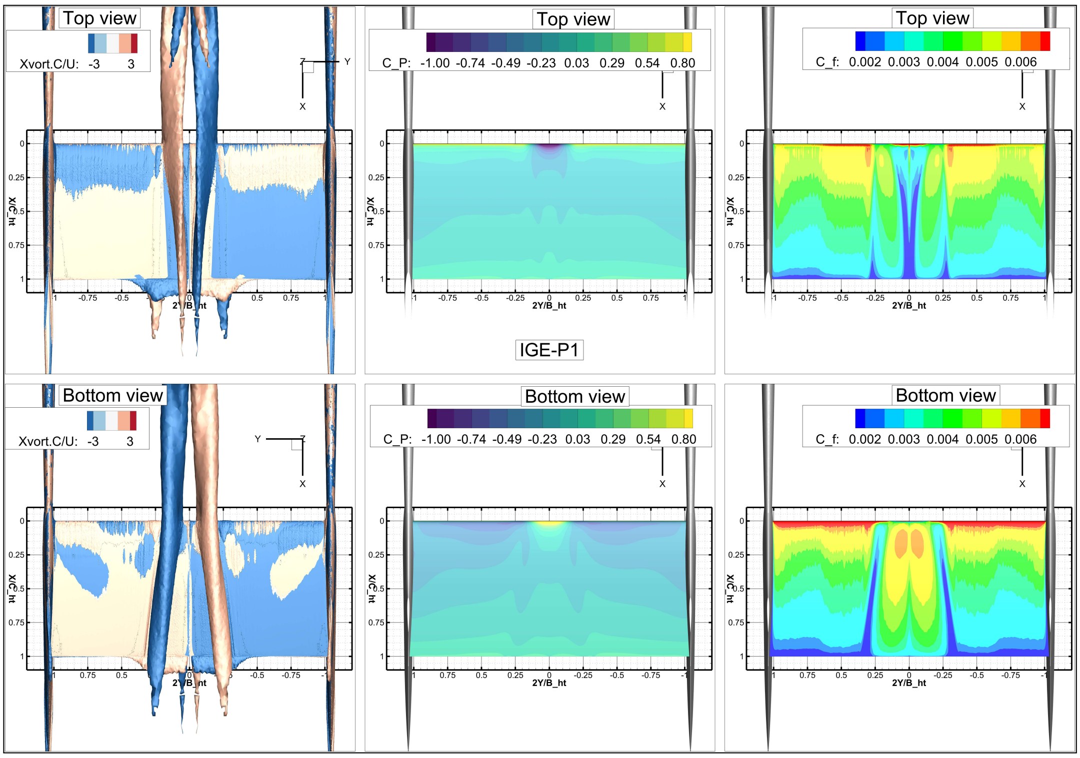

Figure 5.28: Influence of fuselage wake vortex on C_P and C_f distribution on HT Ground-run, $Re_{\mathrm{MGC}} = 3.87 \times 10^6$, $\alpha = 2°$, $C_L = 0.5512$, Powered.

Figure 5.29 shows the streamtraces of the wall shear stress on the top and bottom side of the tail for the powered ground-run. There does not seem to be any distinct separation or reattachment lines. However, the streamtraces bunch in a separation like fashion on the outer edges of the vortex core, on both the upper and lower sides.

The edge of the propeller streamtube is visible as a kink in iso-lines at $2y/b_{HT} \approx 0.6$. Within the streamtube, the C_f is higher for a longer chordwise length. Outside of it, it has a lower value at the same chord location. But, the value again increases towards the vertical tail due to interaction of the boundary layers.

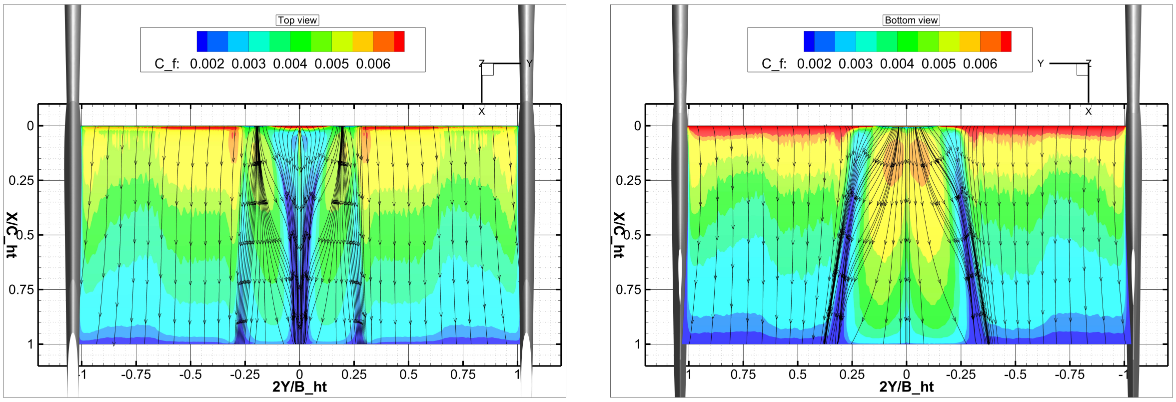

(a) Top **(b)** Bottom

Figure 5.29: Streamtraces of wall shear on the top and bottom side of the horizontal tail Ground-run, $Re_{\text{MGC}} = 3.87 \times 10^6$, $\alpha = 2°$, $C_L = 0.5512$, Powered.

5.6.3. Dynamic pressure ratio at the tail

The dynamic pressure ratio is defined as the local dynamic pressure to freestream dynamic pressure. It indicates the tail's effectiveness and ability to generate a downward lift force.

$$\frac{q_{HT}}{q_{\infty}}$$

With the centreline of the rear propeller situated below the leading edge of the tail, it is designed to blow more of the higher velocity air underneath the tail, thereby increasing its effectiveness. The increase in dynamic pressure ratio due to the propeller is clear in both the cases as seen in Figure 5.30 for the quarter chord location.

In unpowered ground-run, the reduction in velocity due to the mirror image translates to a reduced dynamic pressure ratio with a slight vertical offset to the flow-field. The powered ground-run does not achieve the same increase in dynamic pressure ratio as free-flight. This could be a combination of the lower thrust coefficient of the propellers for the ground-run study, as reported earlier in Table 5.7, the flow retardation due to the mirror vortex system, and the ground influenced restriction to the flow-field that prevents it forming as it would have in free-flight.

This distribution will also provide future researchers with information on the location of installation of probes to measure the dynamic pressure at the tail.

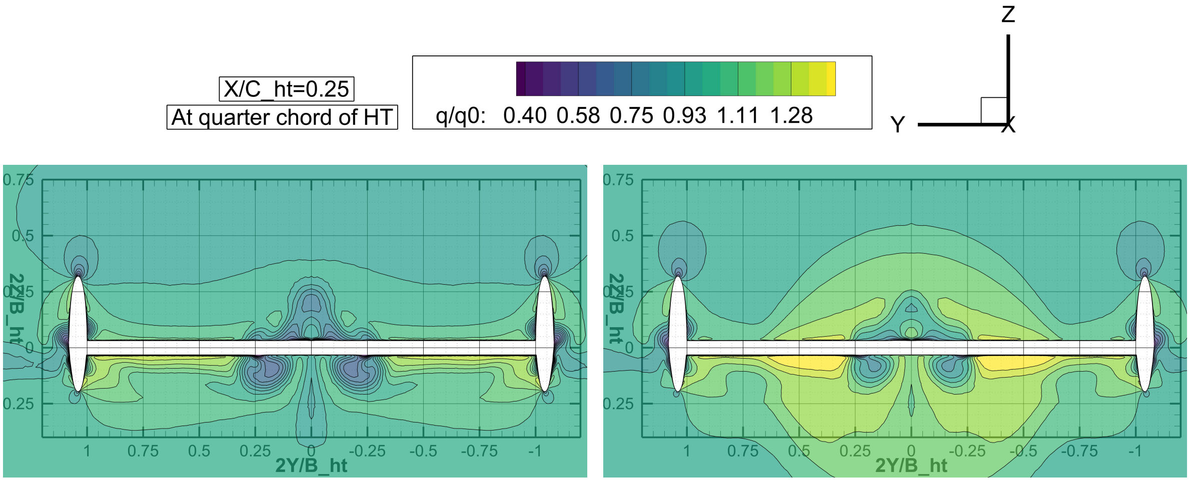

(a1) Unpowered, $C_L = 0.5091$

(a2) Powered, $C_L = 0.5030$

(a) Free flight, $Re_{\text{MGC}} = 6.38 \times 10^6$, $\alpha = 2^\circ$

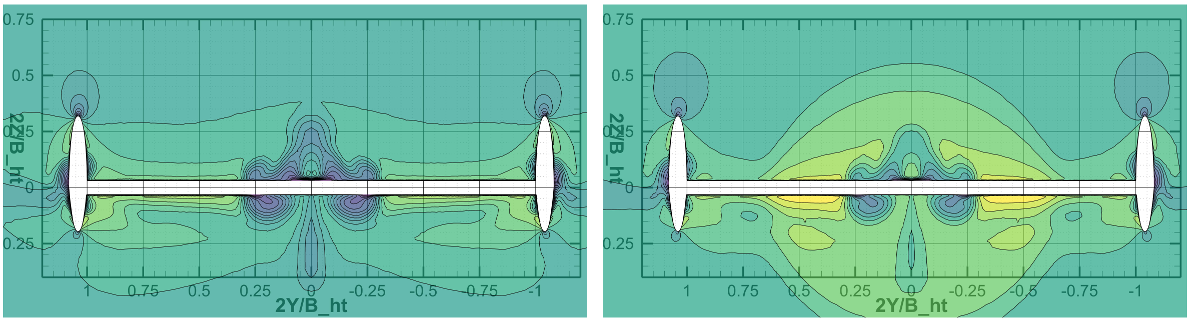

(b1) Unpowered, $C_L = 0.5516$

(b2) Powered, $C_L = 0.5512$

(b) Ground-run, $Re_{\text{MGC}} = 3.87 \times 10^6$, $\alpha = 2^\circ$

Figure 5.30: Dynamic pressure ratio at the quarter chord location of the horizontal tail.

5.7. Spanwise loading

The lift distribution across the span of the main wing and the horizontal tail were calculated and visualised. These two lifting surfaces were split into smaller strips of 2.5% of their span over which the pressure and shear forces were integrated to obtain the lift forces.

The VLM results from AVL for the spanwise loading were compared for the mainwing only. For the tail, it was seen that the absence of the fuselage made a huge difference and the comparison would add no value. The VLM analyses did not show the positive lift force generated near the mid-section of the tail. Moreover, the boundary layer interference between the horizontal and vertical tail were not captured as the VLM models were inviscid analyses.

It was mentioned earlier that the influence of the oncoming streamwise oriented vortex was to tilt the lift force vector forward and that the local drag would act in a thrust like fashion. It was found that the drag forces required much smaller strips than the ones used for lift here. An attempt at creating an automatic macro to do the calculation was unsuccessful and the manual effort was too much, hence, the drag distribution is not reported. However, a notional representation is given in section C.2.

5.7.1. Mainwing

Figure 5.31 shows the spanwise lift distribution for the mainwing from the CFD and VLM studies in free-flight and ground-run.

There is more lift produced on the wing in ground-run. The increase in lift decreases towards the tips, as expected from literature and covered in subsection 2.2.2. At this moment, no distinction between influences of the ground effect and Reynolds number is made. Coincidentally, the lift predicted by AVL in free-flight is similar to the CFD results in ground-run.

The front propeller covers approximately 0.18 $2y/b_W$. The increased dynamic pressure and axial velocity in the slipstream increases the lift generated over the wing section it influences, which is inboard of the booms. The propellers have no influence over the lift distribution outboard of the booms, in ground-run. In free-flight, there is a very slight reduction in lift, the reason for which is unknown.

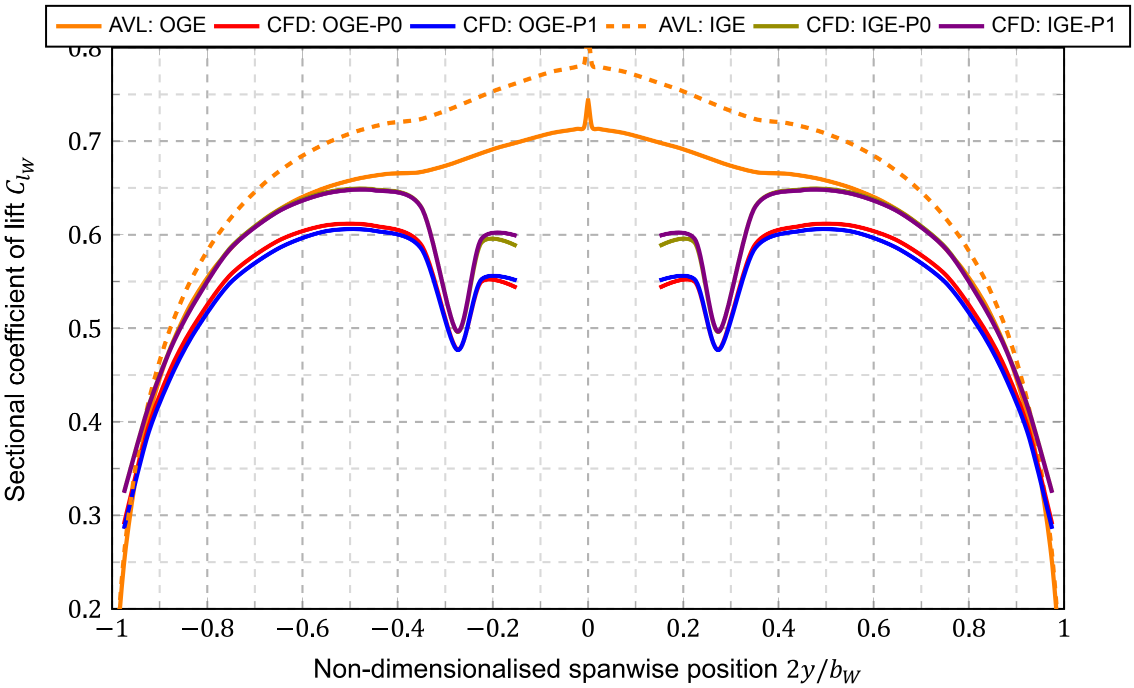

Figure 5.31: Spanwise lift coefficient distribution of the main wing.

5.7.2. Horizontal tail

The lift distribution across the horizontal tail calculated from the CFD studies is shown in Figure 5.32. The inversion of forces within the vortex contained upwash region is quantified here. The reason for the visible *waviness* in the ground-run lift distributions is unfortunately, unclear.

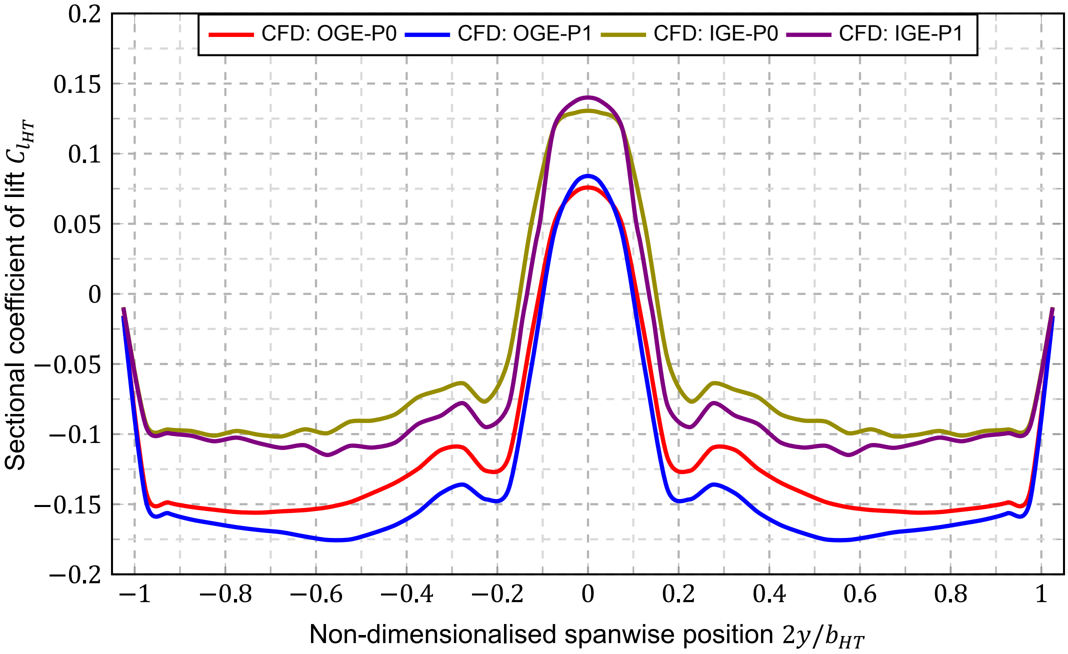

Figure 5.32: Spanwise lift coefficient distribution of the horizontal tail.

The local flow angle at the tail affects the sectional lift coefficient. The resulting angle of attack is comprised of the installed tail setting angle, the angle of attack of the aircraft, and the local downwash field. Figure 5.33 depicts the local flow angle at a location ahead of the leading edge of the tail at a distance of 1% of the tail's chord. The flattening of the downwash in ground-run is seen as a reduction in the contour height depicting the most downward directional flow angle. There is a very slight increase in width of the region of the upward flow (generating positive lift) in ground-run.

The angle of attack at the tail could experimentally be measured using a differential pressure system [128]. The angle of attack with the respect to the fixed tail incidence angle would utilise the difference between the flow angles seen on the upper and lower geometric sides in the presented results.

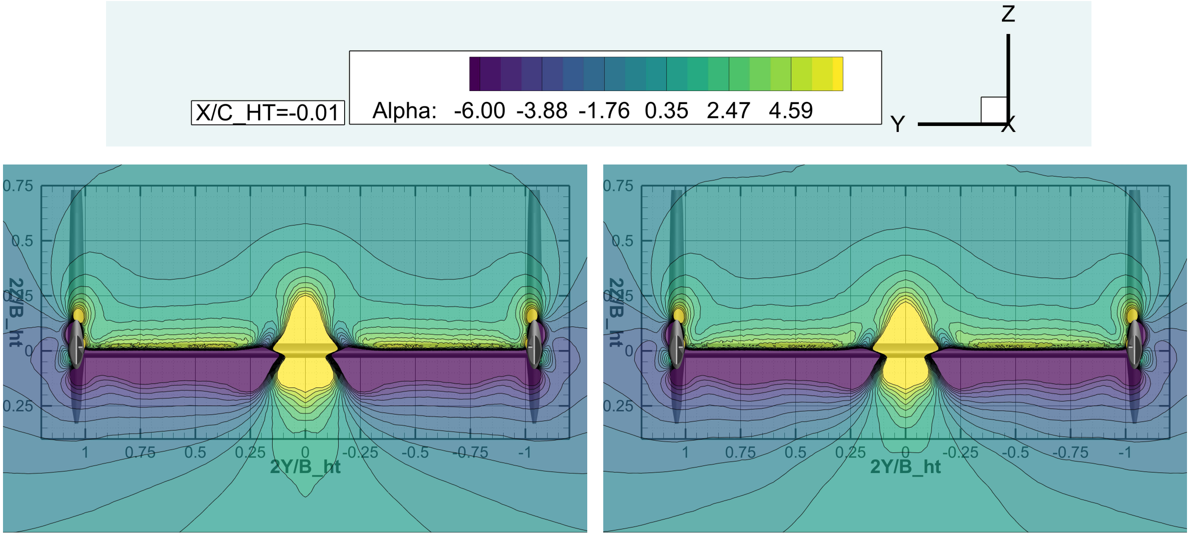

(a1) Unpowered, $C_L = 0.5091$

(a2) Powered, $C_L = 0.5030$

(a) Free flight, $Re_{\text{MGC}} = 6.38 \times 10^6$, $\alpha = 2^\circ$

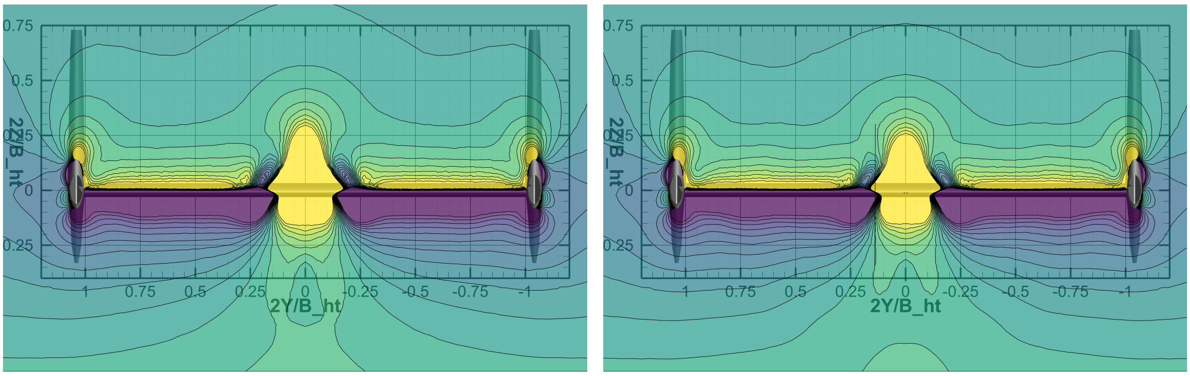

(b1) Unpowered, $C_L = 0.5516$

(b2) Powered, $C_L = 0.5512$

(b) Ground-run, $Re_{\text{MGC}} = 3.87 \times 10^6$, $\alpha = 2^\circ$

Figure 5.33: Two dimensional local flow angle distribution, at a location 1% of the horizontal tail's chord, ahead of the leading edge of the horizontal tail.

But, importantly, the flow-field is not two dimensional as these images might indicate. The interaction of the streamwise oriented fuselage wake vortex and the tail results in three-dimensional flow.

It has been seen that the influence of power is to decrease vorticity, increase the axial velocity and dynamic pressure, and regain some of the lost total pressure in the wing's wake, fuselage's wake, and the pressure minimum within the shed vortical structures that make up the vortex, while moving the vortex radially inward and closer to its pair on the other side of the symmetry plane. The axial velocity increment slightly decreases the relative local flow angle, both in the positive and negative force generation regions. This was shown and mentioned alongside Figure 4.9 where the isolines of the axial velocity ratio were seen to be forced to remain parallel to the rear propeller plane rather than follow the trajectory in the freestream ahead of the propeller plane

However, the influence of power to increase the lift force generated by the wing sections and also diminish the region of upwash and vortex influenced upward positive lift force, occurs due to the the increase in local dynamic pressure and contraction of the streamtube.

The influence of the propeller power to increase the lift can be seen through changes reflected in the chordiwse pressure coefficient distribution when compared between unpowered and powered simulations. Figure 5.34 shows the influence of power for free-flight and Figure 5.35 shows its influence for the ground-run at the spanwise locations shown earlier in Figure 5.10 while comparing the powered cases at the same locations (Figure 5.11).

To remind the reader, the rear propeller centreline is staggered with respect to the leading edge of the tail. The centreline has a negative vertical offset, which means, the offset is in the direction of the intended suction side of the tail. Hence, by looking at the influence of power on the spanwise distribution in Figure 5.32, it is seen that the increase in downward lift force is greater than the increase in upward lift force. This is expected based on a comparison from literature shown earlier and discussed in Figure 2.12a (for $Z_P > 0$), as a larger region of the slipstream passes underneath the tail than over.

This is seen in the below C_P distributions as a larger increase in the suction pressure on the lower side rather than any visible change to the upper pressure side. For the case of $2y/b_{HT} = 0$ that falls within the region of inverted forces, the upper side suctional region does show a significant increase. This would be better attributed to the low thickness airfoil being exposed to a high angle of attack.

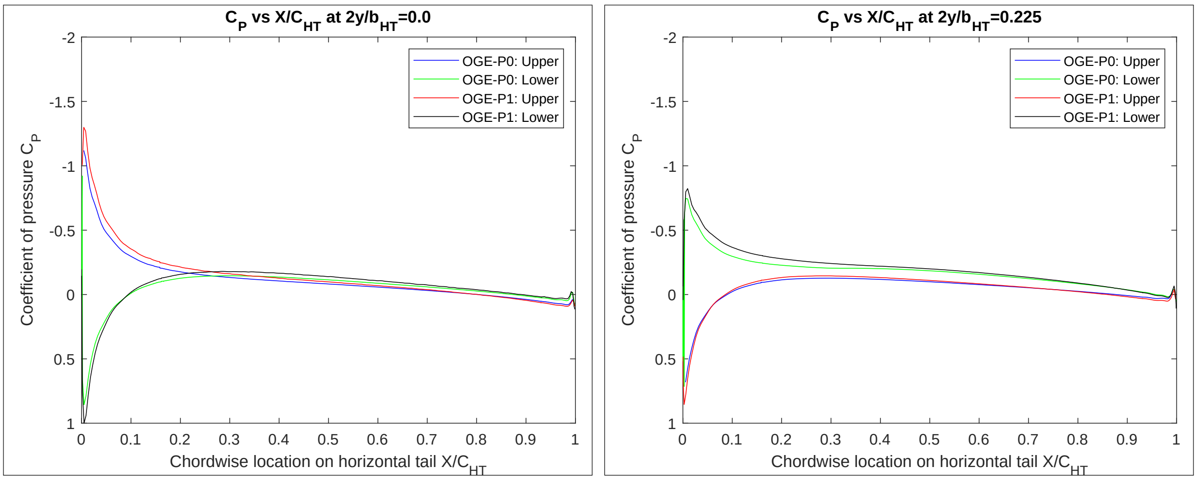

(a) $2y/b_{HT} = 0.0$ **(b)** $2y/b_{HT} = 0.225$

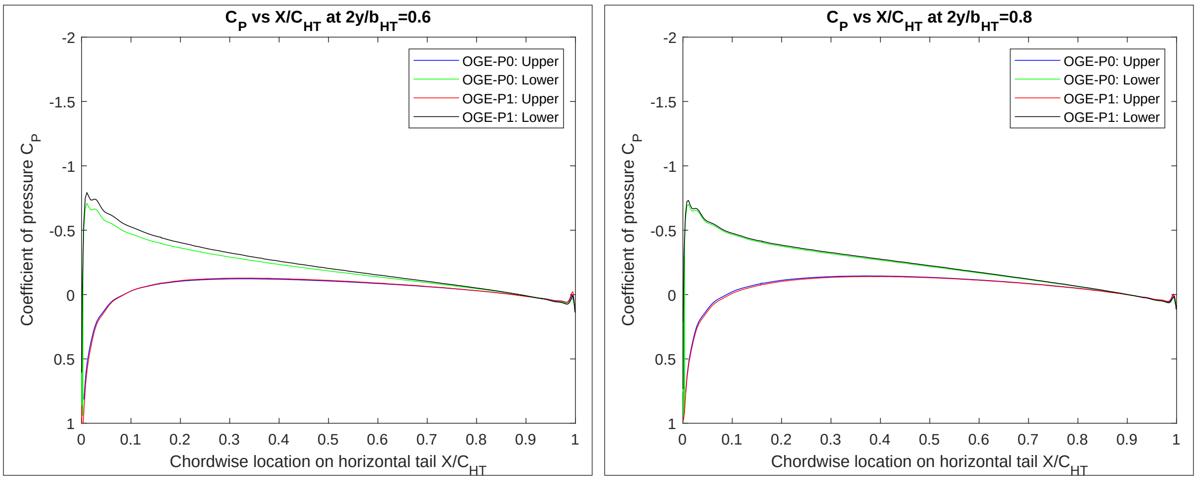

(c) $2y/b_{HT} = 0.6$ **(d)** $2y/b_{HT} = 0.8$

Figure 5.34: Pressure along the chord of the HT at different spanwise locations comparing unpowered free-flight with powered free-flight
Blue- OGE:P0:Upper, Green- OGE:P0:Lower, Red- OGE:P1:Upper, Black- OGE:P1:Lower.

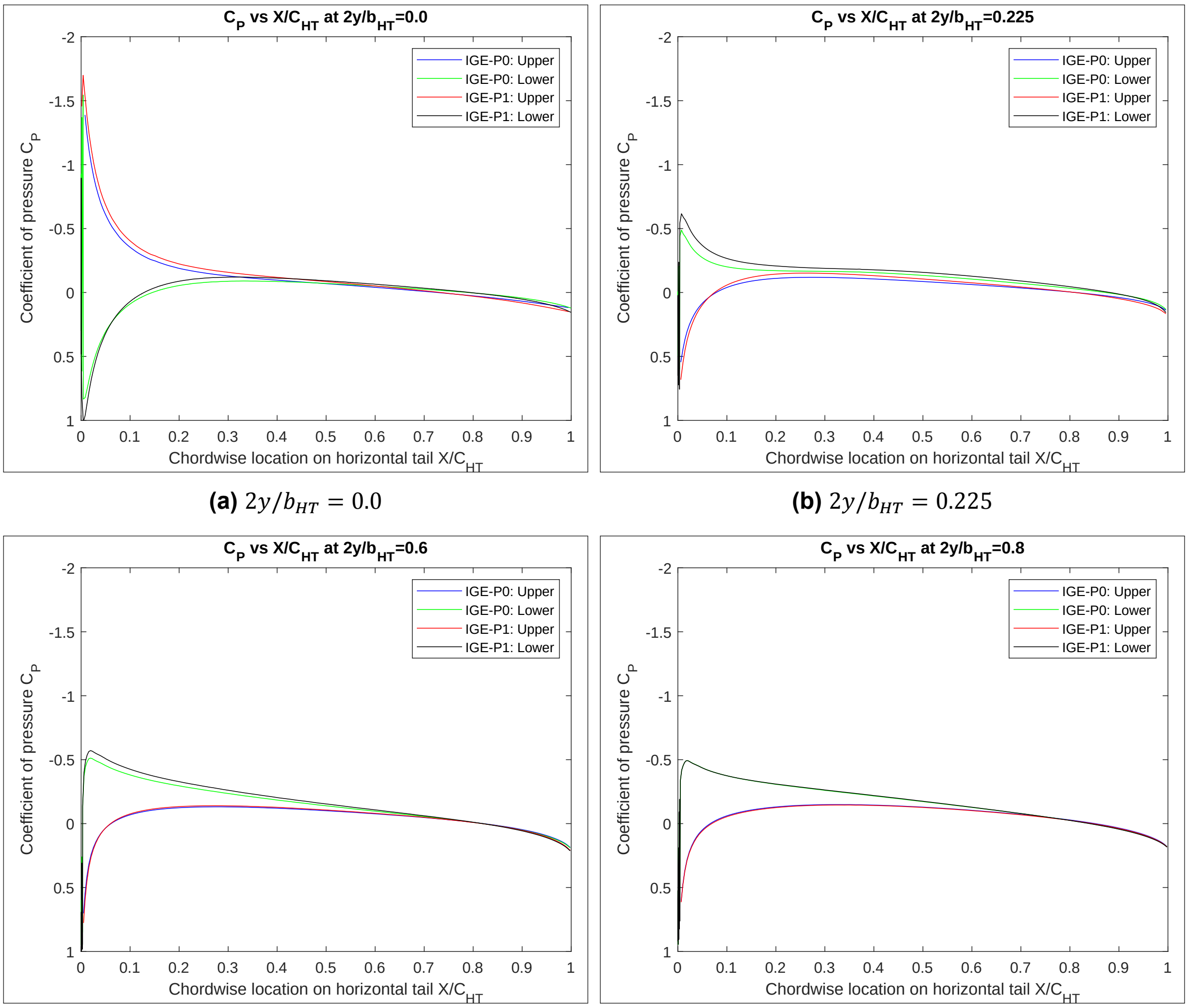

(a) $2y/b_{HT} = 0.0$ **(b)** $2y/b_{HT} = 0.225$

(c) $2y/b_{HT} = 0.6$ **(d)** $2y/b_{HT} = 0.8$

Figure 5.35: Pressure along the chord of the HT at different spanwise locations comparing unpowered ground-run with powered ground-run
Blue- IGE:P0:Upper, Green- IGE:P0:Lower, Red- IGE:P1:Upper, Black- IGE:P1:Lower.

While comparisons between the propeller's influence (comparing unpowered with powered) on the suction peak and general pressure distribution for the same spanwise locations between the free-flight and ground-run cases can be made, the student researcher refrains from doing so due to the difference in the trailing edge geometry between these two cases, as described in section A.1. The rounded tip in free-flight would decrease the adverse pressure gradient due to an extension of the chord beyond its finite tip location. Given that this airfoil is thin with only a 9% thickness, this apprehension is deemed acceptable.

The difference between the sectional lift coefficient in powered free-flight and powered ground-run is approximately $\Delta C_{l_{HT}} \approxeq 0.06$ consistently across the span. This is shown in Figure 5.36.

The gradient of transition between upward positive lift and downward negative lift is very similar between the powered cases even though it is clear from Figure 5.32 that in ground-run, the peller decreases the region of positive lift force more than in free-flight.

The ground-run case shows a wider area of lift near the peak lift at the symmetry plane. This has been attributed to the vertical offset in vortex cores that causes a change in local angle of attack over a slightly wider region, in addition to the ground effect.

In Figure 5.24 shown earlier, a secondary satellite vortical structure of opposite rotational direction is seen to strike the lower side of the tail in free-flight, but not ground-run. The influence of the primary vortices is to influence a downward directional flow across the span outboard of $2y/b_{HT} = 0.2$. As the secondary structure has an opposite sense of rotation, it diminishes the influence of the primary structure. The absence of this structure (because it gets shifted to the upper surface) in ground-run is seen on the kink in the lower side lift at $2y/b_{HT} \approx> 0.2$. In ground-run, the peak of this kink is pushed marginally more outboard.

The shift of this secondary structure to the upper surface which has the same sense of rotation as the split vortex on the upper surface strengthens the combined effect of increasing the negative angle of attack (relative positive to produce downward force), leading to an increase in the peak negative lift coefficient in this vortex influenced region seen as a kink.

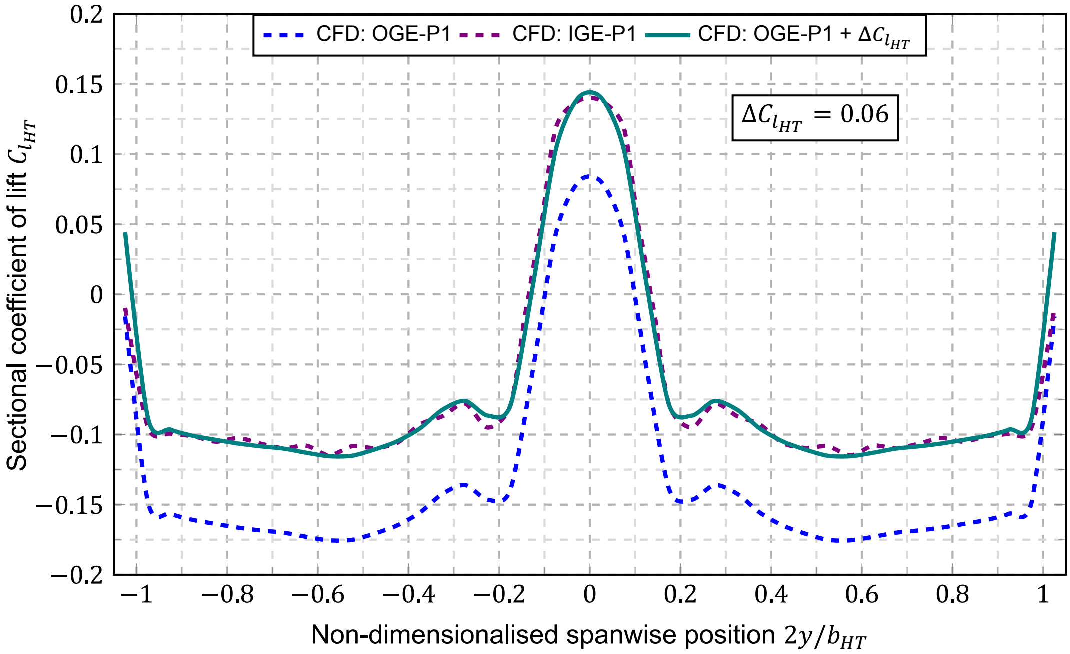

Figure 5.36: Comparing spanwise lift distribution on the tail between powered free-flight and powered ground-run, and approximating the near constant increment of sectional $C_{l_{HT}}$ in ground-run.

5.8. Reynolds number vs ground effect

The angle between the fuselage centreline and the undisturbed freestream flow has been referred to as the angle of attack for free-flight related discussions and as angle of incidence for ground-run related discussions. As earlier summarised in Table 3.4, this angle along with the Reynolds number and wing clearance from the ground, have been considered as parameters important to this reported research. By keeping this defined angle the same at a value of $2°$, the Reynolds number and ground clearance are the two parameters that vary. This section of the report discusses the influence of varying these two parameters between a cruising free-flight test case and a ground-based high-speed taxiing-test scenario.

The importance of considering the Reynolds number while characterising the state of the viscous boundary layer is well known to those familiar with aerodynamics, like the reader, and briefly mentioned in section 2.4. The boundary layer can broadly be classified as being fully laminar, fully turbulent, or as having mixed laminar-turbulent flow with transition either occurring over a finite length or instantaneously.

Figure 3.4 showed the Reynolds number for each major component of the Skymaster's digital twin calculated at the free-flight and ground-run testing conditions with its respective characteristic length. The representation of the variation in skin-friction coefficient with Reynolds number for a sustained laminar flow was shown with the Blasius solution from Equation 2.8, the turbulent flow with a formulation by Schlichting from Equation 2.9, and the notional mixed transitional flow by a Prandtl-Schlichting formulation from Equation 3.3.

The Reynolds numbers in ground-run were 60% of their values in free-flight. As a result of decreasing the Reynolds numbers, the expected boundary layer state shifted from being either almost or fully turbulent to a more transitional region. This indicates that during a ground-run operation, by considering that the growth of instabilities that cause transition depend only on the Reynolds number, more mixed flow might be present.

However, other factors such as protruding nuts, bolts, rivet heads, and other objects, deformations to the surface contour of the decades old aircraft that could alter the pressure gradients, stall strips on the main wing located inboard to the strut-boom fairings, and the acoustic and turbulence energy in the surrounding atmosphere, amongst other instability generating sources, will influence the nature and location of transition.

The lack of information on the expected nature of transition on the different surfaces, and with the assumption that these sources of instability would amplify them sufficiently to promote transition, motivated the choice of using the fully turbulent Spalart-Allmaras turbulence model for the high-fidelity fully viscous RANS CFD numerical simulations, as was discussed earlier with greater detail in subsubsection 4.3.2.2. The low activation Reynolds number for this model, and the fact that it has not been designed to predict the nature of transition [112], resulted in the boundary layers across all surfaces of the digital twin to transition to turbulent almost instantaneously after starting to be developed.

The horizontal tail of the aircraft was a body of interest in this study focusing on propeller-airframe interactions. From the CFD analyses with the chosen turbulence model, it was seen that the tail encountered the turbulent wake of the upstream airframe. A larger spanwise extent of the tail was subjected to this wake in ground-run, as discussed earlier by comparing Figure 4.6 and Figure 5.13, which indicated the numerically esimated turbulence as the ratio of turbulent to molecular viscosity $\mu_T/\mu \geq 1$. The region influenced by this wake would undergo bypass transition.

The location of numerically estimated transition obtained from XFLR5 that was used for VLM analyses coupled with the integrated 2D panel-method based XFoil tool that uses the e^N method to predict the occurence of transition, at the Reynolds numbers of free-flight and ground-run, were shown in Figure 4.4a and Figure 4.4b for simulations not considering the ground effect.

For the free-flight Reynolds number shown in Figure 4.4a, transition does occur ahead of the trailing edge on both surfaces of the mainwing, which is a positive confirmation to an expected turbulent wake (not laminar wake) interacting with the downstream tail. Moreover, with the above mentioned reasons, it is reasonable to expect this to occur.

For the ground-run Reynolds number shown in Figure 4.4b, transition was seen to occur on the upper surface of the mainwing ahead of the trailing edge. The lower surface of the mainwing however, does not experience transition till the trailing edge, at least away from the wing tips. This would question the ability of the mainwing to generate a fully turbulent wake as predicted by the CFD results. However, considering that instabilities due to the above mentioned reasons and the presence of the stall strips located inboard of the wing-strut fairings near the leading edge would promote transition [129], the generation of a turbulent wake from the wing that would interact with the tail appears reasonable.

Moreover, the interaction of the tail with the oncoming streamwise oriented fuselage wake vortex could also generate instabilities that could promote transition on the tail surfaces, as was shown in subsection 2.5.1 based on findings in literature.

Furthermore, the NACA 0009 airfoil that makes up the tail is commonly referred to as a ‘turbulent airfoil’ as its low thickness-to-chord ratio and small leading edge radius would be favourable to produce large suction peaks and strong adverse pressure gradients in its recovery region, and promote transition.

In conclusion, it is reasonable to expect the boundary layer across all surfaces to be predominantly turbulent in free-flight.

In ground-run, the student researcher believes that the fuselage and boom will feature a turbulent boundary layer that starts developing close to their leading edges. The mainwing could feature some laminar flow, but will probably transition to a turbulent boundary layer on both its surfaces. The flow at the horizontal tail is expected to be predominantly turbulent. However, closer inspection into this boundary layer to characterise it would not be valuable for experiments if done with the results discussed here, due to the differing surface contours that would alter surface pressure gradients, as was mentioned previously at different instances. To keep the

Though the resulting boundary layers have now been discussed as being turbulent, the difference in Reynolds numbers would still affect them differently. As the Reynolds number is decreased, for a fully and sustained turbulent flow, the boundary layer would grow in thickness. This would lead to *decambering* of the airfoil and cause changes to its lift, friction drag, and pressure drag, as was briefly discussed in subsection 2.4.2. To keep the occurrence of this decambering to a minimum in the results obtained with the CFD numerical methods, the inlet turbulence setting was kept low as per the discussions in subsubsection 4.3.2.3 relevant to this inlet boundary condition.

The horizontal tail of the Skymaster can be described as a finite wing with large endplates. It would be reasonable to assume that the tail would have predominantly two-dimensional flow away from the interference of the vertical tail due to the absence of finite wing tip-effects, if investigated as a stand-alone object not influenced by the rest of the airfame. However, in this case, and even more so due to its interaction with the streamwise oriented fuselage wake vortices, the flow on its surface was three-dimensional.

The behaviour of the airfoil section that makes up the tail, the NACA 0009 airfoil, at its chord and freestream based Reynolds numbers in free-flight and ground-run, was investigated using the 2D panel-method based XFoil tool. Though this analysis is not representative of the three-dimensional flow seen with the CFD results, it is still valuable in making limited remarks on the influence of the Reynolds number. This analysis, which is described below, was performed at an angle of attack of $2°$. This is the default incidence angle at which the tail is installed at.

As earlier discussed in subsubsection 4.2.3.2, a user-specified trip location at 10% of the chord (x/c) was made in all analyses utilising XFoil, to keep the boundary layer similar to the behaviour expected with the fully turbulent Spalart-Allmaras turbulence model for the CFD analyses. Additionally, for the independent 2D panel-method based analysis with XFoil to investigate the horizontal tail's NACA 0009 section at an angle of $2°$, a user-specified trip location at 15% of the chord was also done. This was to understand the changes to the airfoil characteristics as a result of having more laminar flow, a scenario that could be expected in ground-run when compared with free-flight.

Table 5.8 lists the lift and drag coefficients obtained from XFoil for the NACA 0009 airfoil at an angle of attack of $2°$ at its chord based Reynolds numbers in free-flight and ground-run, for user specified trip locations at 10% and 15% of its chord.

Case	Re_{HT}	Lift coefficient	Drag coefficient		
			Total	Pressure	Friction
Inviscid	-	0.2361	-	-	-
Trip location at 10% of x/c					
Free-flight	3.75×10^6	0.2275	0.00768	0.00100	0.00668
Ground-run	2.28×10^6	0.2266	0.00841	0.00112	0.00728
Trip location at 15% of x/c					
Free-flight	3.75×10^6	0.2282	0.00730	0.00093	0.00637
Ground-run	2.28×10^6	0.2273	0.00802	0.00105	0.00697

Table 5.8: Change in lift and drag coefficients with Reynolds number, comparing free-flight with ground-run, for the horizontal tail's NACA 0009 airfoil at the installed angle of $2°$, from 2D panel-method based simulations in XFoil with user-specified boundary layer trip locations.

The conclusions drawn from this table can be linked to the literature covered earlier in section 2.4.

The effect of viscosity addressed with the Reynolds number is compared with the inviscid result also obtained from XFoil.

For a given trip location, the lift coefficient is higher for the higher Reynolds number. The thicker boundary layer for the lower Reynolds number has a decambering effect on the airfoil that decreases its lift coefficient. The friction drag coefficient decreases with increasing Reynolds number due to decreasing interaction between the surface particles and the sub-viscous region of the thinner boundary layer [79]. The pressure drag coefficient decreases with increasing Reynolds number due to a thin and relatively less diffused boundary layer being more able to overcome adverse pressure gradients and decrease trailing edge separation.

By delaying transition and increasing the amount of laminar flow present on the airfoil surfaces, the loss in lift due to decambering is decreased. This is due to a larger amount of thinner laminar boundary layer being present. The pressure drag is also decreased. The shorter distance between the location of tripping and trailing edge makes the turbulent boundary layer relatively less diffused at the trailing edge, resulting in less trailing edge separation. The friction drag also decreases due to the larger chordwise presence of laminar flow. Laminar flow exerts lower shear stress on the surface due to a less steep velocity gradient.

Figure 5.37 shows the chordwise pressure distributions for the two Reynolds numbers of interest as obtained from XFoil for the NACA 0009 airfoil studied with user-specified trip locations at 10% of the chord and at angle of attack of 2°. To remind the reader as to the reason of showing the plot with this trip location: The choice of this trip location was initially based on a study found in literature [113] for comparing the characteristics of a wing in a wind tunnel with CFD results obtained using the same fully turbulent Spalart-Allmaras turbulence model. A similar comparison between XFoil and CFD results obtained here is made in the following paragraphs.

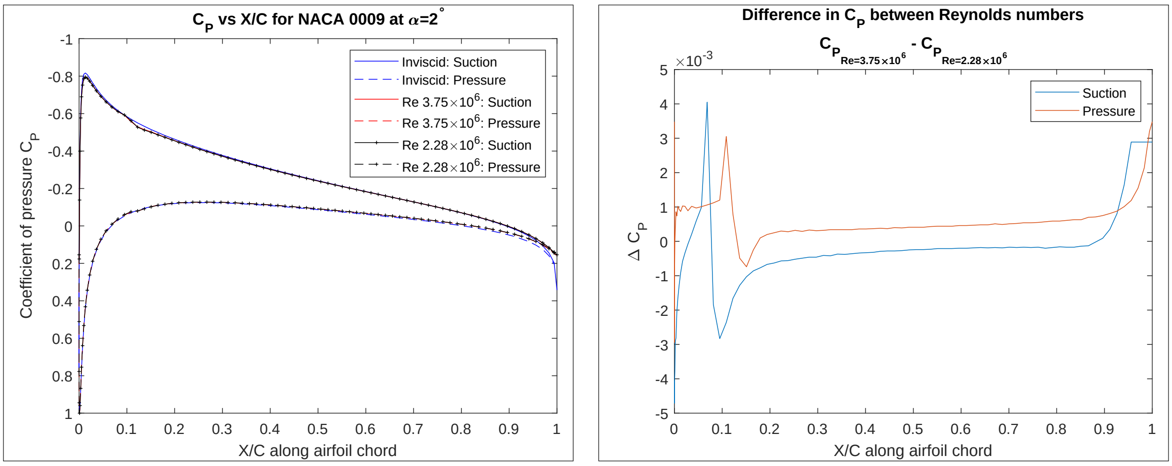

(a) C_P at different Reynolds numbers **(b)** Difference in C_P between Reynolds numbers

Figure 5.37: Influence of Reynolds number on C_P vs X/C_{HT} on the horizontal tail's NACA 0009 airfoil at fixed installed angle of 2° from XFOIL simulations with user-specified trips at 10% x/c .

The chordwise pressure distributions reported so far in Figure 5.11, Figure 5.34, and Figure 5.35, for the same spanwise locations shown in Figure 5.10, included results of the powered configurations. To keep the type of CFD results similar to the XFoil results, the comparison of the unpowered cases is compiled and presented in Figure 5.38.

The changes to the pressure coefficients and the resulting lift forces, due to the decambering of the airfoil occurring with increasing boundary layer thickness with decreasing Reynolds number is seen, both from the tabular results in Table 5.8 and the plot in Figure 5.37b that shows a decrease in both suction side pressure magnitude and pressure side pressure magnitude. However, the magnitude of this decrease is far less than the magnitude of the change to the pressure distributions seen in Figure 5.38. This is a comparison of the influence of a lower Reynolds number in only out-of-ground configurations from potential flow 2D panel-method based simulations, with fully viscous RANS CFD simulations showing the combined influence of change in pressure distribution due to ground proximity and lower Reynolds number in the presence of strong three-dimensional flow.

The added influence of the vertical tails at the end of the horizontal tail, that would act like a large endplate and help in building up a large ram pressure on the underside of the wing [40], as was mentioned in subsection 2.2.3, is another reason for the large change in magnitude of lower side pressure in addition to just the ground effect (the ground effect on a simple wing with no end plates).

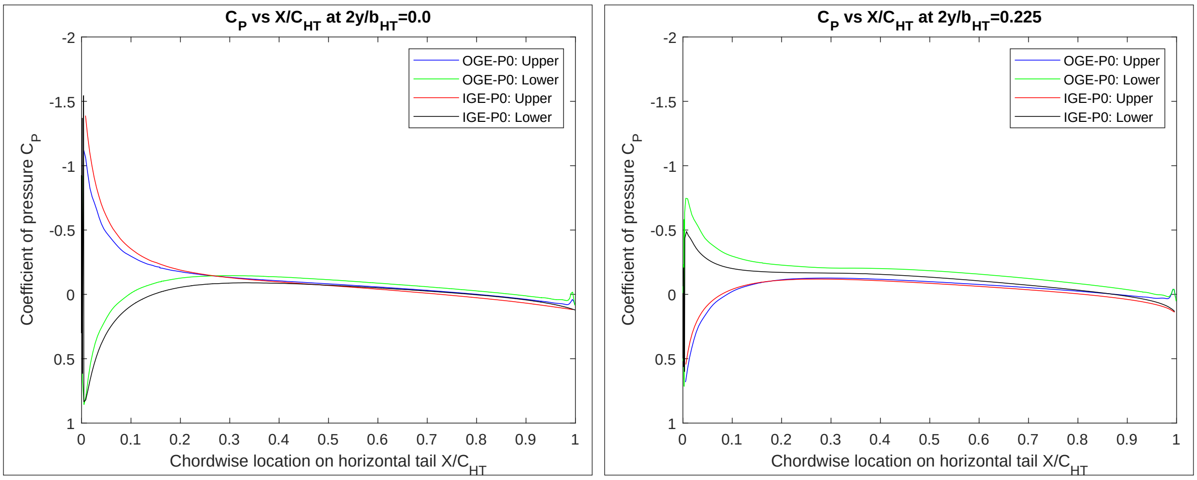

(a) $2y/b_{HT} = 0.0$ **(b)** $2y/b_{HT} = 0.225$

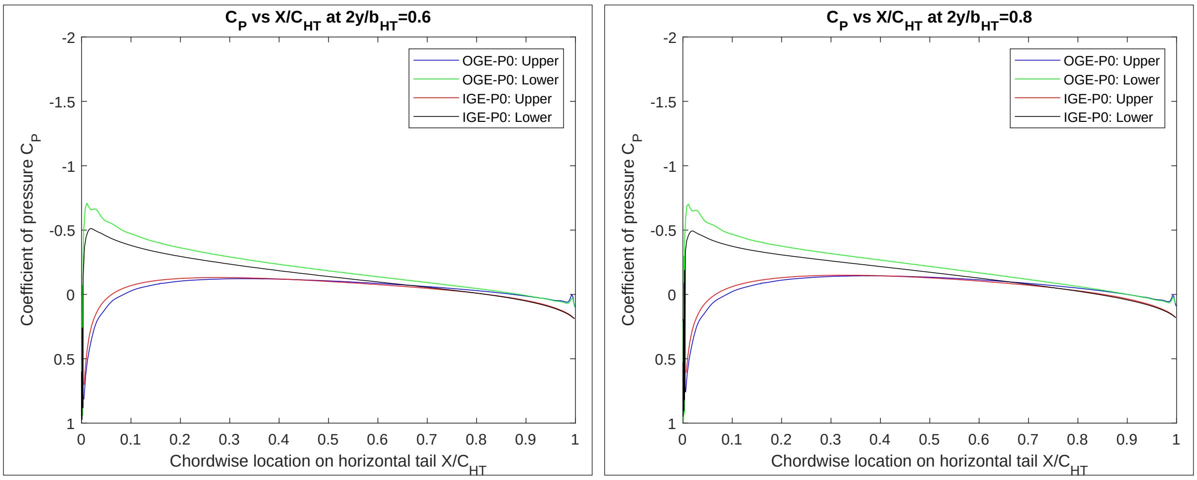

(c) $2y/b_{HT} = 0.6$ **(d)** $2y/b_{HT} = 0.8$

Figure 5.38: Pressure along the chord of the HT at different spanwise locations comparing unpowered free-flight with powered ground-run
Blue- OGE:P0:Upper, Green- OGE:P0:Lower, Red- IGE:P0:Upper, Black- IGE:P0:Lower.

Hence, with the reasoning followed here and the approach taken to the analyses, while looking at the pressure distributions and the lift coefficients that can be obtained from the integration of the pressure plots, it is the ground effect that is a more dominant parameter than the decrease in Reynolds number that changes these characteristics of the horizontal tail.

Another strong argument that is hidden in this statement is that the influence of the oncoming streamwise oriented fuselage wake vortex is not significantly different between the two CFD results presented. The consequence of the shift in the vertical location has been quantified earlier in Figure 5.36, that showed that the difference between the spanwise lift distributions in free-flight and ground-run. The differences in this distribution due to the relative position of the vortices was deemed as comparatively low, and was mentioned in the paragraphs in subsection 5.7.2 that support this Figure 5.36.

For a further understanding into the consequences of decambering, Figure 5.39 was generated from XFoil for the NACA 0009 airfoil at the two Reynolds numbers of interest. Both free transition and a user-specified trip at 10% were compared with the inviscid results.

With increasing angle of attack, the viscous results deviate from invscid estimations of the lift coefficient. The difference between the two Reynolds numbers of interest with trips is very minute across all angles. So, even though the above discussed pressure distribution and remarks were made based on the results of a single angle of attack, it is reasonable to assume a similar behaviour occurs at other angles as the lift coefficients, which are also the integrated sums of the pressure distributions, hardly differ. The airfoil is not expected to behave in any strange ways that would alter the pressure distribution unexpectedly but, retain the total lift generated. The presence of a strong suction with increasing angle of attack, and a rapid and steep pressure recovery towards the trailing edge is expected to be maintained, thus removing any confusion of possible changes occurring to the pressure distributions due to airfoil behaviour at angles of attack not reported here.

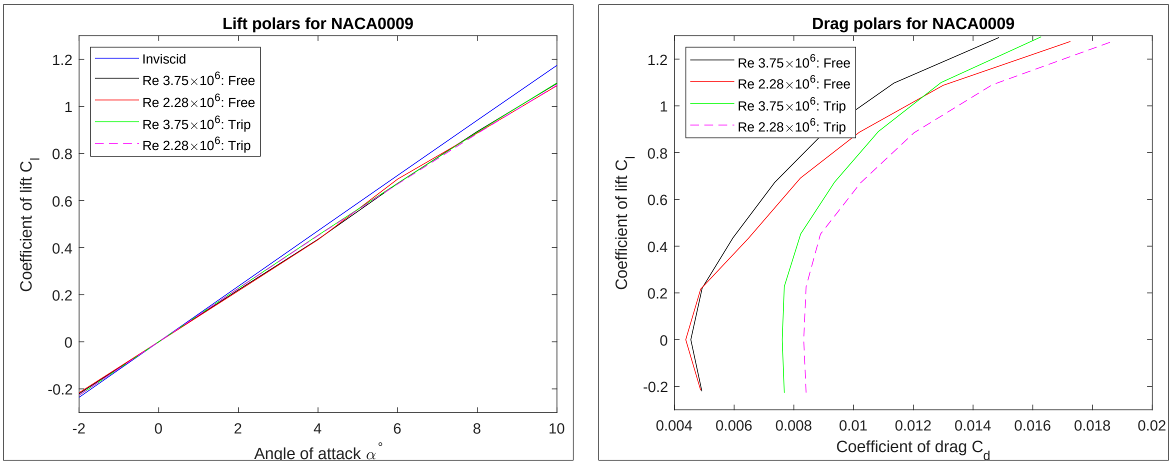

(a) Lift polar **(b)** Drag polar

Figure 5.39: Influence of Reynolds number on lift and drag polar of the horizontal tail's NACA 0009 airfoil, from XFoil simulations with free transition and user-specified trips at 10% of the chord.

The viscous drag coefficient shown in Figure 5.39b for this investigated 2D airfoil section clearly shows a larger dependence on the Reynolds number than that shown by the lift coefficient in Figure 5.39a, by looking at the results with the tripped boundary layer. The relative difference in the drag coefficients between the two Reynolds numbers with the user-specified trip location, is constant across all lift coefficients, due to the absence of any lift dependent drag in this 2D scenario. Only the pressure and friction drag are present.

The analysis of the drag coefficient was extended to the lifting surfaces developed on XFLR5. The VLM results coupled with XFoil to include viscous results to the drag coefficient are given in Figure 5.40. The change to the total drag coefficient for out-of-ground numerical simulations at the two Reynolds numbers of interest, do not show an overly large difference. As the induced drag coefficient will be the same for a given lift coefficient, the delta between the polars is the viscous drag component.

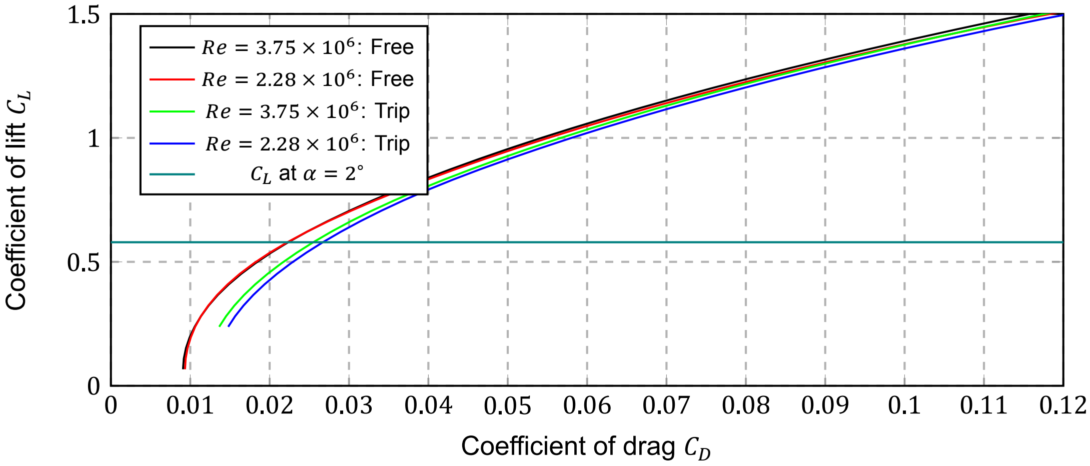

Figure 5.40: Influence of Reynolds number on the drag polar of the lifting surfaces modeled on XFLR5, from VLM results coupled with integrated XFoil simulations for 2D viscous corrections, with free transition and user-specified trips at 10% of the local chord on every surface.

It was mentioned previously that the interaction of the streamwise oriented fuselage wake vortices with the horizontal tail rotated the lift vector forward in such a manner that the drag locally acted in a thrust like manner within the region of inverted forces. This is notionally shown in section C.2, where the drag results are still sensitive to the chosen value of spanwise strip size over which the pressure and shear forces were integrated. The three-dimensional nature of the flow due to the vortex-wing interaction, not just in this region but across the span, limits the comparison of the CFD results with these potential flow-based tools for making comments on the dependence of the drag coefficient to Reynolds number and ground effect. Drag is more sensitive to the effects of viscosity than lift for the low to moderate angles seen here, as was discussed in the preceding paragraphs.

Hence, no strict conclusion is made for the dependence of the drag coefficient on the Reynolds number and ground effect, based on these simple 2D analyses that have proven sufficient for the lift characteristics and pressure distributions for sections of the tail.

However, while comparing the skin-friction coefficients across all surfaces, it was seen to be higher in ground-run. This is expected given the lower Reynolds number. The higher values on the tail have been displayed in Figure 5.25 to Figure 5.28.

In continuation, no hard comments can be made on the nature and behaviour of boundary layer transition, as the high-fidelity CFD results were fully turbulent. Without any experimental data to help understand its importance, it is currently unknown whether a rigorous treatment of transition is required to be included into the numerical model.

The above sections attempted to make statements on the influence of the Reynolds number on the drag coefficient for mixed laminar-turbulent flow states with numerical results from potential flow-based methods.

An attempt at addressing the different contributions of the ground effect and Reynolds to the total drag coefficient, with results obtained from the executed CFD studies, is discussed below.

Table 5.9 repeats previously discussed CFD results of the unpowered configuration of the digital twin in free-flight and ground-run. C_L and C_D are the numerically obtained total lift and total drag coefficients. C_{D_i} is the induced drag estimated from Figure 5.4. The induced drag in free-flight is from the ‘CFD:OGE-P0’ polar that estimated the induced drag as the difference between total drag coefficient and minimum drag coefficient. The induced drag in ground-run is from the ‘Wieselsberger’ polar that was obtained by converting ‘CFD:OGE-P0’ using Equation 2.2 and Equation 2.3 for $h/b = 0.167$. The induced drag coefficients reported correspond to their respective lift coefficients.

Case	C_L	C_D	C_{D_i}
OGE-P0	0.5091	0.0303	0.0101
IGE-P0	0.5516	0.0281	0.0066

Table 5.9: Coefficients of lift, drag, and induced drag obtained from CFD simulations of the unpowered configuration for an angle of $2°$.

The contribution of the errors in numerical modelling that would have inevitably been included, to these values, are not considered in this discussion, as they have not been estimated.

The total drag coefficient decreases by 22 drag counts from free-flight to ground-run. The decrease in estimated induced drag coefficient is 34 drag counts. Therefore, it is estimated that there is an increase of 12 drag counts due to the lower Reynolds number at which the ground-run simulations were performed.

This breakdown of the contribution of the ground effect and Reynolds number is based on fully turbulent CFD analyses that do not consider the presence of mixed laminar-turbulent flow on any surface of the digital twin, which could possibly be present during an experiment.

Moreover, this breakdown utilises the comments made in literature and covered in subsection 2.2.3, that the influence of the ground is only to decrease the induced drag of a wing but leave its profile drag unaffected. The presence of the other bodies to the airframe were not considered in those comments.

5.9. Limitations and inferences based on literature

An effort to compare all discussed results with literature has been made in many of the preceding sections. This section is dedicated to comparing the features discovered in the flow-field analysis with sources from literature, and links the discussed results to topics covered in chapter 2.

The results presented and discussed in this report, indicate to the existence of underlying unsteady phenomena that cannot be captured by this half-model steady-state study. Hence, differences between the reported results and the *expected* or *possible* unsteady phenomena for a full-model based on literature have been presented in this section.

A comparison of these differences between free-flight and ground-run has not been made. Hence, every topic of interest should be read as a general difference between the results obtained with the current half-model steady-state analysis and an expected full-model unsteady analysis, with a further possible difference between free-flight and ground-run.

Vortex formation

Along with the formation of the primary vortical structures on the top and bottom sides of the fuselage, secondary structures were also formed. While some of the secondary structures diffused very early on, other satellite secondary vortical structures were seen to last till the tail and influence the lift distribution along its span.

The interaction between primary and satellite secondary vortices are unsteady. While the strength of secondary structures could vary only slightly, they influence the strength and location of the primary structure in an unsteady manner [65]. They could also alter the spread of the vorticity.

Hence, in an unsteady time dependent simulation, the vortex strength, radius, and location could vary and cause further differences downstream, which cannot be derived from this study.

As was discussed in subsection 2.5.1, the size and nature of the oncoming streamwise oriented vortex along with its relative vertical height, is an important factor that determines the spanwise extent it influences, and how far ahead of the interacting wing it starts to be influenced by [28].

Though the existence of these fuselage vortices need to be confirmed through experiments, the presence of detached vortices from helicopter fuselages, which the mid to rear part of the Skymaster resembles (student researcher's opinion), is a positive indication to their presence [130].

Inclusion of swirl & propeller interaction

The relative rotational directions between both propellers and the fuselage wake vortices on a plane downstream of the pilot's view is shown in Figure 5.41.

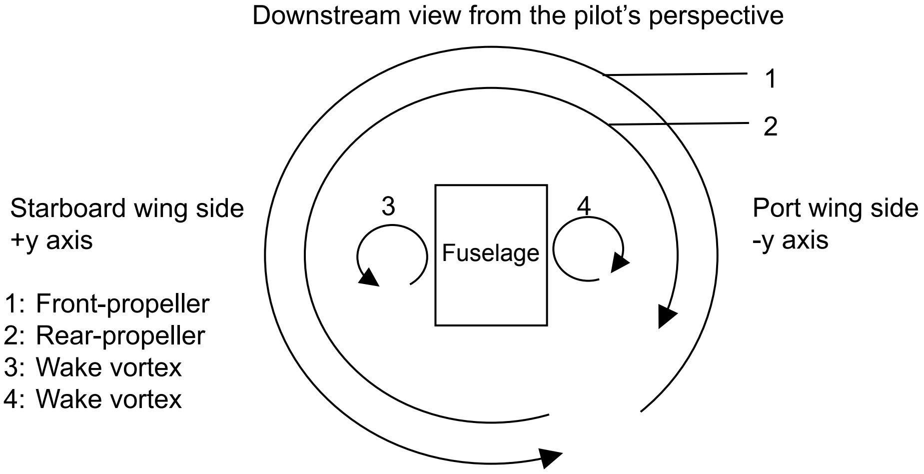

Figure 5.41: Downstream view from the pilot's perspective showing the relative rotational directions between both propellers and the fuselage wake vortices formed on either side.

The slipstream of the front propeller is expected to impact the evolution of vorticity at the fuselage. The slipstream has a swirl direction such that the vortical structures have opposite relative rotational senses. The vortical structure to the pilot's left (the view maintained in the images in this report) on the starboard wing side is co-rotating whereas the other vortical structure on the other side of the fuselage is counter-rotating with respect to the front propeller slipstream.

Hence, the swirl will have different shearing influences and the distortion to the vortical structures will not be the same. The co-rotating vortex could see an increase in strength and the counter-rotating, a decrease [66], based on the direction of the swirl velocity. The direction of shed vorticity could also affect the formation of the vortices. This will cause a non-symmetry that cannot be seen in this study.

Yang [33] comments in a reported blade-vortex-interaction (BVI) study, that the vorticity shed by a propeller tip is of opposite sign to the vorticity in its wake. Hence, the consideration of relative location of the fuselage vortices at any instant of time and space, is influenced by the direction of propeller-shed vorticity it interacts with.

As the detached vortical structures pass through the rear propeller plane, they will move radially inward and be convected in the direction of rotation. The change in vorticity and ability to sustain the change in tangential velocities depends on the shed propeller vorticity in addition to whether they are co- or counter-rotating [33].

The combined passage of co- and contra-rotating vortical structures of different strengths and radial location will possibly affect propeller thrust and torque coefficients, as was shown and just mentioned in Figure 2.23, but not explained in detail due to it relying on the presence of a propeller blade, which was not present in this reported study.

The rear propeller will have the swirl component of its slipstream influence the forces at the tail. Relative to the tail, the propeller centreline has a negative vertical offset. This results in the offset being in the direction of the suction side of the tail. The influence of the strong rear propeller swirl would be something as shown in Figure 2.12b with $Z_P > 0$. The opposite directional swirl from the front propeller would also be faintly present, based on its witnessed existence at the tail shown in and discussed with Figure 5.20 with its current treatment in these CFD analyses, and consequently, influence the tail.

The tip vortices from the propellers will affect the surface pressure distribution on the tail as shown in Figure 2.24. Hence, the reported distributions in Figure 5.11, Figure 5.34, Figure 5.35, and Figure 5.38 would all be modified.

The wing wake and downwash will individually affect the propeller loads [118], when the blades are considered. The downwash in ground-run would be modified as compared to free-flight. In ground-run, the increased suction on the mainwing will result in a steeper adverse pressure gradient to be overcome. At the lower Reynolds number in ground-run, the resilience of the thicker boundary layer to the adverse gradient would be less. Hence, the wake and axial velocity deficit profile could be different between the two cases. The profile would also have a positive shift in vertical location. For further implications to acoustics and structures, the propeller blades are required to be considered in numerical models. However, the confirmation of the presence of laminar flow and a mixed laminar-turbulent boundary being produced on the wing would, and determining its requirement to be treated by the numerical models, would give better results for experimental validation, in regards to this comment.

The rear propeller is seen to interact with many flow features originating upstream of it. Changes to propeller forces and moments could occur which cannot be derived from this study due to it neglecting the blades.

It is expected that the propeller will be affected by the surrounding flow-field. However, these changes can be derived by studying a bladed propeller with suction and pressure sides and not as actuator disks.

Vortex interaction with the tail

The interaction of the fuselage wake vortices with the tail has been so far described as the tail ‘splitting’ the vortices into two structures and was discussed as such in subsection 5.6.2. The associated unsteady phenomena due to vortex instabilities is a time-mean bifurcation, where the vortex structure alternatively attaches to the upper and lower sides of the wing as it re-orients itself due to wing leading-edge stagnation induced instabilities [29].

The stagnation at the tail will lead to flow velocity reduction or reversal ahead of it and impact the oncoming vortex [32]. Instabilities will be introduced into the vortex core and seen as a hollow core with an opposite sense of vorticity [28]. Neither of these, which is shown in Figure 2.19 and Figure 2.21 is seen here in Figure 5.24,

By increasing the Reynolds number from 20,000 [29] or 30,000 [28] to 2.0×10^5 [32], vortex instabilities were seen to be strong enough to cause an abrupt change to the vortex structure, only at the highest value. The tendency of instabilities to cause an abrupt change to the structure increases with Reynolds number [32]. At the higher Reynolds numbers of the Skymaster, such an abrupt change to the vortex structure could occur and lead to unsteady loading (buffeting).

The induced upwash and downwash across the span due to the interacting vortex, could affect transition in a time-mean bifurcated way [28][32].

This kind of unsteady behaviour of the vortex possibly leading to buffeting of the structure, could generate unsteady pressure loads on the tail. Such loads would be localised to a small chordwise region originating from the location of vortex interaction and extending outward, as shown in Figure 2.22. The kinks in the C_P distribution discussed using Figure 5.11, and also seen in every consequent pressure plot of the free-flight case, could provide an early indication to the possible location of such unsteady loads.

There is close proximity between the location of formation of vortex and the wing it interacts with. The vortex is shearing and caught between the upwash and downwash. It is non-symmetrical and the vortex tube is stretching and tilting. The literature compared with here and presented as limitations to this study deal with a well formed isolated vortex sufficiently downstream of its source of origin and free from shear.

Hence, a crucial detail about the vortex that is to be known is the spread of vorticity within it, in addition to its wake-like or jet-like nature at these Reynolds numbers [131] [132]. The non-symmetrical tangential velocity spread along with the wake-like velocity deficit calculated at a location midway between the formation of the vortex and the tail it interacts with, taken along a vertical axis, is shown in Figure 5.42. This shown velocity deficit exists in the powered configuration of ground-run.

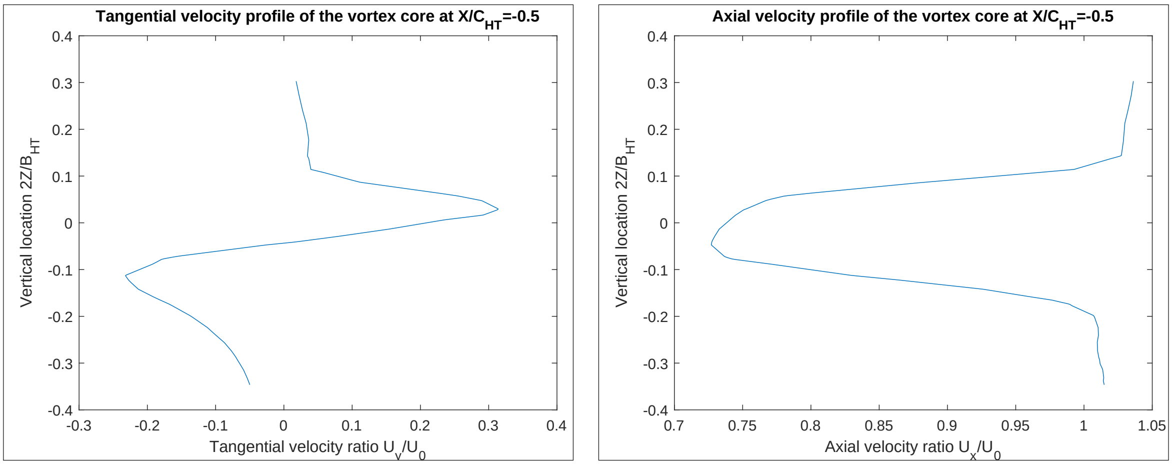

(a) Tangential velocity distribution within the vortex **(b)** Axial velocity distribution within the vortex

Figure 5.42: Velocity distributions taken along the vertical axis of the vortex at a location midway between its complete formation and leading edge of the tail $X/C_{HT} = -0.5$.

CAD and solution convergence

It is quite clear that the effects seen and discussed are unsteady in nature. As the CAD was self-developed, modifications were made in an evolutionary manner to achieve a converged steady-state solution, as it was difficult to consistently achieve one. As the boundary condition for the rear engine air intake was initially unknown, the entire scoop inlet body was removed from the digital twin. However, second order solutions could not be achieved with fine meshes capable of resolving the flow between the fuselage and the tail.

Even by including the body and defining the boundary condition, a converged solution could not be achieved with the required model. The original front and rear propeller rounded-tip spinners from OpenVSP resulted in horrible mesh element quality at the tips. The unfavourable orthogonality was attributed to the occurrence of divergence. A self-designed rounded-tip spinner on which mesh element quality was far better still could not prevent divergence for fine wake-resolved grids.

The rounded tips of both spinners were ‘cut’ to form sharp edges. Due to the angle of attack and the negative installed incidence of the front spinner, the turbulent wake from the sharp edge of the spinner passed over the fuselage and into the rear air intake. Stagnation at the intake forced the wake to pass over the scoop inlet body. This wake joined with the wake from the cut rear spinner. The vortical structures from the fuselage stabilised around this joint wake having a low pressure core.

This is seen in the vorticity contours as the regions above the primary vortex cores located between the earlier mentioned horns of vorticity. The low total pressure in this small core along with the attachment it has to the merged vortex core, provides a clearer understanding.

It is the student researcher's belief that the absence of this stabilising core prevented the numerical solution from converging for steady-state flows. The vertical location finally estimated by the solutions reported here is a result of the vortices stabilising about this low pressure core that originated from the wake of the front spinner.

As there was no prior information found on the aerodynamics of the Skymaster, this steady-state study was essential to the preliminary investigation. It is entirely possible that in an unsteady study with a better geometry, the fuselage wake vortices have different vertical locations and have a different influence on the spanwise loading of the HT.

Figure B.4 in Appendix B shows the modifications to the pressure distribution on the geometric upper side of the tail that was numerically calculated by neglecting the scoop inlet body on a non-wake-resolved grid. The change in pressure isolines around the region of inverted forces, as compared with results discussed here so far, point to a different interaction between the oncoming streamwise oriented fuselage wake vortex and the horizontal tail.

5.10. Influence on airframe & acoustics

The influence of the propeller slipstream on the airframe and airplane acoustics are unsteady phenomena and should be treated as such. Additionally, the presence of these fuselage vortices and their development, trajectories, and interaction are also unsteady, as discussed.

Further information on the propeller and engine settings need to be known, such as the engine power, phase angles, propeller coefficients and blade pitch, and rotational speed.

6

Conclusions and Recommendations

This chapter presents the conclusions of this study and makes recommendations for developing this work.

6.1. Conclusions

Propellers are a prime choice for use in regional aviation due to their inherently higher propulsive efficiencies over turbofan and turbojet engines at the low speeds that such aircraft would fly at. However, they do have their drawbacks on being noisy and generating unsteady loads on the airframe. Therefore, the investigation of the influences, behaviour, and characteristics of an installed propeller, has been of interest in the past, but also in the current day, as many of the new and cleaner aerodynamic designs and propulsion systems being developed by the aviation industry in its response to decreasing its contribution to the ongoing climate crisis, are based on utilising the propeller to produce thrust.

Most current day turboprop aircraft and new conceptual designs have their propellers installed into the mainwing in a tractor arrangement. In such an arrangement, the propeller slipstream interacts with the wing altering its lift distribution and causing unsteady loads on the airframe. Additionally, the propeller would generate noise that could decrease the cabin comfort.

The DEAC possesses and uses a Cessna Skymaster 337F aircraft as an experimental flying testbed to investigate propeller-airframe interaction effects. The horizontal tail of this aircraft is situated directly behind the fuselage-installed rear pusher propeller and interacts with the propeller slipstream. This arrangement and expected interaction is likened to what is seen on larger aircraft.

The DEAC intends to experimentally study this interaction to gather data to benefit the understanding and development of larger airplanes. While tests would normally be done in cruise flight, performing high-speed taxi-tests on an airport runway offers advantages over an in-flight test. The safer testing environment allows for the use of more equipment and personnel having easier access to the aircraft. Shorter turn around times could also increase the number of tests executed in a certain timeframe. However, there are changes to the testing environment and operational settings of the aircraft which are expected to affect its characteristics.

This study was aimed at understanding such a testing approach through numerical simulations and comparing the scenario with a typical free-flight case, so as to evaluate the feasibility of experimentally investigating propeller-airframe interaction with the use of the chosen testbed. This evaluation has been done on a self-designed and developed digital twin of the DEAC's Cessna Skymaster testbed and the findings are intended to aid future experiments to be done with the testbed.

Summary of the cases investigated

The airplane in ground-run had a Reynolds number 60% of its free-flight value. The quarter-chord location of the mean geometric chord of the mainwing had a ground clearance of 16.7% of a full wing span. Propeller thrust requirements were also different and chosen to be the same as the drag force obtained from an unpowered simulation at the condition of interest, so as to maintain steady flight. The angle of attack in free-flight was the same as the angle of incidence of the aircraft while on the ground at 2°.

Numerical steady-state RANS based CFD studies were performed on a self-developed half-airplane half-propeller model digital twin in an incompressible fluid with constant density and viscosity representative of the altitude of interest. The propellers were modelled as actuator disks with a constant pressure rise across their face. The pressure rise was calculated from the momentum theory for a required thrust value that would ensure steady flight. The Spalart-Allmaras turbulence model was used with a numerically recommended inlet turbulence setting estimate. Second order spatial discretisation schemes were implemented.

Aerodynamic characteristics of the digital twin of the Skymaster

The fuselage of the Skymaster digital twin was seen to generate vortical structures from its upper and lower sides. These structures merged into a single vortex just after passing the rear propeller plane. It is likely that the vertical location of the vortices was a result of modifications made to the CAD model to achieve the elusive numerical convergence of the steady-state analyses sought here.

The vortex was shearing as it was caught between the fuselage upwash and wing downwash. Secondary satellite structures were present. The vortex was convected downstream and interacted with the tail. The tail split the vortex at its core. A part of it passed above and the other part below.

The vortex parts on the upper side of the tail moved towards each other due to their senses of rotation. They strongly diffused each other and aligned almost parallel (asymptotically) to each other. The vortex parts on the lower side of the tail had opposite directions and moved away from each other, preserving themselves. The vorticity shed by the tail had the opposite sense as the vortices interacting with their respective symmetrical halves. Hence, the shed tail vorticity acted as a barrier and prevented the split fuselage wake vorticity from rejoining into a single structure.

The region between the two vortices on either side of the symmetry plane had a local upwash and resulted in a positive lift force at the tail section contained between them. The outboard side had a local downwash and increased relative positive angle of attack (to generate downward force). Hence, the spanwise lift distribution of the horizontal tail changed from positive to negative from the symmetrical plane to the outboard vertical tail.

No significant boundary layer separation was present on the rear part of the fuselage apart from small areas where the vortical structures left the surface. However, a wake along its centreline was generated and convected till the tail.

Influence of power

The propellers increased the drag coefficient in free-flight by 38 counts and relatively decreased the lift-to-drag ratio by 12.2%. In ground-run, the increase in drag coefficient was 37 counts with a relative decrease of 11.9% to the lift-to-drag ratio.

The rear propeller encountered the wing downwash, fuselage wake, and the fuselage wake vortical structures. In ground-run, the propeller was unable to recover pressure in the wing wake to the extent possible in free-flight.

The propellers have no impact on the spanwise lift distribution of the mainwing in ground-run. In free-flight, there was a very slight decrease in sectional lift.

The propeller power caused an increase in sectional lift, both positive and negative, along the tail's spanwise loading. Within the propeller streamtube's influence at the tail, the skin friction coefficient was higher.

The propeller slightly decreased the axial vorticity of the structures passing through it, and slightly regained the pressure within the vortical cores and the fuselage wake. The propeller slipstream contraction caused the vortex cores to radially shift inward.

Influence of change in testing environment and operating settings

The flowfield was seen to have a slight positive vertical offset in ground-run, when investigated in proximity to the airplane surfaces. The fuselage wake vortices were split in a different ratio when interacting with the tail. The vertical location of the vortical structures and the wing wake at the propeller plane was also positively offset.

The ground increases the pressure at the front of the fuselage. However, the pressure decreases towards the rear as it forms a convergent passage with the ground. The stronger suction peaks at the throat of this passage between the fuselage and ground. The steeper adverse pressure gradient in the recovery region causes a vertically longer wake.

The suction along the leading edge of the mainwing increased due to ground effect. The suction in the (vertical positively offset core location) vortex-upwash influenced region at the tail was also further increased. The reduction in upper side (pressure side) pressure of the tail due to the increased suctional pressure in ground effect was of lesser magnitude than increase in suction in the inverted force region. There was an increase in pressure on the lower side due to the reduction in velocity between the wing and the ground.

The lift distribution along the span of the mainwing was higher in ground effect with the increment more pronounced at the inboard side. For the tail, the increment in sectional lift coefficient was approximately a value of 0.06 with the location of peaks influenced by the vertical location of the primary and secondary vortical structures. The total lift coefficient in ground-run was higher due to these differences.

There was a decrease in computed total drag coefficient in ground-run with a relative increase in unpowered lift-to-drag ratio of 16.9% . The skin friction coefficient across the aircraft was higher in ground-run indicative of the increased friction drag at the lower Reynolds number. The reduction in induced drag was dominant.

The relative decrease in the required dynamic pressure based thrust coefficient between free-flight and ground-run for each propeller was 7.07% . The relative increase in powered lift-to-drag ratio was 17.3% .

Based on potential flow-based 2D panel method investigations performed into the influence of the Reynolds number on the characteristics of the airfoil that constitutes the Skymaster’s horizontal tail, it can be concluded that changes to the pressure distribution in ground-run and the resulting lift force, are more a consequence of the ground effect than the decambering due to decreased Reynolds number. The ability of the larger vertical tails to act as endplates and aid in the build up of a ram pressure, further stresses the importance of ground influenced changes to the loading on the tail.

No similar remark can be made for the sensitive drag coefficient, as the CFD results pointed to strong three-dimensional flows that make the drag distribution not very comparable with 2D results.

The feasibility of a ground-based approach to testing propeller-airframe interaction

The evaluation of the feasibility of the testing approach was performed on a digital twin of the DEAC’s Cessna Skymaster with the intention to translate the numerical results to flight experiments.

This preliminary investigation into the aerodynamics of the Skymaster involves many uncertainties. The geometry was self-designed and developed. The propellers were modelled as thin actuator discs with infinite blades. The operating parameters were also self-defined and estimated based on literature. Another simplification was the neglect of the swirl velocities of both propellers.

The high-fidelity fully viscous RANS CFD numerical studies strongly indicated the presence of underlying unsteady flow structures that interact with the rear propeller and will be influenced by the front propeller. Additionally, they will also interact with the tail as they move downstream.

The involved steps in the formation, evolution, trajectory, and airframe-interaction of these flow structures is expected to be unsteady in nature, as shown through comparisons with literature.

This preliminary steady-state analyses does not do justice to the unsteady nature of the flowfield that is expected and prevents the student researcher from forming a definitive conclusion on the feasibility of such an approach, based on the chosen testing and operational settings of a simplified digital twin representing the testbed.

With this baseline model established, future researchers can develop more detailed and intricate numerical models and perform their investigations into identified factors most relevant to them.

6.2. Recommendations

Recommendations to future researchers based on the results discussed from the numerical findings of this reported research that tried to evaluate the feasibility of investigating propeller-airframe interaction effects in a novel manner with a certain experimental flying testbed, are reported here.

- The scanned 3D geometry should be preferred over the self-designed and developed geometry studied here.

  The inclusion of equipment such as pressure belts and the extra material required to secure it could affect the characteristics measured [133]. Given that the thickness of the horizontal tail is only 9%, any addition to its thickness could alter the behaviour of the section.

  Similarly, other equipment such as the wing-boom or pressure probes are also recommended to be included in numerical models while preparing data required to correct for modifications to upwash field that would be measured by any aerodynamic pressure based sensor.

  Having an accurate CAD for the digital twin is essential for obtaining accurate data for experimental validation.

- The operating conditions of the airplane that make up the boundary conditions were mostly estimated. Determining the operational configuration and settings would provide more accurate information for the numerical model.

- Many underlying unsteady non-symmetrical phenomena were discovered and they need to be studied as such.

- The pilot sets the engine power and rotational speed for both propellers. It is recommended to perform full bladed analyses with the same numerical specification and derive the thrust calculated. The interaction of the flowfield with the propeller will possible influence the thrust and torque produced. Specifying a pre-determined pressure rise is not representative of the real case, unless it accounts for any changes to the local force distribution that would occur due to the propeller interacting with the surrounding flow-field features.

- Additional information on the propellers, such as relative phase angles, pitch settings, and coefficients are recommended to be considered for detailed numerical models and based on the operational setting of the testbed.

- The results discussed here are quite generic. By first knowing what experiments are to be done with the testbed and what factors are of interest, more specific and relevant information can be derived.

- Different incidence angles in ground-run were not simulated. However, it would be interesting to compare a free-flight angle of $2°$ with a ground angle of $1°$ to check if the flows (vertical location of all flow features) are more similar and would allow for experiments to be run with a more representative flowfield at the tail.

- The SA turbulence model is a simple model with limited ability to solve for shear layers. A two-equation or complex model could be used before the experiments to remove doubt over the validity of the SA model for this application.

Bibliography

[1] M. Hepperle, “Electric Flight - Potential and Limitations”, in *NATO MPAVT-209-09, Energy Efficient Technologies and Concepts of Operation*, Lisbon, Portugal, 2012, pp. 1–30.

[2] B. J. Brelje and J. R. Martins, “Electric, hybrid, and turboelectric fixed-wing aircraft: A review of concepts, models, and design approaches”, *Progress in Aerospace Sciences*, vol. 104, no. August 2018, pp. 1–19, 2019, ISSN: 03760421. DOI: `10.1016/j.paerosci.2018.06.004`. [Online]. Available: `https://doi.org/10.1016/j.paerosci.2018.06.004`.

[3] *Regional Aircraft: what are the challenges?*, 2020. [Online]. Available: `https://www.clean-aviation.eu/regional-aircraft`.

[4] NASA, *Quest for Performance: The Evolution of Modern Aircraft. Appendix E: Mass-Flow Rate, Thrust, and Propulsive Efficiency*. [Online]. Available: `https://history.nasa.gov/SP-468/app-e.htm`.

[5] ——, *LIQUID HYDROGEN AS A PROPULSION FUEL,1945-1959. Appendix B - Propulsion primer, performance, parameters and unit*. [Online]. Available: `https://history.nasa.gov/SP-4404/app-b3.htm`.

[6] R. D. Hager and D. Vrabel, “Advanced turboprop project”, *NASA SP-495*, 1988.

[7] L. L. M. Veldhuis, “Propeller Wing Aerodynamic Interference”, PhD Thesis, Delft University of Technology, 2005.

[8] T. Sinnige, “Aerodynamic and Aeroacoustic Interaction Effects for Tip-Mounted Propellers An Experimental Study”, PhD Thesis, Delft University of Technology, 2018, ISBN: 9789055841745. DOI: `10.4233/uuid`.

[9] *Dutch Electric Aviation Centre*. [Online]. Available: `https://deac-teuge.nl/`.

[10] N. S. L. Elbers, “Assessment of an aircraft propeller noise model by verification & experimental validation”, Master of Science, Delft University of Technology, 2021.

[11] W Frijters, “Test Cell Design for the Development of a Hydrogen Internal Combustion Engine: Risk Mitigation of Hydrogen Leakages in a 20-feet Container”, Master of Science, Delft University of Technology, 2021.

[12] L. Hosking, “Safety Considerations for Developing an H2ICE for Aviation Applications”, Master of Science, Delft University of Technology, 2021.

[13] Jane’s, “Aircraft - Fixed-Wing - Civil / Military - Cessna 337 Skymaster”, *Jane’s All the World ’ s Aircraft : In Service*, p. 16, 2020.

[14] E. Obert, *Aerodynamic Design of Transport Aircraft*. Delft: Delft University Press, 2009.

[15] S. Gudmundsson, *General Aviation Aircraft Design*, First. Elsevier, 2014, pp. 1–1034, ISBN: 9780123973085. DOI: `10.1016/C2011-0-06824-2`.

[16] *Ampaire*. [Online]. Available: `https://www.ampaire.com/`.

[17] *Voltaero*. [Online]. Available: `https://www.voltaero.aero/en/`.

[18] A. B. Connor, D. A. Hilton, and R. C. Dingeldein, “Noise Reduction Studies for the Cessna Model 337 (0-2) Airplane”, Langley Research Center, Hampton, VA, Tech. Rep., 1975.

[19] D. A. Hilton, H. R. Henderson, and B. W. Lawton, “Ground noise measurements during the static and flyby operations of the Cessna O2-T turbine powered airplane (NASA)”, *NASA TM X-72642*, 1975.

[20] *McCauley Propeller*. [Online]. Available: `https://mccauley.txtav.com/`.

[21] *MT Propeller*. [Online]. Available: `https://www.mt-propeller.com/`.

[22] R. D. Kimberlin, “Certification flight tests of 3-bladed MT propellers on the Cessna 337 aircraft”, in *AIAA’s Aircraft Technology, Integration, and Operations (ATIO) 2002 Technical Forum*, Los Angeles, California: AIAA, 2002, ISBN: 9781624101250. DOI: `10.2514/6.2002-5808`.

[23] C Wieselsberger, “Wing resistance near the ground”, *NACA TM 77 (English translation)*, 1922.

[24] R. J. Poole, “Takeoff and Landing of Fixed-Wing Aircraft”, *Encyclopedia of Aerospace Engineering*, pp. 1–12, 2010. DOI: `10.1002/9780470686652.eae246`.

[25] H. Schlichting and K. Gersten, *Boundary-Layer Theory*, Ninth edit. Springer Berlin Heidelberg, 2016. DOI: `10.1007/978-3-662-52919-5`.

[26] I. H. Abbot and A. E. V. Doenhoff, *Theory of wing sections*. New York: Dover Publications Inc, 1959.

[27] N. van Arnhem, R. de Vries, T. Sinnige, R. Vos, G. Eitelberg, and L. L. Veldhuis, “Engineering method to estimate the blade loading of propellers in nonuniform flow”, *AIAA Journal*, vol. 58, no. 12, pp. 5332–5346, 2020, ISSN: 1533385X. DOI: `10.2514/1.J059485`.

[28] C. Barnes, M. Visbal, and P. Huang, “On the effects of vertical offset and core structure in streamwise-oriented vortex-wing interactions”, *Journal of Fluid Mechanics*, vol. 799, pp. 128–158, 2016. DOI: `10.1017/jfm.2016.320`.

[29] D. Garmann and M. Visbal, “Interactions of a streamwise-oriented vortex with a finite wing”, *Journal of Fluid Mechanics*, vol. 767, pp. 782–810, 2015, ISSN: 0022-1120. DOI: `10.1017/jfm.2015.51`. [Online]. Available: `https://www.cambridge.org/core/product/identifier/S0022112015000518/type/journal{\_}article`.

[30] L. L. Veldhuis and S. Nebiolo, “Analysis of calculated and measured wake characteristics of a propeller-wing model”, *38th Aerospace Sciences Meeting and Exhibit*, 2000. DOI: `10.2514/6.2000-908`.

[31] D. Rockwell, “Vortex-Body Interactions”, *Annu. Rev. Fluid Mech.*, vol. 30, pp. 199–229, 1998.

[32] D. J. Garmann and M. R. Visbal, “Interactions of a trailing vortex with a downstream NACA0012 wing”, *47th AIAA Fluid Dynamics Conference, 2017*, no. June, 2017. DOI: `10.2514/6.2017-3319`.

[33] Y. Yang, T. Zhou, A. Sciacchitano, L. Veldhuis, and G. Eitelberg, “Propeller and inflow vortex interaction: vortex response and impact on the propeller performance”, *CEAS Aeronautical Journal*, vol. 7, no. 3, pp. 419–428, 2016, ISSN: 1869-5582. DOI: `10.1007/s13272-016-0198-z`. [Online]. Available: `http://link.springer.com/10.1007/s13272-016-0198-z`.

[34] Y. Yang, “Aerodynamic Interaction between Propeller and Vortex”, PhD Thesis, Delft University of Technology, 2017, p. 289. DOI: `10.4233/uuid`.

[35] A. Betz, “Lift and Drag of a Wing Near a Horizontal Surface”, *Zeitschrift fur Flugtechnik und Motorluftschiffahrt*, 1912.

[36] K. V. Rozhdestvensky, *Aerodynamics of a Lifting System in Extreme Ground Effect*, First. Springer Berlin Heidelberg, 2000, ISBN: 9783642085567.

[37] E. G. Reid and T. Carroll, “A Warning Concerning the Take-off with Heavy Load”, *NACA TN 258*, 1927.

[38] Q. Qu, L. Huang, P. Liu, T. Hu, and R. K. Agarwal, “Aerodynamics of an airfoil in dynamic ground effect during take-off”, in *55th AIAA Aerospace Sciences Meeting*, Grapevine, Texas: AIAA SciTech Forum, 2017. DOI: `10.2514/6.2017-1659`.

[39] E. G. Reid, “A full-scale investigation of ground effect”, *NACA TR 265*, 1927.

[40] A Carter, “Effect of Ground Proximity on the Aerodynamic Characteristics of Aspect-Ratio-1 Airfoils With and With-out End Plates”, *NASA TN D-970*, 1961.

[41] G. C. Furlong and T. V. Bollech, “Effect of ground interference on the aerodynamic and flow characteristics of a 42degree swetpback wing at Reynolds number up to 6.8x10E6”, *NACA Report 1218*, 1955.

[42] E. Torenbeek, *Synthesis of Subsonic Airplane Design*. Delft: Delft University Press, 1982, vol. 22, ISBN: 9024727243. DOI: `10.1016/0377-0257(83)85028-9`.

[43] M. Ahmed and S. Sharma, “An investigation on the aerodynamics of a symmetrical airfoil in ground effect”, *Experimental Thermal and Fluid Science*, vol. 29, no. 6, pp. 633–647, 2005. DOI: `10.1016/j.expthermflusci.2004.09.001`.

[44] M. R. Ahmed, “Aerodynamics of a Cambered Airfoil in Ground Effect”, *International Journal of Fluid Mechanics Research*, vol. 32, no. 2, pp. 157–183, 2005, ISSN: 1064-2277. DOI: `10.1615/InterJFluidMechRes.v32.i2.30`. [Online]. Available: `http://www.dl.begellhouse.com/journals/71cb29ca5b40f8f8,1b99553346c82f39,3767278824b6e009.html`.

[45] M. R. Ahmed, T. Takasaki, and Y. Kohama, “Aerodynamics of a NACA4412 airfoil in ground effect”, *AIAA Journal*, vol. 45, no. 1, pp. 37–47, 2007. DOI: `10.2514/1.23872`.

[46] Q. Qu, W. Wang, P. Liu, and R. K. Agarwal, “Airfoil aerodynamics in ground effect for wide range of angles of attack”, *AIAA Journal*, vol. 53, no. 4, pp. 1048–1061, 2015. DOI: `10.2514/1.J053366`.

[47] N. Deng, Q. Qu, and R. K. Agarwal, “Numerical study of the aerodynamics of DLR-F6 wing-body in unbounded flow field and in ground effect”, in *AIAA SciTech Forum - 55th AIAA Aerospace Sciences Meeting*, Grapevine, Texas: American Institute of Aeronautics and Astronautics (AIAA), 2017. DOI: `10.2514/6.2017-1424`.

[48] J. Gross and L. W. Traub, “Experimental and theoretical investigation of ground effect at low reynolds numbers”, *Journal of Aircraft*, vol. 49, no. 2, pp. 576–586, 2012. DOI: `10.2514/1.C031595`.

[49] L. W. Traub, “Experimental and analytic investigation of ground effect”, *Journal of Aircraft*, vol. 52, no. 1, pp. 235–243, 2015. DOI: `10.2514/1.C032676`.

[50] L. S. Rolls and D. G. Koenig, “Flight-Measured Ground Effect on a Low-Aspect-Ratio Ogee Wing Including a Comparison with Wind-Tunnel Results”, *NASA TN D-3431*, 1966.

[51] W. Schweikhard, “A method for in-flight measurement of ground effect on fixed-wing aircraft”, in *AIAA 4th Aerospace Sciences Meeting*, Los Angeles, California, 1966. DOI: `10.2514/6.1966-468`.

[52] R. E. Curry, B. J. Moulton, and J. Kresse, “An in-flight investigation of ground effect on a forward-swept wing airplane”, *NASA TM 101708*, 1989.

[53] Q. Qu, X. Jia, W. Wang, P. Liu, and R. K. Agarwal, “Numerical simulation of the flowfield of an airfoil in dynamic ground effect”, *Journal of Aircraft*, vol. 51, no. 5, pp. 1659–1662, 2014. DOI: `10.2514/1.C032452`.

[54] S. Katzoff and H. H. Sweberg, “Ground Effect on Downwash Angles and Wake Location”, *NACA TR 783*, 1943.

[55] C. O. O’ Leary, “Flight Measurements of Ground Effect on the Lift and Pitching Moment of a Large Transport Aircraft (Comet 3B) and Comparison with Wind Tunnel and Other Data”, *Aeronautical Research Council R\&M 3611*, 1968.

[56] A. W. Carter, “Effects of ground proximity on the longitudinal aerodynamic characteristics of an unswept aspect-ratio-10 wing”, *NASA TN D-5662*, 1970.

[57] M. P. Fink and J. L. Lastinger, “Aerodynamic Characteristics of Low-Aspect-Ratio Wings in Close Proximity to the Ground”, *NASA TN D-926*, 1961.

[58] L. Nicolai, *Fundamentals of Aircraft Design*. Dayton, Ohio, 1975.

[59] J. Roskam and C.-T. E. Lan, *Airplane Aerodynamics and Performance*. Lawrence, Kansas: Design, Analysis and Research Corporation, 1997, ISBN: 1-884885-44-6.

[60] S. Ravi, H. Winarto, R. Carrese, and Z. Louli, “Combined Chordwise and Spanwise Effects Acting on a Wing Near the Ground”, in *2008 International Joint Conference in Engineering*, Jakarta: International Journal of Science Education, 2008.

[61] R. Rose and F. W. Dee, “Aircraft vortex wakes and their effects on aircraft”, *Royal Aircraft Establishment, Technical Note 2934*, 1963.

[62] F. W. Dee and O. P. Nicholas, “Flight Measurements of Wing-Tip Vortex Motion near the Ground”, *Aeronautical Research Council CP No 1065*, 1968.

[63] J. Harvey and F. Perry, “Flowfield produced by trailing vortices in the vicinity of the ground”, *American Institute of Aeronautics and Astronautics*, vol. 9, no. 8, pp. 1659–1660, 1971.

[64] Q. Qu, L. Huang, P. Liu, and R. K. Agarwal, “Near-field wingtip vortex characteristics of a rectangular wing in ground effect”, in *54th AIAA Aerospace Sciences Meeting*, San Diego, California: AIAA SciTech Forum, 2016. DOI: `10.2514/6.2016-1781`.

[65] L. Zuhal and M. Gharib, “Near field dynamics of wing tip vortices”, in *31st AIAA Computational Fluid Dynamics Conference & Exhibit*, Anaheim, CA: AIAA, 2001. DOI: `10.2514/6.2001-2710`.

[66] R. L. Ash, Z. C. Zheng, and G. C. Greene, “Cross wind effects on turbulent aircraft wake vortices near the ground”, in *25th AIAA Fluid Dynamics Conference*, Colorado Springs: AIAA, 1994. DOI: `10.2514/6.1994-2381`.

[67] T. J. Barber, E. Leonardi, and R. D. Archer, “Technical note on the appropriate CFD boundary conditions for the prediction of ground effect aerodynamics”, *The Aeronautical Journal*, vol. 103, no. 1029, pp. 545–547, 1999. DOI: `10.1017/s0001924000064368`.

[68] D. Steinbach, “Comment on “Aerodynamic Characteristics of a Two-Dimensional Airfoil with Ground Effect”, *Journal of Aircraft*, vol. 34, no. 3, pp. 455–456, 1997. DOI: `10.2514/2.2195`.

[69] C. M. Hsiun and C. K. Chen, “Aerodynamic characteristics of a two-dimensional airfoil with ground effect”, *Journal of Aircraft*, vol. 33, no. 2, pp. 386–392, 1996. DOI: `10.2514/3.46949`.

[70] T. Barber and S. Hall, “Aerodynamic ground effect: A case study of the integration of CFD and experiments”, *International Journal of Vehicle Design*, vol. 40, no. 4, pp. 299–316, 2006. DOI: `10.1504/IJVD.2006.009068`.

[71] ESDU, “Low-Speed Normal Force and Pitching Moment of Slender Wings in Ground Effect”, *Engineering Sciences Data Unit: 71007*, 1971.

[72] ——, “Low-Speed Longitudinal Aerodynamic Characteristics of Aircraft in Ground Effect.”, *Engineering Sciences Data Unit: 72023*, 1972.

[73] R. Slingerland, “Prediction of tail downwash, ground effect and minimum unstick speed of jet transport aircraft”, Doctorate, Delft University of Technology, 2005.

[74] J. Mark Janus, “General aviation propeller-airframe integration simulations”, in *38th Aerospace Sciences Meeting and Exhibit*, Reno, Nevada: AIAA, 2000. DOI: `10.2514/6.2000-357`.

[75] ——, “General aviation propeller-airframe integration simulations”, *Journal of Aircraft*, vol. 43, no. 2, pp. 390–394, 2006, ISSN: 15333868. DOI: `10.2514/1.15354`.

[76] T. Sinnige, “Propeller Integration Aerodynamics”, *AE4130 Aircraft Aerodynamics 2019-20, Class notes, TU Delft*,

[77] Cessna Aircraft Company, *Cessna Super-Skymaster: Owner’s Manual*. Wichita, Kansas, 1971.

[78] Frank M. White, *Viscous Fluid Flows*, Third. 2006, ISBN: 007124493X.

[79] R. Vos and S. Farokhi, *Introduction to Transonic Aerodynamics.* Delft: Springer Science.

[80] R. Liebeck, “Laminar separation bubbles and airfoil design at low Reynolds numbers”, in *10th AIAA applied aerodynamics conference*, Palo Alto, CA, USA: American Institute of Aeronautics and Astronautics (AIAA), 1992, pp. 441–456. DOI: `10.2514/6.1992-2735`.

[81] C. Wells.Jr, “Effects of freestream turbulence on boundary-layer transition”, *AIAA Journal*, vol. 5, no. 1, pp. 172–174, 1967.

[82] C. van Dam, “The aerodynamic design of multi-element high-lift systems for transport airplanes”, *Progress in Aerospace Sciences*, vol. 38, pp. 101–144, 2002.

[83] R. B. Langtry and F. R. Menter, “Transition modeling for general CFD applications in aeronautics”, in *43rd AIAA Aerospace Sciences Meeting and Exhibit*, Reno, Nevada: AIAA, 2005. DOI: `10.2514/6.2005-522`.

[84] E. M. Greitzer, C. S. Tan, and M. B. Graf, “Boundary layers and free shear layers”, in *Internal Flow: Concepts and applications*, Cambridge University Press, 2004, ch. Chapter 4, pp. 166–216. DOI: `10.1017/cbo9780511616709.006`.

[85] R. F. Janssen, “The influence of laminar-turbulent transition on the performance of a propeller”, Master thesis, Delft Unversity of Technology, 2015.

[86] J. D. Anderson Jr, *Fundamentals of Aerodynamics*, 5th. McGraw Hill, 1984.

[87] T. C. Stokkermans, N. Van Arnhem, T. Sinnige, and L. L. Veldhuis, “Validation and comparison of RANS propeller modeling methods for tip-mounted applications”, *AIAA Journal*, vol. 57, no. 2, pp. 566–580, 2019. DOI: `10.2514/1.J057398`.

[88] *OpenVSP*. [Online]. Available: `http://openvsp.org/`.

[89] *CATIA*. [Online]. Available: `https://www.3ds.com/products-services/catia/`.

[90] M. Drela and H. Youngren, *XFoil*. [Online]. Available: `http://web.mit.edu/drela/Public/web/xfoil/`.

[91] ——, *AVL Overview*, 2004. [Online]. Available: `http://web.mit.edu/drela/Public/web/avl/`.

[92] A. Deperrois, *XFLR5*. [Online]. Available: `http://www.xflr5.tech/xflr5.htm`.

[93] *ANSYS*. [Online]. Available: `https://www.ansys.com/`.

[94] *Ansys Fluent*. [Online]. Available: `https://www.ansys.com/products/fluids/ansys-fluent`.

[95] *Tecplot*. [Online]. Available: `https://www.tecplot.com/`.

[96] A. Kagkaras, “Laser scanning modelling of a Cessna Citation for Computational Fluid Dynamics Studies”, Master thesis, Delft University of Technology, 2006.

[97] J. Yin, A. Stuermer, and M. Aversano, “Aerodynamic and aeroacoustic analysis of installed pusher-propeller aircraft configurations”, *Journal of Aircraft*, vol. 49, no. 5, pp. 1423–1433, 2012, ISSN: 15333868. DOI: `10.2514/1.C031704`.

[98] B. Litherland, *Cessna 337 Super Skymaster*, 2015. [Online]. Available: `http://hangar.openvsp.org/vspfiles/286`.

[99] D. Felix Finger, R. de Vries, R. Vos, C. Braun, and C. Bil, “A comparison of hybrid-electric aircraft sizing methods”, in *AIAA Scitech 2020 Forum*, Orlando: AIAA SciTech Forum, 2020. DOI: `10.2514/6.2020-1006`.

[100] K. Wood, *Technical Aerodynamics*, Third Edit. 1955.

[101] J. Katz, V. R. Corsiglia, and P. R. Barlow, “Cooling air inlet and exit geometries on aircraft engine installations”, *Journal of Aircraft*, vol. 19, no. 7, pp. 525–530, 1982, ISSN: 00218669. DOI: `10.2514/3.57425`.

[102] “IO-360 Series Engine Maintenance and Operator’s Manual”, *Continential Motors*, 1994.

[103] ESDU, “Introduction To Installation Effects on Thrust and Drag for Propeller-Driven Aircraft.”, *Engineering Sciences Data Unit: 85015*, 1985.

[104] S. Watkins, “Turbulence Characteristics of the Atmospheric Boundary Layer and Possibilities of Replication for Aircraft”, in *Third Symposium Simulation of Wing and Nacelle Stall*, Braunschweig, 2012.

[105] J. Katz and A. Plotkin, *Low Speed Aerodynamics*, 2nd. Cambridge University Press, 2001.

[106] A. Deperrois, *XFLR5-Ground effect*. [Online]. Available: `https://sourceforge.net/p/xflr5/discussion/679396/thread/ae41f21a/`.

[107] M. Agten, “Aerodynamic Analysis of Wings in Airborne Wind Energy Applications”, Master of Science, Delft University of Technology, 2012.

[108] XFLR5, “XFLR5 Analysis of foils and wings operating at low Reynolds numbers”, Tech. Rep. October, 2009, pp. 1–71.

[109] M. Drela and H. Youngren, *XFoil primer*. [Online]. Available: `https://web.mit.edu/drela/Public/web/xfoil/xfoil_doc.txt`.

[110] J. L. Van Ingen, “The eN method for transition prediction. Historical review of work at TU Delft”, in *38th AIAA Fluid Dynamics Conference and Exhibit*, Seattle: AIAA, 2008, pp. 1–49, ISBN: 9781563479427. DOI: `10.2514/6.2008-3830`.

[111] L. L. M. Veldhuis, “AAP - Handout 1: Some Fundamentals”, TU Delft, Delft, Tech. Rep., 2014.

[112] C. L. Rumsey and P. R. Spalart, “Turbulence model behavior in low reynolds number regions of aerodynamic flowfields”, *AIAA Journal*, vol. 47, no. 4, pp. 982–993, 2009, ISSN: 00011452. DOI: `10.2514/1.39947`.

[113] N. van Arnhem, R. de Vries, R. Vos, and L. L. Veldhuis, “Aerodynamic performance of an aircraft equipped with horizontal tail-mounted propellers”, *AIAA Aviation 2019 Forum*, pp. 1–19, 2019. DOI: `10.2514/6.2019-3036`.

[114] J. Blazek, *Computational Fluid Dynamics: Principles and Applications*, Third edition. 2015, ISBN: 9780080999951.

[115] H. Versteeg and W Malalasekera, *An Introduction to Computational Fluid Dynamics*, Second edi. Pearson Education Limited, 2007, ISBN: 9780131274983.

[116] J. Tu, G. H. Yeoh, and C. Liu, *Computational Fluid Dynamics: A Practical Approach*, Third. 2008, ISBN: 9780750685634.

[117] F. Goetten, D Felix, M. Marino, C. Bil, M. Havermann, and C. Braun, “A review of guidelines and best practices for subsonic aerodynamic simulations using RANS CFD”, in *11th Asia-Pacific International Symposium of Aerospace Technology*, Gold Coast: APISAT 2019, 2019, pp. 227–245, ISBN: 978-1-925627-40-4.

[118] N. van Arnhem, R. Vos, and L. L. Veldhuis, “Aerodynamic loads on an aft-mounted propeller induced by the wing wake”, in *AIAA Scitech 2019 Forum*, San Diego, California: AIAA SciTech Forum, 2019. DOI: `10.2514/6.2019-1093`.

[119] P. R. Spalart and S. R. Allmaras, “One-equation turbulence model for aerodynamic flows”, in *AIAA-92-0439, 30th Aerospace Sciences Meeting & Exhibit*, Reno, Nevada, 1992. DOI: `10.2514/6.1992-439`.

[120] J. Dacles-Mariani, G. G. Zilliac, J. S. Chow, and P. Bradshaw, “Numerical/Experimental Study of a Wingtip Vortex in the Near Field”, *AIAA Journal*, vol. 33, no. 9, pp. 1561–1568, 1995.

[121] P. R. Spalart and C. L. Rumsey, “Effective inflow conditions for turbulence models in aerodynamic calculations”, *AIAA Journal*, vol. 45, no. 10, pp. 2544–2553, 2007, ISSN: 00011452. DOI: `10.2514/1.29373`.

[122] T. Sinnige, T. C. Stokkermans, N. van Arnhem, and L. L. Veldhuis, “Aerodynamic performance of a wingtip-mounted tractor propeller configuration in windmilling and energy-harvesting conditions”, *AIAA Aviation 2019 Forum*, pp. 1–17, 2019. DOI: `10.2514/6.2019-3033`.

[123] ANSYS.Inc, “ANSYS FLUENT Solver Settings Training Material”, *ANSYS Customer Training Material*, no. December, pp. 1–32, 2010.

[124] J. Slater, *NPARC Alliance CFD Verification and Validation Web Site*. [Online]. Available: `https://www.grc.nasa.gov/www/wind/valid/tutorial/spatconv.html`.

[125] L. Eça and M Hoekstra, “Discretization Uncertainty Estimation based on a Least Squares version of the Grid Convergence Index”, *Proceedings of the Second Workshop on CFD Uncertainty Analysis, Instituto Superior Tecnico, Lisbon, Oct*, no. October, pp. 1–27, 2006.

[126] W. F. Phillips and D. F. Hunsaker, “Lifting-line predictions for induced drag and lift in ground effect”, *Journal of Aircraft*, vol. 50, no. 4, pp. 1226–1233, 2013. DOI: `10.2514/1.C032152`.

[127] I. Sadrehaghighi, “Vortex & Vorticity”, Annapolis, MD, Tech. Rep. DOI: `10.13140/RG.2.2.10930.15043/3`.

[128] R. M. Granzoto, L. A. Algodoal, G. J. Zambrano, and G. G. Becker, “Horizontal tail local angle-of-attack and total pressure measurements through static pressure ports and kiel pitot”, in *31st Congress of the International Council of the Aeronautical Sciences*, Belo Horizonte, Brazil, 2018. DOI: `10.1017/aer.2019.68`.

[129] F. Zahle, N. Sørensen, and J. Johansen, “CFD study of a NACA 63-415 aerofoil fitted with stall strips”, Tech. Rep. September, 2002. [Online]. Available: `http://forskningsbasen.deff.dk/Share.external?sp=Se11d42bf-8932-4cdb-ac8e-0ace5847901f{\&}sp=Sdtu`.

[130] U. Kowarsch, M. Keßler, and E. Krämer, “CFD-simulation of the rotor head influence to the rotor-fuselage interaction”, *40th European Rotorcraft Forum 2014*, vol. 1, no. September 2014, pp. 382–393, 2014.

[131] F. De Souza and D. Faghani, “Near-field wing tip vortex measurements via PIV”, in *19th AIAA Applied Aerodynamics Conference*, Anaheim, CA: AIAA, 2001. DOI: `10.2514/6.2001-2451`.

[132] D. Birch, T. Lee, F. Mokhtarian, and F. Kafyeke, “Rollup and near-field behavior of a tip vortex”, *Journal of Aircraft*, vol. 40, no. 3, pp. 603–607, 2003. DOI: `10.2514/2.3137`.

[133] R. Radespiel, R. Niehuis, N. Kroll, and K. Behrends, “Numerical Investigation of the Influence of Pressure Belts on the Stall of a Transport Aircraft in Landing Configuration by David Rohlmann”, in *Advances in simulation of wing and nacelle stall*, vol. 131, 2016, pp. 381–395, ISBN: 9783319211275. DOI: `10.1007/978-3-319-21127-5_23`.

[134] K. C. Leung, “Aerodynamic analysis of the closure flap mechanism in- side the NACA ram-air intake”, Master of Science Thesis, Delft University of Technology, 2020.

[135] F. Nicolosi, S. Corcione, and P. D. Vecchia, “Commuter aircraft aerodynamic design: Wind-tunnel tests and CFD analysis”, *29th Congress of the International Council of the Aeronautical Sciences, ICAS 2014*, pp. 1–13, 2014.

Appendices

A

Geometry: Supplementary material

A.1. Additional information on geometry

Trailing edge shape

The shape of the trailing edge of an airfoil has implications on the physics and numerical solution. Sharp TE are sometimes replaced with round or blunt edges to improve the quality of the grid at the trailing edge of wings [117]. By doing so, however, the Kutta point is shifted ‘behind’ the edge. There is a small wake region which extends the chord length of the airfoil. The thickness at the physical TE also increases. These modifications decrease the adverse pressure gradient and change the pressure distribution across the chord [15]. There is also a slight drag penalty due to the additional wake.

In this study, a sharp TE was used for the cases in ground-run. However, a similar sharp TE geometry in free-flight did not converge for all mesh distributions and numerical settings, irrespective of whether the wake was sufficiently refined or not. It was found that the direction of the side-force measured on the vertical tail acted in the opposite direction. The only way to achieve converged solutions for all cases with wake-refined grids was to replace the sharp TE with a round TE for all wings.

The rounding of the TE was done in OpenVSP. The radius was 1% of the chord length, as per the recommendations of Goetten et al [117].

Dimensions

Once the 3D scanned geometry was made available, the self-developed digital twin was compared with it.

The fuselage shape was very similar between the two. At the rear end, the 3D scanned model had a slightly ‘tighter’ packaging with a sharper upsweep.

The nature of the underside, especially near the main landing gear installations, was more contoured and three-dimensional.

The location of the leading edge of the horizontal tail in the scanned geometry was found to be 125 mm further behind. This was the largest dimensional difference seen between the two models.

A.2. Final geometry: Views

The different views of the finalised geometry are presented here.

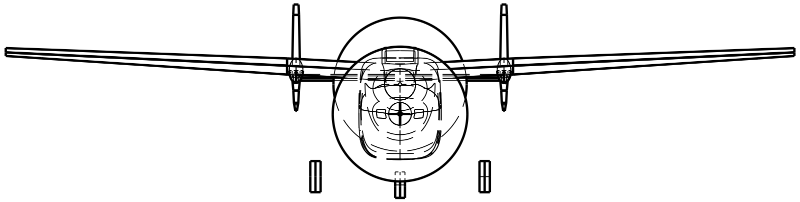

Front view

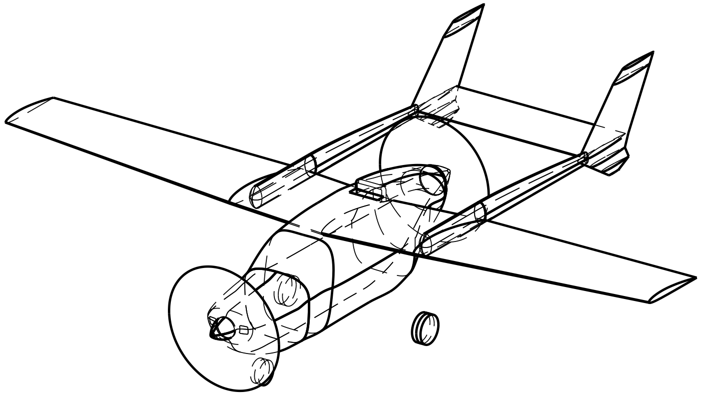

Isometric view

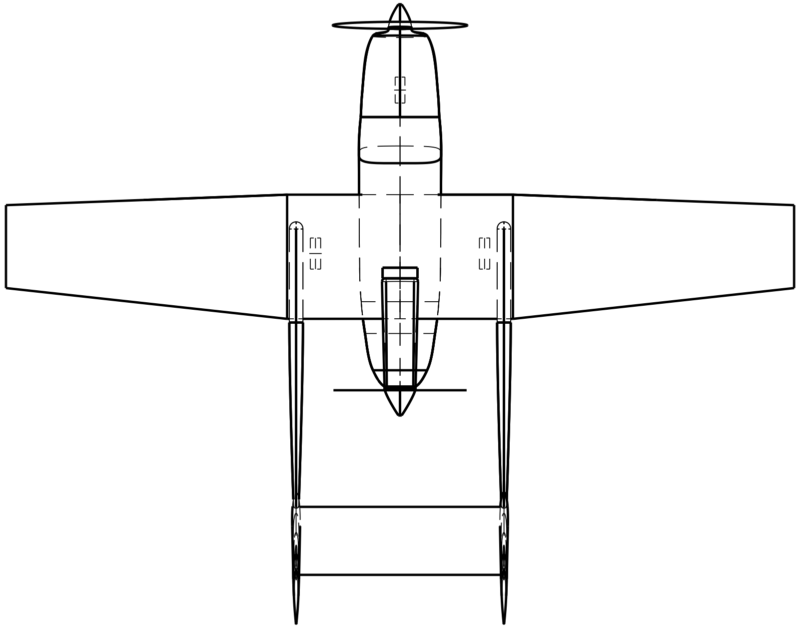

Top View

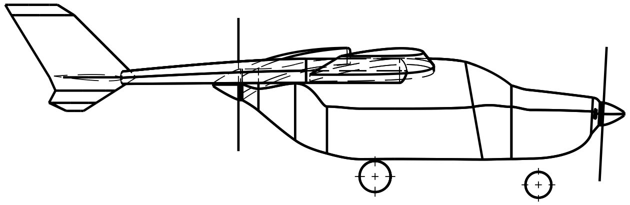

Side View

Skymaster model for the DEAC
Model developed by A. Ramesh

Scale 1:100

A.3. Sources for design

Dimensional data was available in Jane’s [13], Gudmundsson [15], Roskam [59], and the Pilot Operating Handbook (POH) [77].

The geometry was checked against the following diagrams sourced from the POH and through internal communications with students from Deltion College.

Principal Dimensions

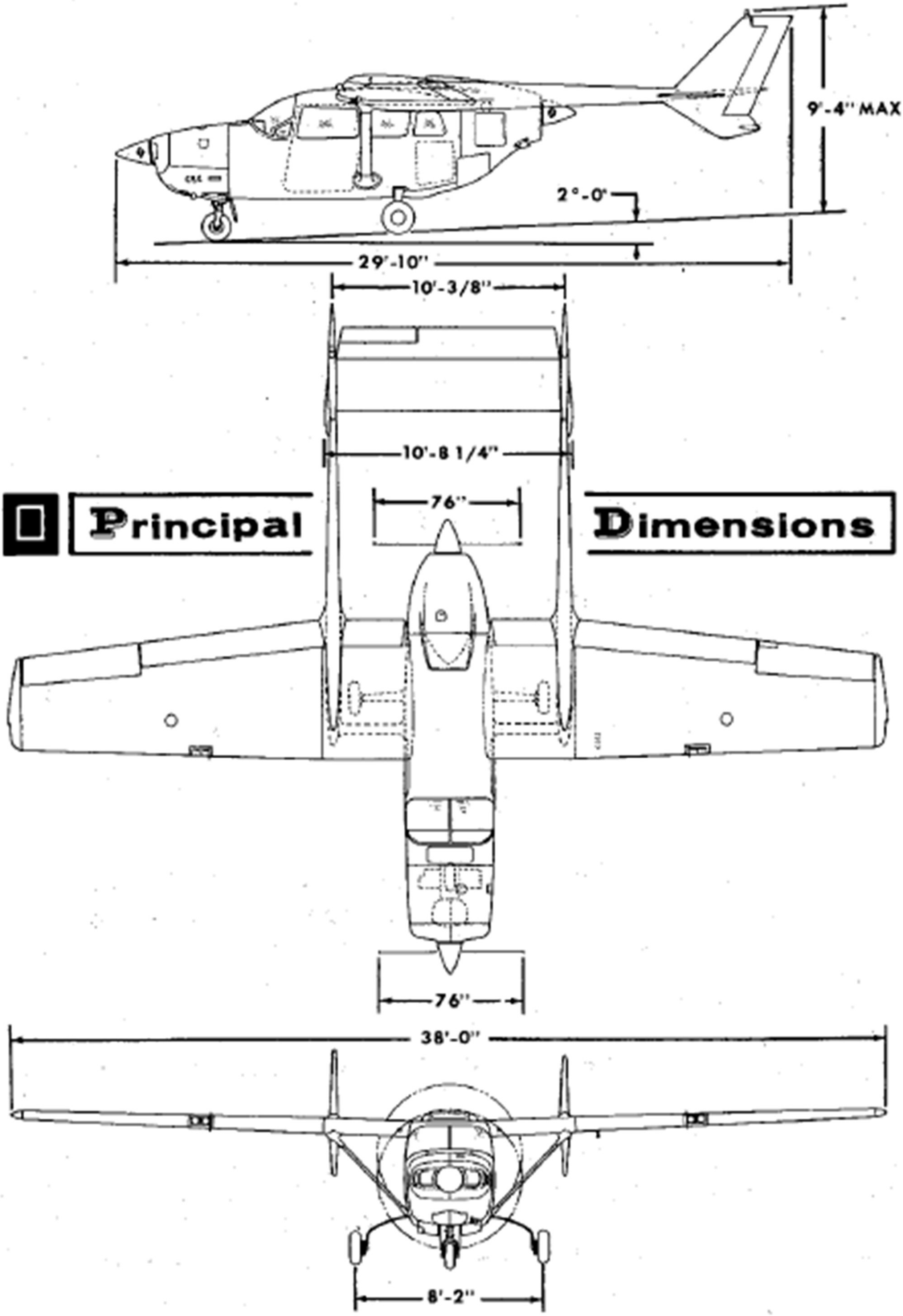

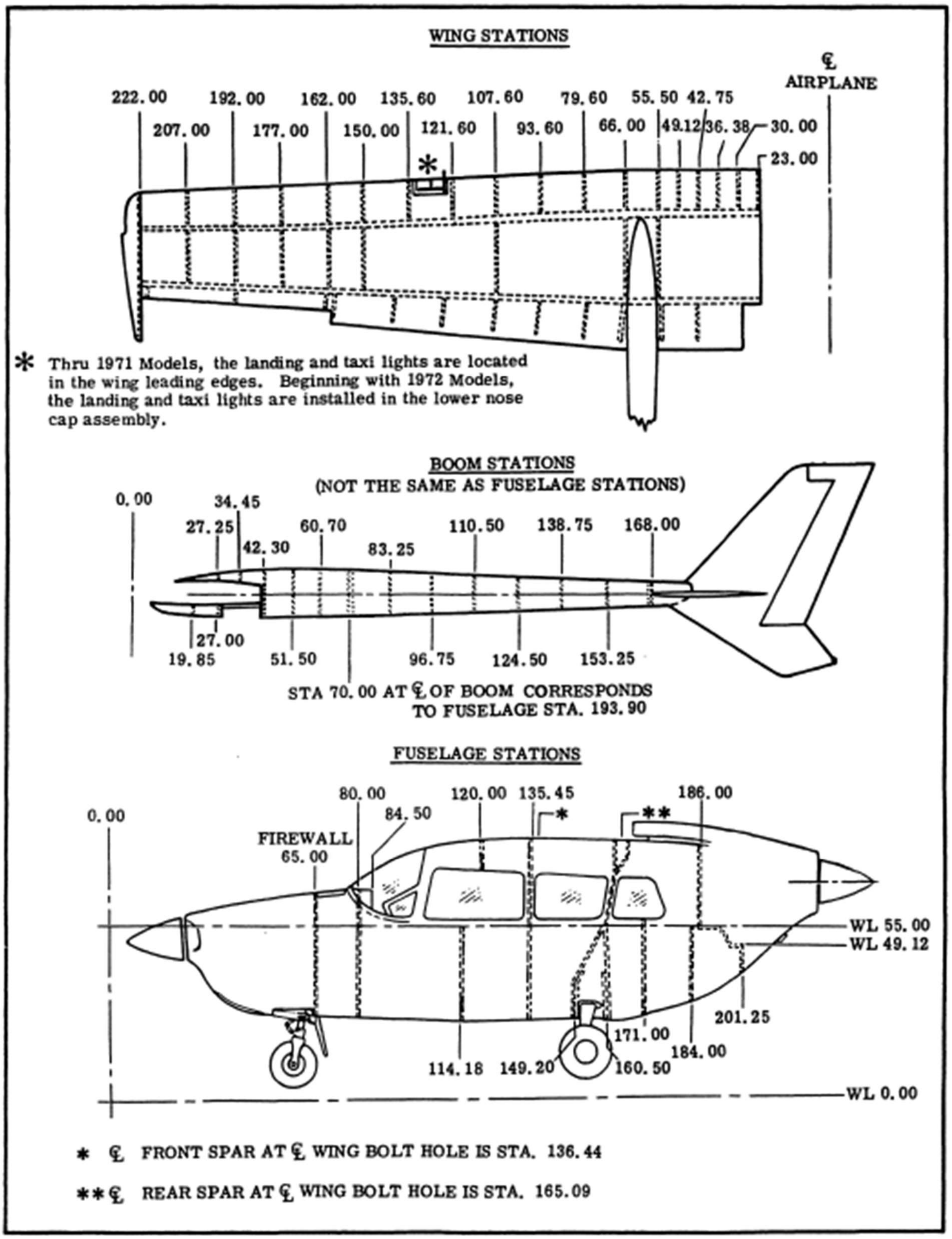

* Thru 1971 Models, the landing and taxi lights are located in the wing leading edges. Beginning with 1972 Models, the landing and taxi lights are installed in the lower nose cap assembly.

STA 70.00 AT ℄ OF BOOM CORRESPONDS TO FUSELAGE STA. 193.90

* ℄ FRONT SPAR AT ℄ WING BOLT HOLE IS STA. 136.44

** ℄ REAR SPAR AT ℄ WING BOLT HOLE IS STA. 165.09

Figure 1-2. Fuselage, Wing and Boom Stations

1975 Cessna.

PRESSURIZED SKYMASTER

&

REIMS / CESSNA PRESSURIZED SKYMASTER

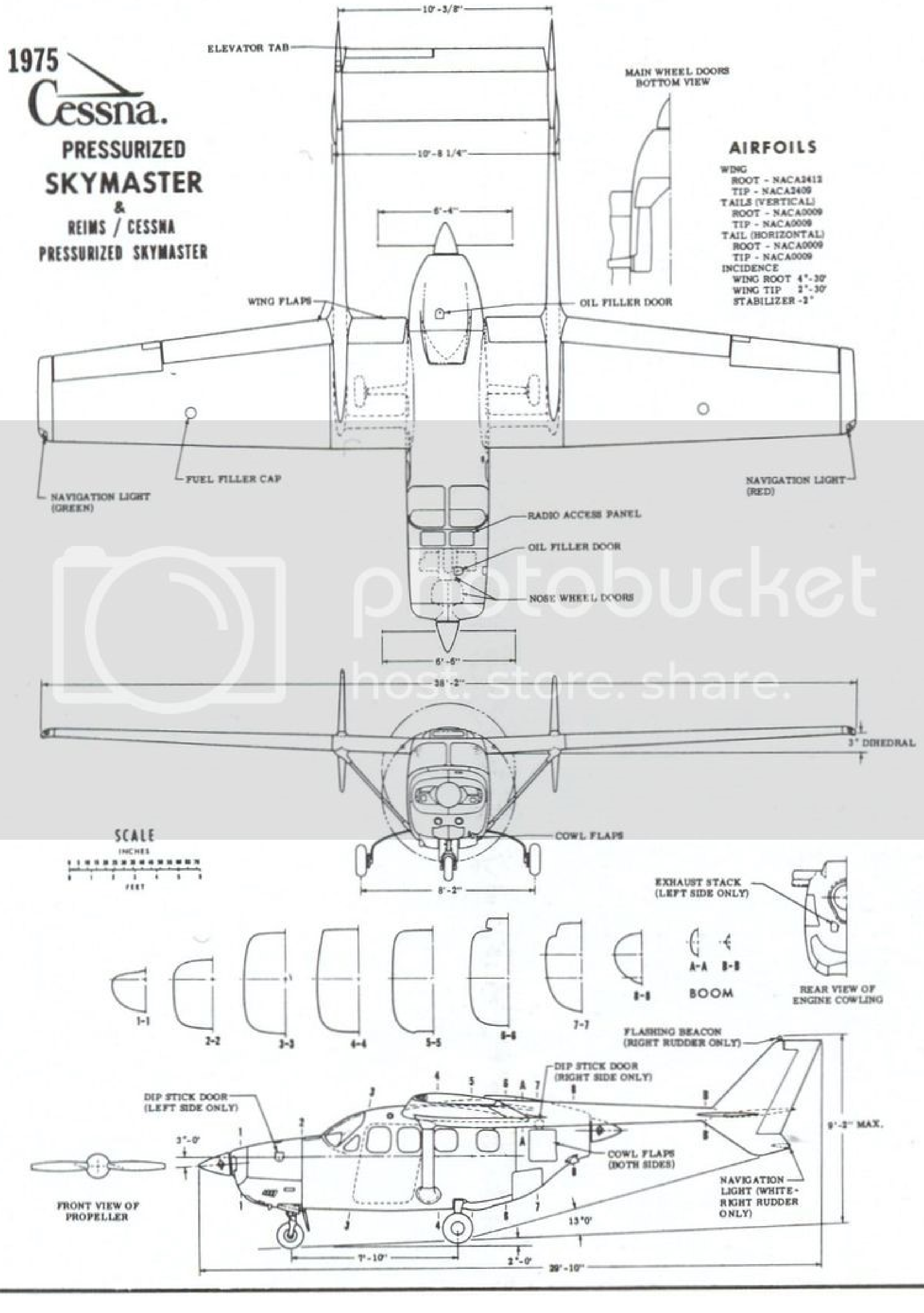

B

Rear engine air intake of the Cessna Skymaster: Supporting information

The rear air intake for the engine and cooling systems of the Skymaster has been a feature of interest and concern in this study.

Of the different locations for the intake face on which to define the numerical boundary condition were studied, two are shown in Figure B.1. It was difficult to design a flow-though nacelle due to the complicated shape of the passage and no information on pressure recovery or such.

By choosing Figure B.1a, the streamlines entering the passage would be allowed to straighten and prevent erroneous results at the boundary. Recirculation was seen within the passage. However, this choice of a tunnel affected the solution in other ways. The scaled residuals of the solution only dropped two orders of magnitude and the forces in newtons being monitored at every iteration showed significant variation in the thousands. This was found to be similar to the work by Leung [134] within the Faculty which was dedicated to air intakes and used the same boundary condition as here.

With the location in Figure B.1b, the residuals dropped an order further and the forces steadied to within a couple of newtons. The unphysical results seen at the boundary face were numerically corrected by changing the definition of the boundary condition as discussed in subsubsection 4.3.2.3.

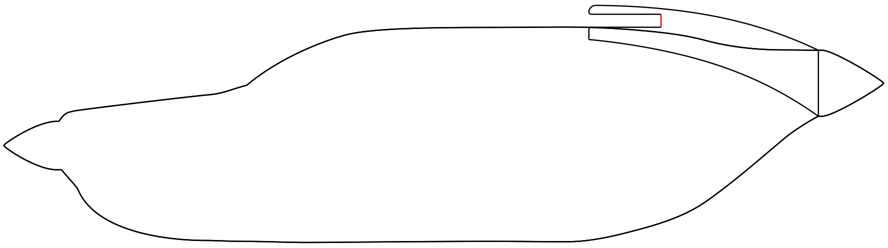

(a) Preferred location of inlet face in a closed passage to straighten the incident streamlines

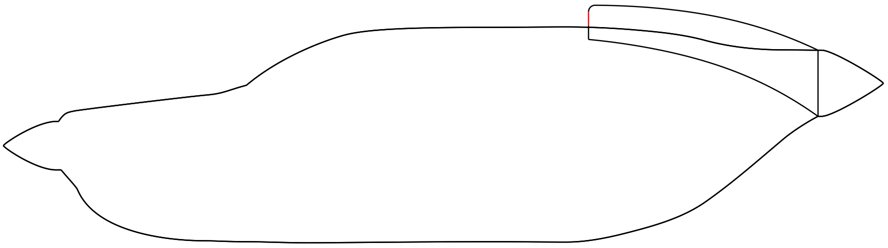

(b) Finalized choice with the inlet face at the lip of intake body

Figure B.1: Different locations, in red, of the inlet face considered for this study (a) preferred (b) final.

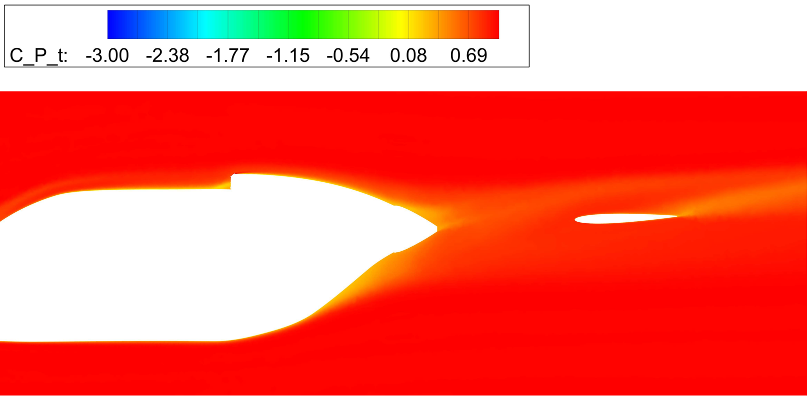

(a) Prescribed mass flow rate on intake face

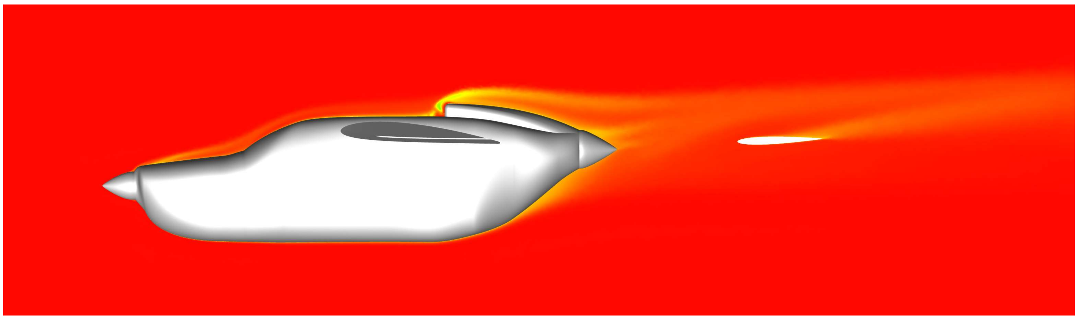

(b) Intake face being treated as a wall

Figure B.2: C_{P_T} contour on symmetry plane comparing the influence of the boundary condition of the rear intake inlet face (a) specified mass flow rate (b) wall.

Figure B.2b shows the large pressure deficit being introduced into the wake due to the inlet face being specified as a wall. In addition to having a known erroneous contribution to the drag force as based on similar experiences in literature [135], the separated flow caused a change to the surface distribution at the tail and is shown in Figure B.3. In comparison, the flow with the specified and treated intake boundary condition shown in Figure B.2a was considered more representative of the testbed and finally used.

It was discussed in section 5.9, that during the development process of the CAD, this scoop inlet body was entirely disregarded. That however, led to the numerical simulations never achieving the specified convergence criteria when investigated on wake-refined grids. It was discussed that the vortical structures behaved differently due its absence. Figure B.4 shows the pressure distribution on the geometric upper side of the tail that was numerically calculated from an analysis where the scoop inlet body was not considered. The changes to the pressure isolines around the region of inverted forces indicates that the vortices formed and interacted differently with this model than in the final reported CFD results.

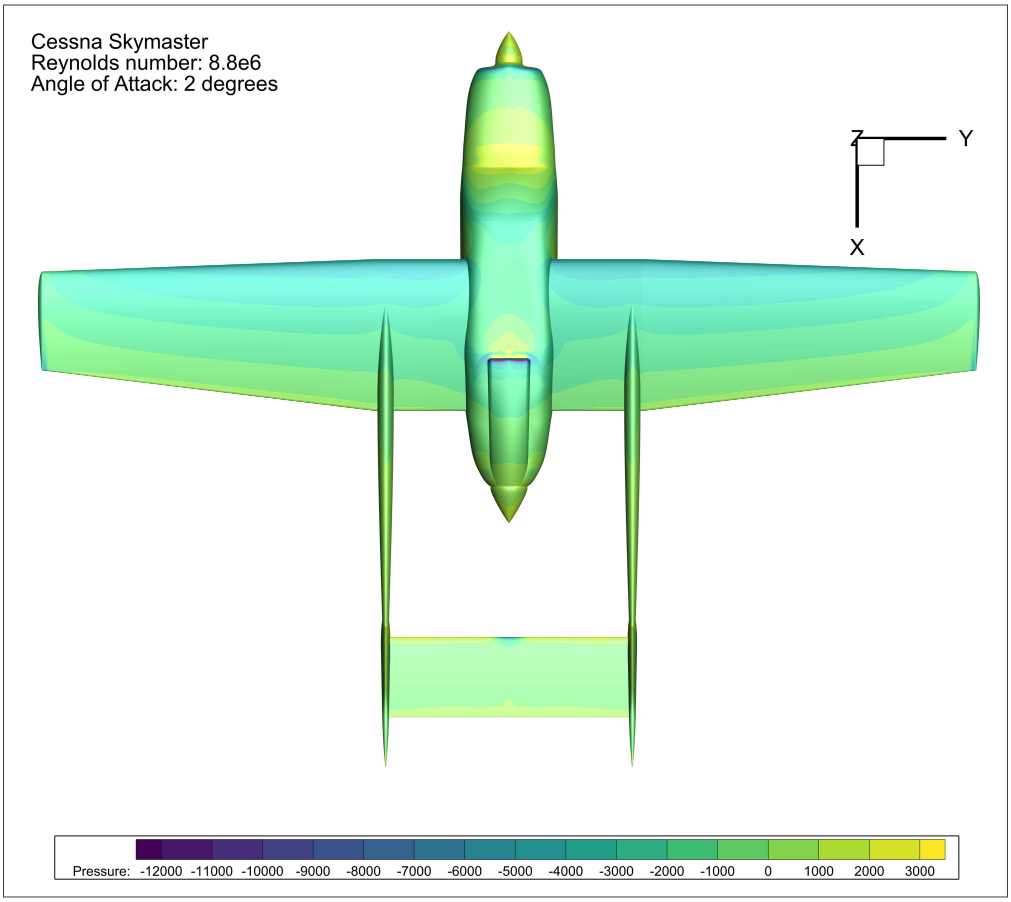

Figure B.3: Effect on pressure distribution on the geometric upper side of the tail due to treating the rear engine air inlet as a wall.

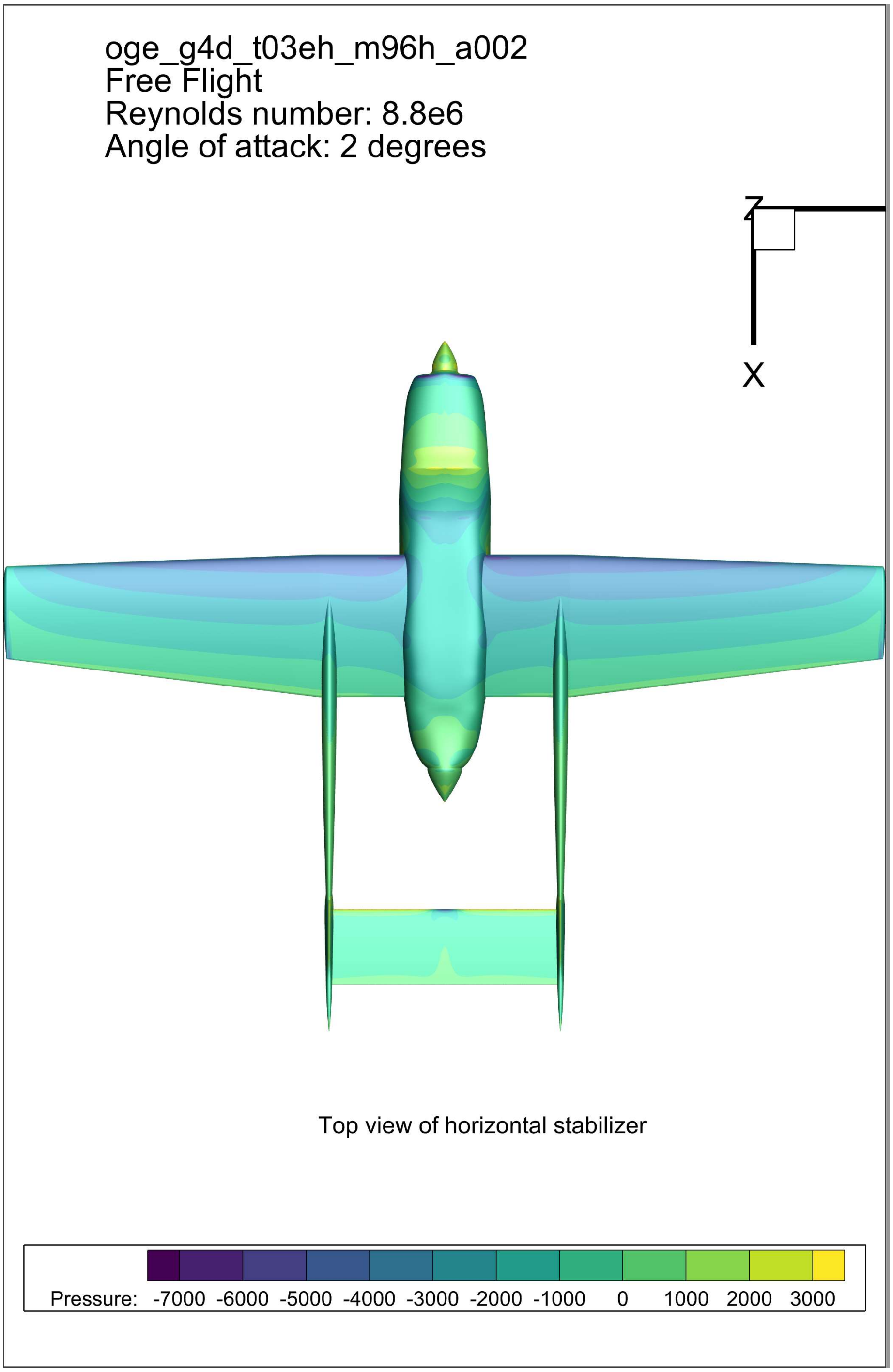

Figure B.4: Effect on pressure distribution on the geometric upper side of the tail due to neglecting the scoop inlet body. Focus on the pressure isolines around the region with the inverted force distribution indicating a difference in the nature of interaction as when compared with the final reported CFD results.

C

Numerical results: Supplementary material

C.1. Oswald efficiency factor

A comparison of the Oswald efficiency e obtained in this study with available values for Cessna aircraft was done to justify the obtained value and its usage in Equation 5.7 to estimate the $C_{D\text{min}}$ from the POH as per the procedure in subsection 5.2.2.

Name	AR	k	e	L/D_{max}	C_L at L/D_{max}
CFD	7.1	0.0590	0.766	17.1	0.6857
From Roskam [59]					
C-150	7	0.0592	0.77	11.3	0.74
C-172	7.5	0.0552	0.77	12.7	0.71
C-180	7.5	0.0572	0.75	13.3	0.66
C-182	7.5	0.0506	0.84	13	0.75
C-185	7.5	0.0494	0.86	15.6	0.65
C-310	7.3	0.0596	0.73	12.6	0.66
From Gudmundsson [15]					
C-OE-2	7.45		0.7		
C-180	7.38		0.75		
C-150	6.94		0.77		
C-172	7.48		0.77		
C-182	7.45		0.84		
C-185	7.38		0.86		
C-177	7.24		0.57		
C-AT-8	5.96		0.61		
C-310	7		0.73		

Table C.1: Drag relevant data on Cessna aircraft as found in literature.

C.2. Drag force distribution on horizontal tail

The influence of a vortex interacting with a wing is to tilt the lift force vector forward on the wing-side influenced by the vortex's relative upward direction. This forward tilting makes the drag force act in a thrust like manner [32]. This was seen in the CFD results obtained in this study.

The method of reporting the force distribution on the horizontal tail, was by integrating the surface pressure and shear forces over sections 2.5% of the span. This was found sufficient for the lift force distribution, but not the drag force distribution. An attempt at creating an automatic macro to peform this was unsuccessful and the manual effort was too much. Hence, the drag forces were not reported in the main content of the report.

Figure C.1 shows the still sensitive results to notionally indicate this characteristic of the force distribution on the tail. This data should not be used as a source of comparison, even for the qualitative difference between free-flight and ground-run, as it not satisfactorily obtained.

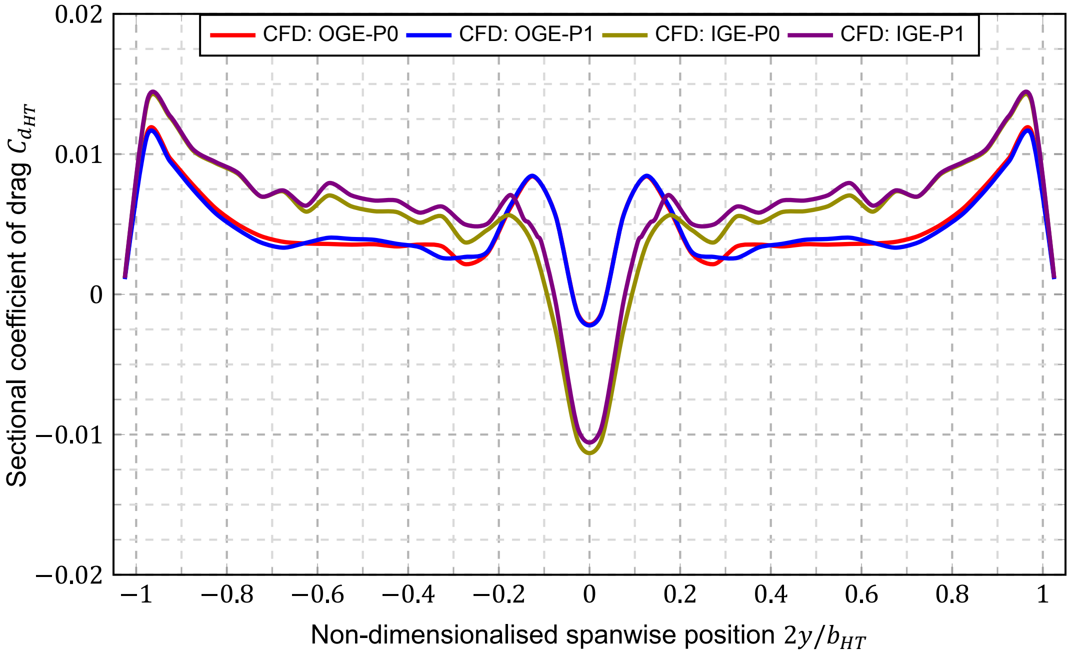

Figure C.1: Spanwise drag distribution of the horizontal tail The results are still sensitive to the size of the strip over which they were calculated. Not to be used as is.